Pulsed Laser Deposition of Iridate and $YBiO_3$ Thin Films

Von der Fakultät für Physik und Geowissenschaften

der Universität Leipzig

genehmigte

DISSERTATION

zur Erlangung des akademischen Grades

Doctor rerum naturalium,

Dr. rer. nat.,

vorgelegt von

Herrn Marcus Jenderka, M. Sc.,

geboren am 22. September 1987 in Halle (Saale).

Gutachter: Prof. Dr. Michael Lorenz
Prof. Dr. Bernd Büchner

Tag der Verleihung: 13.02.2017

Bibliographische Beschreibung

Jenderka, Marcus
Pulsed Laser Deposition of Iridate and $YBiO_3$ Thin Films
Universität Leipzig, Dissertation
113 Seiten, 163 Zitate, 53 Abbildungen, 5 Tabellen

Referat

Die vorliegende Arbeit befasst sich mit dem Dünnfilmwachstum der ternären Oxide Na_2IrO_3, Li_2IrO_3, $Y_2Ir_2O_7$ und $YBiO_3$. All diesen oxidischen Materialien ist gemein, dass sie Verwirklichungen sogenannter Topologischer Isolatoren oder Spin-Flüssigkeiten sein könnten. Diese neuartigen Materiezustände versprechen eine zukünftige Anwendung in der Quantencomputation, in magnetischen Speichern und in elektrischen Geräten mit geringer Leistungsaufnahme. Die Herstellung der hier gezeigten Dünnfilme ist daher ein erster Schritt zur Umsetzung dieser Anwendungen in der Zukunft. Alle Dünnfilme werden mittels gepulster Laserplasmaabscheidung auf verschiedenen einkristallinen Substraten hergestellt. Die strukturellen, optischen und elektrischen Eigenschaften der Filme werden mittels etablierter experimenteller Verfahren wie Röntgenbeugung, spektroskopischer Ellipsometrie und elektrischen Widerstandsmessungen untersucht.

Die strukturellen Eigenschaften von erstmalig in der Masterarbeit des Authors verwirklichten Na_2IrO_3-Dünnfilmen können durch Abscheidung einer ZnO-Zwischenschicht deutlich verbessert werden. Einkristalline Li_2IrO_3-Dünnfilme mit einer definierten Kristallausrichtung werden erstmalig hergestellt. Die Messung der dielektrischen Funktion gibt Einblick in elektronische Anregungen, die gut vergleichbar mit Li_2IrO_3-Einkristallen und verwandten Iridaten sind. Des Weiteren wird aus den Daten eine optische Energielücke von ungefähr 300 meV bestimmt. In $Y_2Ir_2O_7$-Dünnfilmen wird eine mögliche (111)-Vorzugsorientierung in Wachstumsrichtung gefunden. Im Vergleich mit der chemischen Lösungsabscheidung zeigen die hier mittels gepulster Laserplasmaabscheidung hergestellten $YBiO_3$-Dünnfilme eine definierte, biaxiale Kristallausrichtung in der Wachstumsebene bei einer deutlich höheren Schichtdicke. Über die gemessene dielektrische Funktion können eine direkte und indirekte Bandlücke bestimmt werden. Deren Größe gibt eine notwendige experimentelle Rückmeldung an theoretische Berechnungen der elektronischen Bandstruktur von $YBiO_3$, welche zur Vorhersage der oben erwähnten, neuartigen Materiezuständen verwendet werden.

Nach einer Einleitung und Motivation dieser Arbeit gibt das zweite Kapitel einen Überblick über den gegenwärtigen Forschungsstand der hier untersuchten Materialien. Die folgenden zwei Kapitel beschreiben die Probenherstellung und die verwendeten experimentellen Untersuchungsmethoden. Anschließend werden für jedes Material einzeln die experimentellen Ergebnisse dieser Arbeit diskutiert. Die Arbeit schließt mit einer Zusammenfassung und einem Ausblick.

Bibliographic Record

Jenderka, Marcus
Pulsed Laser Deposition of Iridate and $YBiO_3$ Thin Films
Leipzig University, Doctoral thesis
113 Pages, 163 References, 53 Figures, 5 Tables

Abstract

The present thesis reports on the thin film growth of ternary oxides Na_2IrO_3, Li_2IrO_3, $Y_2Ir_2O_7$ and $YBiO_3$. All of these oxides are candidate materials for the so-called topological insulator and spin liquid, respectively. These states of matter promise future application in quantum computation, and in magnetic memory and low-power electronic devices. The realization of the thin films presented here, thus represents a first step towards these future device applications. All thin films are prepared by means of pulsed laser deposition on various single-crystalline substrates. Their structural, optical and electronic properties are investigated with established experimental methods such as X-ray diffraction, spectroscopic ellipsometry and resistivity measurements.

The structural properties of Na_2IrO_3 thin films, that were previously realized in the author's M. Sc. thesis for the first time, are improved significantly by deposition of an intermediate ZnO layer. Single-crystalline Li_2IrO_3 thin films are grown for the first time and exhibit a defined crystal orientation. Measurement of the dielectric function gives insight into electronic excitations that compare well with single crystal samples and related iridates. From the data, an optical energy gap of ≈ 300 meV is obtained. For $Y_2Ir_2O_7$ thin films, a possible (111) out-of-plane preferential crystal orientation is obtained. Compared to chemical solution deposition, the pulsed laser-deposited $YBiO_3$ thin films presented here exhibit a biaxial in-plane crystal orientation up to a significantly larger film thickness. From the measured dielectric function, a direct and indirect band gap energy is determined. Their magnitude provides necessary experimental feedback for theoretical calculations of the electronic structure of $YBiO_3$, which are used in the prediction of the novel states of matter mentioned above.

After the introduction and motivation of this thesis, the second chapter reviews the current state of the science of the studied thin film materials. The following two chapters introduce the sample preparation and the employed experimental methods, respectively. Subsequently, the experimental results of this thesis are discussed for each material individually. The thesis concludes with a summary and an outlook.

Contents

1 Introduction and motivation

Today's conventional computers are reaching the physical limits of how fast and small they can be built. The need of ever faster and more flexible computing requires research to explore new routes towards novel and intelligent computational devices. One promising route are quantum computers offering the potential to significantly increase computational power. Quantum computers could perform calculations today's digital computers cannot. Such tasks are for instance searching large databases, simulating quantum systems and finding prime factors of large numbers. The latter has particular real-world application in encryption-breaking. However, a physical realization of a scalable quantum computer still requires enormous scientific and engineering efforts. It is hindered by the very fragile superposition states due to their interaction with the environment via, e.g., thermal fluctuations. This decoherence ultimately leads to high computational error rates. The difficult task is hence to construct a machine with a large number of well-enough isolated quantum bits and low error rate.

The so-called topological quantum computer is a proposed class of quantum system with a particular fault-tolerance [1, 2]. Such a quantum system is based on non-abelian, anyonic quasiparticles appearing in two dimensions [3]. These anyons have been predicted to exist in fractional quantum Hall states and ultracold atoms in optical lattices [2], in quantum spin liquids [4] and at the interface of superconductor-topological insulator heterostructures [5]. Of relevance for this thesis is the topological insulator which is a novel kind of quantum matter discovered in recent years. Topological insulators were predicted theoretically in 2006 [6] prior to their experimental discovery in 2007 [7]. Two- and three-dimensional topological insulators have an insulating bulk energy band gap, but harbor metallic edge or surface states, respectively. These states are topologically protected against lattice distortions and non-magnetic impurities and enable nearly dissipationless coherent transport with very high mobilities - properties, that may also lead to application in magnetic memory or low-power electronic devices [8–10]. A detailed review on topological insulators can be found in an extensive colloquium by M.Z. Hasan and C.L. Kane [11]. This thesis is concerned with the experimental study of novel oxide material candidates for such topological insulators.

Topological insulators have been realized in very common materials under standard ambient conditions, i.e., without the need for low temperatures and high magnetic fields. In 2006, the theoretical prediction was made that a two-dimensional topological insulator, having quantized edges states, may be realized in (Hg,Cd)Te quantum wells without external magnetic field [6]. This so-called quantum spin Hall effect was indeed observed experimentally a year later in

molecular beam epitaxy-grown (Hg,Cd)Te quantum wells exceeding a critical well width of 6.3 nm: A quantum-Hall-like plateau in the longitudinal resistance as a function of gate voltage at zero magnetic field and 30 mK was the signature for the proposed quantized charge conductance [7]. Through further theoretical efforts it was realized, that a three-dimensional variant, the strong topological insulator, is possible [12–14]. Subsequently, in 2008 and 2009 binary chalcogenides Bi_2Se_3, Bi_2Te_3 and Sb_2Te_3 were proposed and observed to be three-dimensional topological insulators having large bulk gaps and metallic surface states with linear dispersion [15–20]. They were considered as the most promising materials for future experiments. Since then, experimental and theoretical efforts in the novel field of topological insulators have been devoted to the synthesis of optimized samples, the characterization of the topological surface states by either surface sensitive spectroscopy - such as angle-resolved photoelectron spectroscopy - or transport measurements, device fabrication, and the search for novel candidate materials. The challenge with current topological insulators, however, still is the high conductivity of the underlying bulk hindering purely surface dominated transport. In fact, many topological insulators have only a small bulk bandgap and are degenerately *n*-doped. There is hence a need for novel material candidates with large enough bulk bandgap allowing operation at room-temperature and with high bulk resistance to discern surface from bulk conduction.

First-principles methods such as density functional theory have been widely used to predict topological insulators [21]. The methods involved must give a proper estimate of the bandgap and also consider spin-orbit coupling and electronic correlations. If all these ingredients play a role in describing the system, the calculations become more involved and expensive. Hence, the first materials predicted all had negligible electronic correlations, such as Bi_2Se_3. With the inclusion of electronic correlations in the calculations, a wider spectrum of novel candidate materials apart from binary compounds is possible. Among the novel materials with greater material flexibility are ternary XYZ Heusler [22–24], chalcogenides [25–28] and ABC_2 chalcopyrite [29] compounds. In 3*d* transition metal oxides spin-orbit coupling is merely perturbative. But when going to the 5*d* elements spin-orbit coupling increases, while electronic correlations decrease due to the more extended orbitals. The result is a system with spin, orbital and charge degrees of freedom of comparable size that can be investigated for non-trivial topology. Among such systems are the honeycomb lattice iridates Na_2IrO_3 and Li_2IrO_3, as well as the pyrochlore $Y_2Ir_2O_7$ [30–36]. Together with cubic $YBiO_3$, whose electronic structure including spin-orbit coupling and Coulomb interactions was recently revisited by theorists [37, 38], they were proposed as novel material candidates for either a topological insulator or a spin liquid. All four material are the object of study in this thesis.

Since 2003, experiments on honeycomb iridate single crystals and polycrystalline powders

found antiferromagnetic order below 15 K. In Na_2IrO_3, the dominant antiferromagnetic Heisenberg exchange interactions place the material far within a zig-zag magnetically ordered regime [39–42]. Li_2IrO_3, in contrast, exhibits incommensurate spiral order and is placed in the vicinity of the predicted spin liquid phase due to stronger competing ferromagnetic and anisotropic Kitaev interactions [43–45]. Subsequently, the author realized the first heteroepitaxial Na_2IrO_3 thin films by means of pulsed laser deposition (PLD) and a weak antilocalization effect, associated with topological surface states [46], was observed in magnetoresistance [MJ1]. Later, Alidoust *et al.* [47] reported on a metallic surface band feature in Na_2IrO_3. A review of the current state of the science can be found in Sec. 2.1. So far, $Y_2Ir_2O_7$ could not be realized in single-crystalline form. This restricts the accurate determination of its magnetic ground state configuration, which is critical to the existence of the proposed exotic phases. This situation is detailed in the material review contained in Sec. 2.2. Generally, experimental results on Na_2IrO_3, Li_2IrO_3 and $Y_2Ir_2O_7$ are often based on powder-averaged data because of the very small size of available single crystals. A precise investigation of the microscopic structure is thus difficult. For example, neutron diffraction experiments are a challenge due to the high absorption cross-section of iridium and the low sample volume. Heteroepitaxial, single-crystalline films, however, have inherently large surface-to-volume ratios that could resolve this issue. In the present work, heteroepitaxial thin films with defined out-of-plane and in-plane orientation are prepared on up to 2”-diameter substrates via PLD. Moreover, these films lay the foundation for terahertz pump-probe spectroscopy, compositional studies on $(Na_{1-x}Li_x)_2IrO_3$ currently not available in single crystals, and the investigation of strain-induced effects in the future. In fact, by way of chemical doping, epitaxial strain or pressure, it is predicted to realize a topological insulator [36, 48] or spin liquid [44, 49] phase in Na_2IrO_3 and Li_2IrO_3. Generally, heteroepitaxial thin films are a prerequisite for future device application of the proposed novel states of matter.

In this work, the structural, surface-morphological and stoichiometrical properties of the heteroepitaxial iridate thin films are monitored *ex situ* in order to optimize the deposition process. Initially, the preparation and phase analysis of polycrystalline source targets, prepared by different sintering methods, is described. The present study of Na_2IrO_3 thin film represents a continuation of the author’s previous experimental efforts [MJ1,MJ 2]. Here, Na_2IrO_3 films are deposited on up to 2”-diameter substrates. Neutron diffraction on 1.5” samples is performed to determine the magnetic ordering vector but is impeded by a sizeable in-plane mosaicity. Mosaicity is reduced significantly by deposition of an intermediate *c*-ZnO layer. A larger focus is put on the first heteroepitaxial Li_2IrO_3 thin films [MJ3]. Temperature- and magnetic field-dependent electrical transport measurements are performed and compared with single crystal and powder data given in the literature. Three-dimensional Mott variable range hopping con-

duction is found as similarly observed in Na_2IrO_3 thin films [MJ1]. By means of spectroscopic ellipsometry the dielectric function is determined, and electronic excitations and an optical band gap of $\approx$ 300 meV are observed. Heteroepitaxy of $Y_2Ir_2O_7$ gives tentative indications of a defined (111) out-of-plane orientation on ZrO_2:Y(111) substrates.

Within the last ten years, $YBiO_3$ thin films were investigated primarily in terms of a buffer layer for epitaxial $YBa_2Cu_3O_{7-\delta}$ superconductors [50–53]. Furthermore, there exist two recent but conflicting theoretical studies on the topology of the electronic structure of $YBiO_3$ [37, 38]. However, in both band structure calculations assumptions with respect to the crystal structure of $YBiO_3$ were made, that do not agree with previous experimental findings. In this work, heteroepitaxial $YBiO_3$ thin films are successfully grown on $LaAlO_3$, $SrTiO_3$, MgO, ZrO_2:Y and Al_2O_3 single-crystalline substrates by means of PLD. The direct and indirect electronic bandgaps of YBO, which have not been reported before, are determined via spectroscopic ellipsometry and optical transmission spectroscopy. Together with the experimentally observed crystal structure, this provides critical feedback for revisiting electronic band structure calculations in the future. Furthermore, the thin film's surface morphology is scrutinized with respect to their usefulness in future angle-resolved photoelectron spectroscopy (ARPES) measurements. ARPES could directly detect the proposed topological surface states, but requires atomicly flat surfaces.

This work is embedded within the Deutsche Forschungsgemeinschaft (DFG) research project LO790/5-1 "Oxide topological insulator thin films" and the collaborative research centre (SFB) 762 "Functionality of Oxide Interfaces" at the Semiconductor Physics Group, Leipzig University. The following people have made significant contributions to this work: Polycrystalline source targets were prepared by G. Ramm via solid-state synthesis. Spark plasma-sintered targets were provided by Dr. Ji Zou and Prof. Dr. Z.J. Shen, of Stockholm University. Gas pressure sintering was performed in collaboration with Prof. Dr. Y. Joseph and U. Sczech of Institut für Elektronik- und Sensormaterialien, TU Bergakademie Freiberg. A major part of the electrical contacting and photolithography was carried out by M. Hahn. Neutron diffraction on Na_2IrO_3 films was performed at the Institut Laue-Langevin in Grenoble together with Prof. Dr. Dmytro Inosov of TU Dresden. A collaboration with Dr. Z. Alpichshev, group of Prof. Dr. N. Gedik at Massachusetts Institute of Technology, was initiated for terahertz and optical pump-probe spectroscopy experiments. Scanning electron microscopy and energy-dispersive X-ray spectroscopy were performed by J. Lenzner. Additional chemical analyses were provided by G. Ramm via secondary neutral mass spectroscopy. Optical transmission data were provided by U. Teschner. The more involved spectroscopic ellipsometry measurements and data modeling were done by S. Richter and Dr. R. Schmidt-Grund. Magnetic field-dependent, low-temperature electrical

transport and magnetometry measurements were performed by Dr. J. Barzola-Quiquia and F. Bern of the Division of Superconductivity and Magnetism, Leipzig University.

Part I

Materials and methods

2 Materials

In $5d$ transition metal oxides (TMOs) new physics arise due to the interplay of strong spin-orbit coupling (SOC) and electronic correlations on comparable energy scales, as well as strong crystal field effects and lattice geometry. As a matter of fact, when going from $3d$ to $5d$ orbitals electronic correlations decrease due to a larger extent of the $5d$ electronic wave functions. Simultaneously, SOC increases as it is proportional to the fourth power of the atomic number Z. For iridium atoms, $Z = 77$. Among these TMOs, the iridates are promising candidates to show a lot of unconventional physics. Most significant recent attention was attracted by the layered perovskite Sr_2IrO_4, the pyrochlore Y_2Ir_2O7, and by the honeycomb lattice materials A_2IrO_3 (A = Na, Li). These materials have been put forward as potential high-T_C superconductors [54], quantum spin liquids [30, 32], novel $j_{\text{eff}} = 1/2$ spin-orbital Mott insulators [55, 56], topological (Mott) insulators [31, 33–36], or as Weyl semimetals [57, 58].

In the last decade, the fluorite-type ternary oxide $YBiO_3$ was studied in terms of a buffer layer for epitaxial $YBa_2Cu_3O_{7-\delta}$ high-temperature superconductors [50–53]. Recent theoretical studies, however, debated the topology of the electronic band structure of $YBiO_3$ [37, 38].

2.1 Honeycomb lattice iridates A_2IrO_3 (A = Na, Li)

In A_2IrO_3, with A being either Na or Li, magnetic Ir atoms with pseudospin-1/2 moments form a quasi-two-dimensional honeycomb lattice. Each atom is coordinated by six oxygen atoms forming edge-sharing IrO_6 octahedra that mediate the superexchange between neighboring spins. The IrO_6 octahedra are fairly symmetric but exhibit a slight flattening perpendicular to the layer stacking [41, 42]. Such structural distortions indicate the presence of a trigonal crystal field in addition to the cubic crystal field. The trigonal crystal field plays an important role in determining the electronic band structure [36]. The voids of the honeycomb lattice are filled by the A atoms. These AIr_2O_6 layers stacked along the c axis alternate with A-only layers. An in-plane offset of successive Ir honeycombs gives rise to a monoclinic distortion. In Na_2IrO_3, a large amount of stacking faults along the c direction of the $NaIr_2O_6$ layers is common [39, 41, 42]. The final crystal structure can for Na_2IrO_3 be described by a monoclinic $C2/m$ unit cell with unit cell parameter of about $a = 5.43$ Å, $b = 9.39$ Å, $c = 5.61$ Å and $\beta = 109.04°$ as confirmed by single crystal X-ray diffraction and structural optimization calculations [41, 42]. Li_2IrO_3 is best described by a $C2/c$ unit cell with 20 % smaller volume. In this sense, Li effectively induces chemical pressure.

The honeycomb iridates are based on Ir^{4+} ions with $5d^5$ electronic configuration. While simple band theory suggests they should be metallic, experiments showed insulating behavior. The $5d$ electron correlations alone are too weak to drive a conventional Mott insulator transition as in many $3d$ TMOs with much stronger electron correlations. Instead, a combination of much stronger SOC and modest electron correlations leads to the observed novel spin-orbital Mott insulator with a $j_{\text{eff}} = 1/2$ ground state. The presence of strong spin-orbit coupling in Sr_2IrO_4, Na_2IrO_3, and $Y_2Ir_2O_7$ was recently confirmed and quantified by X-ray absorption spectroscopy [59]. A good example for such j_{eff} physics is Sr_2IrO_4 where $j_{\text{eff}} = 1/2$ states arise from t_{2g} levels being split by spin-orbit coupling [55, 56]. For both Na_2IrO_3 and Li_2IrO_3, the description of the underlying electronic structure by j_{eff} physics was justified by resonant inelastic X-ray scattering (RIXS) [60]. The octahedral crystal field emanating from the oxygen octahedra causes a fairly large splitting $10Dq \approx 10$ eV between t_{2g} and e_g states and yields a t_{2g}^5 low spin state for the Ir^{4+} ions [61]. Now, for strong SOC the t_{2g} states effectively correspond to orbital angular momentum $L = 1$ and split into effective total angular momentum $j_{\text{eff}} = 1/2$ and $j_{\text{eff}} = 3/2$ doublet and quartet bands, respectively. The $j_{\text{eff}} = 1/2$ band is half-filled and now the moderate electron correlations can open a Mott gap. Trigonal distortions of the IrO_6 octahedra [41, 42] produce further crystal-field splittings within the t_{2g} manifold. If this splitting becomes comparable to the SOC, the $j_{\text{eff}} = 1/2$ and $j_{\text{eff}} = 3/2$ states mix and the relevant microscopic model becomes a different one [62–64]. In RIXS measurements on Na_2IrO_3 and Li_2IrO_3, low energy excitations around 0.7-0.8 eV from $j_{\text{eff}} = 1/2$ to $j_{\text{eff}} = 3/2$ states showed a splitting arising from the trigonal crystal field of about 110 meV [60]. This value is much smaller than the SOC energy scale of about 0.4 eV in Na_2IrO_3 and also $Y_2Ir_2O_7$ [59] and thus validates the applicability of j_{eff} physics in Na_2IrO_3 and Li_2IrO_3 similar to Sr_2IrO_4 [55, 56].

A significant structural detail in A_2IrO_3 is that the ideal 90° Ir-O-Ir bonding geometry causes a suppression of isotropic magnetic interactions between the Ir atoms [30]. As a consequence, otherwise subdominant bond-dependent anisotropic interactions play the main role in this material. Together with the strong SOC of the Ir atoms with spin-1/2, this bond anisotropy on a honeycomb lattice takes the form of the Kitaev model. The Kitaev model harbors a quantum spin liquid ground state with non-abelian anyonic particle excitations which are desired for realizing a so-called topological quantum computer [4]. The possibility of realizing the Kitaev model explains the current research interest in Na_2IrO_3, Li_2IrO_3, its three-dimensional structural extension, the hyper- and harmonic honeycomb structure [65, 66]. and other material candidates such as Li_2RhO_3 [67, 68] and $RuCl_3$ [69]. Recently, direct evidence for bond-directional interactions in Na_2IrO_3 leading to strong magnetic frustration was found by diffuse magnetic X-ray scattering [70].

On the other hand, tight-binding model analyses and first-principles band structure calculations [31, 36], as well as density-matrix renormalization group calculations [71] suggest Na_2IrO_3 and Li_2IrO_3 as a possible topological insulator showing the quantum spin Hall (QSH) effect at room temperature. In these theories the topologically non-trivial band structure, with protected metallic surface states and Dirac cone at the *M* point, is the result of a stacked quantum spin Hall state. In earlier works of the author [MJ1,MJ 2], a signature of such a topological phase was found in the magnetoresistance of Na_2IrO_3 thin films by observing the weak antilocalization effect that is associated with topological surface states [46]. In addition, recent angle-resolved photoelectron spectroscopy (ARPES) experiments on Na_2IrO_3 found a metallic surface band feature crossing the Fermi level with nearly linear dispersion [47]. However, the Fermi level crossing is at the Γ point, which is in contrast to theory and the correct description of surface metallicity in Na_2IrO_3 might hence be more exotic.

A characteristic of a quantum spin liquid is the absence of magnetic ordering down to zero Kelvin. However, Na_2IrO_3 and Li_2IrO_3 show long-range antiferromagnetic order at low temperatures as inferred from susceptibility, heat capacity and isothermal magnetization [39, 44]. Such magnetic order is a clear deviation from the Kitaev model prediction. The susceptibility follows the Curie-Weiss law down to about 200 K and gives an effective local magnetic moment of μ_{eff} = 1.79(2)μ_B and μ_{eff} = 1.83(5)μ_B for Na_2IrO_3 and Li_2IrO_3, respectively [39, 44]. These values are close to the value of 1.74μ_B expected for effective spin-1/2 moments on the honeycomb lattice. In contrast, a neutron diffraction study on Na_2IrO_3 yielded a considerably smaller magnetic moment of 0.22(1) μ_B/Ir [41]. In both materials, magnetic susceptibility and heat capacity measurements show a sharp anomaly at T_N = 15 K indicating antiferromagnetic ordering [39, 44]. Negative Curie-Weiss temperatures Θ = -125(6) K and Θ = -33(3) K for Na_2IrO_3 and Li_2IrO_3, respectively, suggest substantial antiferromagnetic geometric and magnetic frustration in these compounds [44]. However, in Li_2IrO_3 they are weaker. Resonant X-ray magnetic scattering on Na_2IrO_3 explicitly showed that the moments point mainly along the crystallographic *a*-direction and that the alternating honeycomb planes are antiferromagneticly coupled [40]. Inelastic neutron scattering [42] and neutron diffraction [41] experiments found that the magnetic ordering pattern is of zig-zag type as supported by density functional theory calculations [40, 44]. In contrast, Li_2IrO_3 shows incommensurate spiral order [45].

Temperature dependent in-plane dc electrical resistivity of both single crystals [39] and thin films [MJ1] follows an insulating three-dimensional Mott variable hopping dependence in a large range of temperatures between 300 and 40 K. The local moments and long-range antiferromagnetic order together with variable range hopping conductivity indicate that Na_2IrO_3 and Li_2IrO_3 are Mott insulators. ARPES with *in situ* potassium doping and optical conductivity

measurements on single crystals of Na_2IrO_3 give an 340 meV insulating gap for particle-hole excitations [72]. In addition, the insulating gap is open well above T_N = 15 K. In Na_2IrO_3 thin films a smaller optical gap of 200 meV was found by Fourier-transform infrared transmission [MJ1,MJ 2]. Using RIXS, the electronic structure of Na_2IrO_3 and Li_2IrO3 was investigated and crystal-field-split *d*-*d* excitations were resolved. The level splitting induced by noncubic crystal-fields is much smaller than the SOC energy scale, validating the applicability of j_{eff} physics in A_2IrO_3 [60].

Following the proposal [30] that the Kitaev model [4] can be realized in the honeycomb lattice iridates A_2IrO_3, a minimal magnetic Hamiltonian was introduced: the Heisenberg-Kitaev (HK) model [32]. It interpolates between the antiferromagnetic Heisenberg and the exactly solvable, ferromagnetic Kitaev model. Theoretical analyses reveal the presence of an extended spin liquid phase near the Kitaev limit, an intermediate stripy antiferromagnetic state, and a Néel-ordered state close to the Heisenberg limit. Neighboring Ir moments can communicate via two 90° Ir-O-Ir superexchange paths, i.e., hopping between Ir 5*d* and O 2*p* orbitals, or via direct Ir-Ir 5*d* overlap. In the Ir-O-Ir exchange paths, the isotropic part exactly vanishes leaving a finite anisotropic magnetic interaction. This results in the ferromagnetic Kitaev term with three distinct types of nearest-neighbor bonds hosting Ising-like couplings [30]. The direct Ir-Ir overlap is the antiferromagnetic Heisenberg exchange. The later experimental findings of zigzag and incommensurate spiral order in Na_2IrO_3 [40–42] and Li_2IrO_3 [45], respectively, required modifications of the HK model. Extending the parameters of the HK to a previously overlooked range found zigzag-type order and reproduced the high-temperature magnetic susceptibility data [73]. To reproduce the spin-wave spectrum obtained from inelastic neutron scattering data [42], substantial longer range Heisenberg exchange up to third neighbors was included in the HK model, which stabilize the observed zig-zag magnetic order [74]. Longer range Heisenberg exchange alone was not sufficient to account for a spiral ordered phase in Li_2IrO_3, but instead also next-nearest-neighbor Kitaev interactions had to be included [45]. The detailed comparisons of experiment and theory suggest that Na_2IrO_3 is in a deeply antiferromagneticly ordered regime [44, 49], and Li_2IrO_3 is close to the desired spin-liquid phase [44]. By way of epitaxial strain, *c*-axis pressure or chemical pressure, i.e. doping, it is predicted that both materials can still be pushed into the topological insulator [36, 48] or spin-liquid phases [44, 49].

Magnetic depletion by random substitution of Ir^{4+} by nonmagnetic Ti^{4+}, i.e, the series $Na_2(Ir_{1-x}Ti_x)O_3$ and $Li_2(Ir_{1-x}Ti_x)O_3$ was achieved up to $x \leq 0.3$ and $x \leq 0.55$, respectively [75, 76]: Due to very similar ionic radii of Ir^{4+} and Ti^{4+} the changes in lattice parameters are within 1 % only. The Curie-Weiss temperature continuously changes from -125 K to -18 K at x = 0.26. Only for the lowest doping x = 0.015 long-range magnetic order is still observed.

Otherwise, non-magnetic Ti doping quenches the magnetic long range order. Instead, a separation of zero-field cooled and field cooled curves suggest spin-glass behavior at low temperature as also confirmed by ac susceptibility. For the Li system the Curie Weiss temperature remains unchanged and spin glass freezing persists up to $x = 0.55$. Also magnetic doping with Ru ions resulted in an enhancement of magnetic frustration indicated by an increase of Θ and a reduction of T_N [76].

Substituting Na by smaller Li ions reduces chemical pressure along the c axis and is suggested to induce spin-liquid behavior in Na_2IrO_3 [49]. Recently, single crystals of $(Na_{1-x}Li_x)_2IrO_3$, $0 \leq x \leq 0.9$, were presented as a continuous solid solution [77]. With this isoelectronic doping a controlled structural interpolation between Na_2IrO_3 and Li_2IrO_3 was achieved. Li doping caused a systematic decrease in the lattice parameters (the ionic radius of Li is approximately 25% smaller than that of Na) maintaining the honeycomb structure. At intermediate doping of $x \approx 0.7$ the Néel temperature is maximally suppressed, $T_N = 1.2$ K, and magnetic frustration is highest. In contrast, K doping achieving negative chemical pressure was shown to increase T_N. The results led to speculate that at this intermediate doping the material is closest to the spin liquid phase. Contrary to Ref. [77], a second study of isoelectronic doping in the series $(Na_{1-x}Li_x)_2IrO_3$ showed that only for $x \leq 0.25$ uniform solid solutions are formed [78]. The X-ray study of structural changes in this low Li doping region suggests that there is no effective c-axis pressure. This isoelectronic doping region shows antiferromagnetic order with a gradual reduction of T_N from 15 to 5 K and no spin glass freezing as in doping with Ti. Furthermore, heat capacity data suggest a suppression of the ordered moment by Li doping. For larger Li content, $0.25 \leq x \leq 0.6$, a miscibility gap emerges. In this region a phase separation into ordered $Na_2LiIr_2O_6$, with alternating Na and $LiIr_2O_6$ planes, and a Li-rich phase close to pure Li_2IrO_3 is found. In another study, suppression of long-range magnetic order even at smallest doping levels was confirmed [79]. The magnetic excitation spectrum in inelastic neutron scattering changes significantly with doping and reveals the formation of a spiral magnetic phase in Li-doped Na_2IrO_3 [79].

2.2 Pyrochlore lattice iridate $Y_2Ir_2O_7$

Rare-earth pyrochlore iridates with composition $A_2Ir_2O_7$ provide a playground to study the effects of strong spin-orbit coupling and geometric frustration on magnetic and electronic properties of a correlated material. These geometrically frustrated model systems have the possibility to show a variety of phenomena such as spin-liquid behavior in $Pr_2Ir_2O_7$ [80]. In certain regimes of electronic correlations, the strength of which can be varied by choice of the A-site

ion, topologically nontrivial phases have been predicted, such as a topological Mott insulator [33–35] or a Weyl semimetal [57, 58]. For $Y_2Ir_2O_7$ the antiferromagnetic all-in/all-out magnetic configuration is suggested resulting in the Weyl semimetal state [57]. For this reason much experimental effort has so far been put into determining the Ir^{4+} magnetic order in the pyrochlore iridates which is critical to the theoretical predictions.

$Y_2Ir_2O_7$ has a cubic pyrochlore structure with space group $Fd3m$ (no. 227) and lattice constant a = 10.18 Å [81]. The structure consists of Y_2O and Ir_2O_6 sublattices and each of them form a three-dimensional network of corner-sharing, slightly distorted octahedrons [81, 82]. In $Y_2Ir_2O_7$, the tetravalent Ir^{4+} ions are in the low-spin S = 1/2 configuration.

Temperature-dependent static magnetic susceptibility shows a clear magnetic transition around T_{M1} = 150 K [81–84], which is related to a weak ferromagnetic contribution [84]. The Curie-Weiss temperature, obtained from a fit above 200 K, is negative suggesting strong antiferromagnetic interactions [84]. Below this onset of strong magnetism at T_{M1}, a bifurcation of zero-field-cooled and field-cooled curves is observed that is attributed to the Ir^{4+} sublattice as Y^{3+} is a diamagnetic ion [81, 85]. In two studies, evidence for a second magnetic transition was found around T_{M2} = 190 K [84, 85]. Below T_{M1}, muon spin rotation and relaxation measurements found a well-defined spin precession frequency, indicating commensurate long-range magnetic order [85]. The intermediate temperature magnetic phase below T_{M2} = 190 K shows short-range order. Further analysis of the measured muon spin precession frequencies by probabilistic modeling and *ab initio* calculations determined the magnetic structure to be of the all-in/all-out type [86]. The antiferromagnetic interactions indicated by negative Curie-Weiss temperatures and the small magnitude of magnetization are consistent with this magnetic configuration [84]. These results are particularly important with respect to the existence of proposed exotic ground states such as the Weyl semimetal state.

However, small hysteresis loops observed in magnetization versus magnetic field curves below 150 K [82, 84] cannot be explained by an ideal all-in/all-out antiferromagnetic ground state. Instead, it suggests the existence of a weak ferromagnetic component in addition to the antiferromagnetic background. A comprehensive study of undoped and Ca-doped $Y_2Ir_2O_7$ demonstrated the enhancement of this weak ferromagnetism by Ca hole doping through a combination of magnetic characterizations and electron spin resonance measurements [84]. A vertical shift in M-H curves suggests strong coupling between the weak ferromagnetic phase and the large antiferromagnetic background. X-ray photoelectron spectroscopy showed the existence of both Ir^{4+} and impurity Ir^{5+} ions in the $Y_2Ir_2O_7$ samples. The amount of Ir^{5+} increases with Ca doping. Hence, the possible origin of the weak ferromagnetism is associated with these Ir^{5+} ions [84].

$Y_2Ir_2O_7$ is a Mott insulator and shows nonmetallic behavior between 300 and 10 K [83–85, 87]. Resistivity has a kink at the magnetic transition T_{M1} [84, 85] and is dominated by three-dimensional variable range hopping below and above T_{M1} [85, 88]. Hole-doped $Y_{2-x}Ca_xIr_2O_7$ polycrystals showed a metal-insulator transition between $x = 0$ and $x = 0.2$ [83, 84]. In the $R_2Ir_2O_7$ series (R = rare-earth element) a metal-nonmetal transition is also observed between Eu and Gd in the periodic table. This transition is well correlated with the ionic radius of the A-site element and attributable to a tuning of electron correlations among Ir 5*d* electrons [85, 87]. In Mott-insulating $Y_2Ir_2O_7$, high-resolution photoelectron spectroscopy found evidence for strong Coulomb interactions among the Ir 5*d* electrons [89].

Specific heat measurements give no indication of a magnetic phase transition down to 1.8 K, i.e., an onset of magnetic ordering [81, 87]. However, a gradual increase of C/T is indicative of the freezing of magnetic moments. Powder-neutron-diffraction experiments found no evidence of a structural phase transition or long-range magnetic order between 290 and 3.4 K, but put an upper bound on the ordered Ir^{4+} moment of $0.5\mu_B$ [82]. The lack of long-range order in neutron scattering is explained by the large absorption cross section of the Ir nuclei and inherently small ordered moments. These factors prevent the observation of any spin order in these polycrystalline samples.

To accurately determine the Ir^{4+} ground state configuration, large volume, high quality single crystals are necessary. Thus far, their preparation was unsuccessful by means of conventional solid state synthesis or floating-zone techniques. Polycrystalline samples often contain impurity phases, namely unreacted starting materials Y_2O_3 and IrO_2 [81, 82, 84, 85]. However, both phases are either paramagnetic or diamagnetic and thus have negligible influence on the magnetic properties. In any case, pulsed laser deposition can be an alternative route for obtaining single-crystalline $Y_2Ir_2O_7$ samples that might, in turn, lead to more precise results in, e.g., neutron diffraction experiments.

2.3 Fluorite-type $YBiO_3$

Apart from the iridium-based oxides there is also a prediction for $YBiO_3$ (YBO) to be a novel topological insulator candidate [37]. According to band structure calculations by Jin *et al.* [37], $YBiO_3$ could provide several advantages for a practical application of topological insulator-based devices. Its bandgap is large enough to enable operation at room temperature. The bulk resistivity is very high, in the order of several MΩm [51], and much larger than in the Bi_2Se_3 family. In transport experiments, this highly insulating phase is argued to be beneficial in distin-

guishing surface from bulk degrees of freedom. In the past, YBO was successfully deposited on $LaAlO_3$ and $SrTiO_3$ single-crystalline substrates as a buffer layer for epitaxial high-temperature superconductor $YBa_2Cu_3O_{7-\delta}$ films [50–53]. YBO has hence shown its potential to form interfaces with band insulators and superconductors and presents a promising platform to realize the exotic phenomena predicted to emerge at these interfaces, such as Majorana Fermions [5].

Solid solutions of $Y_xBi_{(1-x)}O_{1.5}$ with $0.1 < x < 0.5$ are stable at room temperature and crystallize in a face-centered cubic (fcc), defective fluorite-type structure with space group $Fm\bar{3}m$ [90–93]. The crystal structure is illustrated in Fig. 2.1(a). Bi^{3+} and Y^{3+} cations are randomly distributed on the cation sublattice at the $4a$ $(0,0,0)$ sites. Oxygen ions with only a 75 % occupancy have a complex distribution over lattice and interstitial sites. Primarily, oxygen ion displacement is from the ideal $8c$ $(0.25,0.25,0.25)$ sites along <111> to the $32f$ $(x,x,x,)$ sites. A small amount of oxygen and cation displacement to $48i$ $(0.5,y,y)$ and $24e$ $(z,0,0)$ was also suggested [91]. Overall, Bi^{3+} and Y^{3+} are coordinated to six oxygen ions distributed over the eight corners of a cube; the remaining corners are vacant which is expressed in the 25 % oxygen deficiency. With Y-doping x, the <111> displacement and the oxide ion conductivity are reduced [91]. Similarly, a linear decrease of the lattice parameter a following Vergard's rule was observed [92, 93]. At $x = 0.5$, YBO has a cubic lattice constant a of 5.4188 Å [93]. The pseudo-cubic primitive cell of YBO has a lattice constant $a' = a/\sqrt{2}$, which is closely matched to $YBa_2Cu_3O_{7-\delta}$ but also to cubic $LaAlO_3$ and $SrTiO_3$.

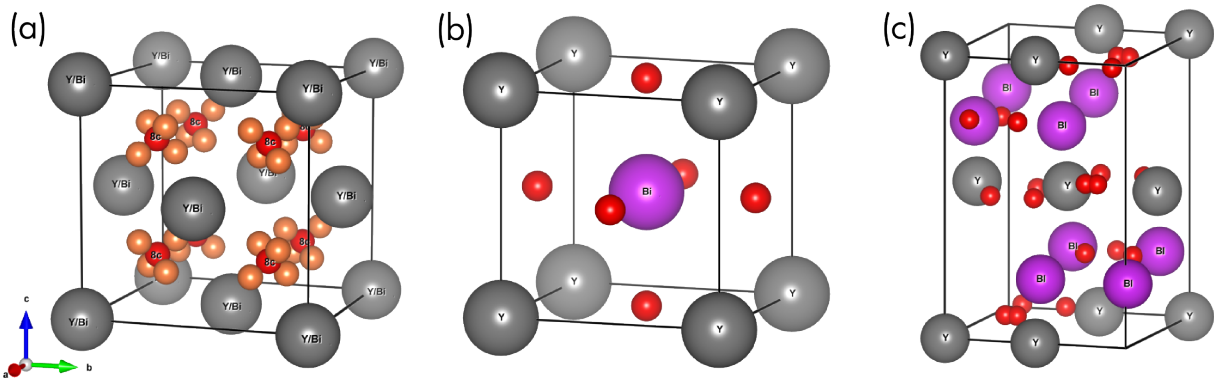

Figure 2.1 (Experimental and theoretical crystal structures of YBO. (a) Experimentally observed fcc defective fluorite-type structure with space group $Fm\bar{3}m$ [90–93]. Y^{3+} and Bi^{3+} cations are randomly distributed over the $4a$ sites (gray). The six oxygen anions are distributed over the $8c$ sites (red) and a fraction of these anions is displaced along <111> to the $32f$ sites (orange). For this illustration, the structural parameters of Ref. [93] were used. (b) The Undistorted $CaTiO_3$-type $Pm\bar{3}m$ perovskite structure with a = 5.428 Å, as used in band structure calculations by Jin *et al.* [37], is proposed to be topologically *non-trivial*, but structurally unstable [38]. (c) Instead, the distorted $GdFeO_3$-type perovskite *Pnma* structure is predicted to be structurally stable and also lowest in energy, but topologically *trivial* [38].

In 2013, Jin *et al.* [37] investigated the electronic structure of YBO with the inclusion of spin-orbit coupling (SOC) by first-principles calculations. For unknown reasons, they assumed

an undistorted, simple cubic $CaTiO_3$-type perovskite structure ($Pm\bar{3}m$) for their calculations together with the larger lattice constant $a = 5.428$ Å [50] of the defective fluorite-type structure, see Fig. 2.1(b). As discussed below, this assumed crystal structure was shown to be unstable in a subsequent paper by Trimarchi *et al.* [38]. Nevertheless, the essence of the initial band structure calculations shall be discussed in the following.

Without inclusion of SOC, YBO shows a topologically trivial semi-metallic phase. The valence bands near the Fermi level are composed mostly of oxygen *p* states. The valence band maximum at the *R* point originates from a hybridization of Bi 6*s* and O 2*p* orbitals into an *s*-like singlet. Upon inclusion of SOC, a band inversion of the $j_{\mathrm{eff}} = 1/2$, split off from the Y 4*d* t_{2g} band by SOC, and the *s*-like singlet bands occurs at the *R* point and a transition to a topological insulating phase takes place. YBO then has an indirect gap of 0.183 eV and a topologically non-trivial gap of 0.330 eV around the *R* point. In case of the (001) and (110) surface configurations of the $Pm\bar{3}m$ space group, the Dirac cone appears within the bandgap; for (111)-orientation, the Dirac cone lies within the bulk conduction band. The transition to the topological insulator is not caused solely by the SOC of Y 4*d*, which is in fact relatively small, but rather driven by the SOC of the Bi 6*p* states and their *d*-*p* hybridization with Y 4*d*.

The subsequent electronic band structure calculations by Trimarchi *et al.* [38] found, by means of density functional theory and total energy minimization, that the undistorted simple cubic $Pm\bar{3}m$ perovskite structure of YBO is unstable. Depending on the position of the Bi ion, either on the O_{h} or cavity site, the equilibrium lattice parameter is 4.405 and 4.349 Å, respectively, and the system is in either a metallic or a topologically trivial insulator state. If one allows the oxygen octahedra to tilt and the Y^{3+} and Bi^{3+} cations to shift, the lowest-energy distorted orthorhombic *Pnma* perovskite structure is obtained that is also predicted to be a trivial insulator, see Fig. 2.1(c). No theoretical lattice constants were given for this orthorhombic structure. Furthermore, the total energy of the experimentally observed defective fluorite-type $Fm\bar{3}m$ structure was found to be very close to the theoretical, topologically trivial *Pnma* structure. Although no electronic band structure was calculated for the experimentally observed defective fluorite-type structure, Trimarchi *et al.* conclude, that YBO is not a topological insulator.

There clearly exists a discrepancy between experimentally observed $Fm\bar{3}m$ crystal structure of YBO [90–93] and those used in theoretical band structure calculations aimed at identifying the topology of the ground state [37, 38]. Consequently, the ground state's true nature remains yet to be uncovered in theory but especially in experiment. In this work, the band gap energy will be determined via optical transmission and spectroscopic ellipsometry in order to corroborate either of the two theoretical reports mentioned above. Moreover, an experimental band gap energy might greatly help in revisiting the band structure theoretically.

In the past, epitaxial YBO thin films with (100) preferential orientation have primarily been prepared by chemical solution deposition on $LaAlO_3$(001) and $SrTiO_3$(001) substrates [50, 51, 53]. YBO powders are paramagnetic and showed no phase transition between room temperature and 1050 °C. Surface-morphology is "pebble-like" and grain sizes are in the order of 50 nm [51]. Root-mean-squared surface roughness ranges from 2.6 to 1.8 nm at a film thickness of 150 and 40 nm, respectively [53]. Reflection high-energy electron diffraction analyses found an amorphous or nano-crystalline surface texture at a thickness of 150 nm and a discrete biaxial texture component at 40 nm. Reports on pulsed laser deposition of YBO thin films are rather scarce [52, 94]. PLD-grown (001)-oriented YBO thin films on $LaAlO_3$ substrates were epitaxially grown with a root-mean-squared roughness of as low as 3.4 nm [52]. For higher growth temperatures, $\approx$ 700 °C, YBO layers have improved compactness and surface flatness. On LSAT(001) substrates, stoichiometric YBO(100) films growth was optimized at an oxygen partial pressure of 0.1 mbar and at 670 °C [94].

3 Sample preparation

3.1 Pulsed laser deposition of ternary oxide thin films

In this work, heteroepitaxial ternary oxide thin films are prepared by pulsed laser deposition (PLD) on various oxide single-crystalline substrates. Starting from multi-element solid-state source targets, prepared mostly by solid-state synthesis, the material systems are realized with the optimal set of accessible deposition parameters. Because of its flexibility, various material systems such as large-area high-T_c superconductor, wide-bandgap semiconductor and multiferroic thin films have been realized with PLD at Leipzig University in the past 25 years [MJ4]. The following section gives a brief overview about the deposition method. It is mostly based on the discussions given in Refs. [95] and [96], and the references therein.

Experimental setup Pulsed laser deposition is a physical vapor deposition process, performed in a vacuum. A schematic of the PLD setup is shown in Fig. 3.1. In the deposition chamber an atmosphere with oxygen partial pressures of as low as 10^{-4} mbar exists. Through a quartz glass window, a pulsed 248-nm KrF excimer-laser (Coherent Lambda Physik LPX305) is directed into the chamber. The excimer laser is focused via an adjustable lens onto a rotating polycrystalline target at an angle of about 45°. At a pulse width of 25 ns and a laser energy of 600 mJ, the used 24 × 10 mm^2 aperture results in an energy density, or laser fluence, of about 2 Jcm^{-2}. The lens position affects the laser fluence at the target surface by defocusing the laser beam. Since the photon energy of the laser is larger than the bandgap of the target material, the laser pulse is absorbed and transformed into heat. Absorption and dissipation of the incident laser energy is confined to the immediate area and results in the vaporization of the target surface. The ablated material consists of vaporized elemental, ionized and excited species of preferably low mass, as well as heavier, clustered target constituents. All ejecta constitute a so-called plasma plume that propagates normal to the target and towards the substrate. Substrate and target have a separation of about 8 cm. The substrate is held at a defined temperature by means of a resistive heater. When the plasma plume reaches the substrate, the species adsorb onto its surface and a film grows.

The resistively heated substrate is being rotated to ensure homogeneous film growth and thickness, because the material in the quite nonuniform, highly forward-directed plasma plume has a $\cos^n(\Theta)$ density distribution [97]. An eccentric motion and simultaneous rotation of the target disc causes a uniform ablation of the target material. Deposition parameters such as oxygen partial pressure p_{O2} and growth temperature T_g are significant for the structural and morphological

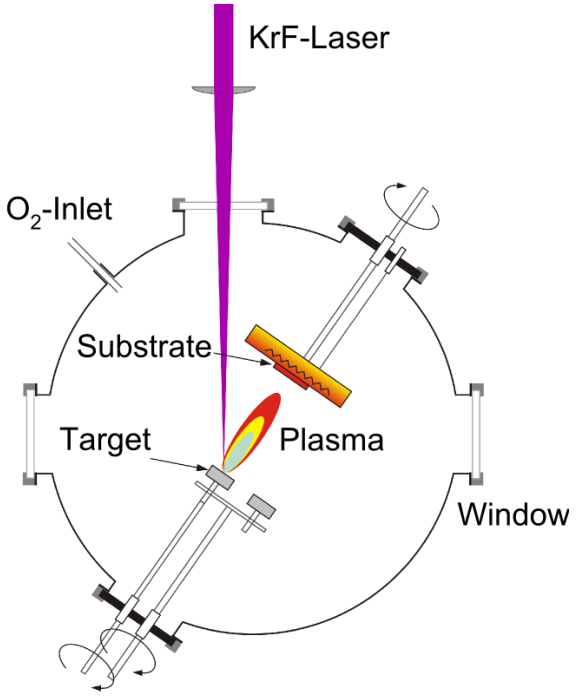

Figure 3.1 Pulsed Laser Deposition. Schematic view of a PLD setup. [By courtesy of M. Lange, formerly Leipzig University.]

properties of the thin films. Oxygen partial pressure affects the formation of oxygen vacancies and reduces the kinetic energy of the plasma species via scattering processes. The scattering of plasma species and background gas is dependent on the size and mass of the species. Oxygen can also react with, i.e. oxidize, the plasma species. Thus, the gas atmosphere plays a significant role in adjusting the film stoichiometry. The kinetic energy of the plasma species also affects the growth rate. For large values, even resputtering can occur. The substrate temperature determines the reorganization of the adsorbed material on the surface; it affects their diffusion and desorption, and the growth mode of the film.

The used substrate holders enable the mounting of 5 $\times$ 5 and 10 $\times$ 10 mm^2, as well as 1.5" and 2" diameter substrates. Prior to deposition, the chamber and substrate are usually heated up to elevated temperatures between 550 and at most 650 °C, which corresponds to heater powers of 400 and 600 W, respectively; p_{O2} is set to 0.01 mbar. To allow for thermal equilibration and a removal of possible volatile contaminants, the temperature is held for at least 60 minutes. Always, 300 laser pulses with a frequency of 1 Hz are applied to the target, in order to form a nucleation layer on the substrate surface. Subsequently, pulse frequency is increased to usually 15 Hz. After deposition, the sample is annealed *in situ* for 5 min at an oxygen partial pressure of 800 mbar. During all these steps, the growth temperature remains unchanged. Finally, a 15-min cool-down step follows.

Physical processes of PLD To date, a complete model of the many physical processes encompassing PLD is still not available and optimization of a novel thin film system still requires experimental exploration of a large part of the parameter space. Yet, for a basic understanding of the physics involved in PLD, three locally separated processes are usually considered: the laser-target interaction, the physics of the plasma plume, and the growth kinetics at the substrate surface.

The desired stoichiometric transfer arises from the non-equilibrium absorption of high laser energy within a small volume of the target. Short high-intensity pulses limit the dissipation of absorbed photon energy, because the thermal penetration depth $l_t \approx 2(D\tau)^{1/2}$, with thermal diffusion constant D, is low for pulse durations of, e.g., $\tau = 25$ ns. Also, a high absorption coefficient α of the target material at the applied laser wavelength is responsible for a low penetration via the optical penetration depth $l_\alpha = \alpha^{-1}$. Note, that all materials deposited in this work fulfill this condition, because their bandgap energies are all well below the laser photon energy. Moreover, the energy density, or laser fluence, must exceed a certain ablation threshold in order to enable the formation of a plasma. Below that threshold, thermal evaporation of particles occurs, for which the stoichiometry of the particle flux is determined primarily by the individual vapor pressures of the species. However, at higher laser fluence, the ablated species absorb more energy than is required for evaporation. The surplus in energy is absorbed by the ablated species and leads to the formation of the plasma. Now, the stoichiometry of the plasma no longer depends on the vapor pressure and is instead determined mainly by the target composition. Typical laser fluences required for inorganic insulators are between 0.5 and 2 Jcm^{-2} [98]. Finally, the combination of all these factors leads to a congruent laser-induced ablation that preserves the target stoichiometry and results in the stoichiometric transfer to the substrate.

In the plasma plume, ablated species have different kinetic energies ranging from a few tenth to several hundred eV [97]. At these energies, however, stress might be introduced through defect formation [99]. In oxides, also preferential sputtering of oxygen can occur at high kinetic energies that results in oxygen-deficient films. Effective control over the kinetic energy of the ablated species is possible via the laser energy and via collisions with the background gas, i.e, via the oxygen partial pressure.

For the deposition of ternary oxides from a stoichiometric, polycrystalline source target, the oxygen background serves several purposes. First, the applied partial pressure p_{O2} depends on the thermodynamic stability of the desired phase. Second, the interaction between ablated species and oxygen gas often produces oxidized molecular species in the plume, that, in turn, may have improved surface wetting properties over their reduced counterparts. Third, inelastic

scattering with the oxygen background determines the kinetic energy of the ablated species that is intimately connected to the growth kinetics on the substrate. At a fixed partial pressure, the distance between target and substrate can be adjusted to obtain a similar effect. Since inelastic scattering depends on the mass and size of the species, the background can critically influence the stoichiometry of both plasma and film. Lastly, the oxygen partial pressure also affects the shape and expansion of the plasma plume.

Growth temperature T_g affects the diffusion and desorption of adsorbed species on the substrate surface. While the former is relevant for the growth mode, the latter affects the stoichiometry of the film. Although short high-intensity laser pulses usually facilitate stoichiometric transfer of the target composition, this does not necessarily provide stoichiometric film growth at elevated substrate temperatures. If any of the cation species posses a high vapor pressure, the sticking coefficient on the substrate surface becomes problematic and a corresponding deficiency arises. Typical examples are K, Li, Na, Mg, Pb, Cd, Zn [97] and Bi, as observed in this work. As a consequence of this cation evaporation, there will be an upper constraint on the deposition temperature. To compensate for the loss of volatile species, both mosaic [97] and off-stoichiometric targets are an option.

Each laser pulse provides sufficient material for the deposition of a submonolayer of the desired phase only. The achieved growth rates in PLD are thus typically between 0.001 and 1 Å per pulse [97] and depend on, e.g., the laser spot size and fluence, as well as the target-substrate separation and oxygen partial pressure. Hence, under ideal conditions PLD allows submonolayer control of epitaxial film growth that is relevant for defined multilayers and interfaces.

Growth modes Since PLD is a non-equilibrium process, film growth must be understood from kinetic processes instead of thermodynamical ones [96]. Kinetic processes on the substrate surface involve diffusion, desorption and adsorption of ablated species. Diffusivity, in general, is limited by the substrate temperature, the terrace width of vicinal substrates and the pulse frequency. It accounts for an incomplete surface reorganization of ablated species between two laser pulses. Crystallization of a heteroepitaxial film requires nucleation of ablated species on the substrate surface. PLD allows for a high supersaturation and thus for extremely high nucleation rates.

Nucleation takes place at the solid-vapor interface formed by the substrate, or the grown film, with the plasma plume. Plasma and solid have vapor pressures p and p_0, respectively. Vapour pressure describes the tendency to leave the solid state. If $p > p_0$, the vapour is supersaturated with respect to the solid and nucleation occurs. This usually holds for laser induced ablation for which p is extremely large. Supersaturation is expressed via the Gibbs-Thompson equation

[96]

$$\Delta\mu = kT\ln(p/p_0). \tag{3.1}$$

Since the difference in chemical potential $\Delta\mu$ of vapor and solid is positive, nucleation represents an increase in free enthalpy.

As a consequence of supersaturation and limited diffusivity, three fundamental growth modes exist depending primarily on the surface energies γ of substrate and nucleation center, as well as on the diffusivity and nucleation rate. The surface energies relate the height h and length l of a cuboidal nucleation center via [96]

$$\frac{h}{l} = \frac{\gamma_f + \gamma_i - \gamma_s}{2\gamma_f}, \tag{3.2}$$

with indices f,i, s denoting the interface, substrate and film surface energies, respectively. The three fundamental growth modes are described as follows [95].

If $\gamma_s = \gamma_i + \gamma_f$ and $h = 0$, two-dimensional layer-by-layer, or Frank-van-der-Merve, growth occurs. Expected in particular for homoepitaxy, this growth mode corresponds to two-dimensional nucleation centers, which are stable at one monolayer and at a critical lateral expansion of length l^*.

In the case of a poor wetting of the substrate by the ablated species, $\gamma_s < \gamma_i + \gamma_f$ and $h > 0$. Nucleation centers require a minimal height and three-dimensional islands are formed. This mode, denoted as Vollmer-Weber growth, requires high supersaturation.

The converse case corresponds to an attractive substrate. Initially, it involves two-dimensional growth of a few monolayers. However, epitaxial strain and the steady coverage of the substrate lead to an increase in γ_i and, consequently, to the formation of islands (Stransky-Krastanov growth).

Lattice mismatch and epitaxial strain Of importance for heteroepitaxy is the lattice mismatch between substrate and film. For a given in-plane epitaxial relationship between substrate and heteroepitaxial film, the lattice mismatch is defined as $(1 - a_f/a_s)$, where a_s and a_f are certain in-plane lattice dimensions of substrate and film, respectively. For cube-on-cube growth, these dimensions simply correspond to the respective cubic lattice constants. Generally, a positive lattice mismatch is expected to give rise to compressive epitaxial strain; negative mismatch leads to tensile strain. Depending on the degree of lattice mismatch, epitaxial film growth is expected to have the following additional characteristics [95]:

Low lattice mismatch, < 7 - 8 %, is considered as lattice-matching epitaxy for which tensile or compressively strained, pseudomorphic growth occurs. Compared to the single-crystal value, the film out-of-plane lattice constant is either reduced for tensile or increased for compressive strain. This substrate-mediated, epitaxial strain is maintained only up to a critical film thickness. Above, relaxed growth sets in and the epitaxial strain is gradually released by formation of lattice dislocations and other structural defects.

An intermediate mismatch above 7 to 8 %, so-called domain-matching epitaxy takes place and lattice matching is achieved via multiples of the lattice constants. In particular, the critical thickness for lattice relaxation is expected to be much lower than for lattice-matching epitaxy.

3.2 Target preparation

For pulsed laser deposition of stoichiometric, epitaxial thin films, a suitable source target has to fulfill certain minimal requirements. Congruent, laser-induced ablation requires a high absorption coefficient at the laser wavelength. At least the cation stoichiometry should be identical to the desired phase, provided that chemical transfer is stoichiometric and evaporation off the film surface is negligible. Furthermore, a high density is key in reducing particulate formation during ablation. In this work polycrystalline targets are prepared by the following three methods.

Solid-state synthesis. The majority of thin film samples in this work are grown from targets prepared by this method. The desired target material is prepared as a polycrystalline pellet by means of solid-state synthesis. Oxide powders are homogenized in a zirconia ball mill in the respective stoichiometric ratio. It may, however, be necessary to add excess amounts of volatile species, such as sodium or lithium carbonate, to account for their loss during synthesis and, later, during film deposition. In a furnace, the mixture is calcined at high temperatures for several hours in a closed alumina crucible in either air or pure oxygen. Afterwards, it is reground and pressed to obtain a cylindrical one-inch diameter target. Usually, several sinter steps follow to obtain consolidated targets.

Gas pressure sintering Gas pressure sintering (GPS) [100] is suitable for sintering materials that tend to decompose at elevated temperatures and generally do not sinter well using conventional pressureless sintering methods, such as solid-state synthesis as described above. Applying an overpressure suppresses the decomposition of the sample and allows sintering and densification at higher temperatures. GPS is aimed at achieving nearly maximal theoretical

density. The driving force of the densification process is the applied external pressure. Gas pressure results in isostatic pressure unlike in hot pressing, where dies and punches achieve uniaxial pressure. Advantageous effects of higher pressure and temperature during sintering are reduced pore diameters and improved densification. Also, the process is not limited to certain shapes of a sample such as cylinders and complex-shaped samples can be densified. Compared to hot pressing, much higher pressures can be applied. In GPS, temperatures and pressures up to 2200 °C and 10 MPa are applied. During GPS it is required that the sample surface be gas-tight to prevent gas becoming entrapped in the pores. Hence, powders are usually uniaxially pressed or even sintered at ambient pressure prior to GPS. Pre-sintering will result in a dense surface with reduced porosity.

Spark plasma sintering Spark plasma sintering (SPS), also known as field assisted sintering technique [101], is based on a modified hot pressing technique. As both a consolidation and synthesis method it combines mechanical pressure with electric and thermal fields. Similar to the hot pressing (HP) process, a powder is placed inside a die and uniaxially pressed between two counter-sliding punches. A constant and defined pressure in the order of MPa is exerted by a hydraulic press. Under vacuum or a gas atmosphere a high pulsed dc current is directly passed through the conducting graphite punches and the powder. Joule heating of the powder generates internal heat that plays the dominant role in the densification process. The supplied current densities in SPS can be very large allowing fast heating rates ($\sim$ 1000 °C/min), much larger than for HP, and short sintering processes altogether. SPS allows very large densification of more than 90 % of the maximally reachable theoretical density of the material below its melting point. It also enhances sintering by, e.g., promoting surface oxide removal. The SPS process employed here uses conducting graphite dies and punches. This limits the applicable pressure to around 100 MPa and also provides a reducing component to the sintering atmosphere (cf. Sec. 5.3) which might be detrimental for oxides.

3.3 Electrical contacting and sample passivation

Sputter deposition of gold contacts For electrical transport measurements dc magnetron sputtering of gold contacts is employed. The sputtering process is performed in a vacuum chamber at an argon partial pressure of 0.023 mbar and a flow of 100 cm^3/min (sccm). The gold target is sputtered for 80 s at a power of 60 W, and the resulting contact layer has a thickness of approximately 280 nm. Shadow masks are used to obtain a van der Pauw or four-point contact geometry.

PECVD of SiN_x for sample passivation and protection To prevent sample degradation due to their instability in the simultaneous presence of CO_2 and H_2O [102] and the volatility of sodium and lithium, Na_2IrO_3 and Li_2IrO_3 samples are at times covered with a SiN_x layer by means of plasma enhanced chemical vapor deposition (PECVD). A similar result is obtained by spin-coating acrylic (PMMA). For resistivity measurements the protective layer is applied after application of gold contacts and wires. For the deposition of SiN_x, a Plasmalab 80 Plus by Oxford Instruments is employed. PECVD is a chemical deposition method where the chemical layer forming process is controlled by a radio frequency (rf) plasma. For deposition, silane SiH_4 and ammonia NH_3 precursors are directed into a vacuum chamber with a mass flow of 28 sccm and 1000 sccm for NH_3 and SiH_4 (2 % in inert N_2 carrier gas), respectively. The total chamber pressure and temperature are set to 1 Torr and 80 °C, respectively. The sample is placed on top of one of two electrodes biased with a 13.56-MHz rf electric field at a power density of 100 mW/cm^2. This rf field leads to the formation of a plasma above the sample. Within the plasma, radicals and ions are formed and react at the sample surface to SiN_x. The resultant SiN_x layer is about 110 nm thick.

4 Experimental methods

4.1 X-ray diffraction

X-ray diffraction (XRD) was employed for the purpose of structural and epitaxial studies of thin film samples. The method is based on the Bragg condition [103]

$$\Delta s = 2d_{\mathrm{hkl}} \sin\theta = n\lambda. \tag{4.1}$$

Electromagnetic radiation with a wavelength λ similar to interatomic distances in a crystalline solid scatters from lattice planes with spacing d_{hkl} and interferes constructively upon fulfillment of the above Bragg condition, i.e., when the path difference Δs between the scattered waves is an integer multiple n of λ. In an X-ray diffraction pattern, high intensity Bragg peaks mark the fulfillment of the Bragg condition. The peak intensity of a corresponding lattice plane is related to the structure factor, eq. (4.6) below.

In this work, two diffractometers were used: a Phillips X'Pert PRO Materials Research Diffractometer with parabolic mirror and PIXcel^{3D} detector and a Philips X'Pert diffractometer equipped with both a wide-angle Bragg-Brentano powder goniometer using diverging/focusing slit optics and a high-resolution goniometer. X-rays are emitted in all cases from a copper anode with λ = 1.5406 Å (Cu $K_{\alpha 1}$). The radiation is monochromatic only for the high-resolution goniometer by means of a Bartels monochromator. It otherwise also contains the Cu $K_{\alpha 2}$ and K_{β} lines, which can be observed in the XRD patterns.

2θ-ω-scans are performed to determine the out-of-plane epitaxial relationship and lattice constants of thin film samples. In such a scan, the detector is rotated at twice the angle as the sample holder around one and the same axis. The axis is in-plane to the samples surface. Essentially, the direction of the measured lattice vectors are fixed but their magnitude is changed. In this way, all lattice planes oriented normal to the growth direction can be measured (symmetric reflexes).

In a rocking curve, also called ω-scan, the diffractometer is set to a specific angle θ of a symmetric or asymmetric reflex and the sample is rotated about ω. The full width at half maximum (FWHM) of such a rocking curve of a symmetric and asymmetric reflex is, among other things, a measure for the tilt and twist of crystallites, respectively. The smaller the FWHM is, the better the crystallites are aligned and the larger their size.

The in-plane epitaxial relationship is studied by ϕ-scans. The sample is rotated about ϕ normal to the sample surface. Sample and detector were previously set to the Bragg angle of a specific lattice plane with an in-plane component, e.g. (10.4) of *c*-plane sapphire. Then, a ϕ-scan about 360° reveals multiple reflexes depending on the surface point symmetry of of the underlying lattice. To exemplify, the sapphire *c*-plane (00.1) has $3m$ symmetry [104] and a ϕ-scan about the asymmetric (10.4) reflex usually shows three 120°-spaced reflexes.

For monoclinic Na_2IrO_3 and Li_2IrO_3, and cubic $Y_2Ir_2O_7$ and $YBiO_3$, the relation between the lattice parameters a, b, c and β of the unit cell and the measured d_{hkl}-values is given as [103]

$$\frac{1}{d_{hkl}^2} = \frac{h^2}{a^2 \sin^2\beta} + \frac{k^2}{b^2} + \frac{l^2}{c^2 \sin^2\beta} + \frac{2hl\cos\beta}{ac\sin^2\beta}, \tag{4.2}$$

and

$$\frac{1}{d_{hkl}^2} = \frac{h^2+k^2+l^2}{a^2}. \tag{4.3}$$

When deriving accurate unit cell dimensions from a 2θ-ω-scan, systematical errors due to, e.g., sample absorption or the eccentricity error have to be considered. These errors lead to an uncertainty δd in the measured d-values, that are used for the calculation of *apparent* lattice dimension via, e.g., eqs. (4.2) and (4.3). However, these errors vanish at $\theta = 90°$, i.e., at total back reflection of the X-ray beam off the sample [105]. Therefore, extrapolation methods can be adopted for an accurate determination of the unit cell dimensions, provided several integer multiples of a structural Bragg reflex *hkl* are measured. Nelson and Riley [105] have provided such a method that is based on the absorption error of d,

$$\frac{\delta d}{d} \propto \left(\frac{\cos^2\theta}{\sin\theta} + \frac{\cos^2\theta}{\theta} \right). \tag{4.4}$$

The uncertainty of a lattice parameter is then obtained from linear regression of eq. (4.4).

Rietveld refinement For quantitative phase analysis of polycrystalline source targets, Rietveld refinement of XRD 2θ-ω-scans is performed using the HighScore Plus 3.0.5 software by PANalytical [106]. Rietveld refinement was also applied to determine the lattice parameters of bulk ceramics of monoclinic β-$(In_xGa_{1-x})_2O_3$ and β-$(Al_xGa_{1-x})_2O_3$ at various molar ratios x [MJ5,MJ 6]. With the Rietveld method, the measured pattern is modeled based on the known crystal structure data of the expected phase(s) present in the sample. If applicable, the relative phase composition is calculated. Various fit parameters can be adjusted. The most important ones are the type of unit cell, its space group, and its lattice parameters. These crystal structure data relate to the atomic positions in the unit cell and ultimately determine, together with the X-ray wavelength, the peak positions and intensity in a Rietveld refinement. Pattern fitting ac-

cording to Rietveld [107] is based on the following expression for the calculated intensity y_{ic} at a point i in the pattern [106]:

$$y_{ic} = y_{ib} + \sum_{p} \sum_{k=k_1^p}^{k_n^p} G_{ik}^p I_k. \tag{4.5}$$

In this expression, y_{ib} is a polynomial background, G_{ik} is a normalized Pseudo Voigt peak profile function, and I_k is the intensity of the Bragg reflex k. Summation over p and k considers that multiple phases and thus Bragg reflexes, respectively, can contribute to the intensity at a point i. The intensity I_k of a structural Bragg peak is proportional to $|F_k|^2$, with the structure factor F_k given by [106, 108]

$$F_k = \sum_{j=1}^{n} f_j \exp\left[i2\pi\left(\mathbf{h}_k \mathbf{r}_j - B_{iso}\sin^2\theta_k/\lambda^2\right)\right]. \tag{4.6}$$

The structure factor includes the scattering factor f_j of the atoms j in the given unit cell; matrices $\mathbf{h}_k$ and $\mathbf{r}_j$ describe the Miller indices (h,k,l) and fractional atomic coordinates (x,y,z), respectively. For simplicity, thermal vibrations of the atoms are assumed isotropic having a mean isotropic temperature factor B_{iso}. Important agreement indices describing the quality of the refinement are the weighted R_{wp} and expected R_{exp} values, given by [109]

$$R_{wp} = \left[\frac{\sum w_i (y_{io} - y_{ic})^2}{\sum w_i y_{io}^2}\right]^{1/2}, \tag{4.7}$$

and

$$R_{exp} = \left[\frac{N-P}{\sum w_i y_{io}^2}\right]^{1/2}. \tag{4.8}$$

Here, y_{io} and y_{ic} are the observed and calculated intensities, w_i is a weighting factor usually assigned the value y_{io}^{-1} [110]; N and P correspond to the number of measured points in the pattern and the least-squares parameters varied, respectively. The goodness of fit is defined as $\chi^2 = (R_{wp}/R_{exp})^2$.

4.2 Neutron diffraction

In collaboration with Prof. Dr. D. Inosov of TU Dresden, a neutron diffraction study on Na_2IrO_3 films was performed in April 2015 at the Institut Laue-Langevin (ILL) in Grenoble, France using the thermal neutron diffractometer D23, see. Sec. 6.2. The following short description of the method is based on Refs. [108] and [111].

In neutron diffraction, the examining probe is a particle beam of neutrons. Because neutrons

have a magnetic moment, they interact with both the nuclei and the unpaired electrons in a sample, e.g. the effective spin 1/2 of Ir^{4+} in Na_2IrO_3 (cf. Sec. 2.1). Unlike X-rays, neutrons are scattered efficiently by all elements such that even the atomic positions of hydrogen or oxygen can be resolved. Due to the large penetration depth of neutrons, bulk studies are possible. These properties of the neutron make their diffraction a viable probe to study for example the structure and excitations of magnetically ordered material.

Instrumental layout D23 is a thermal neutron two-axis diffractometer with double monochromator and lifting detector mounted on an arc [111]. It is installed on a thermal neutron guide with a curvature radius of 9 km and no direct view of the reactor core. This design prevents fast-neutron contamination and thus offers low background levels. As a whole, D23 is designed for single crystal measurements and magnetic structure determination. The instrument layout is shown in Fig. 4.1. Experiments at D23 were performed with unpolarized neutrons using a vertically focussed germanium PG (002) monochromator positioned inside the primary shielding; the incident neutron wavelength is 2.38 Å. Diffracted neutrons are detected by a ^{3}He gas mono-detector. Cryogenic cooling down to 1.5 K is achieved by a liquid helium cryostat with a cylindrical 49-mm diameter sample bore. The diffractometer includes a sample stage, enabling sample rotations around the angle ω. The lifting detector is able to rotate inside the horizontal plane around the sample by an angle γ, thus allowing maximal Bragg angles $2\theta \approx 130°$. Moreover, the arc mounting of the detector covers a tilt angle $\nu = \pm 30°$. Because data collection is monochromatic, the method and instrumentation of neutron diffraction as described here is very similar to X-ray diffraction described in Sec. 4.1.

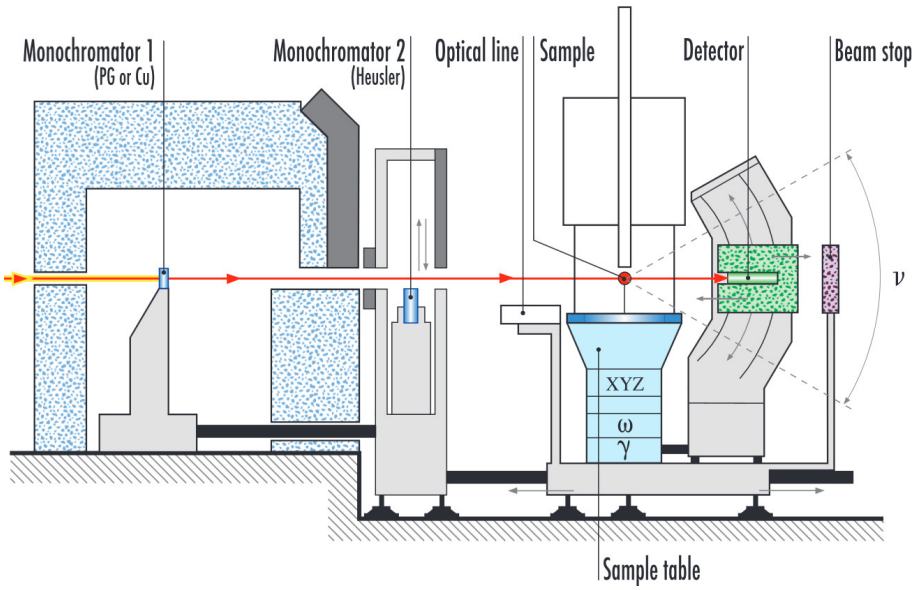

Figure 4.1 Instrument layout of the thermal neutron diffractometer D23 at ILL, Grenoble. [Taken from Ref. [111].

4.3 Atomic force microscopy

The surface roughness and morphology of thin films is studied with atomic force microscopy (AFM) employing the Park Systems XE-150 [112]. The working principle of AFM is based on the interaction between the sample surface and a measuring tip attached to a cantilever. The silicon tip and cantilever are scanned across the sample surface in non-contact mode. The tip-surface distance is small, 10 to 50 nm, such that Van-der-Waals (VdW) forces act on the cantilever. A Piezo element oscillates the cantilever slightly above its resonance frequency at a certain amplitude. Height and oscillations are registered via a laser beam reflecting off the cantilever onto a quadrant photodiode. Acting VdW forces alter resonance frequency and amplitude of the cantilever. The original oscillation of the cantilever is maintained via a feedback loop by feeding back the oscillation signal of the cantilever via a piezo element with a phase shift of 90°. With the help of the feedback loop the amplitude and frequency is kept constant by adjusting the height of the cantilever. From the height of the cantilever the topography of the sample surface can be extracted.

From the measured AFM topographic images, the peak-to-valley height, the root-mean-squared (RMS) roughness, line profiles and other general dimensions are extracted by means of a software tool [113]. Peak-to-valley height corresponds to the difference between highest and lowest point inside the scanned area. RMS surface roughness is equivalent to the RMS *height* via

$$r_{RMS} = \sqrt{\frac{1}{m \cdot n} \sum_{k=1}^{m} \sum_{l=1}^{n} [z(x_k, y_l) - \mu]^2} \tag{4.9}$$

where μ is mean height, $z(x_k, y_l)$ is the pixel height and $m \cdot n$ is the pixel number.

4.4 Scanning electron microscopy and energy dispersive X-ray spetroscopy

To obtain information about the surface morphology and the chemical composition of the thin film samples, scanning electron microscopy (SEM) and energy dispersive X-ray spectroscopy (EDX) are employed. Measurements are performed by J. Lenzner, Leipzig University, using the Novalab 200 by FEI Company. In a high vacuum a focused beam of free electrons is scanned over the sample. The free electrons are created by field emission from a fine metal tip. The electron beam interacts with the sample through ionization, excitation or elastic scattering. A detection system for these interactions is employed to extract topographic and material con-

trast.

A major product of the interactions of the electron beam with the sample are secondary electrons. Atoms in the sample are being ionized and excited such that secondary electrons can diffuse out of the sample and be detected. The yield of secondary electrons is strongly dependent on the angle of incidence onto the surface element and thus leads to a light-dark contrast when scanning edges and flat areas. Hence, secondary electrons provide structural information of the sample surface. Other electrons are being backscattered by elastic collisions with the atoms. The number of backscattered electrons is proportional to the square root of the atomic number $\sqrt{Z}$ and thus provides a material contrast.

The SEM is also equipped with and EDX detector to determine the chemical composition of a sample. Characteristic X-rays are emitted by the sample's atoms upon excitation by the electron beam. The characteristic spectrum is convoluted by bremsstrahlung. Characteristic radiation is emitted when vacancies, that are created in the atomic shells by ionization and excitation via the incident electron beam, are being filled by electrons in energetically higher shells. These level transitions are specific for each element and the characteristic spectrum measured is used to determine the element composition of the sample via the intensity ratios. Elements with $Z \leq 11$ cannot be detected by the system as a polymer foil is used as a window to prevent detector contamination.

4.5 Optical transmission spectroscopy

Measurements of optical transmission are performed on a Perkin Elmer Lambda 19 UV/VIS double beam spectrometer. Light in the spectral range from 185 to 3200 nm (0.4 to 6.7 eV) is provided by a deuterium and halogen lamp, respectively. Coming from the source, the light passes a filter wheel that filters any light outside the desired spectral range. Beam splitters separate the light into a reference and a sample beam, which are then dispersed separately at two identical turnable concave gratings. These monochromators are equipped with adjustable entrance and exit slits. Finally, two photodiodes detect the transmitted light intensities of the reference and sample beam, respectively. The measured quantity is the transmittance T, i.e., the ratio of transmitted light intensity I_t and incident light intensity I_i detected in the reference path. The optical transmission data is used in conjunction with spectroscopic ellipsometry to determine the direct and indirect bandgap energies of $YBiO_3$ thin films, see Sec. 9.2.

4.6 Spectroscopic ellipsometry

For the determination of a thin film's complex dielectric function $\tilde{\varepsilon} = \varepsilon_1 + i\varepsilon_2$, spectroscopic ellipsometry is employed. The dielectric function is related to the complex refractive index $\tilde{n}$ via $\tilde{\varepsilon} = \tilde{n}^2 = (n + i\kappa)^2$, with refractive index n and extinction coefficient κ. Ellipsometry measures the change in light polarization upon reflection from or transmission through a sample. For this purpose, light with well-defined polarization is incident on a sample under various angles. In simple, optically isotropic materials the polarization change of the reflected beam is given by the complex amplitude ratio [114]

$$\tilde{\rho} = \frac{\tilde{R}_\mathrm{p}}{\tilde{R}_\mathrm{s}} = \tan\psi \exp(i\Delta), \tag{4.10}$$

where $\tilde{R}_\mathrm{p}$ and $\tilde{R}_\mathrm{s}$ are the Fresnel reflection coefficients of parallel and perpendicular polarized light with respect to the incidence normal. ψ and Δ are the measured ellipsometric parameters. The experimental spectra are fit by regression analysis using the proper model stack. The model stack consists of of several layers that take into account the sample structure with individual layer thicknesses, model dielectric functions, as well as surface and interface roughnesses among others. From a successful modeling, information about film thickness and the complex refractive index $\tilde{n}$, are obtained. The refractive index may in turn contain information about the transition energies of, e.g., phonons, charge carriers, or magnons within the material. In this work, the infrared, visible and ultra-violet spectral regions from 0.03 to 5.00 eV are covered by spectroscopic ellipsometry employing the M2000, VASE, and IR-VASE ellipsometers by J.A. Woolam Co., Inc. [115]. Thickness, refractive index n and surface roughness of $YBiO_3$ thin films in the transparent spectral region ($\kappa = 0$) are estimated by a simple Cauchy model and the effective medium approximation, as described below. The more involved ellipsometric measurements and modeling of Li_2IrO_3 and $YBiO_3$ films employs the (IR-)VASE instruments and is performed by S. Richter and Dr. R. Schmidt-Grund, Leipzig University.

The Lorentz and Cauchy model dielectric functions The Cauchy model is a reasonable approach to model the dielectric function of a semiconductor in the transparent region, in which ε_1 is a slowly varying function of photon energy E and absorption is zero ($\varepsilon_2 = \kappa = 0$) [114]. Typically, at a higher energy E_0 a transition across the bandgap occurs and the dielectric function at this energy can be modeled by a classical Lorentz oscillator [114]

$$\varepsilon = 1 + \frac{S}{E_0^2 - E^2 - i\Gamma E}, \tag{4.11}$$

with transition energy E_0, oscillator strength S, and half width Γ, see Fig. 4.2(a). Note, that the Lorentz model can also be applied to, e.g., phonon transitions. For vanishing absorption $\mathrm{Im}(\tilde{\varepsilon})$, it is required that $\Gamma \to 0$ in eq. (4.11). Under these assumptions and using $E = hc/\lambda$, the Lorentz oscillator with zero broadening is written as [114]

$$\tilde{\varepsilon} = \varepsilon_1 = 1 + \frac{S}{(hc)^2} \frac{\lambda_0^2 \lambda^2}{\lambda^2 - \lambda_0^2}. \tag{4.12}$$

For $\lambda \gg \lambda_0$, i.e., in the transparent region well below the transition energy, the Cauchy model is finally derived by a series expansion of eq. (4.12) and given by [114]

$$\sqrt{\varepsilon_1} = n = A + \frac{B}{\lambda^2} + \frac{C}{\lambda^4} + \ldots \quad \kappa = 0, \tag{4.13}$$

with free parameters A, B and C.

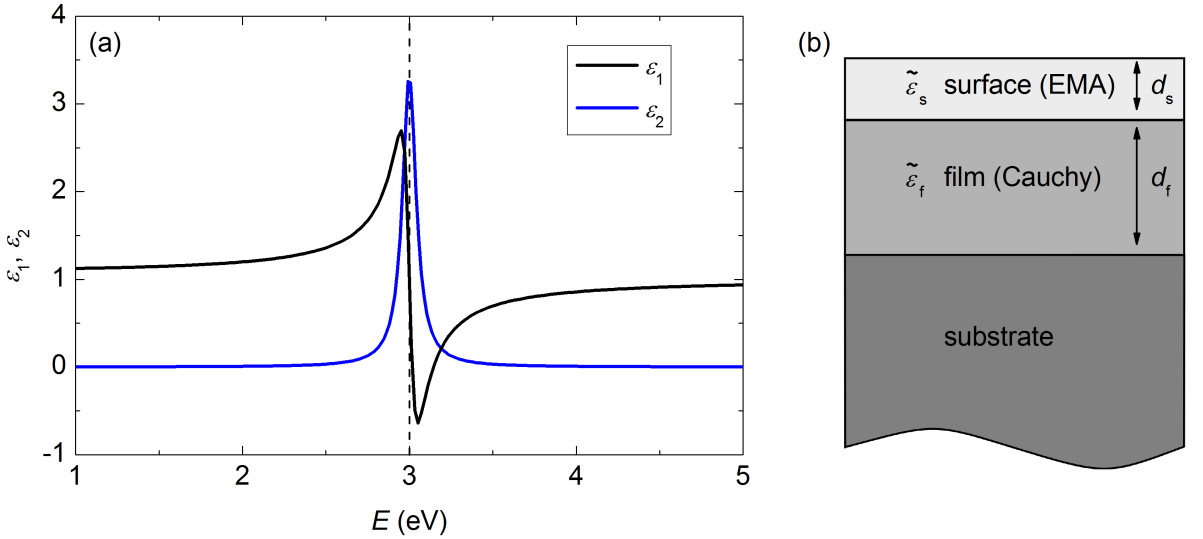

Figure 4.2 (a) Lorentz model dielectric function $\tilde{\varepsilon} = \varepsilon_1 + i\varepsilon_2$ according to eq. (4.11) [114] with E_0 = 3 eV, S = 1 eV, and Γ = 0.1 eV. (b) Simple optical model for the transparent region of a thin film deposited on a substrate. It contains a surface roughness layer with volume fraction f. The optical model includes the unknown quantities film thickness d_f and surface roughness d_s, as well as the corresponding dielectric functions, $\tilde{\varepsilon}_\mathrm{f}$ and $\tilde{\varepsilon}_\mathrm{s}$, which are modeled by Cauchy and EMA models, respectively (see text).

Free carriers Light absorption due to free charge carriers in a semiconductor and its effect on the dielectric function is described by the Drude model, a Lorentz oscillator with zero center energy $E_0 = 0$ [114]:

$$\tilde{\varepsilon}_\mathrm{Drude} = \tilde{\varepsilon}_\mathrm{inf} \left(1 - \frac{E_\mathrm{p}^2}{E^2 + i\Gamma E} \right), \tag{4.14}$$

with high-energy dielectric constant $\tilde{\varepsilon}_\mathrm{inf}$ and plasma energy E_p, which for semiconductors typically is in the infrared region. In principle, from an analysis using eq. (4.14) the charge carrier

concentration and mobility can be inferred if the effective mass is known [115].

Near bandgap absorption In amorphous semiconductors, optical absorption near the bandgap follows the Tauc law

$$\varepsilon_2 = A_(E - E_g)^2/E, \tag{4.15}$$

where E_g corresponds to the bandgap energy [114]. The product of this Tauc and a Lorentz model (cf. eq. (4.11)) leads to the Tauc-Lorentz oscillator, that well describes the asymmetric shape of ε_2 absorption peaks as observed in amorphous materials [114]:

$$\varepsilon_2 = \frac{AE_0C(E-E_g)^2}{(E^2-E_0^2)^2+C^2E^2}\frac{1}{E} \quad (E > E_g) \tag{4.16}$$

$$= 0 \quad (E < E_g). \tag{4.17}$$

The analytical parameters A and C describe the amplitude and half width of the Tauc-Lorentz oscillator. Finally, the real part of the dielectric function ε_1 can be obtained via the Kramers-Kronig relations, see Ref. [114].

Dielectric function at critical points The dielectric function at the so-called M0 critical point (CPM0) of a semiconductor is given by [116]

$$\tilde{\varepsilon}_{\mathrm{CPM0}}(E) = \frac{A}{E_0^{1.5}\chi^2}\left(2 - \sqrt{1+\chi^2} - \sqrt{1-\chi^2}\right), \tag{4.18}$$

with $\chi = (E + i\Gamma_0)/E_0$. The parameters E_0, Γ_0 and A describe the energy, damping and amplitude of the band-to-band transition. The CPM0 corresponds to the lowest direct interband transition between the top of the valence and the bottom of the conduction band.

Modeling the surface roughness In ellipsometric modeling, the surface roughness of a thin film sample is expressed as an additional surface roughness layer with thickness d_s composed of the film material and air in a volume fraction f, see Fig. 4.2(b). Its effective dielectric function $\tilde{\varepsilon}_s$ can be calculated by the Bruggeman effective medium approximation (EMA) using the dielectric functions of the film $\tilde{\varepsilon}_{\mathrm{film}}$ and air $\tilde{\varepsilon}_{\mathrm{air}}$ [115]

$$f\frac{\tilde{\varepsilon}_{\mathrm{air}} - \tilde{\varepsilon}_s}{\tilde{\varepsilon}_{\mathrm{air}} + 2\tilde{\varepsilon}_s} + (1-f)\frac{\tilde{\varepsilon}_{\mathrm{film}} - \tilde{\varepsilon}_s}{\tilde{\varepsilon}_{\mathrm{film}} + 2\tilde{\varepsilon}_s} = 0. \tag{4.19}$$

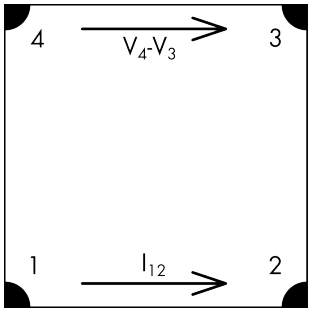

Figure 4.3 Schematic of the van der Pauw contact geometry applied to thin film samples.

4.7 The van der Pauw method

The electrical resistivity ρ of an arbitrarily shaped, but smooth and homogeneous sample with uniform thickness d can be determined by the van der Pauw method [117]. If applied to thin film samples, contacts are applied to the four corners of the samples. Provided that the contact surface is sufficiently small compared to the film surface, the resistivity is given by

$$\rho = \frac{\pi d}{\ln 2}(R_{12,34} + R_{23,41})f, \tag{4.20}$$

where resistance $R_{12,34}$ is defined as $(V_4 - V_3)/I_{12}$, and V and I are the electric potential and current, respectively (cf. Fig. 4.3). An analogous expression exists for $R_{23,41}$. The function f is dependent on the resistance ratio $Q = R_{12,34}/R_{23,41}$ via [117]

$$\frac{Q-1}{Q+1} = f\,\mathrm{arccosh}\left[\frac{1}{2}\exp\left(\frac{\ln 2}{f}\right)\right], \tag{4.21}$$

and is equal to unity for samples with perfectly uniform resistivity. To enhance the confidence of the van der Pauw method, the reversal of current and field polarity, that accounts for thermal and misalignment offset voltages, as well as the sourcing of additional terminals are included in the measurement protocol [118].

4.8 SQUID magnetometry

Magnetic properties of thin films were investigated using the commercial Magnetic Property Measurement System (MPMS) by Quantum Design, Inc. Measurements were performed by José. Barzola-Quiquia and Francis Bern of the Division of Superconductivity and Magnetism, Leipzig University. The following brief discussion of SQUID magnetometry employing the

MPMS is based entirely on Refs. [119] and [120].

Instrumental setup The MPMS is a radio frequency (rf) SQUID-based magnetometer-susceptometer system capable of measuring magnetization and magnetic susceptibility as a function of applied magnetic field and temperature. At the heart of the instrument is the rf SQUID (superconducting quantum interference device) that, intrinsically, is a flux-to-voltage converter. The MPMS combines several superconducting components: the rf SQUID, a 7-T magnet, detection and input coils, a tank circuit driving the rf SQUID and magnetic shielding. A simplified schematic illustration of the instrumental setup is shown in Fig. 4.4. Within a 9-mm sample chamber, the sample is scanned through the center of the detection coil by a linear motor. The detection coil itself is a longitudinal second-derivative gradiometer that detects the changes in the magnetic field components parallel to the applied field when the sample is scanned. The detection coil and the input coil are inductively coupled to each other and to the rf SQUID, respectively. This designs thus represents a double flux transformer. The transformed flux is applied to the rf SQUID which is protected from the magnet's strong field by a niobium shield; it is driven and read out by an inductively coupled tank circuit at radio frequency. As the instrument's output, the rf voltage V_T across the tank circuit is recorded as a function of sample position z along the detection coil. This raw V_T-z response curve is evaluated and converted into the magnetic moment of the sample. Magnetic fields up to 7 T are applied to the detection coil placed in the bore of the superconducting magnet. The MPMS employs low-T_c niobium compounds such that liquid helium-cooling is required for device operation; it is also used to simultaneously cool the sample chamber allowing temperature-dependent measurements from 800 to 1.7 K. The working principle of the MPMS, and the rf SQUID in particular, is based on flux quantization and the Josephson effect, as will be briefly discussed in the following.

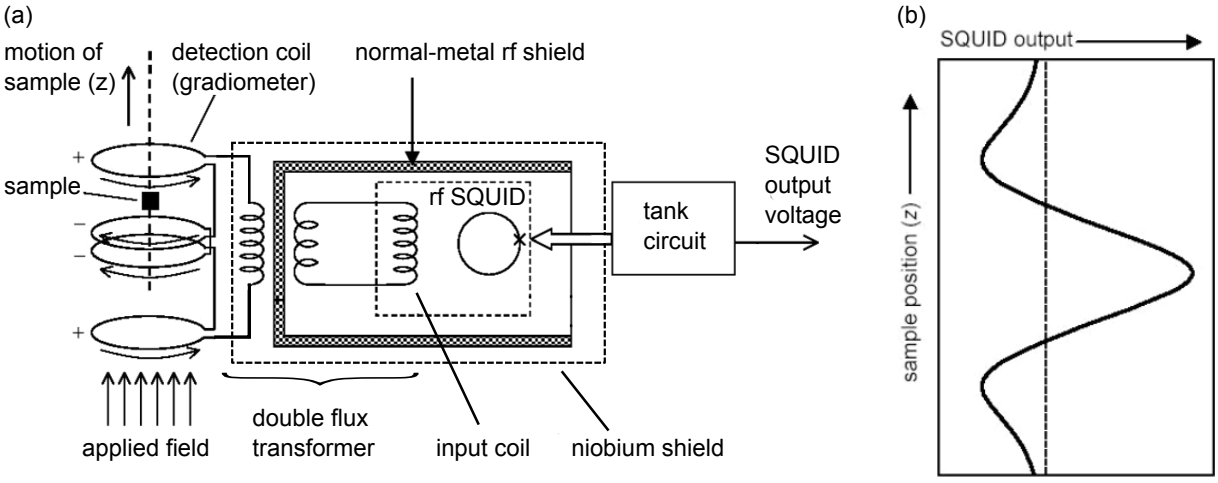

Figure 4.4 Detection circuit of the MPMS with second-derivative gradiometer, double flux transformer and rf SQUID inductively coupled to the tank circuit. (b) Ideal V_T-z response curve at the SQUID output. [Taken from Ref. [120]]

Josephson junction A Josephson junction, also called weak link, is a tunneling contact between two superconducting regions that can be realized by a thin insulating barrier, constrictions or point contacts. In the rf SQUID, a superconducting loop is interrupted by a single Josephson junction. The Josephson junction enables coherent tunneling of Cooper pairs between two superconducting regions. Cooper pairs of each region are associated with a wavefunction Ψ and corresponding phase Θ. Pair tunneling generates a supercurrent

$$I = I_0 \sin \delta, \tag{4.22}$$

where I_0 is the critical current of the junction and δ the phase difference $\Theta_1 - \Theta_2$ of the Cooper pairs from the two regions. The sinusoidal dependence on the phase difference is the direct consequence of flux quantization which states, that in a superconducting loop the enclosed flux is quantized in units of the flux quantum (fluxon) $\Phi_0 = h/2e \approx 2.07 \times 10^{-15}$ Tm^2. Equation (4.22) is valid, provided currents do not exceed I_0. In this case, no voltage appears across the junction. For greater currents $I > I_0$, the junction has a resistance and a measurable voltage V develops. Now, the current across the junction follows

$$I = I_0 \sin \left[\delta(0) - 2\pi U t/\Phi_0\right], \tag{4.23}$$

i.e., current and phase evolve in time according to $\dot{\delta} = 2\pi U/\Phi_0$.

Rf SQUID and tank circuit In the rf SQUID, the superconducting loop with inductance L is interrupted by a single Josephson junction having a resistance R and capacitance C. The rf SQUID is driven by the so-called tank circuit $L_T C_T R_T$, which is coupled to the superconducting loop via a mutual inductance $M = k(LL_T)^{1/2}$. Figure 4.5 shows a schematic of rf SQUID and tank circuit, respectively. The tank circuit is operated at a rf bias current $I_{rf} \sin \omega_{rf}$ with a frequency of 150 MHz. The oscillating bias current induces a current $I_T \sin \omega_{rf}$ at the tank circuit's inductor L_T. Consequently, the SQUID loop is subjected to the rf bias flux Φ_{rf} with peak value MI_T. The flux Φ_a to be measured is applied to the superconducting loop via the double flux transformer. The total external flux, i.e. the rf bias flux and the applied flux, has the effect of changing the phase δ across the Josephson junction and induces a screening current I inside the superconducting loop. The phase shift across the loop due to the external flux is given by

$$\delta = \frac{2\pi}{\Phi_0} \left(\Phi_{rf} + \Phi_a - LI\right), \tag{4.24}$$

where the screening current, in turn, is given by $I = I_0 \sin\left[2\pi(\Phi_{rf} + \Phi_a)/\Phi_0\right]$ according to eq. (4.22). Thus, the total flux Φ_T enclosed in the superconducting loop, and detected by the tank

circuit, is

$$\Phi_T = \Phi_{rf} + \Phi_a - LI. \tag{4.25}$$

To read out the rf SQUID, and detect the applied flux, the voltage across the tank circuit $V_T \sin \omega_{rf}$ is measured. The rf SQUID acts as a flux-sensitive inductor, since Φ_a modulates the effective inductance of the tank circuit and thus, via a change in resonant frequency $\Delta\omega_0$, the rf voltage V_T. The rf voltage is periodic in Φ_a. and the applied flux is read out as a change of *amplitude* of the rf voltage V_T. To obtain maximal sensitivity of the instrument the flux-to-voltage transfer $dV_T/d\Phi - T$ should be large, which holds if the tank circuit is operated slightly off-resonance.

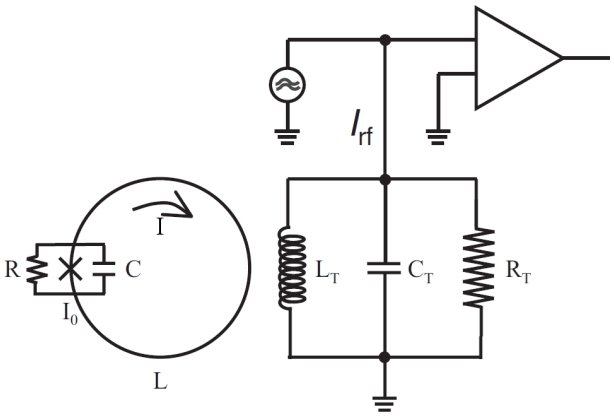

Figure 4.5 Schematic representation of the rf SQUID inductively coupled to the tank circuit. In the SQUID, *X* represents the Josephson junction with corresponding *R* and *C*. The rf amplifier detects the voltage V_T. [Taken from Ref. [119].]

Accuracy When measuring film samples in the MPMS as described above, some specifics in terms of accuracy have to be considered. The measured response curve is fitted to the theoretical response from a point dipole to obtain the sample's magnetic moment. For thin film samples, the accuracy of this fitting procedure can be reduced even if a previous subtraction procedure with an empty substrate was performed. For one, a considerable signal of the substrate, which may stem from impurities during film deposition may have to be considered. Furthermore, if the sample dimension are not small compared to the detection coils (30.4 mm baseline, 20.2 mm diameter), as is true for the measured samples, accuracy can be reduced by several percent. Lastly, when deposited on the substrate, the film may not be radially centered inside the detection coil.

Part II

Results and discussion

5 Target preparation

Polycrystalline source targets required for pulsed laser deposition were primarily prepared in this work by solid-state synthesis (cf. Sec. 3.2). However, the solid-state synthesis of iridates often resulted in rather brittle and poorly densified targets that were at times even destroyed during the first PLD process. Generally, a low target density causes droplet formation, as was observed in many of the film samples. For this reason, gas pressure and spark-plasma sintering of Na_2IrO_3, Li_2IrO_3 and $Y_2Ir_2O_7$ were explored in collaboration with two other universities for the purpose of improving the target density and, if required, the phase purity. $YBiO_3$ targets were at a later time prepared by solid-state synthesis only.

5.1 Solid state synthesis in ambient atmosphere

The majority of Na_2IrO_3, Li_2IrO_3, $Y_2Ir_2O_7$ and $YBiO_3$ targets was prepared by means of conventional solid-state synthesis in air at ambient pressure and elevated temperatures. The sintering was performed by Gabriele Ramm of the Semiconductor Physics Group at Leipzig University. For Na_2IrO_3 and Li_2IrO_3, a 5 to 10 % excess of sodium and lithium carbonate was added to account for a loss of Na and Li during synthesis. XRD 2θ-ω scans of the final targets are Rietveld refined for qualitative phase analysis using the respective crystal structures [42, 82, 93, 121].

Na_2IrO_3 As reported in earlier works of the author [MJ1,MJ 2], polycrystalline Na_2IrO_3 targets were prepared by calcination of stoichiometric amounts of Na_2CO_3 (99.997 %) and IrO_2 (85.45 % Ir) in a ratio of 1.05:1 at 750 °C for 24 h. The powder was then pressed and sintered at 900 °C for 48 h to give a phase-pure polycrystalline target as shown in see Fig 5.1(a).

Li_2IrO_3 Li_2CO_3 (99.999 %) and IrO_2 (85.45 % Ir content) powders in a ratio of 1.1:1 were homogenized in a ball mill and calcined in air for 24 h at 750 °C. The powder was then pressed and sintered in air at 900 °C for 72 h. To improve the mechanical stability of the target disc, a second sinter step, 72 h at 900 °C, was necessary. The final polycrystalline Li_2IrO_3 target is phase-pure as confirmed by Rietveld refinement of XRD data, see Fig 5.1(b).

$Y_2Ir_2O_7$ Stoichiometric amounts of Y_2O_3 (99.99 %) and IrO_2 (85.45 % Ir content) were homogenized, pressed and sintered at 1000 °C for 12 h in air. Phase analysis via Rietveld refinement gave a mixed phase of about 66 % $Y_2Ir_2O_7$, 25.9 % Y_2O_3 and 8.0 % IrO_2. As

a consequence, a second sinter step at 1250 °C for another 12 h was performed to complete the reaction. The amount of $Y_2Ir_2O_7$ and Y_2O_3 increases to 89.0 and 10.5 %, respectively, according to the Rietveld refinement results shown in Fig. 5.1(c). IrO_2 is present in traces, only. Note, that continued sintering at higher temperatures resulted in a steady weight loss. At 1350 °C, $Y_2Ir_2O_7$ decomposed nearly completely (4%).

$YBiO_3$ To obtain a polycrystalline $YBiO_3$ (YBO) target, stoichiometric amounts of Y_2O_3 (99.99 %) and Bi_2O_3 (99.999 %) were pelletized and sintered in air for 24 h at 800 °C. Upon sintering, the size of the target disc increased noticeably. A second and third sinter step were performed for 12 h at 800 °C in oxygen, and 12 h at 1000 °C in air. The target slightly shrunk indicating its densification. Finally, the target was re-sintered at 1000 °C for 12 h in oxygen. The resulting target is of light orange color and appears rather soft an brittle. As shown in Fig. 5.2, the XRD pattern is well matched by the cubic defective fluorite-type structure of YBO with space group $Fm\bar{3}m$ and a lattice parameter a = 5.4279(4) Å, in line with previous reports [90–93]. Additional peaks are probably related to Y_2O_3, Bi and Bi_2O_{3-x} [53] and suggest an incomplete reaction of the starting materials. The relative amount of these phases could, however, not be determined by Rietveld refinement using any of the various known crystal structures. An EDX analysis of the polycrystalline YBO target gave a Bi:Y ratio of 0.98. As discussed in Sec. 2.3, other structural models for YBO, put forward in theoretical works, are the undistorted $CaTiO_3$-type perovskite ($Pm\bar{3}m$) [37] and the distorted, orthorhombic $GdFeO_3$-type perovskite (*Pnma*) [38] However, neither of these structures could explain the experimental XRD pattern; corresponding Rietveld refinements are shown in the appendix, Fig. A.3. For reliable predictions and precise band structure calculations, future theoretical studies should hence turn to the defective fluorite-type structure, instead.

5.2 Gas pressure sintering of iridate powders

In collaboration with Prof. Yvonne Joseph and Uwe Sczech of Institut für Elektronik- und Sensormaterialien, TU Bergakademie Freiberg gas pressure sintering (GPS) was employed to improve the phase purity and densification of Li_2IrO_3 and $Y_2Ir_2O_7$ targets in comparison with solid-state sintered ones. A high argon gas pressure of 10 MPa allowed sintering at 1100 °C that would otherwise have led to a decomposition of the sample under ambient pressure. Li_2IrO_3 and $Y_2Ir_2O_7$ targets were pre-sintered under typical conditions, see Sec. 5.1. For GPS, the targets are placed in a Al_2O_3 crucible together with an Al_2O_3 fill. A pyrometer was used to regulate the temperature. Heating up to around 1100 °C took 40 min. The samples were held for 3 h and cooled down for 1.5 h. The phase composition of the pre-sintered Li_2IrO_3 and

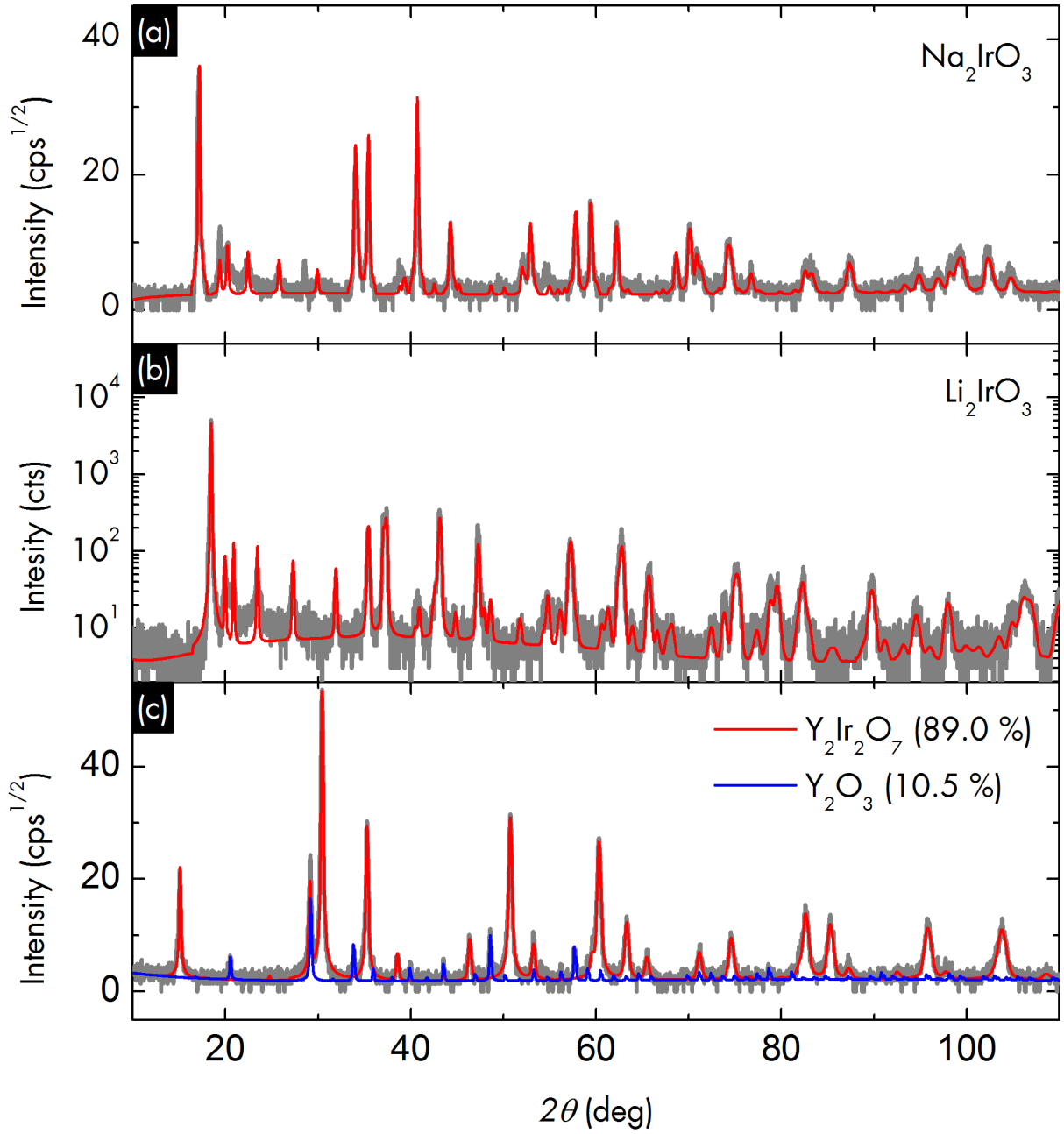

Figure 5.1 Solid-state synthesis of polycrystalline Na_2IrO_3 (a), Li_2IrO_3 (b) and $Y_2Ir_2O_7$ (c) source targets in air. For phase analysis of the final targets, Rietveld refinement (red lines) of XRD 2θ-ω scans (gray) was performed and confirms the phase purity of the Na_2IrO and ${}_3Li_2IrO_3$ targets. The extracted lattice parameters using a $C2/m$ unit cell [41, 121] are: a = 5.425(1) Å, b = 9.400(1) Å, c = 5.625(1) Å and β = 108.95(1)° for Na_2IrO_3; and a = 5.163(1) Å, b = 8.924(2) Å, c = 5.124(1) Å and β = 109.71(1)° for Li_2IrO_3. The $Y_2Ir_2O_7$ target with a = 10.1799(4) is not phase pure, as Rietveld refinement had to include 10.5 % Y_2O_3 and traces of IrO_2 (0.5 %, not shown). Goodness of fits χ^2: 2.31 (a), 2.71 (b), 1.35 (c).

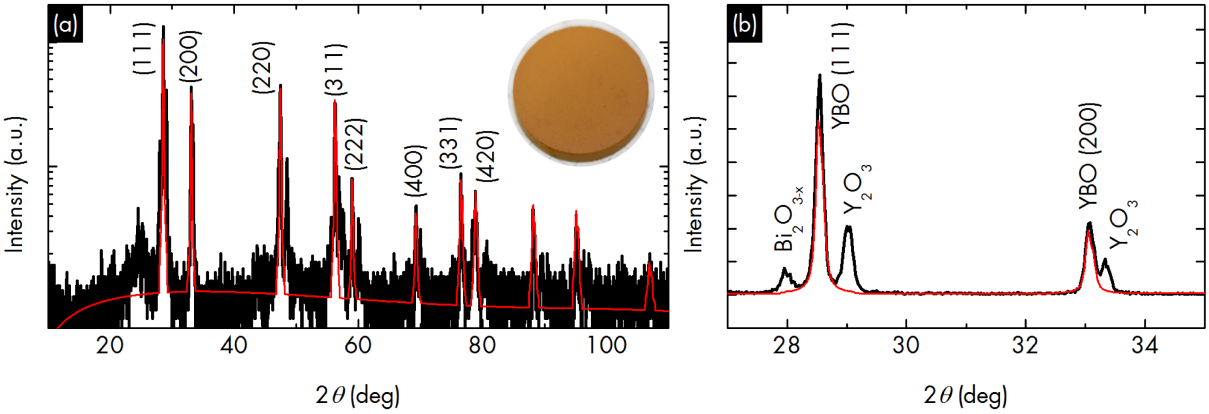

Figure 5.2 Solid-state synthesis of a YBO source target. (a) The XRD 2θ-ω scan of the polycrystalline target is Rietveld-refined using the $Fm\bar{3}m$ structure [93] with $a = 5.4279(4)$ Å and $\chi^2 = 3.98$, and confirms the presence of a YBO majority phase (red line). Inset: Photograph of the pelletized, light orange YBO target after sintering. Minor additional peaks, enlarged in (b), likely relate to the Y_2O_3 and Bi_2O_3 starting materials.

Table 5.1 Gas pressure sintering of Li_2IrO_3 and $Y_2Ir_2O_7$ iridate targets at TU Bergakademie Freiberg. Qualitative phase analysis was performed by Rietveld refinement.

sample	Li_2IrO_3 (%)	Ir (%)	Li (%)
Li_2IrO_3, sintered	100	0	0
Li_2IrO_3, GPS	15.9	54.2	29.9
Li_2IrO_3, ablated	48.4	32.6	19.1
	$Y_2Ir_2O_7$ (%)	Y_2O_3 (%)	Ir (%)	IrO_2 (%)
$Y_2Ir_2O_7$, sintered	75.1	19.3	0	5.6
$Y_2Ir_2O_7$, GPS	82.3	16.9	0.7	0.1
$Y_2Ir_2O_7$, ablated	25.5	23.6	50.1	0.8

$Y_2Ir_2O_7$ targets was estimated by Rietveld refinement and is shown in Tab. 5.1. As expected, pre-sintered Li_2IrO_3 is phase pure, while for $Y_2Ir_2O_7$ the reaction is incomplete (cf. Sec 5.1).

After GPS, the phase composition changed for both materials. Li_2IrO_3 is partly decomposed into Ir and Li. Note, that no oxide phases of Li or Ir could be fit to the XRD data. After ablation of the target surface by PLD, the phase composition changed in favor of Li_2IrO_3, see Tab. 5.1. This suggests that the observed decomposition, limited to the surface, is due to a reducing process atmosphere. Origin of such an atmosphere are the graphite heater (C), the oxide samples (O), residual oxygen and possibly humidity (H_2O). In this case, the graphite heater in conjunction with oxygen leads to a chemical equilibrium mixture of CO and CO_2 (Boudouard reaction). Under GPS conditions, this equilibrium is in favor of CO leading to a

Table 5.2 List of iridate powder samples consolidated by spark plasma sintering (SPS) at Stockholm University (SU). TD: theoretical density.

SU label	label	SPS conditions	estimated density
#17724	Powder 1 (Na_2IrO_3)	50 °C/min heating 800 °C, 80 MPa, 5 min	$\geq$ 86% TD
#17725	Powder 2 ($Y_2Ir_2O_7$, calcined)	50 °C/min heating 1000 °C, 80 MPa, 5 min	$\geq$ 86% TD
#17726	Powder 3 (Y_2O_3 + IrO_2)	50 °C/min heating 1000 °C, 90 MPa, 10 min	$\geq$ 67% TD
#17727	Powder 1 (Na_2IrO_3)	10 °C/min to 150 °C, then 50 °C/min 800 °C, 80 MPA, 5 min	NA

high-temperature reducing environment.

The phase composition of $Y_2Ir_2O_7$ after GPS is shown in Tab. 5.1. The previously observed IrO_2 phase (5.6 %) has nearly disappeared and instead Ir can be fit (0.7 %). This can be caused by either a thermal decomposition of IrO_2 at 1100 °C or the above-mentioned high-temperature reducing atmosphere. Surprisingly, Rietveld refinement of the ablated $Y_2Ir_2O_7$ target shows large amounts of Ir and a drastically reduced $Y_2Ir_2O_7$ phase. It is unclear what could cause such a depth gradient of the phase composition.

5.3 Spark plasma sintering of iridate powders

To improve the target density, its mechanical stability, and the phase purity, sintering attempts were also made by means of spark plasma sintering (SPS). The consolidation was performed by Ji Zou and Prof. Dr. James Shen of the Materials Innovation Arrhenius Laboratory of Stockholm University in Winter 2013. Table 5.2 lists details of the powder samples sent in. Powder 1 was a calcined stoichiometric mixture of Na_2CO_3 and IrO_2powders. Powders 2 and 3 were stoichiometric mixtures of IrO_2 and Y_2O_2 and Powder 2 was additionally calcined at Leipzig University to give $Y_2Ir_2O_7$.

Na_2IrO_3 (Powder 1, #17724) was spark plasma sintered at 800 °C and 80 MPa for 5 minutes. Upon heating at 50 °C/min, a vacuum drop was observed just below 150 °C, at which temperature the current was added during sintering. After sintering, a white precipitate was observed at

Table 5.3 Rietveld refinement of iridate powders consolidated by spark plasma sintering (SPS). The qualitative Rietveld analysis shows the decomposition of the target material into its starting components. The phase quantification (%) should not be too literal.

sample	Na_2IrO_3 (%)	Ir (%)	IrO_2 (%)	γ-Na_2CO_3	graphite
#17724	0.3	21.5	23.6	8.7	45.9
#17727	0.2	15.3	17.0	1.9	65.7
	$Y_2Ir_2O_7$ (%)	Y_2O_3 (%)	Ir (%)	Y (%)	graphite
#17725	0.0	33.3	63.0	0.1	3.5
#17725, ablated	8.7	23.2	67.7	0.0	0.3
#17726	0.0	0.8	42.8	0.2	56.1
#17726, ablated	1.3	12.1	68.1	0.0	18.6

the top and bottom of the sample. XRD data of the precipitate could be matched to monoclinic γ-Na_2CO_3 (ICSD code 168129). Also, a larger amount of Na_2CO_3 was deposited at the top than at the bottom of the sample. This suggests a formation of Na_2CO_3 via a gas phase during the early stage of sintering and indicates that Na_2CO_3 was probably not completely decomposed during calcination prior to SPS.

With a reduced heating rate to 10 °C/min, the vacuum drop in Na_2IrO_3 below 150 °C was avoided (Powder 1, #17727), but a precipitate of Na_2CO_3 was still found on the lower surface. The sample was removed at around 200 °C and found to be broken into many small pieces. This suggests that the material has rather poor thermal shock resistance.

XRD 2θ-ω scans of samples #17724 and #17727 were Rietveld refined, see Tab. 5.3. The SPS samples show no Na_2IrO_3 phases (0.6% and 0.1%, resp.) but instead nominally large amounts of Ir and IrO_2, γ-Na_2CO_3, and even graphite. This clearly indicates the presence of reducing conditions during SPS equivalent to GPS (cf. Sec. 5.2).

$Y_2Ir_2O_7$ was prepared by SPS at 1000 °C and 80 MPa for 5 minutes (Powder 2, #17725) and at 1000 °C and 90 MPa for 10 minutes (Powder 3, #17726). Both samples showed a vacuum drop above 900 °C that might be linked to the densification process but could also indicate a partial reduction of the powder. As shown in Tab. 5.2, the density of #17726 is lower than that of pre-reacted #17725 suggesting an incomplete reaction between IrO_2 and Y_2O_3 even though the holding time was prolonged to 10 min. The surface of the spark plasma sintered pellets is of a silver-like color, see Fig. 5.3 as a result of partial reduction when in contact with the graphite tools.

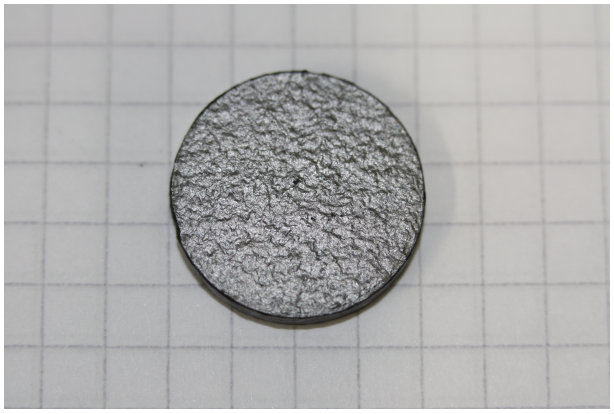

Figure 5.3 Spark plasma sintered $Y_2Ir_2O_7$ target (#17725). The $Y_2Ir_2O_7$ powder was calcined prior to spark plasma sintering (SPS). The silver surface is the result of partial reduction of the target material during SPS.

The phase composition of the $Y_2Ir_2O_7$ SPS samples is also shown in Tab. 5.3. The calcined $Y_2Ir_2O_7$ sample, #17725, no longer contains a $Y_2Ir_2O_7$ phase. Instead, a complete decomposition into mostly Y_2O_3 and Ir occurred during SPS. Neither the pristine powder #17726 contains a $Y_2Ir_2O_7$ phase. The target surfaces of both samples were subsequently laser ablated and XRD measurements were repeated. A subsequent Rietveld refinement found some percentage of a $Y_2Ir_2O_7$ phase in both samples. After surface ablation, the amount of graphite was also significantly reduced. Clearly, the effect of the reducing atmosphere in SPS is limited mostly to the surface of the SPS targets. The origin of a reducing atmosphere in SPS, where conducting graphite dies and punches are used, is assumed to be similar to GPS, see Sec. 5.2.

5.4 Summary

In general, solid-state synthesis of Na_2IrO_3, Li_2IrO_3, $Y_2Ir_2O_7$ and $YBiO_3$ results in polycrystalline and phase-pure targets which can be used for PLD of the respective thin films. However, the targets are mechanically soft and their densities rather low. The low target densities are believed to be the primary cause of droplet formation in the thin films. To improve the densification, gas pressure and spark-plasma sintering were explored with Na_2IrO_3, Li_2IrO_3 and $Y_2Ir_2O_7$. While in all cases the target density was significantly increased, the reducing conditions resulted in a poor phase purity of the targets and thus in a non-ideal cation stoichiometry with respect to the desired phases. Consequently, no films were grown from the gas pressure and spark-plasma sintered targets.

6 Na_2IrO_3

In a previous work [MJ1], heteroepitaxial (001)-oriented Na_2IrO_3 thin films with well-defined in-plane epitaxial relationship were successfully realized on various 5 × 5 and 10 × 10 mm^2 single-crystalline substrates. Those substrates were sapphire, $YAlO_3$ and zinc oxide. Three-dimensional Mott variable range hopping was the dominant conduction mechanism between 40 and 300 K. Moreover, a signature of the proposed topological insulator phase was found in magnetoresistance by observation of the weak antilocalization effect that is associated with topological surface states [5]. Compared to single crystals [72], a smaller, 200-meV optical gap in Na_2IrO_3 thin films was found by Fourier-transform infrared transmission. Following these experimental efforts, the desire arose to prepare single-crystalline Na_2IrO_3 films on large-area substrates, i.e., on 1.5”- and 2”-diameter wafers, as discussed in Sec. 6.1, because the enhanced surface-to-volume ratios can possibly be beneficial for certain experiments, such as neutron diffraction or pump-probe spectroscopy. A subsequent neutron diffraction experiment on these large-area Na_2IrO_3 thin films was performed to determine the magnetic ordering wave vector. This is treated in Sec. 6.2. Furthermore, structural improvements of Na_2IrO_3 thin films were achieved by the deposition of an intermediate zinc oxide layer as a structural template on cheaper *a*-plane and *c*-plane substrates. This is discussed in Sec. 6.3. A previous study of optical excitations by means of ultrafast optical pump-probe spectroscopy found evidence for spin-liquid physics in Na_2IrO_3 single crystals [122]. Future pump-probe spectroscopy in the terahertz range might corroborate the experimental evidence. In the terahertz range, this method benefits from large-area film samples. However, pump-probe spectroscopy on Na_2IrO_3 thin films is yet in the stage of sample preparation which is discussed in Sec. A.2.

6.1 Thin film deposition on large-area sapphire substrates

In the following, the feasibility of Na_2IrO_3 film growth on large-area *a*-plane and *c*-plane sapphire wafers with diameters of 1.5” and 2” is presented. Figure 6.1 shows X-ray diffraction data obtained from a Na_2IrO_3 film prepared on a 2” *a*-plane sapphire wafer under standard growth conditions, i.e. at $T_g \approx 550$ °C and $p_{O2} = 0.016$ mbar; 50,000 laser pulses were applied. In the top part of the image, a usual 2θ-ω-scan at the center of the wafer is shown. The bottom part displays a line scan of 2θ-ω-scans along the diameter of the wafer, with position x ranging from +27 to -27 mm. It is evident from the XRD data that the sample is single-phase along the whole diameter of the wafer. Deviations from the otherwise very homogeneous patterns are

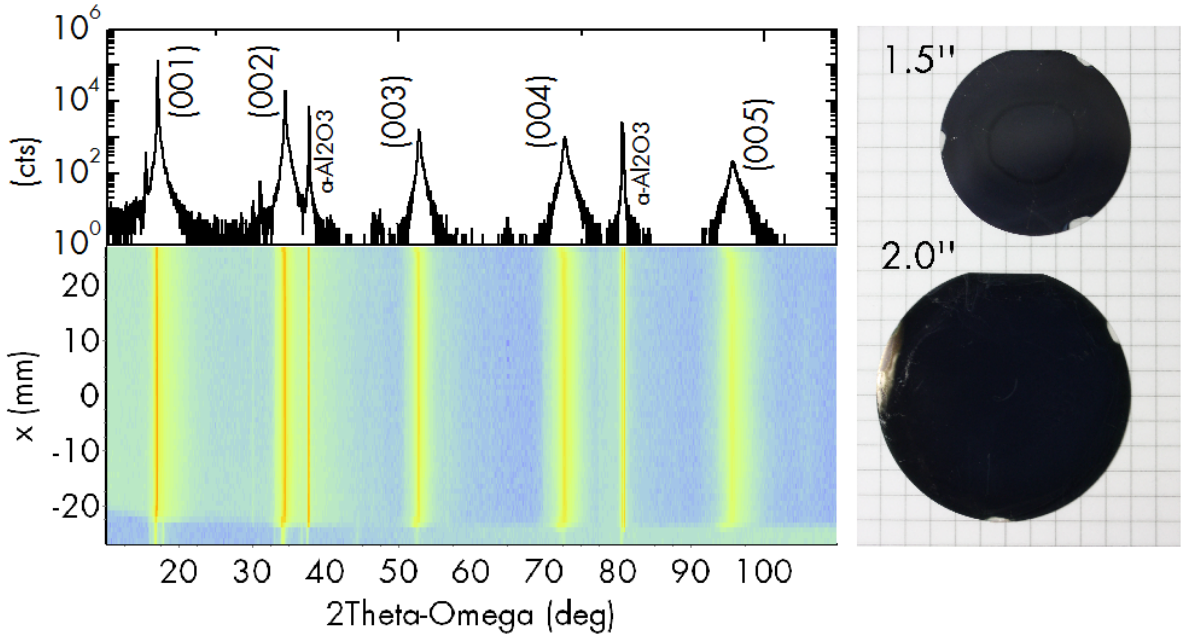

Figure 6.1 Na_2IrO_3 thin film deposited on a 2-inch *a*-plane sapphire wafer. Top: XRD 2θ-ω-scan performed at the center of the wafer, x = 0 mm. Bottom: XRD line scans along position x and the diameter of the wafer, respectively. Right: Photograph of two typical 1.5" and 2.0" Na_2IrO_3 samples on *a*-plane sapphire. [Sample: E3776.]

visible only at the very edge of the wafer. Similar results were also obtained on films grown on 1.5" *a*-plane and *c*-plane sapphire wafers, respectively. Typical structural properties of Na_2IrO_3 films prepared on 1.5" *a*-plane sapphire wafers, which were later used for neutron diffraction as described in Sec. 6.2, are shown in Fig. 6.2. On *a*-plane sapphire, the in-plane epitaxial relationship is $[010]_{Na2IrO3} \| [00.1]_{Al2O3}$. The occurrence of six evenly spaced $Na_2IrO_3\{131\}$ reflexes can be understood, according to Ref. [104], from the $3m$ and m surface point symmetries of the epilayer and substrate, respectively, and a 30° misalignment of the respective mirror symmetry planes leading to two rotational domains. The in-plane epitaxial relationship on *c*-plane sapphire is explained in more detail and with very similar arguments in Sec. 6.3.

6.2 Magnetic order - neutron diffraction on 1.5" samples

Powder and single-crystal neutron-scattering experiments found that the magnetic ordering pattern in Na_2IrO_3 developing below T_N = 15 K is of zig-zag type [41, 42]. Neutron-scattering experiments on Na_2IrO_3 are, however, a challenge because of the high absorption cross-section of iridium and the limited size of available single crystals. In collaboration with Dmytro Inosov of TU Dresden, a low-temperature neutron diffraction experiment was performed on a stack of several co-aligned epitaxial Na_2IrO_3 thin films deposited on 1.5" sapphire wafers. For typical

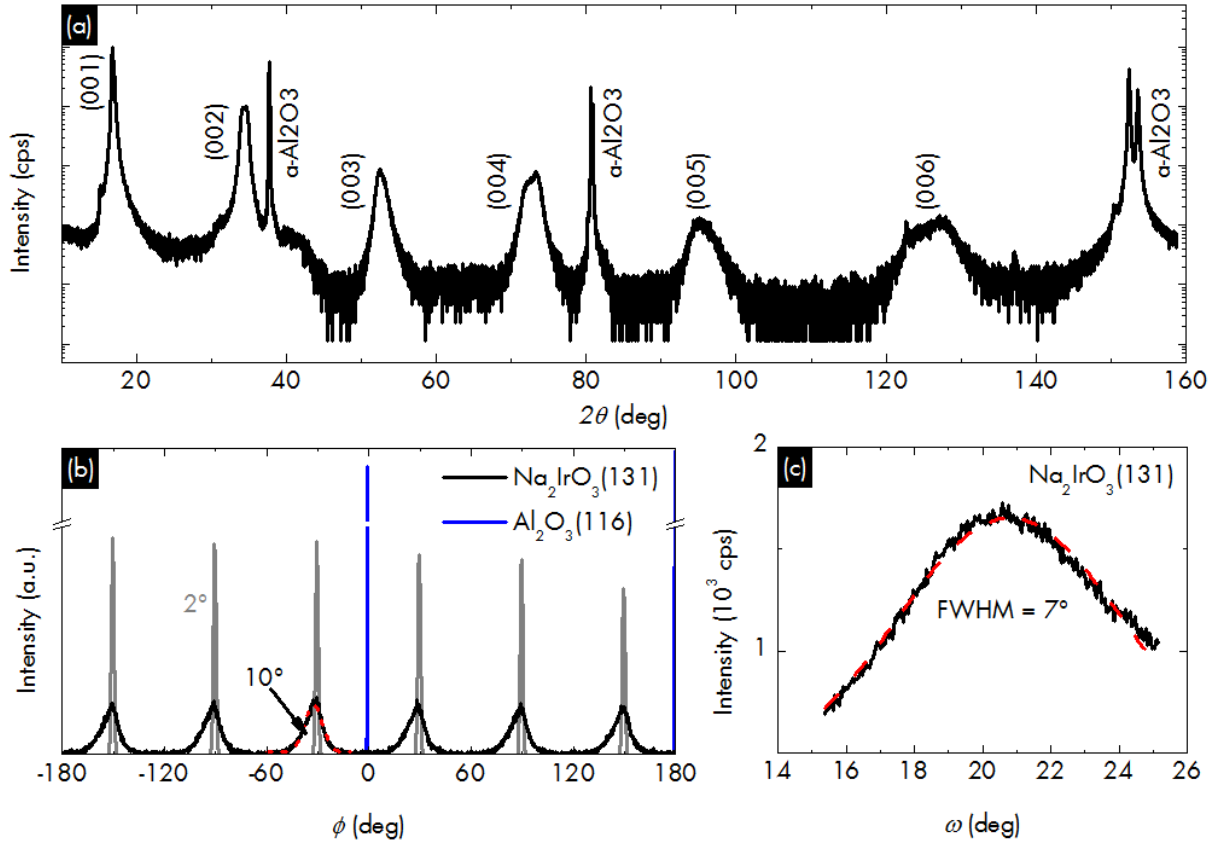

Figure 6.2 A typical Na_2IrO_3 film deposited on a 1.5” *a*-sapphire substrate at 0.016 mbar, 550 °C (450 W) and with 50,000 laser pulses. A stack of seven equivalent samples was used for neutron diffraction (cf. Sec. 6.2). (a) XRD 2θ-ω-scan. (b) An XRD ϕ-scan illustrates the $[010]_{Na2IrO3} \| [00.1]_{Al2O3}$ in-plane epitaxial relationship on *a*-plane sapphire. Peak widths are about 10°. For comparison, a film prepared with intermediate *c*-ZnO layer (gray) has an average half-width of only 2° (cf. Sec. 6.3). (c) XRD ω-scan of the (131) structural Bragg reflex. Gauss fitting gives a peak half-width of about 7°. [Samples: E3884, E4029.]

structural properties, obtained by means of XRD, see Fig. 6.2. The benefits of such a sample design are a large surface-to-volume-ratio and an equivalent volume comparable to that of single-crystals. The aim of the experiment was to determine the magnetic ordering wave vector, which previously was determined to be **q** = (0,1,0.5) [41, 42]. Additionally, this experiment represented a feasibility test for a future systematic investigations of the $(Na_{1-x}Li_x)_2IrO_3$ compositional series. Within this series, magnetic order could be suppressed down to 1.2 K at an intermediate value of $x \approx 0.7$ [77].

For the experiment, seven (001)-oriented Na_2IrO_3 films were deposited on 1.5” *a*-plane sapphire wafers with an in-plane epitaxial relationship of $[010]_{Na2IrO3} \| [00.1]_{Al2O3}$ (cf. Sec. 6.1). The peak widths of about 10° observed in XRD ϕ-scans of Na_2IrO_3 (131) suggest a relatively large in-plane mosaic spread, see Fig. 6.2. In direct comparison, films deposited on a *c*-ZnO buffer layer had significantly lower peak widths of about 2°. For protection and to prevent degradation of Na_2IrO_3, all films were passivated with a 110-nm layer of SiN_x using PECVD. Subsequently,

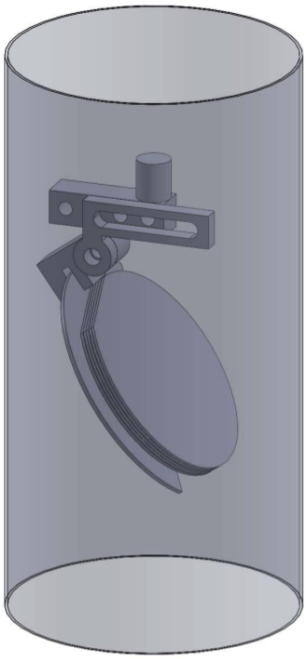

Figure 6.3 Illustration of the sample holder employed for mounting the Na_2IrO_3 film stack within the 49 mm cryostat bore. The stack is glued onto a c-shaped piece of 0.5 mm-thick aluminum that can be fixed and tilted at an arbitrary angle. [Drawing by Pavlo Portnichenko, TU Dresden]

the samples were stacked and glued together on an aluminum holder, of which a schematic is shown in Fig. 6.3. Within the stack, the samples were co-aligned with respect to the wafer's primary flat indicating the [00.1] direction of sapphire. With 50,000 laser pulses, the individual film thickness, determined by spectroscopic ellipsometry, is approximately 500 ($\pm$ 50) nm. Thus, the stack of seven 1.5" wafers yields a total Na_2IrO_3 volume of approximately 4 mm^3 which is comparable to some of the larger Na_2IrO_3 single crystals [41].

Neutron diffraction was performed with the thermal neutron two-axis diffractometer D23 at ILL (Sec. 4.2) and a wavelength of 2.38 Å. As a starting point, the structural $C2/m$ unit cell of Na_2IrO_3 refined by Ye *et al.* [41] was used for the calculation of sample alignment and scattering geometry. Initially, measurements were intended to be performed within the $(h, 2k+h, k-h)$ scattering plane that is spanned by the $(0,2,1)$ and $(1,1,-1)$ allowed structural Bragg reflexes used for sample alignment[1]. Within $(h, 2k+h, k-h)$, the $(0,1,0.5)$ and $(0.5,0.5,-0.5)$ magnetic Bragg reflexes are nearly orthogonal and indicative of antiferromagnetic zig-zag order in Na_2IrO_3. Due to the monoclinic crystal structure, $(0,1,0.5)$ and $(0.5,0.5,-0.5)$ are not equivalent and only the existence of the former reflex has been reported so far in measurements within the $(0,k,l)$ scattering plane [41]. Unfortunately, measurements within $(h, 2k+h, k-h)$

[1] $(h, 2k+h, k-h) = h(0,2,1,) + k(1,1,-1)$.

were unsuccessful because neither the $(0,2,1)$ and $(1,1,-1)$ structural reflexes nor any of the magnetic reflexes were found at or near their expected q-values.

Hence, the sample was reoriented inside the cryostat to allow measurements within the $(0,k,l)$ scattering plane, with $(0,1,0.5)$ again being the magnetic Bragg reflex of interest. For sample alignment in this plane, only the Na_2IrO_3 $(0,0,\pm1)$ structural Bragg reflexes could be clearly measured, as shown in Fig. 6.4(a). In addition, multiple reflexes were measured close to the expected q-value of $(0,\pm6,0)$ and two of these are displayed in Fig. 6.4(b). Due to the 10° in-plane mosaicity, the multiple $(0,\pm6,0)$ reflexes likely stem from different grains within the sample, preventing a precise sample alignment within $(0,k,l)$. Gaussian fits of $(0,0,\pm1)$ and $(0,\pm6,0)$ yield lattice parameters c = 5.492(9) Å and b = 9.45(2) Å, respectively[2]. The c lattice parameter is reliable and differs from the assumed unit cell dimensions by only -0.8 %. It coincides well with previous XRD measurements on the individual films. Note, that the b lattice parameter is unreliable due to the difficulties in sample alignment and given for completion's sake, only.

A subsequent measurement of $(0,1,0.5)$ within $(0,k,l)$ at 1.5 K, i.e. within the magnetically ordered phase, did again not reveal any measurable signal. A repeat measurement at 20 K, i.e., above the Neél temperature, was performed for the purpose of temperature subtraction. However, no magnetic reflex was uncovered by this indirect method, as shown in Fig. 6.5(a).

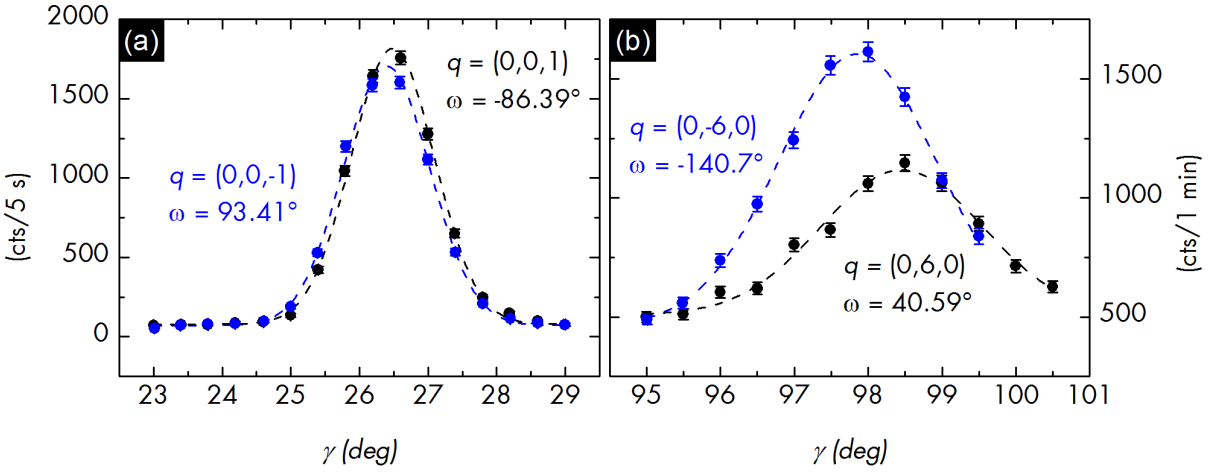

Figure 6.4 γ-scans of structural Bragg reflexes of Na_2IrO_3. (a) $(0,0,\pm1)$ and (b) $(0,\pm6,0)$ measured at 8 and 1.5 K, respectively. All data were fitted by Gaussians (dashed lines) to determine the c and b lattice parameters.

An unexpected finding related to the in-plane epitaxial relationship is that the q-vectors belong-

[2]Calculated via $\frac{1}{d_{0kl}^2} = \frac{k^2}{b^2} + \frac{l^2}{c^2 \sin^2\beta}$, where $d_{hkl} = \frac{\lambda}{2\sin(\gamma/2)}$ and β = 108.67°.

ing to the Al_2O_3 $(0,1,2)$ and Na_2IrO_3 $(0,2,1)$ structural Bragg reflexes are very similar in both size *and* direction, as shown in Fig 6.5(b). This was not considered prior to the experiment but may have had direct consequences for measurements of $(0,1,0.5)$ at only half these q-vectors. Since the experiment was performed using only one monochromator, it is possible that the second order $(0,1,2)$ substrate reflex was still very intense and masked the nearby $(0,1,0.5)$ magnetic reflex.

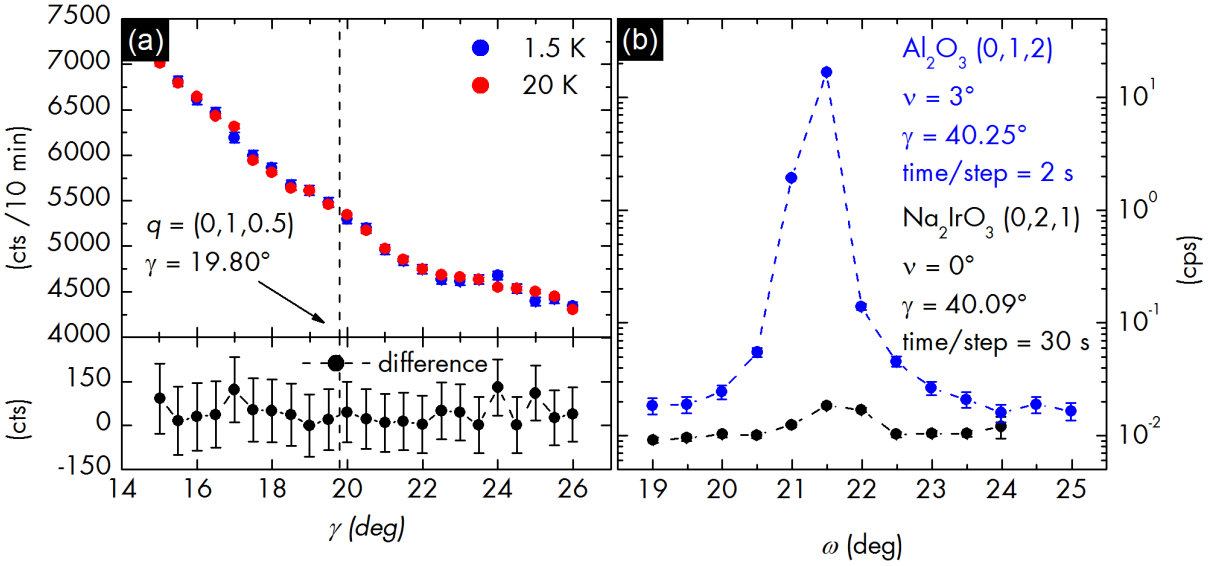

Figure 6.5 (a) Top: Measurement of the $(0,1,0.5)$ magnetic Bragg reflex expected at $\gamma = 19.80°$ (dashed line) at 1.5 and 20 K ,i.e., below and above the Néel temperature of 15 K. Bottom: Temperature subtraction gives no indication of a magnetic reflex. (b) Rocking curves of Al_2O_3 $(0,1,2)$ and Na_2IrO_3 $(0,2,1)$ structural Bragg reflexes measured at 8 K and at angles ν and γ as indicated. Their corresponding q-vectors are similar in size and direction.

In summary, magnetic Bragg peaks were not measurable directly or indirectly using temperature subtraction in a stack of seven Na_2IrO_3 thin films. Sample alignment on both the $(h,2k+h,k-h)$ and $(0,k,l)$ planes was attempted. While some structural Bragg reflexes of both film and substrate were observed within these scattering planes, the $(0,1,0.5)$ magnetic Bragg reflex was not. The lack of signal at the expected magnetic q-vectors is predominantly due to the significant in-plane mosaicity present in the individual films and, in addition, prevented a precise sample alignment. For future attempts, this obstacle has to be tackled primarily. As is shown in Sec. 6.3, deposition of an intermediate buffer layer on either a- or c-plane sapphire leads to a significant and reproducible reduction of in-plane mosaicity, and might justify a renewed neutron-diffraction experiment on Na_2IrO_3 thin films.

6.3 Structural optimization by epitaxial ZnO buffer layers

In Ref. [MJ2] the author reported promising results on an individual Na_2IrO_3 film sample deposited on a *c*-ZnO single-crystalline substrate. In-plane epitaxy was improved over films grown on Al_2O_3 and $YAlO_3$ substrates in the sense, that the intensities of the six-fold asymmetric Na_2IrO_3(202) reflex were significantly enhanced. These results were reproduced after about two years and led to the idea to deposit an intermediate ZnO layer as a structural template on cheaper *a*-plane or *c*-plane sapphire substrates. Furthermore, Al-or Ga-doped ZnO can be used as a bottom electrode material [123]. Bottom electrodes can prove necessary in, e.g., photoelectron spectroscopy to prevent a charging of the sample, or for measurements of the transversal resistance. In the following, the impact of an intermediate ZnO layer on the crystalline quality of Na_2IrO_3 films is exemplified using a *c*-plane sapphire substrate.

On one sample, E4029, a ZnO layer was deposited with 2,500 pulses on *c*-plane sapphire at p_{O2} = 0.2 mbar and $T_g \approx 600$ °C. A 15,000 pulses thick Na_2IrO_3 layer was then grown on top at 0.016 mbar and ≈ 600 °C. For a direct comparison, a second sample, E4028, without ZnO layer was prepared under otherwise identical conditions. Out-of-plane and in-plane epitaxy of both samples was investigated by XRD as follows.

Figure 6.6(a) shows 2θ-ω-scans of both samples. Evidently, an intermediate ZnO layer significantly improves the out-of-plane crystallinity of heteroepitaxial Na_2IrO_3. The peak intensities related to the (001) preferential orientation increase by nearly two orders of magnitude. Furthermore, rocking curves of the Na_2IrO_3 (001) and (202) reflexes, displayed in Fig. 6.6 show, that the half-widths are reduced by more than a factor of two indicating a noticeable reduction if crystallite tilt and twist.

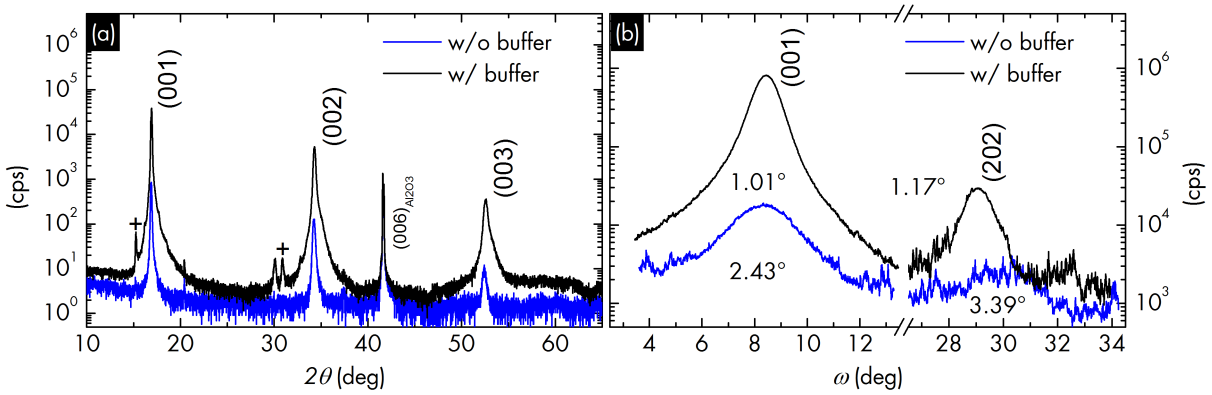

Figure 6.6 Na_2IrO_3 deposited on *c*-plane sapphire with (black) and without (blue) a ZnO buffer layer. (a) Out-of-plane orientation is investigated by XRD 2θ-ω-scans. K_β lines are denoted by a +. (b) Rocking curves of the Na_2IrO_3 (001) and (202) reflexes. The corresponding half-widths are indicated. [Samples: E4028, E4029.]

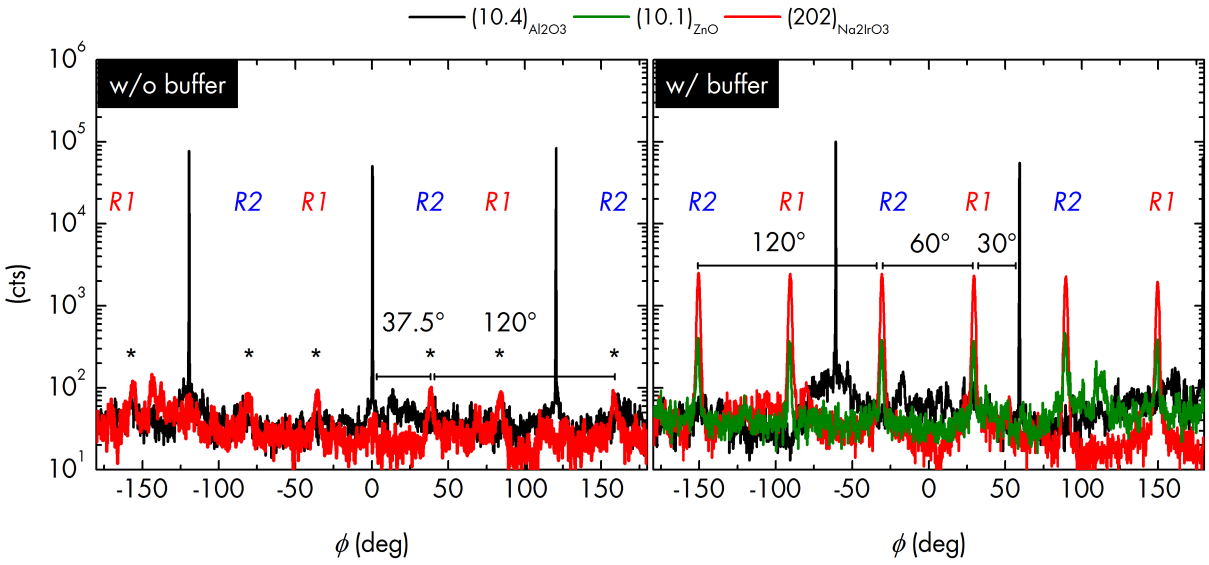

Figure 6.7 In-plane epitaxial relationship of Na_2IrO_3 deposited on *c*-plane sapphire with (right) and without (left) a *c*-ZnO buffer layer investigated by XRD ϕ-scans. In the left diffraction pattern, an asterix (*) highlights the positions of the six $Na_2IrO_3\{202\}$ reflexes belonging to rotational domains *R*1 and *R*2. [Samples: E4028, E4029.]

The in-plane epitaxial relationship between substrate and epilayer was investigated by measuring XRD ϕ-scans of the sapphire (10.4) and the Na_2IrO_3 (202) lattice planes. The typical results for Na_2IrO_3 deposited on *c*-plane sapphire are shown on the left in Fig. 6.7. It is assumed that the ideal surface of *c*-plane sapphire has a two-dimensional (2D) surface point symmetry of $3m$ [104]. For Na_2IrO_3(202), six very weak reflexes with uneven 45°/75° azimuthal spacings are observed. They are rotated alternately by about $\pm 37.5°$ against the nearest *m*-plane. The resulting pattern is thus three-fold with 120° periodicity.

The in-plane epitaxial relationship can generally be understood by a group theoretical treatment of the respective rotational and mirror symmetries of substrate and epilayer or, in other words, their 2D point symmetries [104]. As was mentioned before, the ideal *c*-plane sapphire surface has $3m$ symmetry. Although Na_2IrO_3 is described by a monoclinic $C2/m$ unit cell due to a monoclinic distortion of the atomic layers stacked along the *c*-direction [42], the minimal surface point symmetry of each of these layers is $3m$, as illustrated in Fig. 6.8(a) for the iridium honeycomb lattice with edge sharing NaO_6 octahedra. In fact, the six lattice planes $(\bar{2}00)$, $(\bar{1}\bar{3}0)$, $(\bar{1}30)$, $(1\bar{3}0)$, (130), (200) = {200} are equivalent for an undistorted honeycomb lattice, see Fig. 6.8(b). This holds in particular if $a/b = \tan(60°)$ which applies to all experimental unit cells within 0.001 %. According to Ref. [104], a $3m$-symmetric epilayer is expected to grow on a $3m$ substrate within one rotational domain. If additionally the mirror symmetry planes m_S and m_E of substrate and epilayer are misaligned, the number of rotational domains doubles [104]. Clearly, the observation of six, unevenly spaced (202) reflexes proves, that Na_2IrO_3 does grow within the expected two rotational domains on *c*-sapphire. The data suggest further that a coin-

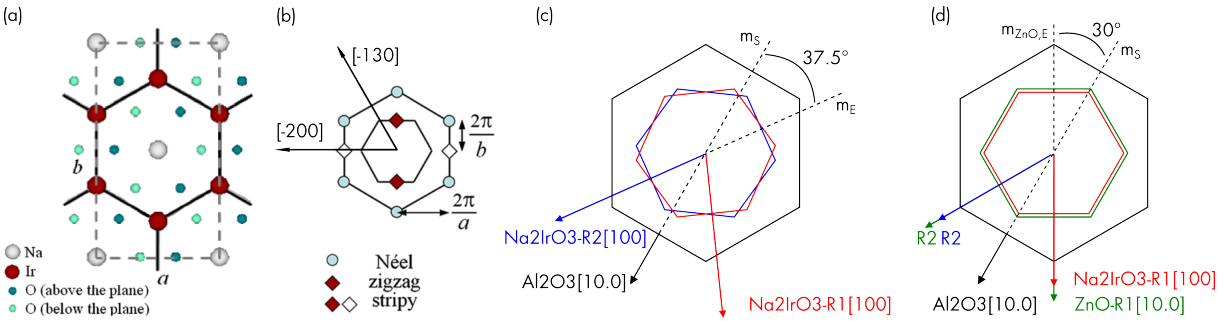

Figure 6.8 (a) Schematic representation of the Ir honeycomb lattice and the edge-sharing NaO_6 octahedra projected in the *ab*-basal plane and stacked along the monoclinic *c*-axis in Na_2IrO_3. Together, they exhibit a 3*m* surface point symmetry. (b) Reciprocal space diagram of the honeycomb lattice showing the first and second Brillouin zone, as well as the positions of magnetic Bragg peaks related to three magnetic ordering patterns. Two of the six equivalent <200> directions are drawn in. (c) The schematic illustrates that 3*m*-symmetric Na_2IrO_3(001) aligns on *c*-sapphire within two rotational domains *R*1 (red) and *R*2 (blue) due to a 37.5° in-plane rotation of the honeycomb lattice against the substrate. (d) On *c*-ZnO, Na_2IrO_3 aligns in-plane within one rotational with $[100]_{Na2IrO3}\|[10.0]_{ZnO}$. The red and blue hexagons in (c,d) represent the Ir honeycomb lattice. All lattice dimensions are to scale. [Samples: E4028, E4029. Figs. (a,b) taken from Ref. [42].]

cidence lattice is formed by a rotation of the Na_2IrO_3 basal layer against the sapphire substrate by approximately 37.5°. Precisely this rotation gives rise to the misalignment of the mirror symmetry planes and a total of two rotational domains *R*1 and *R*2, as illustrated schematically in Fig. 6.8(c).

Na_2IrO_3 deposited on *c*-sapphire together with an intermediate *c*-ZnO layer appears to have a more symmetric in-plane epitaxial relationship. The corresponding ϕ-scan is presented in Fig. 6.7(b). Hexagonal *c*-ZnO has 3*m* point symmetry and grows on *c*-sapphire within two rotational domains due to a 30° in-plane rotation of the lattice, in order to form a coincidence lattice [104]. The in-plane epitaxial relationship is $[10.0]_{ZnO}\|[11.0]_{Al2O3}$. For Na_2IrO_3 deposited on the intermediate *c*-ZnO layer, the ϕ-scan shows six evenly spaced {202} reflexes. Each of the ZnO rotational domains gives rise to one Na_2IrO_3 rotational domain, as expected from the 3*m* surface point symmetries [104]. Thus, also Na_2IrO_3 aligns within two rotational domains on intermediate *c*-ZnO with $[100]_{Na2IrO3}\|[10.0]_{ZnO}$.

Judging by the {202} peak heights and half-widths, the in-plane epitaxial quality of Na_2IrO_3 is significantly improved by the intermediate *c*-ZnO layer. FWHMs are reduced in the present samples from around 3.5 to 1.8°. Very similar results were also obtained with *a*-plane sapphire substrates, for which the in-plane epitaxial relationship without an intermediate *c*-ZnO layer is typically $[01.0]_{Na2IrO3}\|[00.1]_{Al2O3}$, see Fig. 6.2(b).[3] In fact, *c*-ZnO might act as a better structural template than *c*-sapphire because its in-plane unit cell and the iridium honeycomb

[3] The 3*m* and *m* point symmetries of epilayer and substrate, together with a misalignment of the mirror symmetry planes (Na_2IrO_3(131) and Al_2O_3(116) are rotated by ±30°), gives rise to two rotational domains and a total of six evenly spaced {131} reflexes.

lattice in Na_2IrO_3 have very similar dimensions, that differ by only 3.7 %. In contrast, the structural quality of a Li_2IrO_3 thin film was not improved by intermediate *c*-ZnO (cf. Fig. 7.6(c)). There, the lattice mismatch between *c*-ZnO and the Ir honeycomb lattice is about 8 %. The in-plane epitaxial relationship of the final heterostructure is illustrated schematically in Fig. 6.8(d).

Above results demonstrate, that deposition of an intermediate ZnO layer on *c*- or *a*-plane sapphire significantly improves the structural quality of heteroepitaxial Na_2IrO_3 thin films. Similarly, *n*-type conducting epitaxial ZnO/ZnO:Al (AZO) bilayers were realized. Hall-effect measurements of the bilayer gave a resistivity of $\rho = 1.337(2) \times 10^{-2}$ Ωcm, a charge carrier density of $n = 1.2(5) \times 10^{19}$ cm^{-3}, and a mobility of $\mu = 40.1(8)$ cm^2/Vs. Current-voltage (IV) characteristics of Au on Na_2IrO_3 and Au on ZnO/AZO were ohmic with a resistance of 2771(1) and 263.8(1) Ω, respectively. More strikingly, a non-ohmic IV characteristic is observed for Au on ZnO/AZO/Na_2IrO_3 at room-temperature and ambient light, see Fig. 6.9(c). It suggests that a ZnO/AZO bilayer could be used as an epitaxial bottom gate. The depletion of the bulk carrier density by control of a gate voltage might allow to probe the proposed conduction via topological surface states [124, 125]. In conclusion, the structural improvements may even warrant renewed neutron diffraction experiments (cf. Sec. 6.2).

6.4 Summary

Heteroepitaxial Na_2IrO_3 thin films with (001) out-of-plane preferential orientation were deposited on 1.5- and 2.0-inch diameter *a*- and *c*-plane sapphire substrates by PLD. The phase purity of these large-area films is homogenous along the entire sample diameter. Such large-area thin films represent a welcome alternative to the Na_2IrO_3 single crystals of limited size. A stack of seven 1.5-inch samples was investigated by neutron diffraction to determine the magnetic ordering wave vector. However, due to the high in-plane mosaicity the experiment was unsuccessful. Subsequently, deposition of an intermediate *c*-ZnO layer led to a significant improvement of in-plane epitaxial quality and might even warrant renewed neutron diffraction experiments. Such optimized samples were also prepared for pump-probe spectroscopy, but results are pending

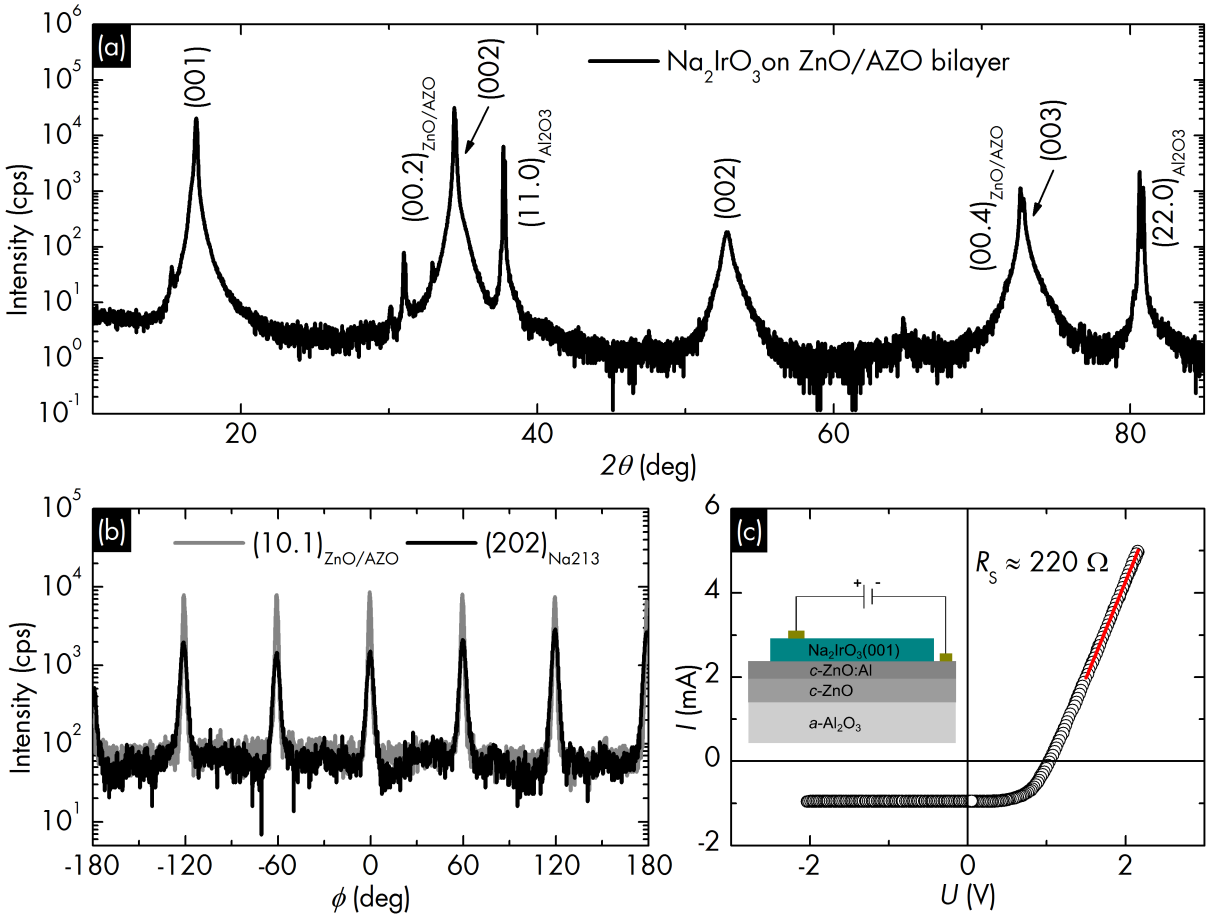

Figure 6.9 Na_2IrO_3 grown on a ZnO/ZnO:Al (AZO) bilayer deposited on a-Al_2O_3. XRD 2θ-ω- (a) and ϕ-scans (b) demonstrate, that the out-of-plane and in-plane epitaxial relationships are $[001]_{Na2IrO3}\|[00.1]_{ZnO/AZO}\|[11.0]_{Al2O3}$ and $[110]_{Na2IrO3}\|[11.0]_{ZnO/AZO}\|[00.1]_{Al2O3}$, respectively. (c) A non-ohmic current-voltage characteristics of the Na_2IrO_3 film and the epitaxial ZnO/AZO bilayer was measured at room-temperature and ambient light using sputtered gold contacts. The low rectifying ratio $I(2V)/|I(-2V)| \approx 4.5$ is likely due to the 0.9 mA photocurrent. $R_S \approx 220\ \Omega$ is an estimate of the series resistance. Inset: Schematic of the bottom gate structure. [Samples: E3909, E3913.]

7 Li_2IrO_3

As mentioned in Sec. 2.1, Li_2IrO_3 is a candidate material for either a topological insulator or a spin-liquid. In comparison with its sister compound Na_2IrO_3, available single crystals are even smaller and experiments were thus often restricted to polycrystalline samples. High-quality, epitaxial thin films might hence alleviate these limitations and might even pave the way for future device applications. Li_2IrO_3 thin films were prepared by means of pulsed laser deposition and studied for their structural properties, Sec. 7.1, as well as their stoichiometrical and surface morphological properties, Sec. 7.2. Transport and magnetic properties were performed in analogy to Na_2IrO_3 thin films [MJ1]. In particular, electrical resistivity was investigated for Mott variable range hopping, Sec. 7.3, and magnetoresistance for a possible weak antilocalization effect, Sec. 7.4. In addition, the dielectric function was determined by means of spectroscopic ellipsometry (Sec. 7.5) to investigate the similarities and differences of electronic excitations compared to Li_2IrO_3 single crystals and other related iridates.

7.1 Structural properties and epitaxial relationship

Li_2IrO_3 films were deposited on four different single-crystalline substrates, namely *a*-plane and *c*-plane sapphire, ZrO_2:Y (YSZ) (001), and $YAlO_3$ (YAO) (001). PLD parameters similar to the deposition of Na_2IrO_3 were chosen: $p_{O2} = 0.016$ mbar and $T_g \approx 550$ °C. XRD 2θ-ω-scans of these four samples are shown in Fig. 7.1. The observed peaks are indexed according to a monoclinic $C2/c$ unit cell [43, 44]; their broadness and low intensity suggests a significant amount of structural disorder. Common to all samples is the presence of a (001)-oriented phase. On *a*-plane sapphire an additional peak at $2\theta \approx 34.8°$ is observed that can be assigned to either the (200) or (13-1) lattice plane at $\approx 35.3°$. However, it also coincides well with the IrO_2 (011) plane at $2\theta = 34.8°$ with much higher relative intensity of 92% as opposed to 32 and 16% of the (200) and (13-1) planes, respectively. The possible presence of a IrO_2 phase is discussed further below. A characteristic of the the monoclinic unit cell in Li_2IrO_3 is that many lattice planes have very similar *d*-spacings. For example, this applies to the (20-2) and (004) lattice planes at $2\theta \approx 37°$. Due to the large peak widths it is assumed that both phases are present with (001) being the preferred out-of-plane orientation. The out-of-plane lattice parameter *c* shows no significant variation among the different substrates. Since both the lattice mismatch to the substrate the film thickness (30,000 laser pulses) are large, a relaxed film growth is assumed.

On *a*-plane sapphire two additional samples at different oxygen partial pressures were prepared.

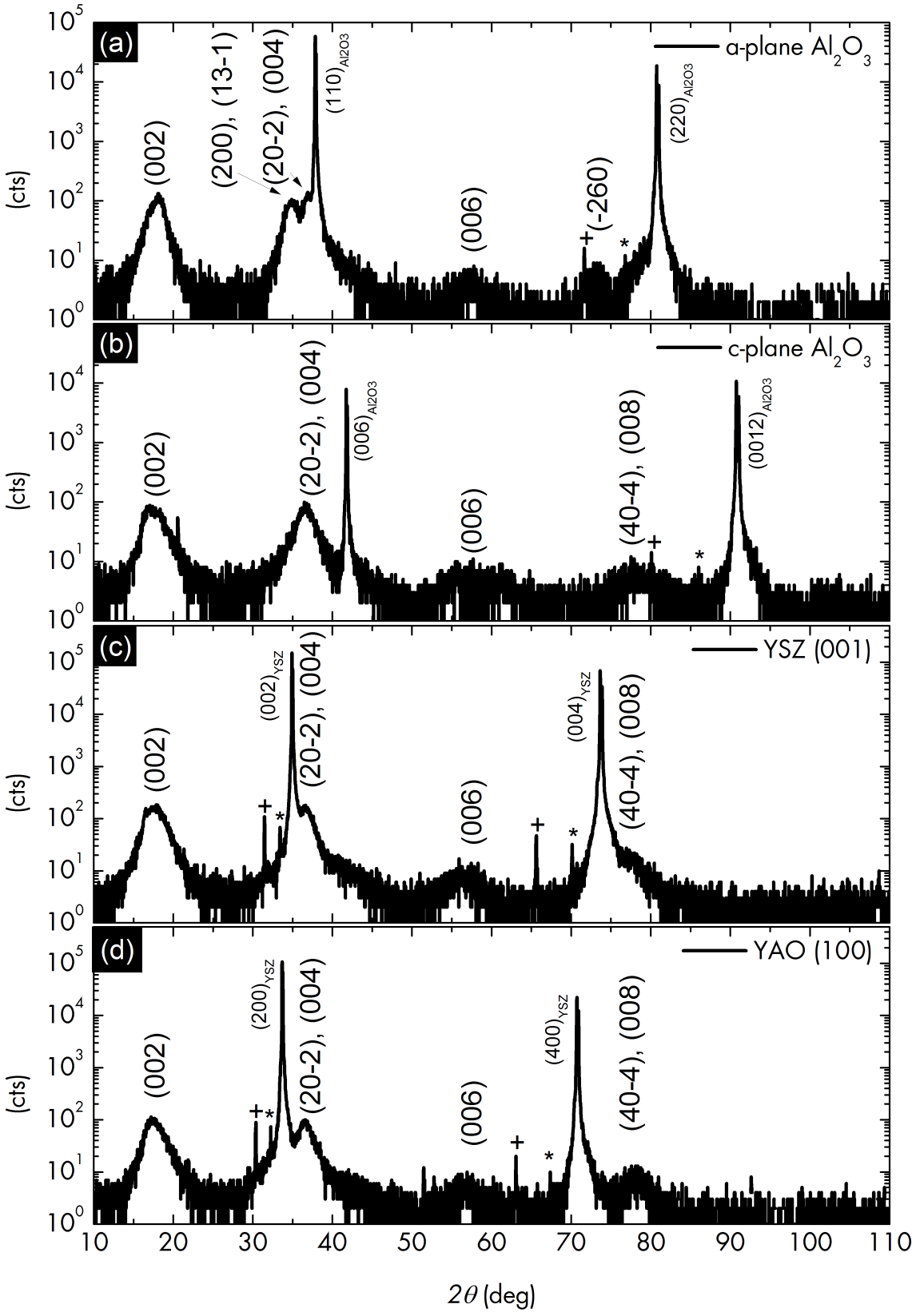

Figure 7.1 Li_2IrO_3 thin films PLD-grown on different single-crystalline substrates at p_{O2} = 0.016 mbar, $T_g \approx 550$ °C: (a) *a*-plane sapphire, (b) *c*-plane sapphire, (c) YSZ (001), (d) YAO (001). K_β and W lines are denoted by + and ∗. [Samples: E3458, E3466, E3468, E3469.]

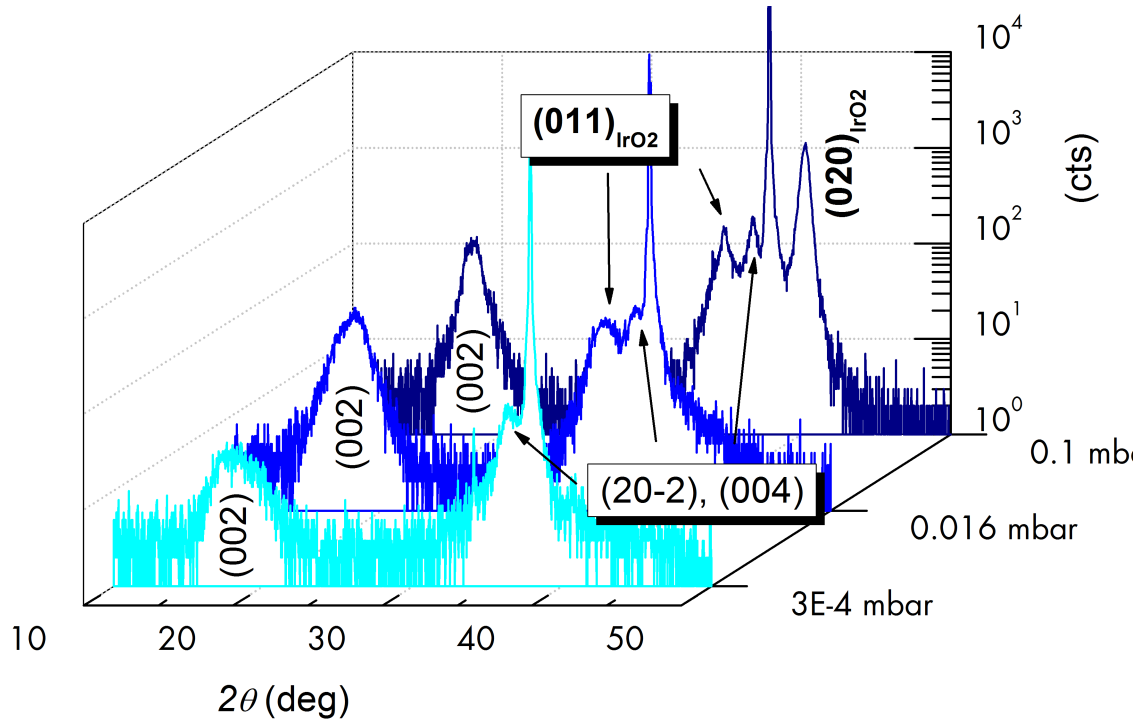

Figure 7.2 XRD 2θ-ω-scans of three Li_2IrO_3 films grown on *a*-plane sapphire at $T_g \approx 550$ °C and oxygen partial pressures as indicated. At higher partial pressures, IrO_2 is present in the films. [Samples: E3458, E3470, E3474.]

The XRD analysis of this pressure series is shown in Fig. 7.2. All three samples show a Li_2IrO_3 (001) phase. The peak intensities decrease with oxygen partial pressure from 0.1 down to 3×10^{-4} mbar, while the peak widths increase from about 1.2° to 2.3° suggesting a larger tilt distribution and poorer crystalline quality. The probable double peak of the (20-2)/(004) planes is always present, as well. At 0.1 mbar two additional peaks at 34.8° and 40.3° exist. The former is also present at 0.016 mbar. As discussed previously, the peak at 34.8° could be related to the Li_2IrO_3 (200) or (13-1) planes. However, in light of the presence of another peak at 40.3° in the 0.1 mbar-sample, the possibility of a IrO_2 phase becomes more probable. Both peaks are a better match with the IrO_2 (011) and (020) planes at approximately 34.7° and 40.1°, respectively. Furthermore, these planes have larger relative intensities of 92 and 27 %. For lowest pressure, 3×10^{-4} mbar, the IrO_2 phase is not observed in the XRD pattern. The likely origin of the IrO_2 phase is the oxidation of Ir-species in the plasma. At sufficiently high oxygen partial pressures measurable amounts of IrO_2 can form and adsorb onto the substrate surface. In fact, temperature dependent resistivity of the 0.1 mbar-sample showed metallic behavior supporting the formation of IrO_2 at high oxygen partial pressures.

All previous films were deposited at a heater power of 400 W ($\approx$ 550 °C). To study the influence of growth temperature on the structural properties, additional films were prepared at

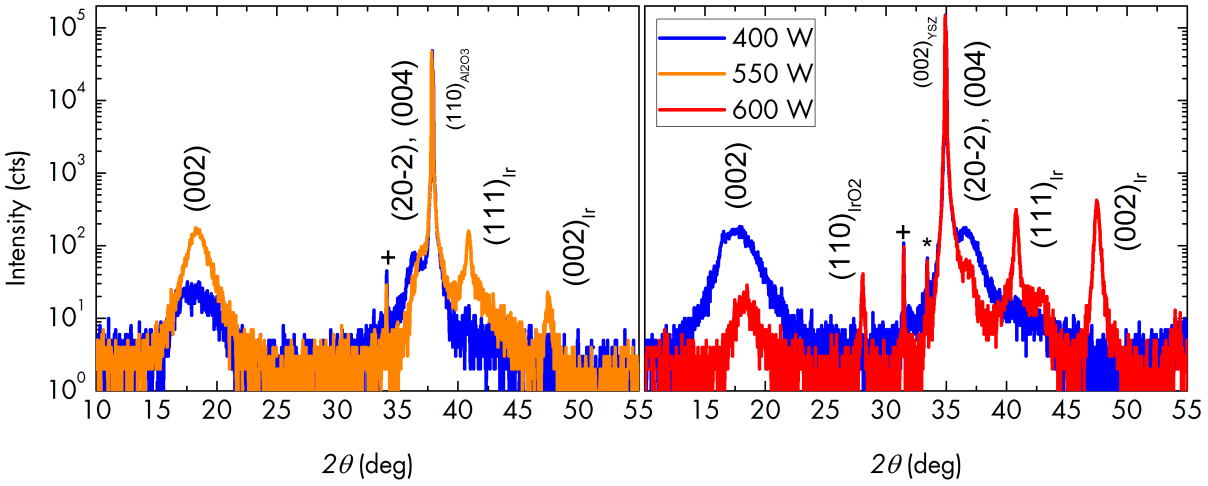

Figure 7.3 Influence of deposition temperature. Shown are XRD 2θ-ω-scans of Li_2IrO_3 films grown on a-plane sapphire (left) and YSZ (001) (right) at $p_{O2} = 3 \times 10^{-4}$ mbar and heater powers as indicated. Heater powers correspond to approximately 550, 650 and 700 °C, respectively. High temperatures favor the formation of Ir and IrO_2. K_β and W lines are denoted by + and ∗. [Samples: E3468, E3470, E3485, E3486.]

3×10^{-4} mbar and heater powers of 500, 550, and 600 W. Figure 7.3 shows two pairs of samples grown at different temperatures on a-plane sapphire and YSZ (001), respectively. Up to 550 W the peaks related to the Li_2IrO_3 (001) phase increase in height. Simultaneously, above 400 W peaks related to Ir phases, (111) and (002), appear that are not present at the lowest temperature shown. At the highest temperature, the Li_2IrO_3 (00l) peaks decrease in intensity while the other peaks increase. Additionally, the IrO_2 (110) plane is observed. The combination of low pressure and high temperature enhances the volatility of lithium with a low melting point of 180 °C and possibly favors desorption or evaporation from the substrate. Consequently, formation of crystalline Ir or the formation of IrO_2 is favored. An off-stoichiometric Ir:O ratio of 1:2.02 obtained from energy-dispersive X-ray analysis supports this claim (cf. Sec. 7.2).

Considering above results, optimized Li_2IrO_3 thin films were grown on YSZ(001) substrates by pulsed laser deposition at $T_g \approx 550$ °C (500 W) and $p_{O2} = 3 \times 10^{-4}$ mbar [MJ3]. A typical XRD 2θ-ω pattern of such a film is shown in Fig. 7.4. In contrast to the YSZ substrate peak, the pattern shows four rather broad film reflexes. Considering that the number of laser pulses was 30,000, the film reflexes have rather low intensity. The pattern is indexed assuming a monoclinic $C2/c$ unit cell [43, 44]. Due to the broadness of the film peaks and for clarity's sake, the XRD pattern of the polycrystalline PLD target is underlayed in Fig. 7.4. This way it becomes apparent that some of the film peaks have contributions of more than one crystal orientation. Pronounced symmetric peaks related to the (001) planes can be seen. A closer inspection of the peak at about 37° reveals that in monoclinic Li_2IrO_3 the (20-2) and (004) planes are very close and likely constitute said peak in the film pattern. The peak at 36.88° was fit with two Gaussians to obtain $d_{(20\text{-}2)}$, $d_{(004)}$, and the domain ratio $I_{(004)}$:$I_{(20\text{-}2)}$. While in polycrystalline targets the

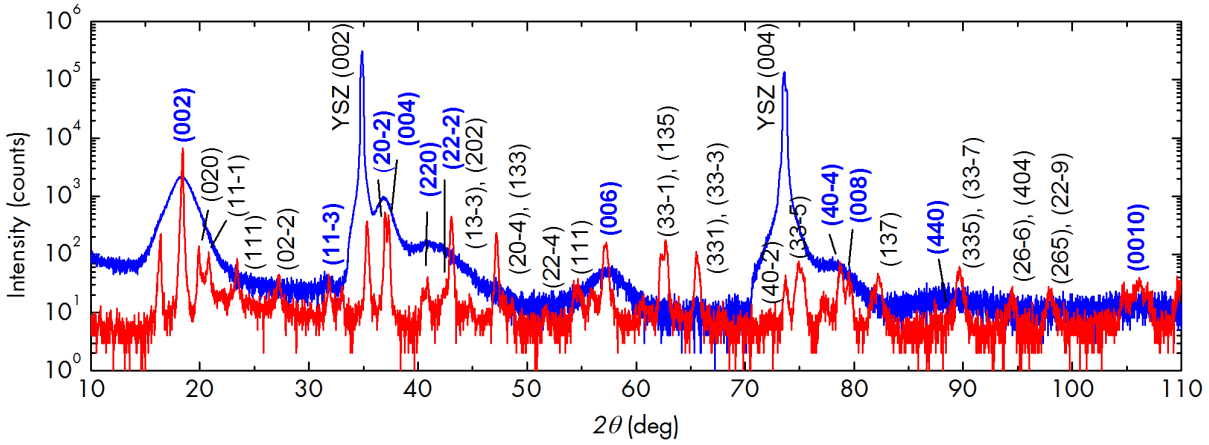

Figure 7.4 Typical X-ray diffraction (XRD) 2θ-ω scan of a PLD-grown Li_2IrO_3 thin film on ZrO_2:Y (001) (YSZ) in blue, underlayed with the pattern of the polycrystalline PLD target in red. Significant film reflexes are labeled in blue. [Taken from [MJ3]. Sample: E3581.]

domain ratio is about 14:1, the ratio is much lower in this pattern (2.3:1). This strongly suggest the presence of (001) *and* (10-1) preferential out-of-plane crystalline orientations. The c lattice parameter is determined as 9.71(1) Å from the d_{00l} values of the (002), (004) and (006) reflexes. Access to the in-plane lattice parameters a and b was gained via 2θ-ω scans of the asymmetric (202) and (131) reflexes of the (001)-oriented phase. Assuming $\beta = 99.992°$ [43], the lattice parameters are $a = 5.20(3)$ Å and $b = 8.99(14)$ Å. These values show only small deviations from the reported values [43, 44], deviating by only +0.6%, +0.7% and -0.8% for a, b and c, respectively. Since Li_2IrO_3 has a considerable lattice mismatch to YSZ(001), these deviations are likely the result of some amount of internal rather than external strain.

The in-plane epitaxial relationship is investigated by ϕ-scans of the asymmetric Li_2IrO_3 (131) reflex of the (001)-oriented phase and of the YSZ (111) reflex, as shown in Fig. 7.5. In cubic, (001)-oriented YSZ, the $\{111\}$ planes are fourfold and the surface point symmetry is $4mm$ [104]. For the Li_2IrO_3 (131) plane, 24 reflexes spaced by 15° and alternating in intensity are observed. The intensity ratio is about 7:1. Similar to Na_2IrO_3(001), the surface point symmetry of Li_2IrO_3(001) is $3m$ (cf. Sec. 6.3). Thus, the (001)-oriented epilayer aligns within at least 4 rotational domains since the mirror symmetry planes of epilayer and substrate are aligned [104]. This explains 12 of the 24 $\{131\}$ peaks with an even 30° spacing. The alignment of the epilayer [130]-direction with YSZ$\langle 111\rangle$ gives rises to an additional 4 rotational domains. This alignment appears to be energetically less favorable, as inferred from the 7:1 domain ratio. A schematic illustration of the in-plane epitaxial relationship is given in Fig. 7.5.

Comparison to Na_2IrO_3 thin films The rocking curve of the Li_2IrO_3 (002) Bragg reflex at $2\theta = 18.29°$ is shown in Fig. 7.6(a). Its full width at half maximum (FWHM) is 9.62° and indicates a large tilt angle distribution of the crystallites. For comparison, the figure displays a

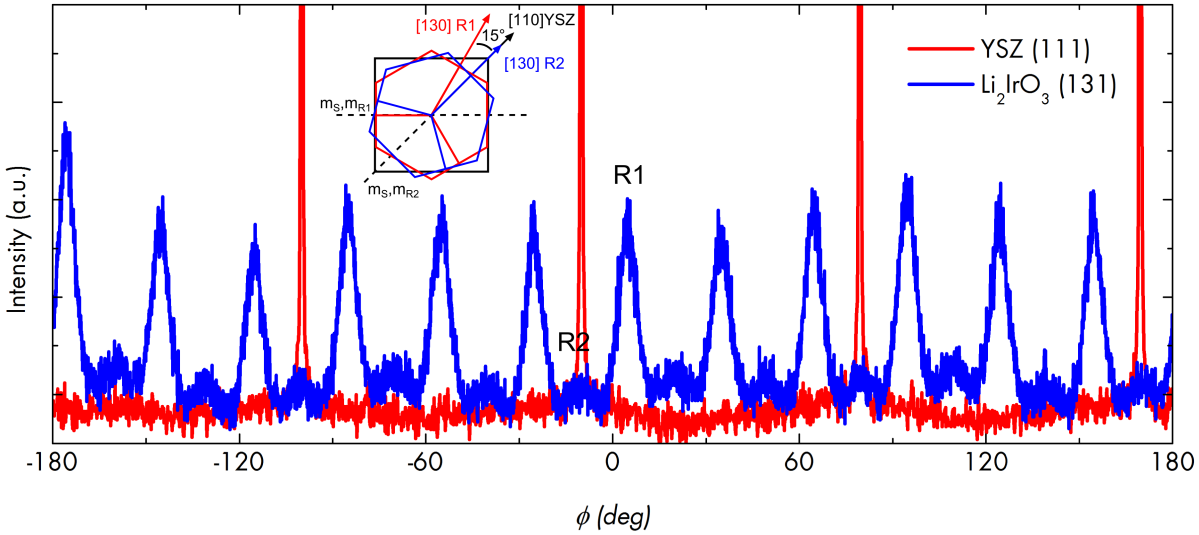

Figure 7.5 XRD ϕ-scans of asymmetric Li_2IrO_3 (131) and YSZ (111) reflexes of the Li_2IrO_3(001) phase. The schematic illustrates the epitaxial in-plane relationship between the 4*mm* substrate (black) and the 3*m* epilayer (red, blue). For clarity, only 2 of the 8 rotational domains R1 and R2 are shown; the others are obtained by applying the C_4 rotation operation to the epilayer. Mirror symmetry planes of substrate and the two principal rotational domains are denoted as m_S, m_{R1} and m_{R2}, respectively. The hexagons represent the Ir honeycomb lattice. [Adapted from [MJ3]. Sample: E3581.]

(001)-rocking curve of a Na_2IrO_3 film grown on top of a *c*-ZnO buffer layer; it has a FWHM of only 1.01°. Hypothetically, the in-plane lattice mismatch of Li_2IrO_3 is minimized on YAO(011) substrates to a relatively even -2.75 and -1.49 % along *a* and *b*, respectively. Fig. 7.6(b) shows a XRD 2θ-ω-scan of Li_2IrO_3 deposited on YAO(011) and cubic YSZ(001), for which the lattice mismatch is at least -0.93 and -74.51 %. Clearly, the structural film quality does not improve on YAO(011). Deposition of an intermediate *c*-ZnO buffer layer did not further improve the epitaxial quality of Li_2IrO_3 thin films either, see Fig. 7.6(c). Note, that the basal plane of *c*-ZnO and the Ir honeycomb lattice of Li_2IrO_3(001) have a lattice mismatch of about 8 % - too large for pseudomorphic growth. These comparisons show that, on the one hand, Li_2IrO_3 films are of lower structural quality than Na_2IrO_3 films. On the other hand, even at optimized deposition conditions there exists an insensitivity to the degree of lattice mismatch with the substrate. Although this can in parts be understood from the films being relaxed at $\approx$ 400 nm, it still is in contrast to Na_2IrO_3 films. It is thus possible, that the more significant limiting factor might instead be the PLD target.

7.2 Chemical composition and surface morphology

A qualitative elemental investigation of Li_2IrO_3 thin films was conducted using secondary neutral mass spectrometry (SNMS). It confirmed the presence of only Li, Ir, and O. Via SNMS

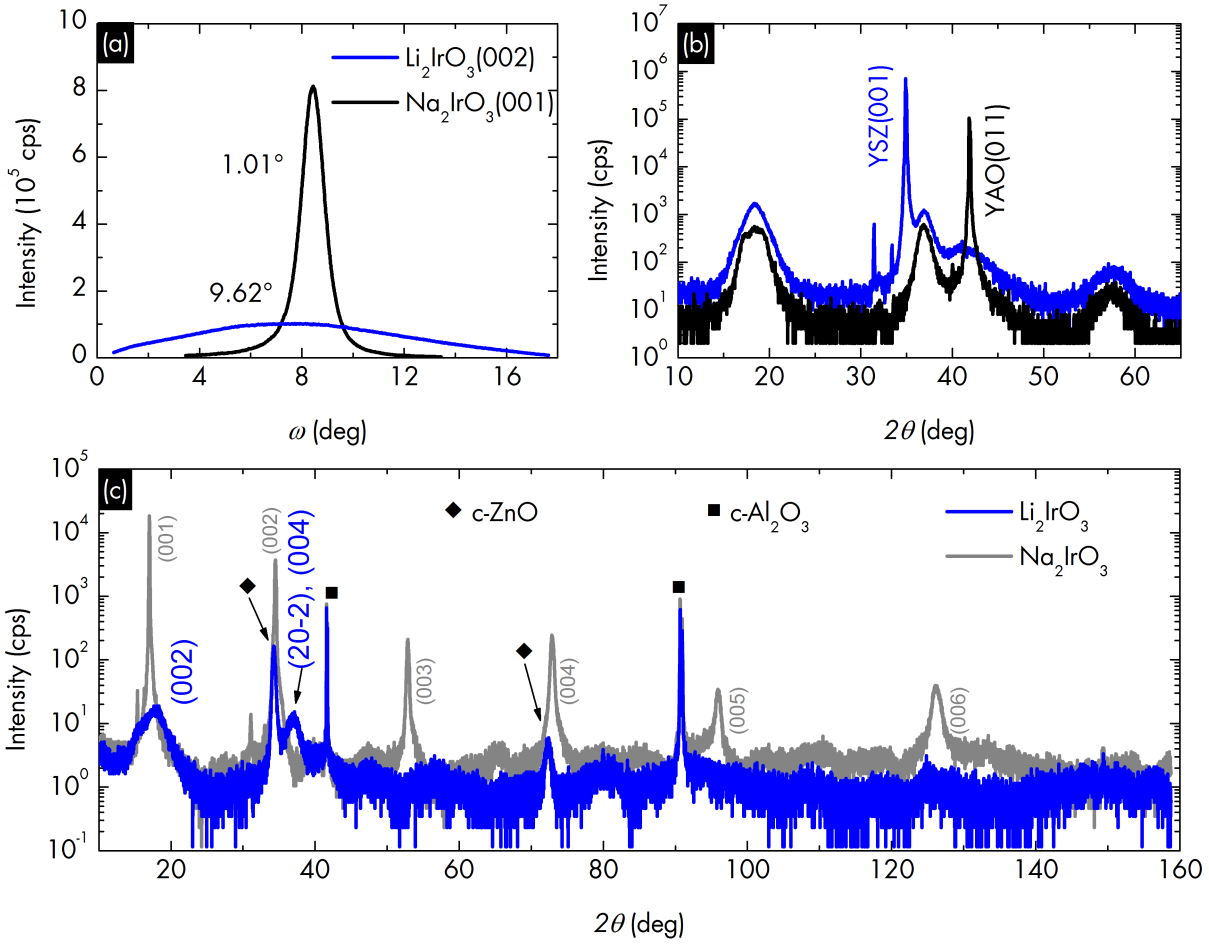

Figure 7.6 (a) Comparison between XRD rocking curves of Li_2IrO_3(002) and Na_2IrO_3(001) reflexes. Peak half-widths are 9.62° and 1.01°, respectively. Li_2IrO_3 was prepared on YSZ(001) under optimized conditions (see text). The Na_2IrO_3 sample was deposited on an intermediate *c*-ZnO layer and exhibits significantly lower tilt mosaicity (cf. Sec. 6.3). (b) Comparison between Li_2IrO_3 deposited on YSZ(001) and YAO(011) by XRD 2θ-ω-scans. Although lattice mismatch with YAO(011) is -2.75 and -1.49 % along *a* and *b*, resp., the structural quality is not improved. Peak assignment can be adopted from Fig. 7.4. (c) XRD 2θ-ω-scan of Li_2IrO_3 deposited on *c*-plane sapphire with an intermediate *c*-ZnO layer. The epitaxial quality is not improved by this approach. For comparison, a pattern of an identically grown Na_2IrO_3(001) film (gray) is underlayed. [Samples: (a) E3622, E4029, (b) E581, E3623, (c) E3925, E3926.]

depth profiling, an accumulation of volatile Li at the film-substrate interface was observed, see Fig. 7.7. However, it is currently not clear if the Ar^+-sputtering in SNMS contributes to this Li accumulation at the interface. Energy dispersive X-ray analysis gave an apparently oxygen deficient Ir:O ratio of 1:2.84 under the optimized PLD conditions of $p_{O2} = 3 \times 10^{-4}$ mbar and $T_g = 550$ °C, as discussed in Sec. 7.1. This ratio points to possible oxygen vacancies, that might in turn explain the deviating lattice parameters due to internal strain as observed in XRD. At the same growth temperature but 0.1 mbar oxygen partial pressure the Ir:O ratio is 1:3.04. This larger ratio is for one indicative of a greater incorporation of oxygen into the Li_2IrO_3 phase with a unit cell volume of 222×10^6 pm^3. However, it can also be attributed to the IrO_2 phase which holds two oxygen atoms in a unit cell volume of only 64×10^6 pm^3, i.e. thrice more oxygen atoms per unit volume. For highest growth temperatures (700 °C and 600 W, resp.), films show a Ir:O ratio of only 1:2.02, which can be explained by the presence of crystalline Ir phases while Li_2IrO_3 is greatly reduced.

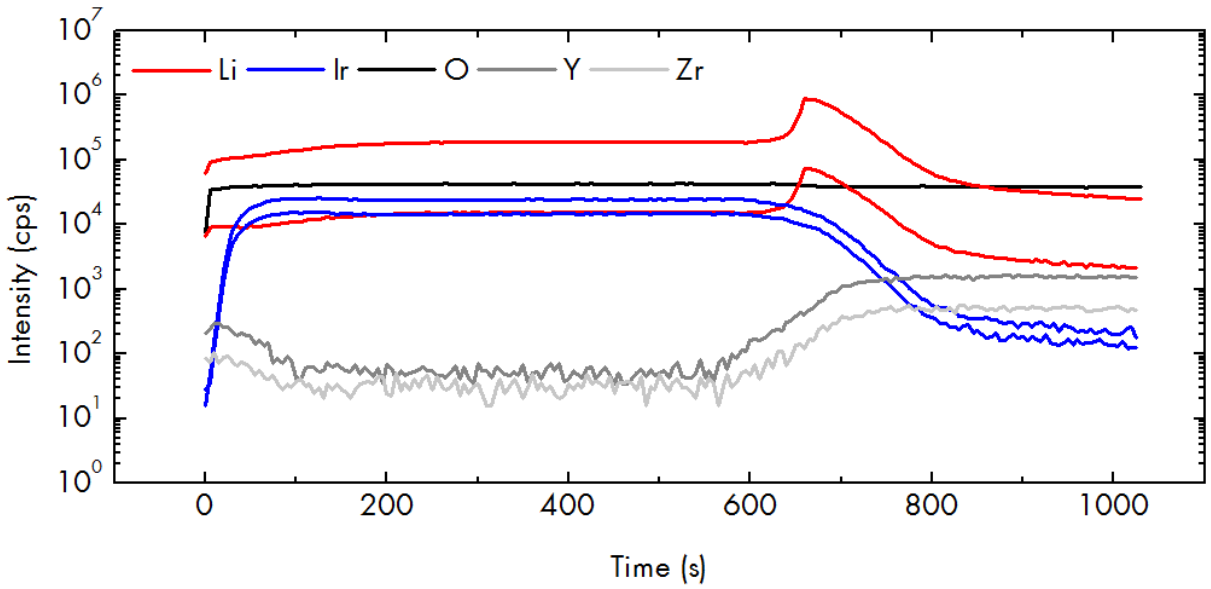

Figure 7.7 Depth profile of a Li_2IrO_3 thin film obtained from secondary neutral mass spectrometry using an argon plasma and a bombardment AC voltage of 600 V. An accumulation lithium at the film-substrate interface is clearly visible in the profile.

Figures 7.8 shows topographic images of the Li_2IrO_3 film surface obtained with non-contact atomic force microscopy and scanning electron microscopy, respectively. The images reveal a granular surface with an rms roughness of 15.7 nm and a peak-to-valley height of 139.0 nm. The surface morphology can be explained by the presence of two preferential orientations and furthermore by the mechanically soft target promoting grain agglomeration. Attempts to grow films on lattice-matched $YAlO_3(011)$ single crystals did not produce any improvement in terms of either crystalline structure or surface morphology. Thus, the observed surface morphology is

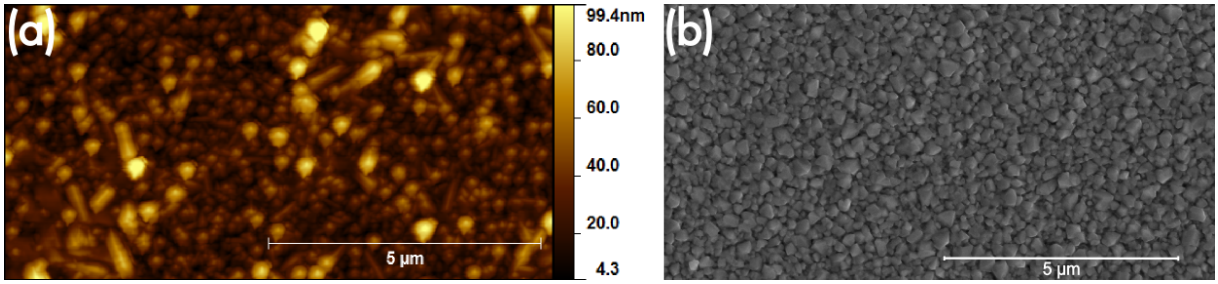

Figure 7.8 The surface morphology of the film is illustrated by non-contact AFM topographic (a) and scanning electron microscopy images (b). [Sample: E3581.]

not primarily the result of film relaxation.

7.3 3D Mott variable range hopping transport

Temperature-dependent electrical resistivity Temperature dependent resistivity was measured from 300 to 25 K in van der Pauw geometry. Figure 7.9 displays the data obtained from the pressure (a) and temperature series (b) of Li_2IrO_3 films prepared on *a*-plane sapphire. For oxygen partial pressures of 0.016 mbar and lower, films exhibit semiconducting resistivity behavior. At lowest temperatures resistivity is tunable by up to three orders of magnitude. For comparison, resistivity data of two samples prepared at 0.016 mbar on YSZ(100) and YAO(100) are also shown in Fig 7.9(a) (open circles). Apparently, film resistivity is largely unaffected by the choice of substrate material and can be understood from the fact, that films exhibit a relaxed growth on all substrates. The 0.1-mbar sample is metallic with resistivity decreasing with temperature within one order of magnitude. Metallic conduction is most likely caused by the IrO_2 phase present in the sample.

Under variation of growth temperature from about 550 to 650 °C only a slight increase in resistivity is observed while the general behavior remains unchanged. Although a metallic Ir phase is present in the film gown at 550 W as discovered in XRD, no metallic resistivity behavior is observed. As the XRD study showed, the crystallinity of the Li_2IrO_3 phase was improved by increasing the heater power from 400 to 550 W. Thus, measuring an increase in overall resistivity suggest that Li_2IrO_3 in its crystalline form is inherently an insulator as was already shown for single crystals [44].

The observed semiconducting behavior does not follow a simple activated law $\rho \propto \exp(-\Delta/T)$ of a classical band insulator, as can be inferred from the Arrhenius plot in Fig. 7.10(a), that can in principle also be associated with nearest-neighbor hopping more befitting of Mott insulators.

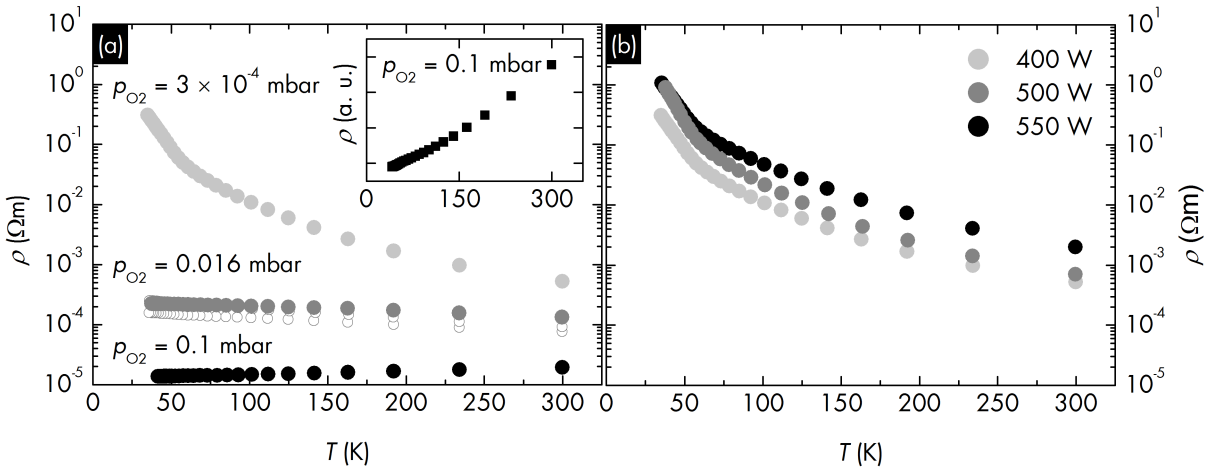

Figure 7.9 Resistivity ρ versus temperature T of Li_2IrO_3 thin films grown on a-plane sapphire. (a) $T_g \approx 550$ °C (400 W) and oxygen partial pressures p_{O2} as indicated. Data for films prepared on YSZ(100) and YAO(100) at 0.016 mbar are shown as open circles. Inset: zoom-in on the metallic 0.1-mbar sample. (b) $p_{O2} = 3 \times 10^{-4}$ mbar, heater powers as indicated. [Samples: E3458,68,69,70,74,86, E3511.

For optimized samples, i.e. $p_{O2} = 3 \times 10^{-4}$ mbar and $T_g = 550$ °C, and the ones already shown in Fig. 7.9(b), resistivity instead follows a $\rho \propto \exp[(\Delta/T^{1/4})]$ dependence down to at least 60 K. This behavior can be associated to three-dimensional Mott variable range hopping (VRH), which was similarly observed in Na_2IrO_3 thin films [MJ1], but also in, e.g., epitaxial doped and undoped TiO_2 anatase thin films [MJ7] and $LaNiO_3/LaAlO_3$ (100) superlattices [MJ8]. Variable range hopping conduction results from localized states within a narrow energy band near the Fermi energy. For further details, the reader is referred to Ref. [MJ1]. As indicated by straight, red lines in Fig. 7.10(b), the resistivity data from 300 to 57 K are fit with the three-dimensional Mott VRH model [126]

$$\rho = \rho_0 \exp[(T_0/T)^{1/4}], \tag{7.1}$$

where ρ_0 is a temperature-dependent resistivity coefficient and T_0 is the localization temperature. From the analysis of variable range hopping within percolation theory, the resistivity coefficient is given by [127, 128]

$$\rho_0 = \rho_0'(T/T_0)^s, \tag{7.2}$$

where $s \approx 1/4$. After fitting of the resistivity data with eqs. (7.1) and (7.2), an estimate for the localization length a can be obtained from T_0 according to [127]

$$T_0 = 21.2/k_B a^3 N(E_F), \tag{7.3}$$

provided that $N(E_F)$, the density of states at the Fermi level, is known. Based on available heat capacity data of Li_2IrO_3 single crystals [44], a density of states $N(E_F) \sim 10^{28}$ eV^{-1}m^{-3} is assumed (for details, see Ref. [MJ1]). All fitted and calculated parameters are shown in Tab.

7.1.

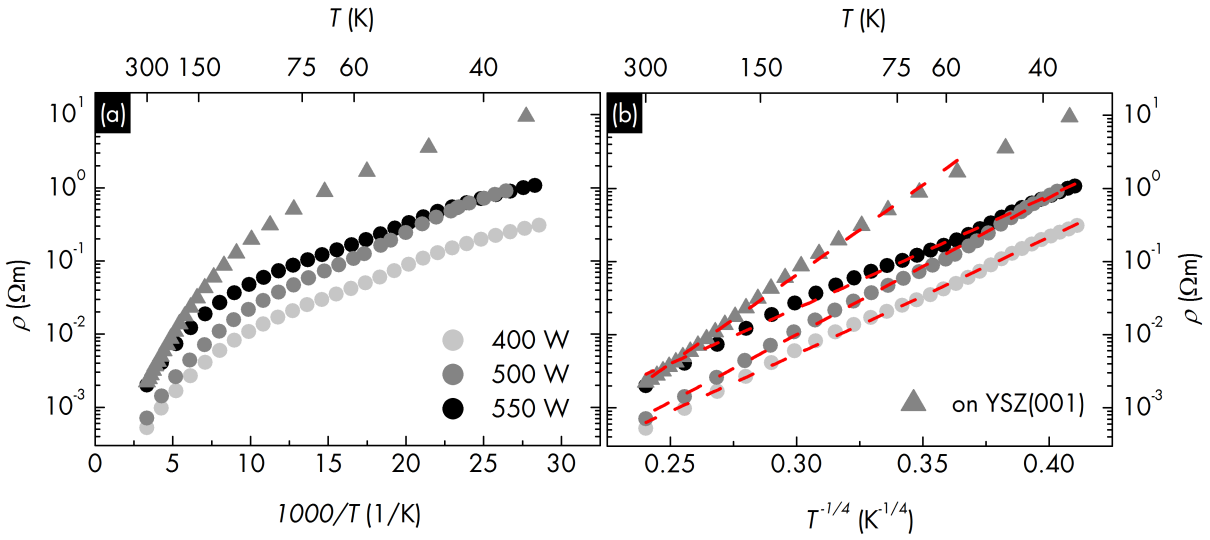

Figure 7.10 Temperature-dependent resistivity ρ versus temperature T of Li_2IrO_3 thin films grown at $p_{O2} = 3 \times 10^{-4}$ mbar and heater powers as indicated. (a) Log(ρ) versus $1000/T$. (b) Log(ρ) versus $T^{-1/4}$. The red dashed line fits according to eq. (8.1) with slope T_0 illustrate the dominant three-dimensional Mott variable range hopping conductivity mechanism. [Samples: E3470,86, E3511, E3753.]

Table 7.1 Li_2IrO_3 thin films grown on *a*-plane sapphire and YSZ(001) at $p_{02} = 3 \times 10^{-4}$ mbar: ρ_0 and T_0 are fit parameters according to eq. (7.1). The localization length a was calculated using eq. (7.3) assuming $N(E_F) = 10^{28}$ eV^{-1}m^{-3}.

heater power (W)	substrate material	ρ_0 (Ωm)	T_0 (K)	a (Å)	R_m/a	R_{max} (nm) (T = 57 K)
400	*a*-Al_2O_3	$4.32(3) \times 10^{-7}$	$2.49(1) \times 10^{6}$	2.17(1)	3.58(1)	0.90(1)
500	*a*-Al_2O_3	$1.40(1) \times 10^{-7}$	$4.48(4) \times 10^{6}$	1.76(2)	4.15(4)	1.05(1)
550	*a*-Al_2O_3	$2.63(3) \times 10^{-6}$	$2.17(3) \times 10^{6}$	2.24(3)	3.46(4)	0.87(1)
400	YSZ (001)	$2.04(2) \times 10^{-8}$	$1.26(2) \times 10^{7}$	1.25(2)	5.37(7)	1.36(2)

The calculated localization lengths a range from about 1.25 to 2.24 Å. They are comparable with the Ir-Ir and Ir-O bond distances of about 3 and 2 Å in Li_2IrO_3 which supports the applicability of Mott VRH. A criterion for the validity of Mott VRH is that the average hopping distance R_M is larger than the localization length a, i.e., [129]

$$\frac{R_M}{a} = \frac{3}{8}\left(\frac{T_0}{T}\right)^{1/4} > 1. \tag{7.4}$$

The ratio R_M/a is always greater than 1 at 300 K satisfying above criterion (cf. Tab 7.1). It is also verified that the maximal hopping distance R_{max} is much smallelrlarger than the film

thickness to exclude Mott VRH with hopping exponent 1/3. This kind of hopping is expected for thin films with a thickness in the order of the maximal hopping distance [130]

$$R_{\max} = \frac{a}{2}\left(\frac{T_0}{T}\right)^{1/4}. \tag{7.5}$$

Using the estimated localization length a, a maximal hopping distance no larger than $R_{\max}$ = 1.36(4) nm at 57 K is obtained, which is much smaller than the film thickness of approximately 400 nm.

Magnetoresistance Magnetic field-dependent electrical resistance, magnetoresistance (MR), of Li_2IrO_3 film samples was measured by Francis Bern of the Division of Superconductivity and Magnetism, Leipzig University. The aim of the experiment was to investigate, if the weak antilocalization effect could also be observed, as it was previously in Na_2IrO_3 thin films [MJ1]. Weak antilocalization in magnetoresistance is considered a signature of topological surface states [46]. Here, MR was measured in van der Pauw geometry at 10, 30, and 100 K and in applied magnetic fields $B = \mu_0 H$ of up to 8 T in both transversal and longitudinal geometries, where $R \perp B$ and $R \parallel B$, respectively. Full field sweeps were performed for all datasets.

Figure 7.11(a) shows the normalized transversal magnetoresistance of a typical Li_2IrO_3 film sample. Here, normalized magnetoresistance is defined as $[R(B)-R(0)]/R(0) = \Delta R/R_0$. Transversal MR is positive and follows a quadratic field dependence for all temperatures measured. However, the magnitude of the effect is small, with $\Delta R/R_0$ never exceeding 1 %, and decreases by nearly one order of magnitude at 100 K. The magnetoresistance displays no saturation up to 8 T. The normalized longitudinal MR at 30 K is presented in Fig. 7.11(b). The relative resistance change $\Delta R/R_0$ is nearly identical to the transversal MR data, i.e., the magnetoresistive effect is isotropic. Similarly, longitudinal MR follows a positive quadratic field dependence. Below 5 T, the data shows a hysteresis which, however, is merely attributed to a temperature drift instead of any kind of magnetoresistive effect.

For a conventional semiconductor a small transversal magnetoresistance can be explained classically by a Lorentz force $F_L = q(\vec{v} \times \vec{B})$ acting on the system's charge carriers. At least two types of carriers (e.g. electrons and holes) with different drift velocities $\vec{v}_i$ are required to prevent the compensation of F_L by a Hall field [131]. For the iridates, charge transport stems to a large part from the indirect Ir-O-Ir hopping via O $2p$, and direct hopping between Ir $5d$ orbitals. In any case, a positive and quadratic MR develops. Given an equal concentration n of both carrier types, magnetoresistance does not saturate at large fields satisfying $\mu_i B \gg 1$[1]; it thus follows

[1] For our carrier i with mobility μ_i we have $\mu_i B = q_i B \tau_i / m_i^* = -\omega_{ci}\tau_i$, where ω_{ci} and τ_i are the cyclotron frequency and relaxation time, respectively.

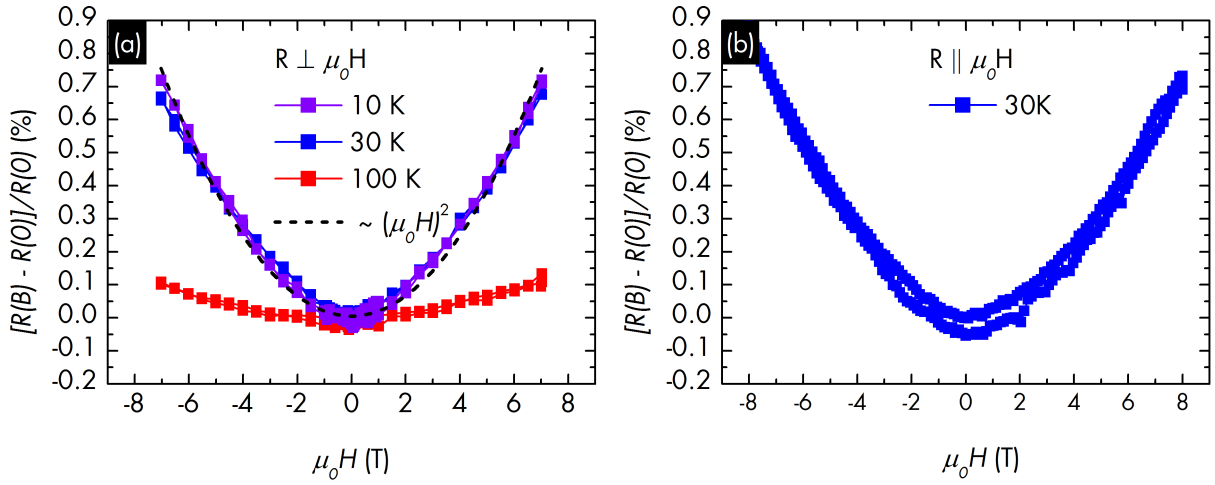

Figure 7.11 Normalized transversal (a) and longitudinal (b) magnetoresistance of typical Li_2IrO_3 film samples measured at 10, 30 and 100 K, is positive and parabolic. It is isotropic and does not saturate. The black dashed line in (a) is a parabolic fit of the 10-K data. The field hysteresis in (b) is due to a temperature drift. [Samples: E3752, E3596.]

the classical dependence $R_\perp \sim [\mu_1\mu_2/(\mu_1+\mu_2)]B^2$ [131]. In the other case, saturation usually sets in around $\mu B \approx 1$. The observed rise of $\Delta R/R_0$ from 100 to 10 K therefore implies a higher carrier mobility at lower temperatures and essentially suggests that charge carriers are scattered predominantly by phonons. On the other hand, the magnitude of $\Delta R/R_0$ itself indicates that the mobility of the measured samples is generally small. In fact, dc-Hall effect measurements did not yield reliable data on charge carrier mobility, as well as charge carrier concentration in Li_2IrO_3 thin films. The same issue occurred in Na_2IrO_3 thin films [MJ2]. While this may in part be caused by a high bulk resistivity, it certainly is also an indication of small mobilities[2] below < 1 cm^2/Vs.

In contrast to transversal MR, the origin of longitudinal magnetoresistance cannot be explained by classical means. According to above-mentioned classic kinetic theory of charge carrier transport, resistance parallel to an applied magnetic field remains unchanged as the Lorentz force is trivially zero in the longitudinal case. However, in quantum mechanics a magnetic field acting on charge carriers produces a system of discrete Landau levels and longitudinal magnetoresistance does not vanish. For the case of elastic scattering of electrons by acoustic phonons in weak applied magnetic fields $\mu B \ll 1$ [132, 133], the longitudinal magnetoresistance is shown to be positive and quadratic, i.e. $R_\parallel \sim \mu(B,T)B^2$. To confirm that applied fields of 8 T can indeed be considered as weak fields for the present samples, a low mobility of 1 cm^2/Vs is assumed; then, $\mu B = 1 \times 10^{-4}$. As a side note, constant and variable range hopping in semiconductors cause an exponential magnetic field dependence of transversal and longitudinal resistance with very

[2] Standard dc-Hall effect setups are usually only sensitive down to μ = 1 cm^2/Vs. For brief details, see e.g. http://www.lakeshore.com/Documents/ACField_AppNote_h.pdf.

small relative anisotropy $(\rho_\perp - \rho_\parallel)/\rho_\parallel$ [127]. But despite the fact that temperature-dependent resistivity is dominated by variable range hopping as shown above, an exponential magnetoresistance is, however, not observed in the present data.

Overall, the magnetoresistance of Li_2IrO_3 thin films is quantitatively very similar to the one observed in a previous work on Na_2IrO_3 thin films [MJ1,MJ 2]. However, while measurements of transversal MR in Na_2IrO_3 films revealed the weak antilocalization effect hinting at topological surface states [MJ1,MJ 2]. no such effect is observed in the present Li_2IrO_3 samples. In light of the very rough film surfaces in typical Li_2IrO_3 samples, this is certainly not surprising. Furthermore, experimental and theoretical evidence rather put Li_2IrO_3 in the vicinity of a spin liquid than a topological insulator phase (cf. Sec. 2.1).

The brief study of field-dependent resistivity of Li_2IrO_3 discussed here revealed that magnetoresistive effects are very small and insensitive to the orientation of the magnetic field. The results are in this sense rather simple for an antiferromagnetic system of Ir $5d$ electrons, where spin orbit coupling is in fact strong and no longer perturbative. Antiferromagnetic Sr_2IrO_4, for example, displays a much larger and negative anisotropic magnetoresistance coupled to both the lattice and magnetic structure [134, 135]. Apart from a conventional reduction of spin scattering via applied magnetic fields, an unconventional scenario is suggested for Sr_2IrO_4, where the electron hopping is enhanced by the magnetic field through a change of the Ir-O-Ir bond angles [134]. Considering the present data it remains unclear, why in Li_2IrO_3 thin films apparently no coupling to the lattice or magnetic structure is observed in magnetotransport. It will be shown in the next section 7.4, that no antiferromagnetic order was detected in Li_2IrO_3 films, and that its absence can in parts be understood by structural disorder. Structural disorder is obvious not only from XRD (cf. Sec 7.1) but in a sense also from resistance measurements. To illustrate this fact, figure 7.12 displays resistance R versus temperature T of a typical Li_2IrO_3 and Na_2IrO_3 film sample. Below 150 K the bulk resistance of Li_2IrO_3 is larger than that of Na_2IrO_3. The former sample, used also for the MR measurements, was prepared at $p_{O2} = 3 \times 10^{-4}$ mbar with 45,000 pulses and the latter at 0.016 mbar with 30,000 pulses. Judging from the growth parameters the Li_2IrO_3 film is therefore considerably thicker. Consequently, the resistivity ρ of Li_2IrO_3 is clearly larger than that of Na_2IrO_3. This comparison corroborates that Li_2IrO_3 films are in fact structurally inferior to Na_2IrO_3 films. In conclusion, it is hence a reasonable assumption that structural disorder in thin films might mask the true intrinsic magnetotransport properties of Li_2IrO_3.

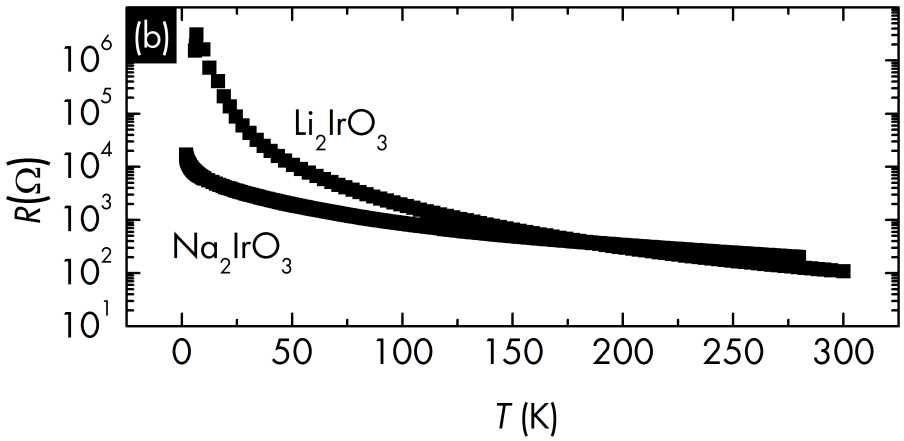

Figure 7.12 Temperature-dependent resistance of typical Li_2IrO_3 (thicker) and Na_2IrO_3 (thinner) films. The higher resistance of Li_2IrO_3 films is attributed to a larger degree of structural disorder compared to Na_2IrO_3 films. [Samples: E3313, E3752.]

7.4 Investigation of magnetic order

For a determination of the Neél temperature in Li_2IrO_3 thin films, magnetization of a sample grown on *a*-plane sapphire was measured using a superconducting quantum interference device (SQUID). The sample mass was unknown. In the experiments, the magnetic field was applied normal to the film surface. Figure 7.13(a) shows magnetic field loops recorded at 5 and 125 K after field cooling at 7 T. The raw data were corrected for a linear and temperature-independent diamagnetic substrate contribution, see Fig.7.13(b). Magnetization values of the film are small due to the low sample volume. Apparently, ferromagnetic impurities are present in the sample as is evident from the small hysteresis visible, in particular, at 125 K and below 0.5 T. Such impurities could have been introduced during sample handling via, e.g., tweezers or the substrate itself was already contaminated. This ferromagnetic background was modeled empirically by a hyperbolic tangent assuming a coercive field H_c of 300 Oe and a saturation magnetization of 4.5×10^{-6} emu for both 5 and 125 K [3]. For a zoom-in on the low field region and the impact of the correction see Fig. 7.13(c). The corrected loops show no hysteresis and saturation magnetization is reached at applied fields larger than 8 T.

Zero-field and field cooled (ZFC, FC) temperature-dependent susceptibility $\chi = M/H$ was measured from 5 to 125 K in an applied field of $\mu_0 H$ = 1 T. The data are presented in Fig. 7.14(a) and are corrected for diamagnetism and impurity ferromagnetism. ZFC and FC curves have no marked differences excluding, e.g., spin glassy behavior, which was observed in the case of nonmagnetic dilution [75]. According to literature [44], antiferromagnetic order sets in below a

[3] Note, that for iron impurities with Curie temperature of about 950 K the magnetization $M(T)$ can be assumed constant at both 5 and 125 K. Consequently, the ferromagnetic contribution to $M(H)$ will equally be the same at these temperatures.

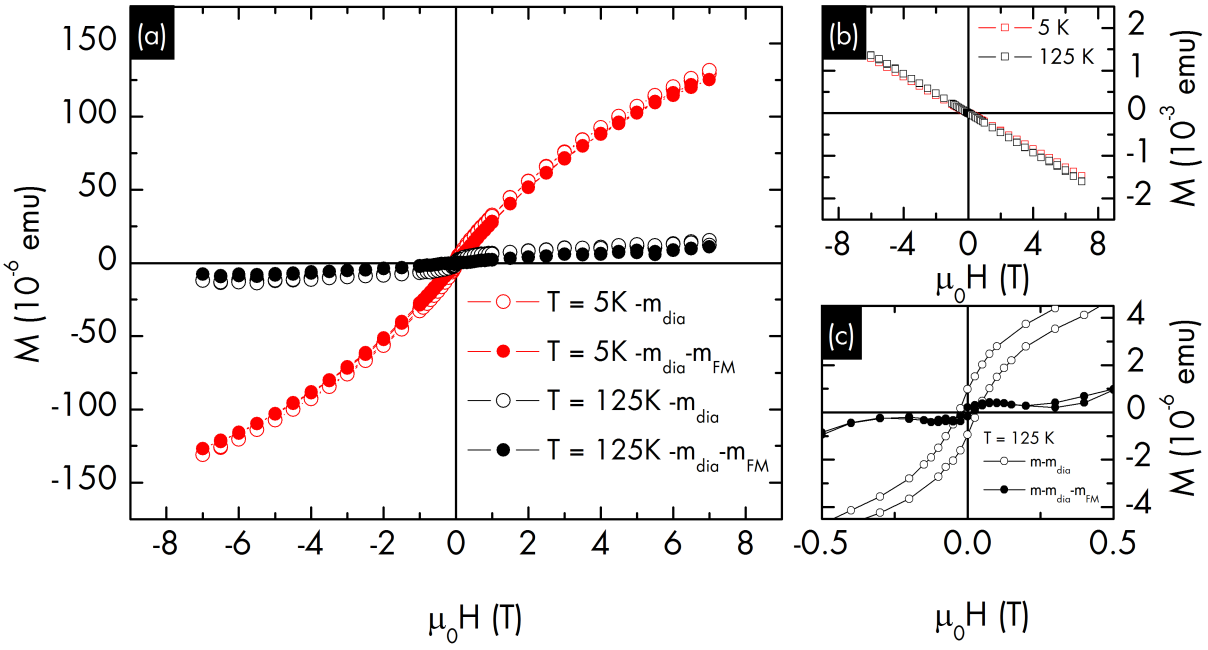

Figure 7.13 Magnetization M versus applied magnetic field $B = \mu_0 H$ of Li_2IrO_3 film sample at 5 and 125 K. (a) $M(B)$ data after correction for substrate diamagnetism and subtraction of a ferromagnetic impurity contribution (open and closed circles, resp.). (b) Raw $M(B)$ data. (c) Zoom-in on the ferromagnetic impurity contribution and its correction at T = 125 K. [Sample: E3752.]

Neél temperature of $T_N \approx 15$ K. However, in the present film sample neither the ZFC nor the FC state show any indication of antiferromagnetic order, such as a cusp around 15 K. Instead, the sample appears to be fully paramagnetic in the entire temperature range measured. Fig. 7.14(b) shows the FC inverse susceptibility which is linear and was fit by the Curie-Weiß law between 5 and 125 K[4]. A Curie-Weiß temperature of θ = -9.3(9) K is obtained which is indicative of rather weak antiferromagnetic exchange interactions. These interactions are not anisotropic as an additional susceptibility measurement $\chi_{\parallel}$ under parallel applied field shows (blue crosses in Fig. 7.14(a)). For comparison, in single crystals susceptibility was anisotropic and for randomly oriented crystals a larger θ of -33(3) K was found [44]. One may speculate, that the apparent absence of long-range antiferromagnetic order and the lack of magnetic anisotropy can be explained by an insufficient structural quality of the film (cf. Sec. 7.1). The formation of an ordered magnetic state is highly dependent on next-nearest neighbor magnetic interactions on the Ir honeycomb lattice [45]. They are likely reduced by structural disorder which is also manifested by the high bulk resistance. Another inherent problem with SQUID studies on thin films is the low sample volume leading in this case to a film-substrate signal ratio of about 1/10 and 1/100 at 5 and 125 K, respectively. Other factors might be the large 10 × 10 μm^2 sample

[4]Note, that the Curie-Weiss law is valid only for $x \ll 1$, where x is the argument of the Brillouin function $B_J(x)$ and equal to $g\mu_B JB/k_B T$. While at 125 K the Curie-Weiss law might still be considered valid ($x \approx 0.005$) under the current experimental conditions, it is certainly not at 5 K ($x \approx 0.134$). For the calculation of x, $g = 2$ and $J = 1/2$ were assumed.

dimensions and an off-center position of the film layer inside the detection coil (cf. Sec. 4.8).

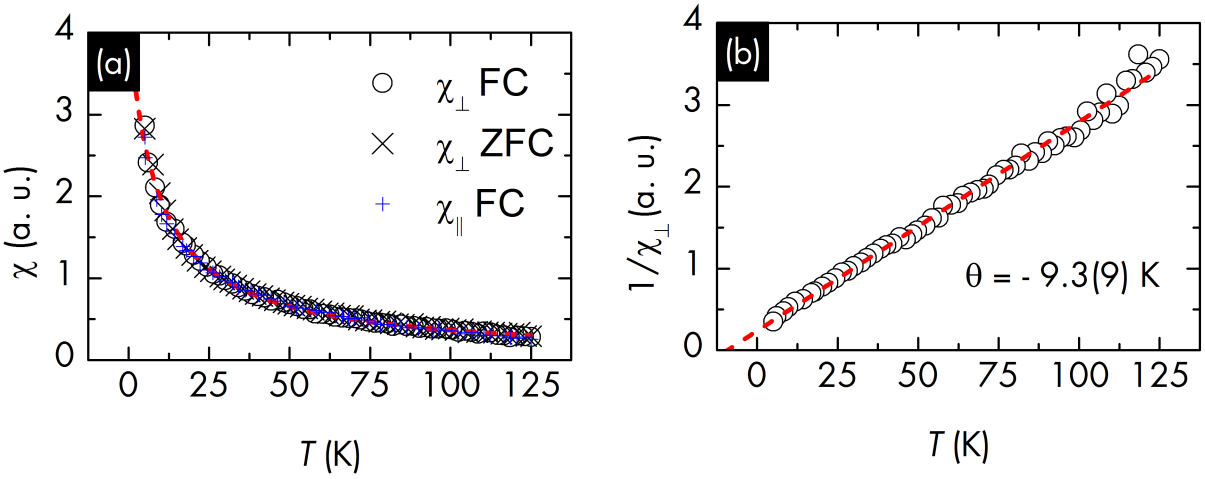

Figure 7.14 Field-cooled magnetic susceptibilities $\chi_\perp$ and $\chi_\parallel$. (a) and inverse magnetic susceptibility $1/\chi_\perp$ (b) versus temperature T of a Li_2IrO_3 film sample measured at B = 1 T. The $\chi_\perp(T)$ data were fit by the Curie-Weiss law in the entire temperature range from 5 to 125 K (red dashed lines). [Sample: E3752.]

7.5 Dielectric function and electronic excitations

The dielectric function (DF) of two Li_2IrO_3 thin films grown at $T_g \approx 550$ °C (500 W) and $p_{O2} = 3 \times 10^{-4}$ mbar on YSZ(001) and a-Al_2O_3, respectively, is determined by modeling spectroscopic ellipsometry data recorded in the 0.041 to 3.34 eV spectral range. The modeling was performed by Dr. Rüdiger Schmidt-Grund, Leipzig University. A model containing layers for the substrate, Li_2IrO_3 film and the surface roughness is used. Each layer is described by its thickness and optical constants. The interface between substrate and Li_2IrO_3 thin film, is modeled by a thin 1-nm intermix layer within the Bruggeman effective-medium approximation (EMA) [136]. For this approximation the DFs of substrate and film are mixed 50:50 in a ratio of 1:1. In consideration of the large root-mean-squared surface roughness in the order of 10 nm, the surface roughness and the columnar structure are accounted for by a 100-nm EMA-layer by mixing the film DF with void. Here, the void fraction is gradually increased from ≈ 20 to ≈ 80 % from bottom to top. For the typically high surface roughnesses of Li_2IrO_3 films, such an EMA-layer approach is not exact. The DF of the surface layer with void fraction gradient strongly correlates with the DF of the film. As a consequence, an uncertainty of $\Delta\varepsilon_2 \approx +20\%/-5\%$ for absolute values of the thin film DF is assumed. Nevertheless, the general lineshape and energy values of electronic excitations and phonon modes are influenced insignificantly and

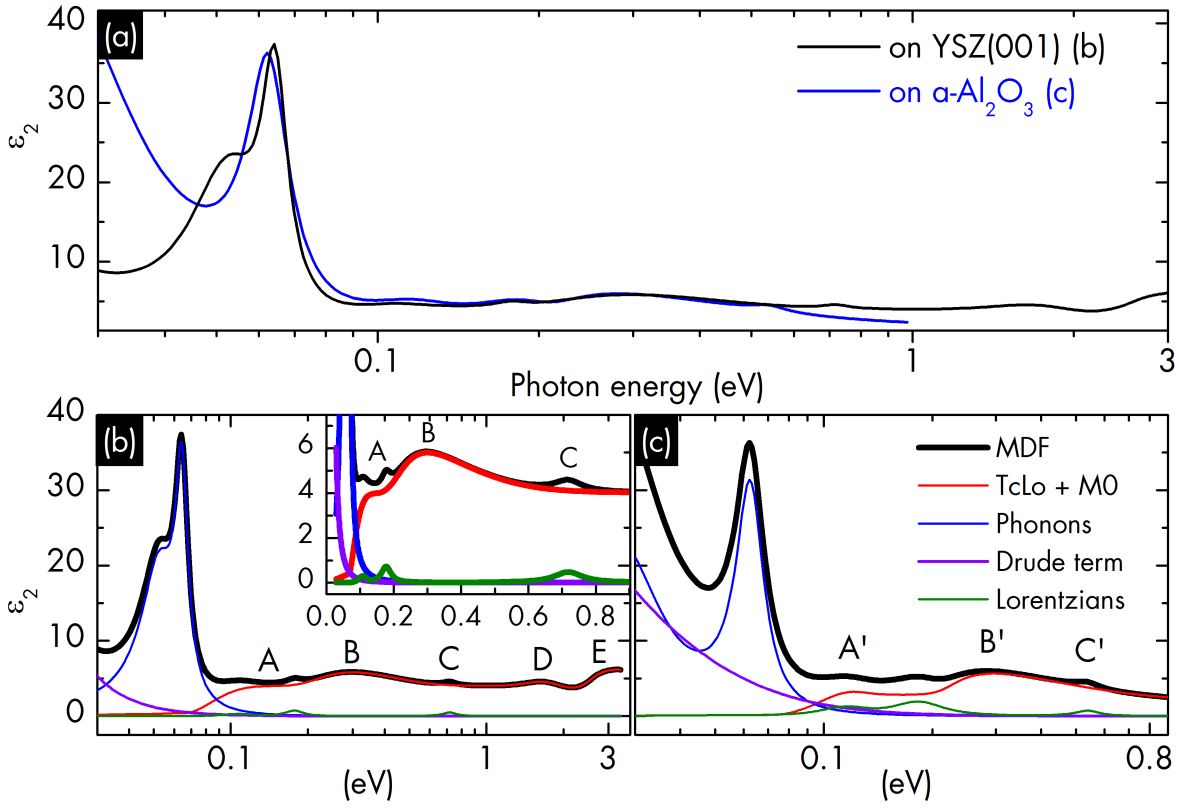

Figure 7.15 (a) Model dielectric function (MDF) as obtained by spectroscopic ellipsometry of two Li_2IrO_3 thin films grown on YSZ(001) (black) and *a*-Al_2O_3 (blue). (b,c) MDFs of both samples are plotted together with their individual components. Labels *A* to *E* and *A′* to *C′* denote electronic excitations, see text and Tab. 7.2. The inset in (b) shows a zoom-in on the electronic excitations below 0.8 eV. [Samples: E3481, E3583.]

therefore reliable. By similar reasoning, the error in ε_1 amounts up to 50 % and is hence not presented.

To model the thin film DF a parametric model dielectric function (MDF) approach is used. It consists of (cf. Fig. 7.15(b,c) and Sec. 4.6): a Drude free charge carrier absorption; two Lorentzians describing the phonon contribution at lowest energies; a near bandgap Tauc-Lorentz (TcLo) absorption function [137] and a series of M0-critical point functions with parabolic onset [116, 138] that describe direct band-band transitions; Gaussian oscillators modeling electronic band-band transitions spread within the Brillouin zone at higher energies. Additional discrete transitions are described by Lorentzians. The dielectric function model and experimental data are matched by regression analysis.

For the two Li_2IrO_3 film samples the final MDF and its individual components are displayed in Fig. 7.15. Both samples have very similar MDFs, in particular within the spectral range from 0.1 to just 0.6 eV, see Fig. 7.15(a). These similarities basically indicate that both samples have similar bandgap properties, as discussed below. The individual components observed in both

Table 7.2 Overview of electronic excitations energies in Li_2IrO_3 thin films on YSZ(001) and a-Al_2O_3 determined by ellipsometry. The uncertainty is in the order of the last digit.

Peak	Energy (eV)	Type of excitation	
A,A'	0.11, 0.18	magnon	(discrete)
B, B'	0.30	Mott gap	(band-band)
C	0.72	$j_{\mathrm{eff}} = 3/2 \rightarrow j_{\mathrm{eff}} = 1/2$	(discrete)
C'	0.53	unknown	
D	1.63	$t_{2g} \rightarrow e_g$	(band-band)
E	3.25	$t_{2g} \rightarrow e_g$	(band-band)

samples represent electronic excitations that can be ascribed to transitions from and within the t_{2g} manifold in line with the picture of j_{eff} physics, as explained earlier in Sec. 2.1. In addition, the measured transitions energies agree fairly well with results from other experiments, such as angle-resolved photoelectron spectroscopy (ARPES), resonant inelastic X-ray scattering (RIXS) and other optical spectroscopy methods, performed on Li_2IrO_3, Na_2IrO_3 and other iridates. The observed excitations are summarized in Table 7.2. The following discussion is based on the film grown on YSZ(001), Fig. 7.15(b), but complemented by a comparison with the film deposited on a-plane sapphire (c).

In the high-energy spectral range above 1.2 eV, two contributions to the MDF at 1.63 and 3.25 eV exist that are attributed to d-d band transitions from occupied t_{2g} to empty e_g bands (*D*, *E*). Very similar transitions have been observed in Na_2IrO_3 and Li_2IrO_3 single crystals [60, 72] and Na_2IrO_3 thin films [MJ1]. For lower energies below 1.2 eV, the MDFs consists of several other transitions. At 55 and 65 meV phonon excitations were measured. In the other sample (c), one phonon energy at 62 meV and a broader flank converging to energies well below the measured range are observed. The peaks at 0.11 and 0.18 eV in (b) represent discrete transitions (*A*). In Sr_2IrO_4, for example, a magnon was found at 0.2 eV within the Mott gap [139]. The same kind of excitations are also found in the sample on a-Al_2O_3 (A' in Fig. 7.15(c)). Further band-band excitations, possibly related to electron-hole pairs [60], are found at 0.15 and more pronounced at 0.30 eV (*B*). They imply a very narrow Mott gap of less than 0.3 eV. For the other sample, these excitations are similarly found at 0.12 and 0.30 (B'). Narrow Mott gaps from 300 meV to 340 meV were also previously found in Na_2IrO_3 and Li_2IrO_3 [60, 72] [MJ1]. At 0.72 eV (*C*) another discrete transition can be discerned. Its energetic position matches well the t_{2g} intraband transition from the $j_{\mathrm{eff}} = 3/2$ to the $j_{\mathrm{eff}} = 1/2$ state. For single crystal samples of Na_2IrO_3 and Li_2IrO_3 it is usually observed between 0.7 and 0.8 eV and is split by the trigonal crystal field of about 110 meV [60]. The same splitting cannot be observed in the present samples due to

a significantly lower crystalline quality. Excitations similar to C were also found in Sr_2IrO_4 [139, 140]. However, for the other sample in (c) a discrete transition (C') is instead observed at about 0.53 eV. This transition energy does not fit into the picture of j_{eff} physics. Thus the origin of C and C' might in fact be of a different nature.

It was shown in Sec. 7.1 that films grown on a-plane sapphire have additional phases with different out-of-plane orientation as compared to films on YSZ(001) (cf. Fig.7.1). This higher degree of disorder might explain the slightly different phonon spectrum observed in the ellipsometry data. It, however, does not explain the energy differences between excitations C and C'.

7.6 Summary

In comparison with the sister compound Na_2IrO_3, ongoing research on Li_2IrO_3 is impeded by an even smaller size of available single crystals and thus often restricted to polycrystalline samples. With the intention of realizing larger single-crystalline samples and possibly pave the way for future device applications, heteroepitaxial Li_2IrO_3 thin films were pulsed laser-deposited on Al_2O_3, YAO, ZrO_2:Y (YSZ) and ZnO substrates.

Structural analysis by XRD showed, that irrespective of the substrate material, relaxed $\approx$ 400-nm Li_2IrO_3 films exhibit a preferential (001) and (10-1) out-of-plane crystalline orientation (Sec. 7.1). The surface morphology was characterized by crystalline grains and RMS surface roughnesses of up to 16 nm. Overall, the results suggest a considerable degree of structural disorder. Compared to Na_2IrO_3 thin films, all samples were structurally inferior. For this reason, no neutron diffraction was performed on Li_2IrO_3 thin films. Furthermore, the epitaxial relationship was not improved by deposition of intermediate c-ZnO. Electrical resistivity is dominated by three-dimensional Mott variable range hopping. Unlike in Na_2IrO_3 films, no weak antilocalization was observed in magnetoresistance. Instead, the magnetoresistive effect is small and explained by phonon scattering and small charge carrier mobilities. SQUID-magnetometry could not detect a transition to an antiferromagnetically ordered state expected at around 15 K. Furthermore, the dielectric function was determined below 3.34 eV and gave insight into electronic excitations. These excitations were associated to d-d transitions from which a splitting of the $5d$-t_{2g} manifold was inferred. In-gap states were attributed to phonons and possibly magnons. In particular, transitions across the Mott gap indicated an optical gap of $\approx$ 300 meV, which is smaller than that of Na_2IrO_3 films [MJ1] and single crystals [72].

The apparent absence of magnetic order and the conventional magnetoresistive effect are associated with the structural quality of the films and their resulting high bulk resistivity, as well as with the general difficulties inherent to performing SQUID magnetometry on thin film samples (cf. Sec. 4.8). Thus, the results do not necessarily reflect the intrinsic properties of Li_2IrO_3 known from experiments on single crystals. It is for these reasons, that in this work no further experimental evidence of the proposed topological insulator or spin liquid state can be given. Similar to its sister compound Na_2IrO_3, future experimental efforts on Li_2IrO_3 thin films must target the structural quality by way of both improving the source target density and further optimization of the deposition process. Due to the low lattice mismatch of -1.5 and -2.8 % for the *a* and *b* lattice parameters, respectively, YAO(011) may be a promising substrate material on which to study the detailed growth process of, initially, very thin Li_2IrO_3(001) films. Again, epitaxial strain may become relevant in this regime and tune into some of the desired properties [36, 44, 48, 49].

8 $Y_2Ir_2O_7$

The rare-earth pyrochlore $Y_2Ir_2O_7$ is a highly correlated material with both strong spin-orbit coupling and geometric frustration of its magnetic and electronic properties. In the past, Mott-insulating $Y_2Ir_2O_7$ was proposed to show a variety of novel, non-trivial physics including the topological insulator [33–35] and spin liquid [80] phase. Subsequent experiments on polycrystalline samples found indications of an antiferromagnetic all-in/all-out configuration [84–86] expected to result in a Weyl semimetal state [57]. However, to precisely determine the ground state magnetic configuration, single-crystalline samples of high quality and large volume are required but are still lacking. To alleviate this problem, attempts were made in the present work to realize heteroepitaxial $Y_2Ir_2O_7$ thin films by means of pulsed laser deposition. The samples were investigated in terms of their structural and electrical transport properties.

8.1 Crystallinity of heteroepitaxial film samples

Using the phase-mixed target prepared by conventional solid-state synthesis (cf. Sec. 5.1), several thin films were prepared by pulsed laser deposition on ZrO_2:Y(001) (YSZ) substrates. YSZ(001) with a = 5.12 Å was chosen as its lattice parameter is roughly half that of $Y_2Ir_2O_7$ (a = 10.17 Å). The conjecture was that this indirect lattice match would lead to domain-matching epitaxy.

Fig. 8.1(a) shows a XRD 2θ-ω scan of a film grown on YSZ(001) with a heater power of 400 W ($T_g \approx 550$ °C) and oxygen partial pressure p_{O2} = 0.016 mbar. Films grown at 3×10^{-4} mbar were qualitatively no different. For an XRD pattern of $Y_2Ir_2O_7$ the most intense peak is (222) and expected to appear at around 30.5°. This (222) peak is clearly absent. The reflex at 33.5° can be assigned to the cubic phase of Y_2O_3 (C-phase). Low-intensity peaks at 40.7° and 47.0° relate to Ir. Another peak at 17.7° cannot correspond to $Y_2Ir_2O_7$ at all; it is 2° off of the expected position of the (111) reflex. To match the current position at 17.4° the unit cell of $Y_2Ir_2O_7$ would have to shrink to around 9 Å which would in turn correspond to unrealisticly high external or internal strain. On the other hand, the reflex at 17.4° matches the (201) orientation of monoclinic B-phase of Y_2O_3. The metastable monoclinic B-phase of polymorphic Y_2O_3, however, can usually only be retained at ambient conditions after high temperature and pressure quenching [141]. In conclusion, the origin of the 17.4°-reflex is unclear. While a crystalline phase of $Y_2Ir_2O_7$ is clearly not present, an X-ray amorphous phase cannot be excluded.

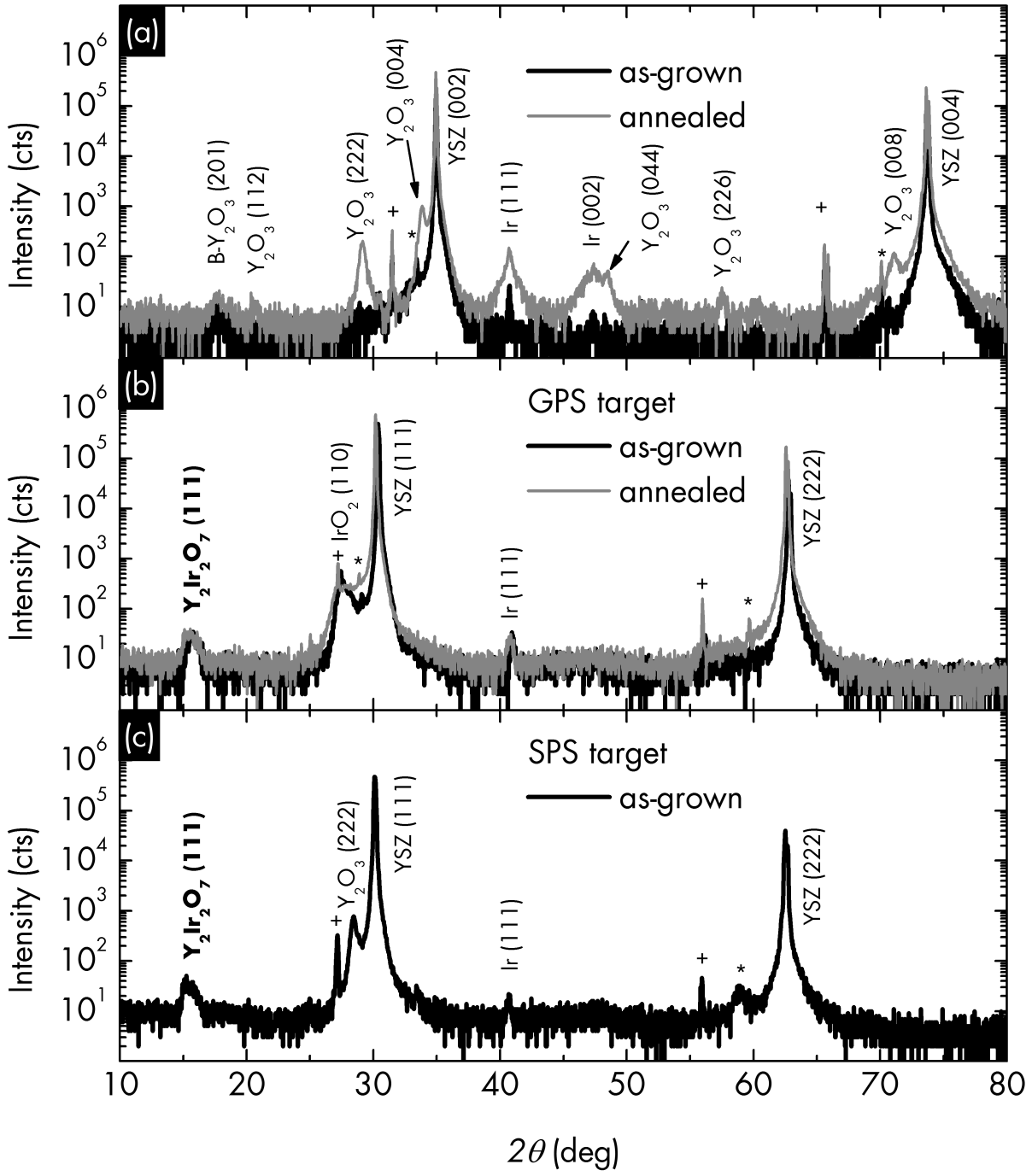

Figure 8.1 (a) Attempts at PLD-grown $Y_2Ir_2O_7$ thin films on YSZ(001) (a) and YSZ(111) (b,c) using solid-state sintered (a), gas pressure sintered (b) and spark plasma sintered (c) source targets. Shown are XRD 2θ-ω scans. The as-grown films (black) in figures (a,b) were subsequently annealed for 1 hour at 900 °C (gray). K_β and W lines are denoted by + and ∗. [Samples: E3564 (a), E3652 (b), E3701 (c).]

In a recent work, using a phase-mixed target, $Eu_2Ir_2O_7$ (111) films were prepared on YSZ (111) by PLD and found to be amorphous after deposition. A pure crystalline phase appears after annealing at 1000 °C [142]. A similar attempt was made with one of the above samples grown at $T_g \approx 550$ °C and $p_{O2} = 0.016$ mbar, see Fig. 8.1(a). However, after annealing at 900 °C for one hour no crystalline $Y_2Ir_2O_7$ phase formed and the XRD pattern instead shows additional peaks related to cubic Y_2O_3 and more intense Ir peaks. If any amorphous $Y_2Ir_2O_7$ was present in the film, it has most likely decomposed after annealing. Deposition at higher temperatures, up to $T_g = 730$ °C, does not yield a crystalline $Y_2Ir_2O_7$ phase either and reflexes related to Y_2O_3 and Ir are observed in the XRD patterns of such films, as well.

With the gas pressure sintered (GPS), phase-mixed target a film was deposited on YSZ (111) at $p_{O2} = 0.025$ mbar and $T_g = 730$ °C. In contrast to the previous films, no reflex at 17.4° is observed in the XRD 2θ-ω scan shown in Fig. 8.1(b). Instead, a reflex of similar intensity appears at 15.4° possibly corresponding to the $Y_2Ir_2O_7$ (111) reflex. The YSZ substrate (111) and a possible $Y_2Ir_2O_7$ (222) film reflex will appear at the same 2θ angle. It is thus difficult to verify the existence of a $Y_2Ir_2O_7$ (222) phase by this XRD pattern alone. The XRD pattern also shows reflexes related to Ir and IrO_2.

Films prepared using the spark plasma sintered target (#17725), that contained only Y_2O_3 and Ir phases according to Rietveld refinement, are very similar to the GPS-films when grown on YSZ (111), see Fig. 8.1(c). In particular, one can also observe a peak at 15.4° possibly related to $Y_2Ir_2O_7$. For films grown on *a*-plane sapphire and YSZ (001) this peak, however, is not observed and instead the 17.4°-reflex appears.

To conclude, preparation of phase pure, single-crystalline heteroepitaxial $Y_2Ir_2O_7$ thin films by pulsed laser deposition has so far been unsuccessful. No crystalline $Y_2Ir_2O_7$ films could be prepared. The presence of amorphous $Y_2Ir_2O_7$ cannot be excluded. The use of single-crystalline YSZ (111) substrates appears to be a more promising route to improve crystallinity compared to YSZ (001) or *a*-plane sapphire substrates. No improvement of film quality was observed after annealing at 900 °C. Possibly, the use of mixed phase targets has a detrimental effect on the film properties, and especially their crystallinity. Energy dispersive X-ray analysis of the films usually gives Y:Ir ratios in the order of 2.5:1 confirming the presence of Y_2O_3 and corroborating that the films are multi-phase. Apart from that, the used PLD parameters appear reasonable, as well. In fact, they are very similar to the parameters used for PLD-grown heteroepitaxial $Eu_2Ir_2O_7$ [142] and $Bi_2Ir_2O_7$ [143] thin films successfully grown on YSZ (111).

8.2 Temperature-dependent electrical resistivity

Temperature dependent resistivity of a film deposited on YSZ(001) at $T_g \approx 550$ °C and $p_{O2} = 3 \times 10^{-4}$ mbar using the solid-state sintered target was measured between 300 and 125 K by the van der Pauw method. Room-temperature resistivity is high with 5219 Ωcm and increases by three orders of magnitude at 125 K. At lower temperatures, resistivity is outside the instrument's range. As shown in Fig. 8.2(a) by a semi-log plot of ρ vs. $1000/T$, the semiconducting behavior neither follows a thermally activated exponential behavior nor the nearest neighbor hopping, i.e. $\rho = \rho_0 \exp(E/k_B T)$. Similar to Li_2IrO_3 films discussed in Sec. 7.3, the resistivity can be fitted by the three-dimensional Mott variable range hopping model (3D Mott VRH) [126]

$$\rho = \rho_0 \exp\left[(T_0/T)^{1/4}\right], \tag{8.1}$$

where ρ_0 is a temperature-dependent resistivity coefficient, given by eq. (7.2), and T_0 is the localization temperature. Fitting of the resistivity data with eq. (8.1), see Fig. 8.2(b), results in $\rho_0' = 2.57(1) \times 10^{-11}$ Ωm and a localization temperature of $T_0 = 2.25(1) \times 10^8$ K. The validity of the Mott VRH is verified using eq. (7.4) for the average hopping distance R_M. At both 300 and 125 K, $R_M/a > 1$ (11.0 and 13.7, resp.). Considering the structural and chemical disorder present in the multi-phase films, 3D Mott VRH seems a reasonable electrical transport mechanism. It is generally associated with carriers localized by disorder and has originally been used to describe the transport in amorphous material. VRH has been previously observed in polycrystalline $Y_2Ir_2O_7$ [88] and $Eu_2Ir_2O_7$ [144].

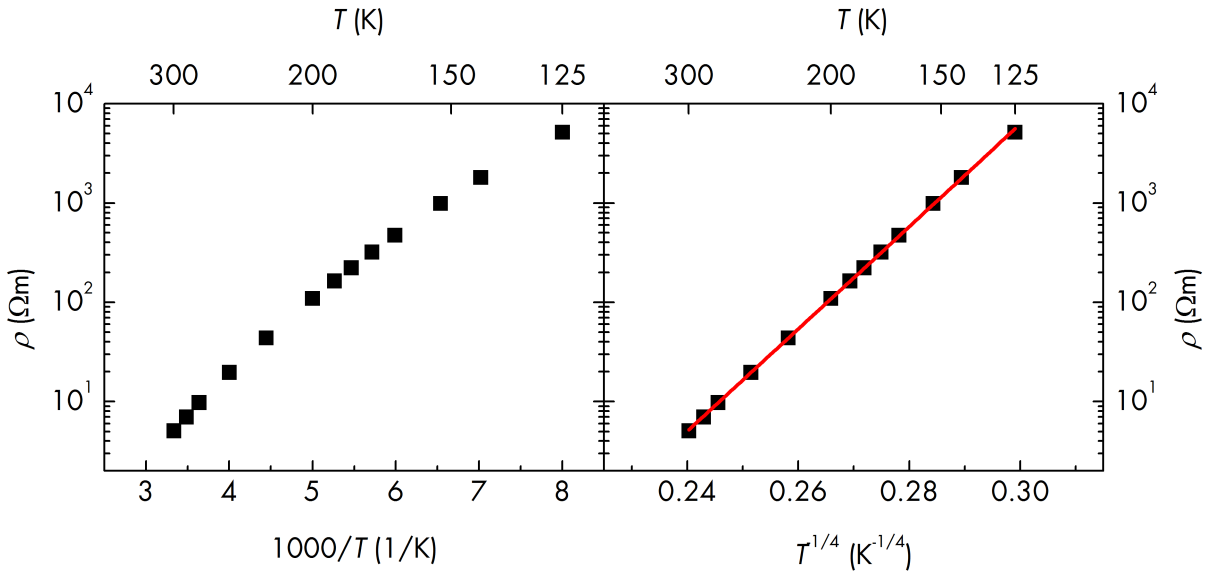

Figure 8.2 PLD of $Y_2Ir_2O_7$: Temperature-dependent resistivity ρ versus temperature T. (a) $\log\rho$ versus T. (b) $\log\rho$ versus $T^{-1/4}$. The data in (b) is fitted by three-dimensional Mott variable range hopping according to eq. (8.1) (red line). [Sample: E3557.]

8.3 Summary

In the past, Mott-insulating $Y_2Ir_2O_7$ was proposed to show a variety of novel, non-trivial physics including the topological insulator [33–35] and spin liquid [80] phase. Unfortunately, large volume, high quality single crystals were unavailable by conventional solid-state synthesis or floating-zone techniques, and experiments were restricted to polycrystalline samples [81–88]. This has yet prevented the accurate determination of the ground state of $Y_2Ir_2O_7$.

To alleviate this problem, heteroepitaxy of $Y_2Ir_2O_7$ on YSZ was attempted. Since the unit cell dimension of $Y_2Ir_2O_7$ are roughly twice that of YSZ, domain-matching epitaxy was expected. On YSZ(001), no evidence of a crystalline $Y_2Ir_2O_7$ phase with defined epitaxial relationship was found. The deposition on YSZ(111) was more promising due to the detection of a possible $Y_2Ir_2O_7$(111) reflex. However, all films were predominantly composed of Y_2O_3, Ir and IrO_2. While an X-ray amorphous $Y_2Ir_2O_7$ phase could not be excluded with certainty, the Y:Ir ratio is in the order of 2.5:1, corroborating a considerable phase impurity. In contrast to $Eu_2Ir_2O_7$(111) [142], high-temperature annealing of these multi-phase samples did not lead to the formation of a crystalline $Y_2Ir_2O_7$ phase. Temperature-dependent resistivity was interpreted as three-dimensional Mott variable range hopping (VRH) (Sec. 8.2). Unlike for Na_2IrO_3 and Li_2IrO_3, here the observed hopping mechanism was associated rather with the sample's structural quality and possible amorphicity, than with the correlated nature of $Y_2Ir_2O_7$(111). Due to the low structural quality, other experiments, such as SQUID-magnetometry, spectroscopic ellipsometry or neutron diffraction, were deemed impractical.

Because the chosen PLD parameters are very similar to those used in the growth of $Eu_2Ir_2O_7$ [142] and $Bi_2Ir_2O_7$ [143] on YSZ(111), it is believed that proper stoichiometric transfer was impeded by the phase impurity of the source targets. Hence, future growth attempts should first focus on the preparation of phase-pure, polycrystalline $Y_2Ir_2O_7$ targets. Second, from the present results heteroepitaxy on YSZ(111) is expected to lead to (111)-oriented $Y_2Ir_2O_7$ and will require a careful structural analysis by high-resolution XRD, since the YSZ(111) and $Y_2Ir_2O_7$(222) Bragg reflexes and their integer multiples share nearly identical d-spacings and directions. In conclusion, the obtained results shall act as a reference for future experimental efforts to realize heteroepitaxial $Y_2Ir_2O_7$ thin films.

9 $YBiO_3$

In the past, $YBiO_3$ (YBO) was investigated as a buffer material for the high-temperature superconductor $YBa_2Cu_3O_{7-\delta}$ [50–53]. Recently, YBO was proposed as a novel oxide topological insulator by first-principles band structure calculations [37]. Its large bulk resistivity and proposed 330-meV non-trivial direct bandgap were predicted to allow truly surface-dominated transport at room temperature. However, these calculations are under debate and instead a trivial insulator state together with a larger bandgap energy was put forward [38]. YBO(001) thin films were previously realized by pulsed laser and chemical solution deposition on $LaAlO_3$(001) [50, 52, 53] and LSAT [94] substrates. In this work, heteroepitaxial YBO thin films were grown by pulsed laser deposition on namely ZrO_2:Y, MgO, $SrTiO_3$ (STO) and STO:Nb, $LaAlO_3$ (LAO), and *a*-plane sapphire. Their varying degree of lattice mismatch allowed the study of epitaxial strain effects. Moreover, the crystalline, morphological and stoichiometrical properties were investigated in dependence of the deposition parameters (Sec. 9.1). The surface morphology is scrutinized with respect to its usefulness in future photoelectron spectroscopy experiments, that allow a direct measurement of the surface band structure. The dielectric function and bandgap energies are determined by spectroscopic ellipsometry and optical transmission spectroscopy. Both were not reported before and might stimulate a critical review of the current band structure calculations.

9.1 Crystalline structure and surface morphology

In the following section, the crystalline structure, surface morphology and stoichiometry of YBO thin films deposited on various single-crystalline substrates will be investigated employing XRD, AFM, SEM and EDX. Film thicknesses are estimated by Cauchy-modeling of ellipsometry data. On each substrate a different degree of lattice mismatch and thus also possible external strain have to be considered. For example, with a cubic lattice constant of a = 5.4188 Å [93], (100)-oriented YBO has a lattice mismatch of -6 % when grown cube-on-cube on YSZ(001). Substrate-induced strain is thus expected to lead to domain-matching epitaxy. Considering the pseudo-cubic cell of YBO (a' = 3.83 Å), the lattice mismatch on LAO(001) and STO(001) is only -0.3 and +2.0 %, respectively. Thus, LAO and STO are expected to be suitable structural templates for (100)-oriented, lattice-matched YBO film growth. Another lattice-matched substrate (+1.0 %) would be LSAT(001) with a = 3.87 Å. While in LAO a cubic-to-rhombohedral transition below 540 °C often generates micro-twins leading to, e.g.,

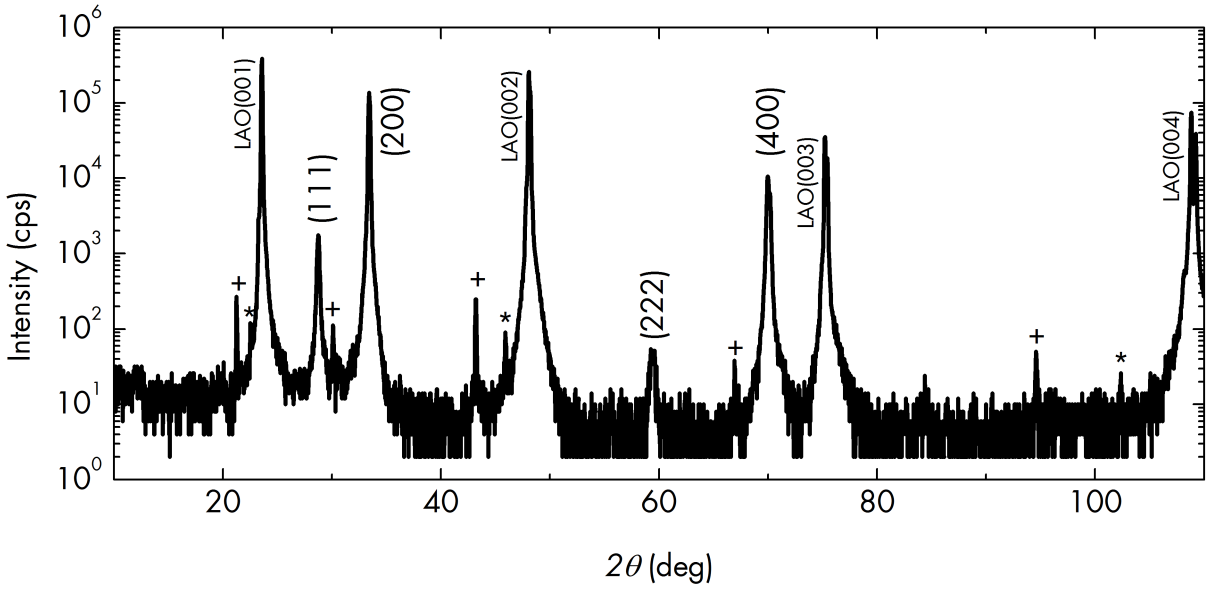

Figure 9.1 Typical XRD 2θ-ω scan of a $YBiO_3$ film deposited on LAO(001) at p_{O2} = 0.002 mbar, T_g = 550 °C and 30,000 laser pulses. The $I_{(200):(111)}$ domain ratio is approximately 80:1. K_β and W lines are denoted by + and ∗. [Sample: E3821.]

surface roughening [145], LSAT does not show such a transition and micro-twins are largely eliminated [146]. Double-sided polished *a*-plane sapphire substrates are solely used for optical transmission measurements on very thick YBO films, see Sec. 9.2.

9.1.1 YBO on LAO(001)

A first series of films Cubic LAO substrates with lattice constant a = 3.82 Å have the smallest lattice mismatch (-0.3 %) to the pseudo-cubic cell of YBO. A first series of nine YBO films was deposited with 30,000 pulses on LAO(001) at a heater power of 400 W (≈ 550 °C) and various oxygen partial pressures ranging from 0.1 to 3×10^{-4} mbar. X-ray diffraction was measured employing the wide-angle powder goniometer in Bragg-Brentano geometry. A typical 2θ-ω pattern of this pressure series is shown in Fig. 9.1. All films have a (100) out-of-plane orientation. In addition, reflexes related to the (111) planes are visible. The domain ratio $I_{(200):(111)}$ varies from 3:1 to 80:1 within the series. Interestingly, neither the domain ratio, nor the individual (200) and (111) peak intensities show any systematic dependence on p_{O2}. Moreover, in some samples low-intensity reflexes related to the (311) and (511) planes were observed indicating film relaxation and some degree of polycrystallinity. Since in powdered samples the domain ratio $I_{(200):(111)}$ was usually found to be about 1:2 [147], all films are believed to have dominant (100) out-of-plane preferred orientation.

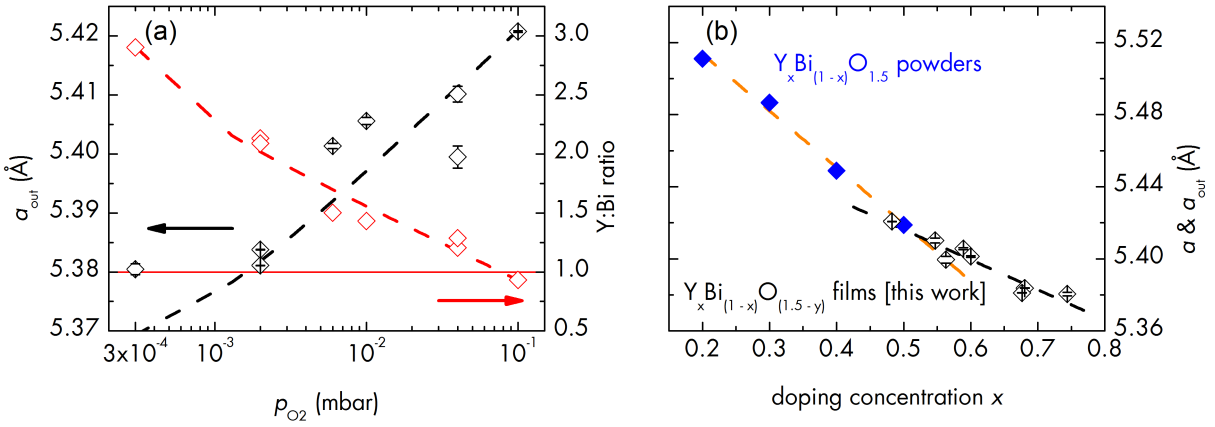

Figure 9.2 Out-of-plane lattice constant and chemical composition of YBO(100) thin films, deposited on LAO(001) at 550 °C, are tunable by p_{O2}. (a) Out-of-plane lattice constant a_{out} and Y:Bi ratio versus p_{O2} (black and red diamonds). Dashed lines are guides to the eye. (b) Lattice parameters a of $Y_xBi_{1-x}O_{1.5}$ powder samples [93] and a_{out} of $Y_xBi_{1-x}O_{1.5-y}$ film samples from (a) versus doping concentration x. [Samples: E3813, E3815-21.]

The out-of-plane lattice constant a_{out}, instead, has a more systematic dependence on oxygen partial pressure, as illustrated in Fig. 9.2(a). Its value is determined from θ_{200}, θ_{400} and θ_{600}, as described in Sec. 4.1, and decreases from 5.4208(1) Å at 0.1 mbar to about 5.3805(9) Å at 3×10^{-4} mbar. Chemical analysis of the films by means of EDX reveals that also the film stoichiometry is sensitive to p_{O2}. In fact, the Y:Bi ratio monotonously increases from a near stoichiometric ratio of 0.9:1 at 0.1 mbar to about 2.9:1 at 3×10^{-4} mbar, see Fig. 9.2(a). Therefore, it is conjectured that optimal stoichiometry will be maintained for oxygen partial pressures between 0.05 and 0.1 mbar. A similar dependence of film stoichiometry on oxygen partial pressure was found in another work on PLD-grown YBO films [94]. Therein, it was argued that for stoichiometric growth a sufficiently large oxygen partial pressure, together with high temperatures, is required to oxidize both Y and the volatile Bi in the plasma. For oxidized Bi, the sticking coefficient is enhanced and re-evaporation of Bi is thus inhibited. Stoichiometric YBO films were grown at 0.1 mbar and 670 °C.

In a subsequent temperature series at 0.002 mbar ranging from 550 to about 650 °C, i.e., from 400 to 600 W, no significant change in either a_{out}, $I_{(200):(111)}$ or Y:Bi stoichiometry was observed.

For a comparison of above films with $Y_xBi_{1-x}O_{1.5}$ powder samples [93] the dependence of a_{out} on the doping concentration x, calculated from Y:Bi, is illustrated in Fig. 9.2(b). In both datasets an approximately linear decrease of lattice parameter with increasing doping level exists, albeit with different slopes. The linearity can be explained with the substitution of Bi^{3+} by smaller Y^{3+} (ionic radii of 1.03 and 0.9 Å, resp.). To understand the differences between both curves, additional strain effects relevant for film samples need to be considered, instead. While internal

strain might stem from oxygen deficiency, the -0.3 % lattice mismatch on LAO(001) might in principle result in compressive epitaxial strain and thus in a relative increase of a_{out}. However, these strain effects are not systematically quantified in this work, such that only tentative conclusions are made.

Substrate annealing It was stated above, that LAO undergoes a crystallographic phase transition at 544 °C from its cubic high-temperature to its rhombohedral low-temperature phase. A cooling through this phase transition, typically causes transformation twinning of the {100} and {110} planes [145]. PLD performed at 550 °C and above indeed causes such twinning and visibly affects the surface morphology, i.e, ridges can be seen explicitly. Due to this macroscopic twinning, X-ray reflectivity measurements were unsuccessful. The phase transition might also be responsible for the change of color observed in all of the LAO substrates after PLD. However, annealing usually promotes the formation of surface steps, that in turn might favor two-dimensional growth and help to improve the film's structural quality. Moreover, pre-annealing may reduce unnecessary structural changes of the substrate during the PLD process. In any case, for all following depositions LAO substrates were pre-annealed in a separate tube furnace at $T = 1050$ °C and $p_{O2} \approx 1000$ mbar for two hours. The presence of surface steps is confirmed by atomic force microscopy, see Fig. A.4.

Droplets For all YBO films discussed above, droplet formation became apparent through AFM, SEM and laser scanning microscopy (LSM). Generally, the surface morphology is rough and largely characterized by crystalline grains, which is indicative of a three-dimensional growth mode. Root-mean-squared surface roughnesses varied unsystematically between 5 and 25 nm. Such a surface morphology is certainly inadequate for future STM and ARPES experiments, or the observation of topological surface states, in particular. In an attempt to decrease the droplet density and simultaneously achieve smoother film surfaces, the laser fluence was reduced from its standard value of 2 Jcm^{-2} down to about 1.6 Jcm^{-2}. A series of films was prepared at 550 °C and 0.05 mbar to ensure good stoichiometry. To avoid film relaxation and instead approach a regime of pseudomorphic growth, the film thickness was reduced to about 400 nm[1] by applying 15,000 laser pulses (ps). Within the series, the laser fluence was varied by changing the position l of the focusing lens. All previous films were deposited at $l = 10$ mm, where the laser beam is focussed onto the target surface and laser fluence is maximal.

In Figure 9.3(a), the domain ratio $I_{(200):(111)}$ is plotted versus the laser fluence; for each datapoint, the corresponding lens offsets Δl from the focus position are given. The domain ratio decreases with laser fluence from 95:1 to as little as 5:1. The cause for the reduced domain ratios

[1] This value was estimated by interpolation of film thicknesses at 7,500 and 60,000 ps, respectively, which were determined by Cauchy modeling of ellipsometry data.

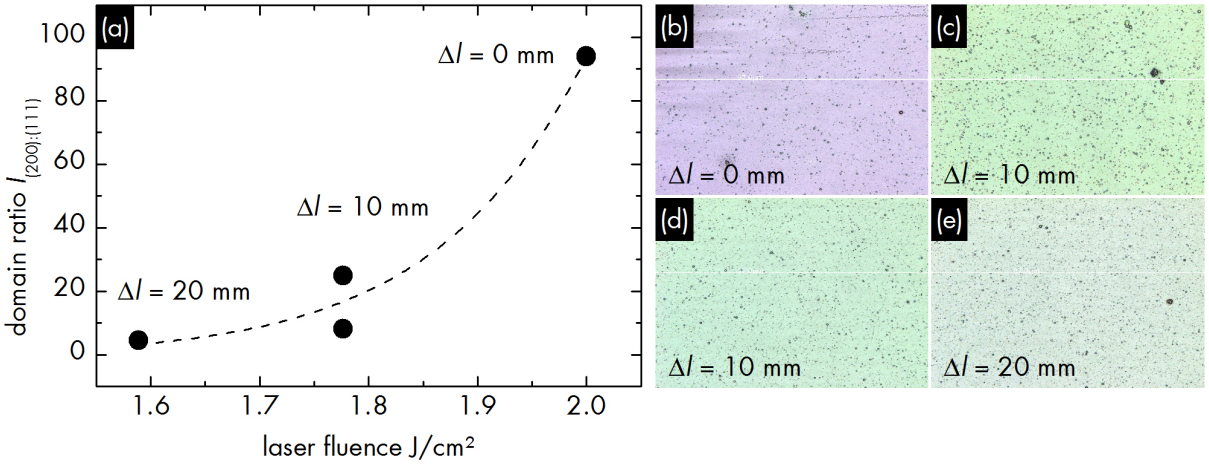

Figure 9.3 Variation of laser fluence. (a) Domain ratio $I_{(200):(111)}$ versus laser fluence. Data points are denoted with their respective lens offsets Δl from the focus position l = 10 mm. The dashed line is a guide to the eye. (b-e) Laser scanning microscopy images of the same YBO films. LSM scan width: 100 μm. [Samples: E3829-32.]

at lower laser fluences was not investigated further. Figures 9.3(b-e) show LSM images of the films grown at their respective lens offsets. In the LSM images no notable difference in droplet density is recognized. Note, that at highest fluence the 15,000-ps film has the highest $I_{(200):(111)}$ domain ratio compared to all thicker 30,000-ps films prepared at the same fluence. This suggests that $I_{(200):(111)}$ can be increased further in thinner films, as discussed below. Moreover, a possible dependence of droplet density on the distance to the center of the plasma plume was investigated by deposition of YBO on a 2" a-plane sapphire wafer, but LSM images showed no difference in droplet density along the diameter of the wafer. Alternatively, an improvement of the target density and mechanical stability might still be a viable strategy to limit droplet formation. In conclusion, the maximum laser fluence of 2 Jcm^{-2} is believed to be the optimal value for achieving fully (100)-oriented YBO.

Thickness dependence Figure 9.4(a) shows XRD 2θ-ω-scans of a series of YBO films grown on pre-annealed LAO(001) at 600 W, or $T_g \approx 650$ °C, at $p_{O2} = 0.05$ mbar and with different numbers of laser pulses (ps) ranging from 7,500 to 600 ps. The higher deposition temperature was chosen to increase the bismuth sticking coefficient and thus ensure proper Y:Bi stoichiometry, as suggested in Ref. [94]. As expected, the intensity of the YBO (200) reflex decreases with decreasing thickness. Layer thicknesses were determined by ellipsometry and range from about 200 to 15 nm. More strikingly, the domain ratio is already greatly enhanced at 7,500 ps and $I_{(200):(111)}$ = 250:1. At lower thicknesses, the (111) reflexes are absent and thus indicates a complete (100) out-of-plane orientation. Furthermore, the out-of-plane lattice parameter a_{out}, determined if possible from the (200), (400) and (600) reflexes, increases continuously with decreasing thickness from 5.4008(4) to 5.41(2) Å. Excellent in-plane epitaxy is confirmed for all films by XRD ϕ-scans within the LAO(111) and YBO(220) lattice planes. Fig. 9.4(b) shows data

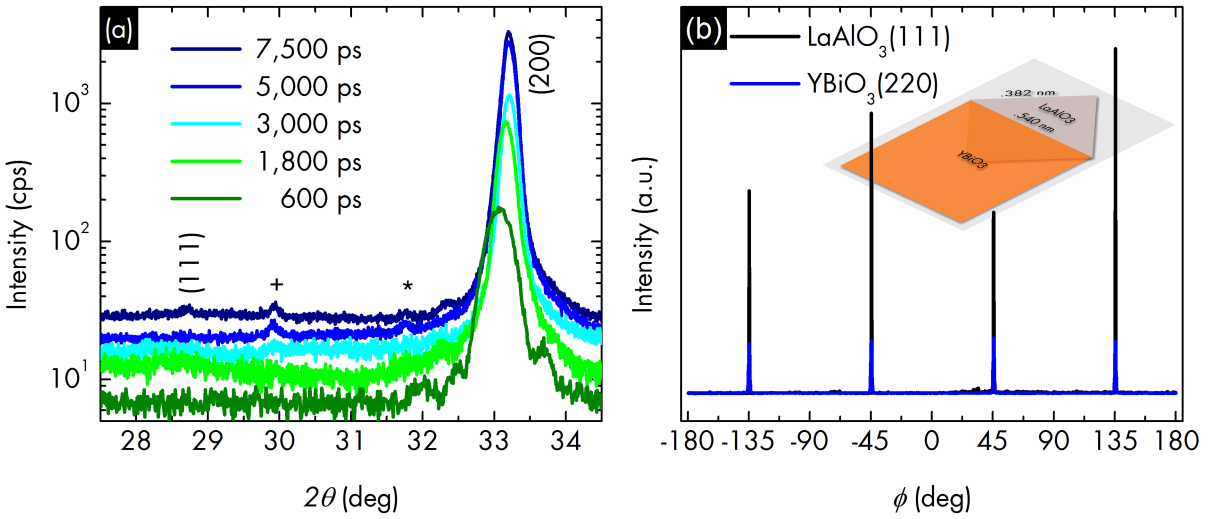

Figure 9.4 Thickness series at $T_g \approx 650$ °C. (a) XRD 2θ-ω scans of fully (100)-oriented YBO films deposited on LAO(001) with varying number of laser pulses (ps), as indicated. For lower pulse numbers , an increase of a_{out} is clearly recognizable and RMS surface roughness decreases from 4.1 to 1.8 nm. For clarity, curves are shifted along the y-axis by up to 20 cps. K_β and W lines are denoted by $+$ and $*$. (b) Excellent $[010]_{YBO}\|[110]_{LAO}$ in-plane epitaxial relationship of a similar 200-nm film (7,500 ps) is confirmed by XRD ϕ-scans of the LAO(111) and YBO(220) lattice planes and is illustrated schematically in the inset of (b). [Samples: E3954, E3993-96 (a), E3998 (b).]

of a similar 200-nm thick YBO film. The in-plane epitaxial relationship is $[010]_{YBO}\|[110]_{LAO}$ due to a 45° rotation of the epilayer [010] with respect to LAO⟨100⟩. This is feasible, because the pseudocubic YBO and the cubic LAO lattice are now aligned cube-on-cube with a lattice mismatch of only -0.3 %. Furthermore, YBO(100) aligns on LAO(001) within 1 rotational domain, since their surface point symmetries are both $4mm$ [148]. A ϕ-χ pole figure of a 29-nm film is shown in Fig. A.7(a). The results confirm that a biaxial texture is maintained up to at least a layer thickness of 200 nm. For chemical solution-deposited YBO thin films this was achieved up to 40 nm, only [53]. Note, that due to this particular in-plane epitaxy, reciprocal space mapping was not possible; there exist no suitable substrate and film reflexes with both a similar q-value and direction.

Also the surface roughness has a systematic dependence on film thickness. Between 7,500 and 600 ps, RMS surface roughness is reduced from about 4 to 2 nm. EDX performed on the 600-ps film revealed an ideal Y:Bi ratio of 1:1.02. Furthermore, laser scanning microscopy confirmed the expected reduction of droplet density with film thickness.

Because growth temperature and oxygen partial pressure were identical for all of these samples, their internal strain, e.g., due to oxygen vacancies, is believed to be similar. Thus, the observed dependence of a_{out} on film thickness might instead be related to epitaxial strain, which is a reasonable assumption considering the excellent in-plane epitaxy. Owing to the -0.3 % lattice mismatch with LAO, compressively strained YBO is assumed. With increasing film thickness,

lattice relaxation will ultimately set in and lead to a decrease of a_{out} and an increase of surface roughness. In particular, for film thickness of larger than 200 nm lattice relaxation leads to the formation of an additional (111)-orientation, which possibly is energetically more favorable. Overall, these results provide further evidence of a three-dimensional growth mode and confirm LAO as an adequate structural template for the growth of (100)-oriented YBO.

Surface morphology and temperature dependence at 600 pulses As was briefly mentioned above, AFM measurements revealed a granular surface structure with root-mean-squared (RMS) surface roughnesses in the order of 10 nm for 30,000-ps YBO films and about 2 nm at 600-ps. Overall, the surface morphology provided evidence for three-dimensional island growth. One explanation for such a surface morphology can certainly be the simultaneous presence of both a (100) and (111) preferential orientation as a result of film relaxation above a critical thickness of the order of 200 nm. Furthermore, it was argued above that the mechanically soft target promotes droplet formation. In general, at 30,000 pulses and about 850 nm, respectively, controlled two-dimensional growth, such as layer-by-layer growth, is unlikely. It might, however, be attained at much lower thicknesses. Hence, in the following the surface morphology is investigated in more detail by non-contact AFM and SEM measurements.

Compressively strained YBO films with thicknesses of the order of 15 nm were deposited on pre-annealed LAO(001) substrates by application of only 600 laser pulses after the initial 300-pulses nucleation layer. The growth temperature was varied between 400 and 650 °C to investigate its effect on crystalline structure and surface morphology. The oxygen partial pressure was set to 0.05 mbar for optimal Y:Bi stoichiometry. For the 650-°C sample a film thickness of about 16 nm was estimated by means of spectroscopic ellipsometry.

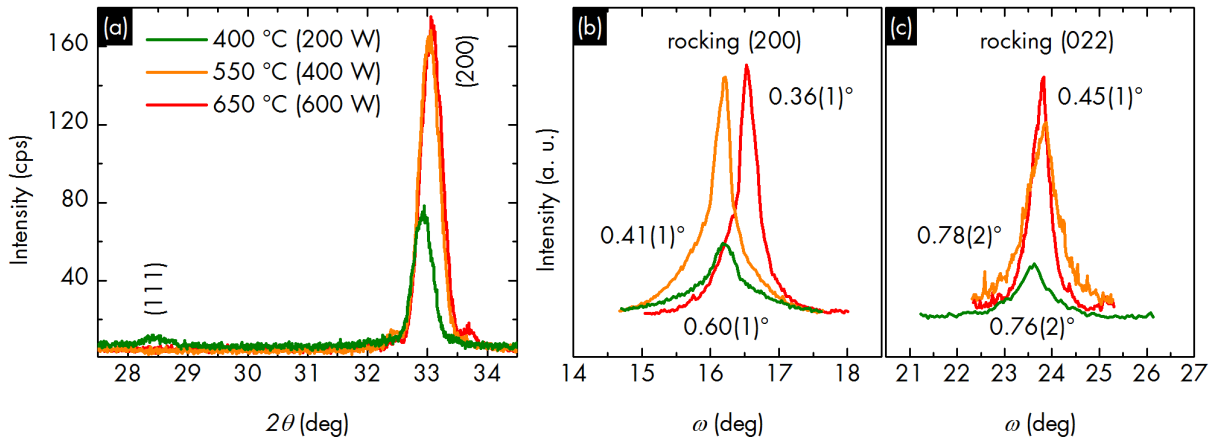

Figure 9.5 XRD 2θ-ω scans (a) of 600-ps YBO(100) films grown on LAO(001) at p_{O2} = 0.05 mbar and T_g as indicated. The YBO (111) reflex at about $2\theta = 28.6°$ is absent at 550 and 650 °C. With increasing T_g, a_{out} decreases from 5.43(5) to 5.41(2) Å. Rocking curves of the YBO (200) (b) and (022) (c) reflexes reveal the decrease of (200) and (022) half-widths, obtained from Lorentzian fits, and indicate an improvement of structural quality. [Samples: E3954, E3955, E3956.]

In line with the previous thickness series, XRD confirms a (100) out-of-plane preferential orientation, see Fig. 9.5(a), as well as a $[010]_{YBO}||[011]_{LAO}$ in-plane epitaxial relationship for all of the 600-ps films. Only at $T_g = 400$ °C an additional (111)-orientation is found. Clearly, $2\theta_{200}$ is significantly smaller at 400 °C. By extrapolation of $2\theta_{200}$ and $2\theta_{400}$, the lattice parameter a_{out} is obtained; it decreases from 5.43(5) to 5.41(2) Å at 400 and 650 °C, respectively. Moreover, the twice larger YBO (200) peak intensities at 550 and 650 °C suggest both a larger growth rate and an improved crystalline quality. Indeed, out-of-plane and in-plane mosaicity is reduced by application of higher growth temperatures as inferred from rocking scans of the YBO (200) and (022) reflexes. As shown in Fig. 9.5(b,c), the half-widths of the (200) and (022) reflexes, that were obtained from Lorentzian fits, decrease at higher growth temperatures.

Topographical AFM images are shown in Fig. 9.6. Although all 600-ps films have a significantly lower surface roughness in comparison with thicker 30,000-ps films ($\sim$ 10 nm), the surface morphology clearly confirms island growth as it is considerably characterized by droplets and crystalline grains with diameters of up to 700 and 100 nm, respectively. Most islands have a height of around 5 nm. RMS roughness values are obtained from figures (e-f). It increases with T_g from 1.27 to 1.78 nm, which is characteristic for island growth. The same applies to the peak-to-valley height.

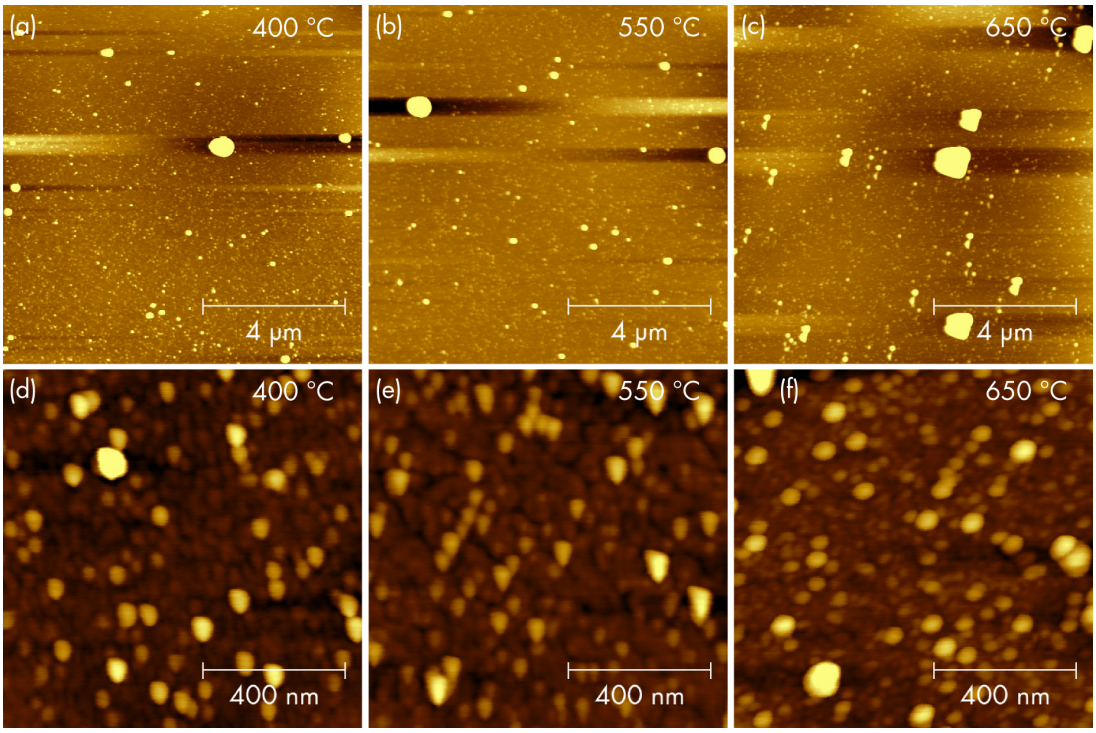

Figure 9.6 Non-contact AFM topographical images of YBO(100) deposited on pre-annealed LAO(001) with 600 ps at $p_{O2} = 0.05$ mbar and T_g as indicated. Droplets visible in (a-c) have diameters of up to 700 nm. Independent of T_g, the larger crystalline grains in (d-f) are about 50 to 100 nm in size. RMS surface roughness increases with T_g: 1.27 nm (d), 1.33 nm (e), 1.78 nm (f). [Samples: E3954, E3955, E3956.]

In line with above results, EDX analysis confirms the ideal Y:Bi ratio of 1.02:1 at $p_{O2} = 0.05$ mbar for all three samples. Furthermore, an EDX mapping of Y and Bi proves that droplets constitute mainly of yttrium, as shown in Fig. 9.7.

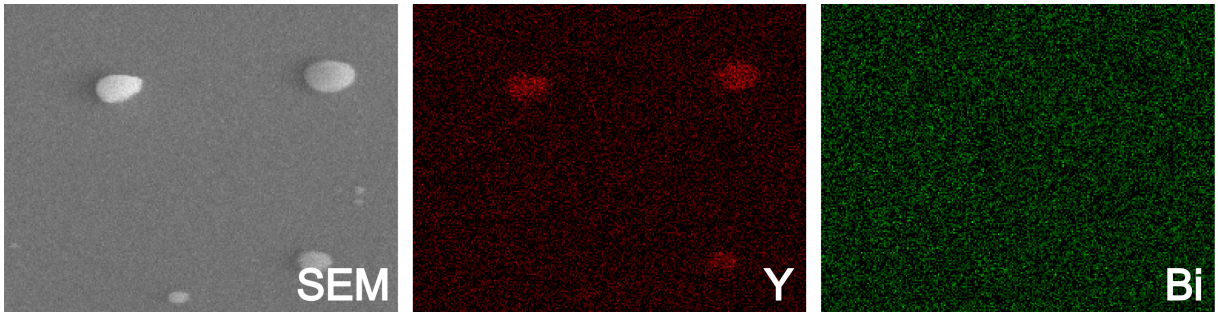

Figure 9.7 EDX mapping of the surface of an approximately 15-nm YBO(100) thin film deposited on LAO(001) at 550 °C and 0.05 mbar. The Y:Bi ratio is found to be stoichiometric with 1.02:1. Droplets on the film surface consist of yttrium. [Sample: E3956.]

In summary, deposition of thin, 600-ps YBO films at 0.05 mbar and 650 °C leads to a noticeable

improvement of crystalline quality and surface morphology when compared to lower growth temperatures. Fully (100)-oriented epitaxial films are obtained together with a reduced twist and tilt mosaicity. AFM measurements indicate further, that island formation is already present well below 15 nm. Possibly, the interaction of the LAO substrate with the YBO film leads to a poor wetting of the substrate surface, as was also suggested in Ref. [94]. Hence, alternative substrate materials were investigated for epitaxial growth of smooth YBO as discussed in the following sections.

9.1.2 YBO on STO(001) and STO(001):Nb

Unlike LAO, STO does not undergo a structural phase transition during the deposition process. Thus, structural twinning and a change of color of the substrate are avoided. This benefits optical studies of YBO thin films, in which usually both a bare substrate and the grown film are measured. Further, the growth mode on STO(001) single-crystalline substrates is to be investigated by depositing thin YBO films with 600 laser pulses. Samples were also grown at a higher 650 °C and $p_{O2} = 0.05$, 0.1 and 0.2 mbar. Increased growth temperatures and oxygen partial pressures were suggested to reduce Bi desorption [94]. Higher partial pressures might also decrease oxygen deficiency in the films and in turn affect the out-of-plane lattice constant a_{out} (cf. Sec. 9.1.1).

Similar to YBO prepared on LAO(001), XRD confirms a complete (100) out-of-plane preferential orientation and a $[010]_{\mathrm{YBO}} \| [110]_{\mathrm{STO}}$ in-plane epitaxial relationship, for all 600-ps films on STO(001). As an example, figure 9.8 shows typical XRD results of a YBO sample prepared at 0.05 mbar; a ϕ-χ pole figure confirming the biaxial texture is shown in the appendix, Fig. A.7(b). From the YBO (200) and (400) reflexes, an out-of-plane lattice constant of $a_{out} = 5.376(20)$ Å is derived. Higher p_{O2} leads to a continuous decrease of $I_{(200)}$ and $2\theta_{200}$ as shown in the inset of Fig. 9.8(a). Together with the mean free path of the plasma constituents, the growth rate is reduced at 0.1 and 0.2 mbar, as expected. From the θ_{200} and θ_{400} values at these partial pressures, a_{out} is estimated to be 5.389(20) and 5.385(80), respectively. Altogether, these results indicate a slight expansion of the epilayer unit cell and thus a trend towards improved bismuth and oxygen incorporation. Compared to typical films grown on LAO(001) under otherwise similar conditions, the out-of-plane lattice parameter is overall smaller. It is conjectured that this is due to the positive +2 % lattice mismatch with STO(001), i.e., tensile in-plane strain can explain this relative decrease in a_{out}. In any case, STO(001) is confirmed as another structural template for (100)-oriented YBO growth.

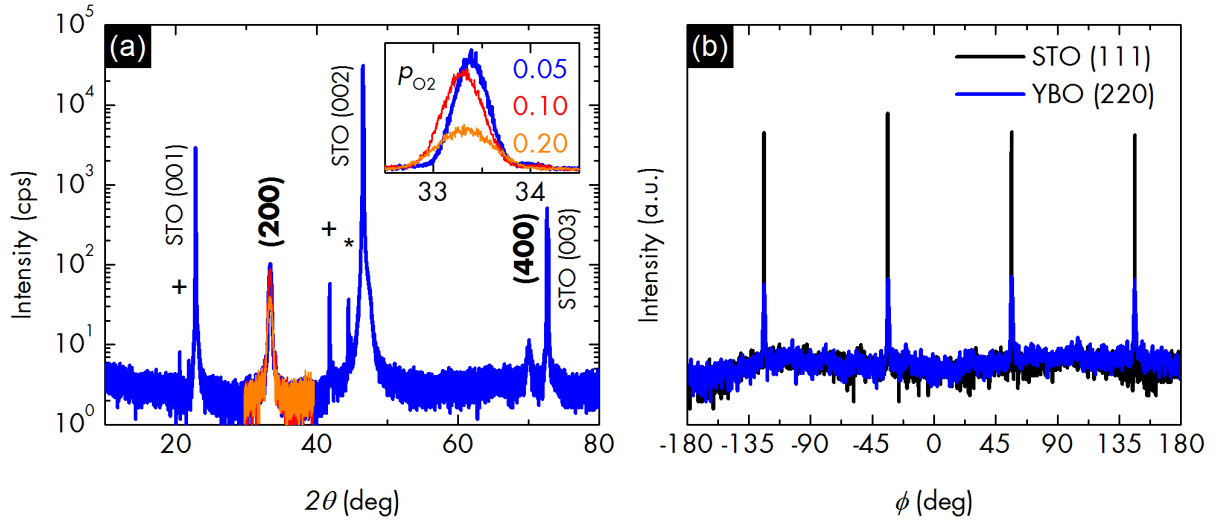

Figure 9.8 YBO on STO(001). (a) XRD 2Θ-ω scans of a film grown with 600 pulses at p_{O2} = 0.05 mbar and 650 °C. K_β and W lines are denoted by + and ∗. Inset: YBO (200) peak positions shift continuously with p_{O2} as indicated. (b) XRD ϕ-scan within the STO (111) and YBO (220) planes. The out-of-plane and in-plane epitaxial relationship is $[100]_{YBO}\|[001]_{STO}$ and $[010]_{YBO}\|[110]_{STO}$, respectively. a_{out} = 5.376(20) Å is obtained from (200) and (400). [Samples: E3987, E3988, E3989.]

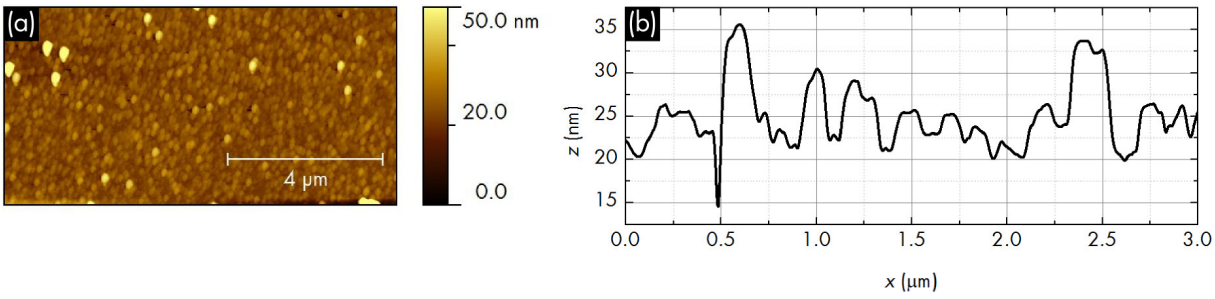

Figure 9.9 YBO on STO. (a) Non-contact AFM topographic image of approx. 10-nm thick YBO(100) deposited on STO(001). (b) A line profile extracted from (a). [Sample: E3989.]

A non-contact AFM topographic image of the 600-ps YBO sample grown at $p_{O2} = 0.2$ mbar is shown in Fig. 9.9(a). The surface morphology is very similar to other YBO films deposited on LAO and characterized by droplets. Here, the RMS surface roughness is 3.4 nm. From a line profile crystallite sizes between 50 and 150 nm are obtained, see Fig. 9.9(b). The crystallites have a height between 5 and 15 nm that corresponds reasonably well with the film thickness of about 10 nm obtained from spectroscopic ellipsometry. The data indicate the same three-dimensional island growth mode as on LAO substrates.

For future photoelectron spectroscopy (PES), which could not be performed in the frame of this thesis, scheduled in collaboration with Prof. Andrés Santander-Syro of Université Paris-Sud, YBO films are deposited on conducting STO(001) doped with 0.1 wt% Nb (STO:Nb). Two YBO films have been prepared at p_{O2} = 0.1 mbar and 650 °C with a pulse frequency of 5 Hz. Under these conditions, the film thicknesses after 600 and 5,000 laser pulses are approximately

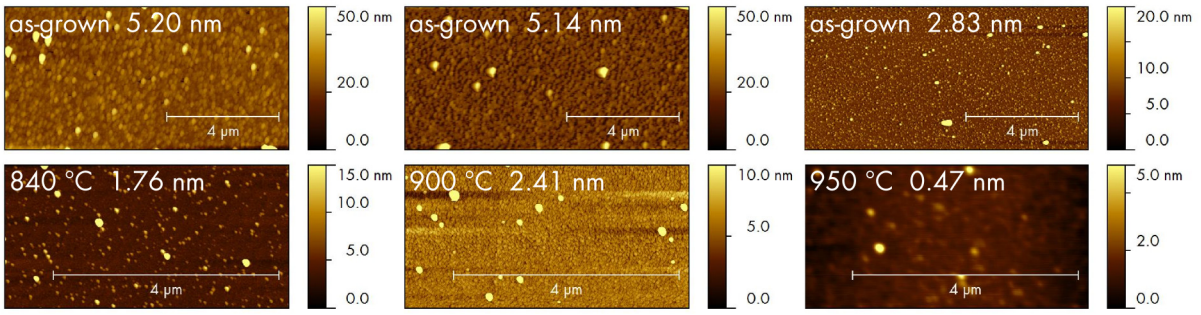

Figure 9.10 AFM topographic images and corresponding RMS surface roughness of YBO thin films deposited on LAO and STO substrates taken before (top row) and after (bottom row) a 2-h annealing at p_{O2} = 700 mbar and approximate temperatures as indicated. [Samples from left to right: E3989, E3988, E3942.]

6 and 42 nm, respectively. XRD confirms the (100) preferential orientation on STO:Nb(001) and yields estimated lattice parameters a_{out} of 5.38(4) and 5.379(8) Å for the 6 and 42-nm films, respectively (cf. Fig. A.5). With film thickness the RMS surface roughness obtained by means of AFM increases from 1.0 to 3.6 nm. Alternatively, epitaxial $LaNiO_3$ thin films might be suited as a bottom electrode for PES and other measurements [MJ9].

Since PES requires very smooth and epitaxial surfaces to achieve optimal resolution, post-annealing attempts were made for 2 h at p_{O2} = 700 mbar and different temperatures. The surface roughness of YBO films before and after annealing was measured by AFM, see Fig. 9.10. Post-annealing results in a significant reduction of RMS surface roughness. The annealing effect increases with temperature from 840 to 950 °C. Naturally, such elevated temperatures favor desorption of bismuth. Consequently, the Y:Bi ratio of the films increases significantly. For example, EDX gives an off-stoichiometric Y:Bi ratio of about 2.5 after post-annealing at both 840 and 900 °C.

In the present state, surface quality of YBO thin films is still insufficient for PES even after post-annealing. To alleviate this problem in future studies, interval PLD supplemented by *in situ* reflection high-energy electron diffraction (RHEED) [149] should be considered as a viable method by stimulating a controlled layer-by-layer growth mode.

9.1.3 YBO on YSZ(001) and MgO(100)

Relatively thick films of YBO (30,000 pulses) were grown on YSZ(001) single-crystalline substrates at p_{O2} = 0.04 mbar and 550 °C. A typical XRD 2θ-ω scan shows both the (111) and (100) lattice planes, see Fig. 9.11. The domain ratio $I_{(200):(111)}$ is around 7.5:1 indicating a (100) preferential orientation. Still, minor peaks with less than 100 cps related to the (220),

(311) and (511) reflexes can be discerned in the pattern suggesting a certain degree of polycrystallinity within the film. From the (200) and (400) peaks an out-of-plane lattice parameter of a = 5.400(12) Å is extrapolated. The Y:Bi ratio is 1.32:1 as measured by EDX. Again, the deviation of a from the reported powder value of 5.4188 Å can be understood by additional internal strain due to a combination of off-stoichiometry and oxygen vacancies. Epitaxial tensile strain probably plays only a minor role because for cube-on-cube growth on YSZ(001) the lattice mismatch is -6 %.

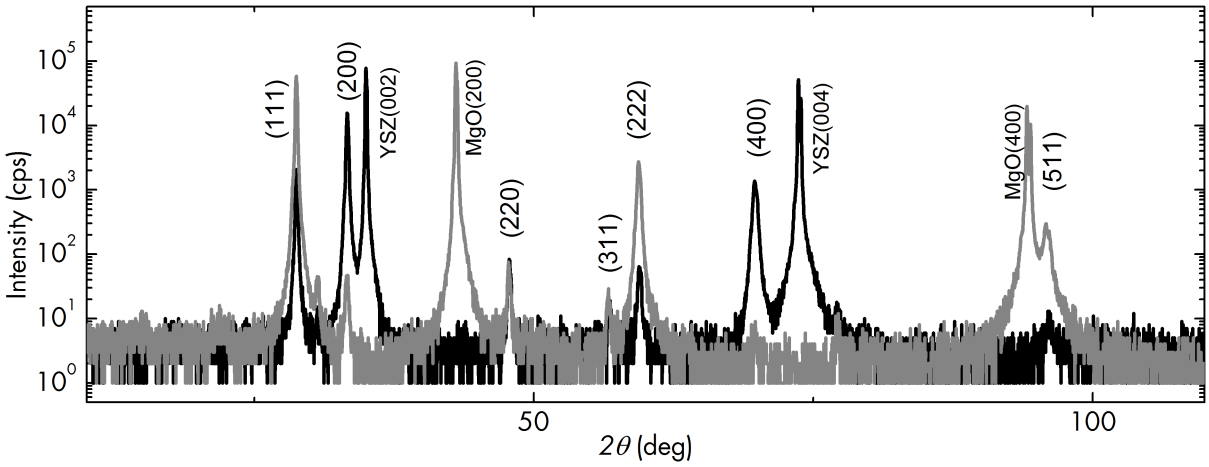

Figure 9.11 Typical XRD 2Θ-ω scans of $YBiO_3$ thin films PLD-grown with 30,000 laser pulses on YSZ(001) (black) and MgO(100) (gray) at p_{O2} = 0.04 mbar and 550 °C. [Samples: E3809, E3810.]

Also on MgO(100) a YBO film was grown under the same conditions. Compared to deposition on YSZ(001), the XRD 2θ-ω pattern, Fig. 9.11, shows very intense (111) and (222) peaks. The preferential orientation is clearly (111) with a domain ratio $I_{(200):(111)}$ of about 1:2000. Similarly, one can observe the (220), (311) and (511) reflexes with low intensity indicating yet again a certain degree of polycrystallinity. The out-of-plane lattice parameter determined from the YBO (111) and (222) reflexes is similar and approximately a = 5.399(9) Å. On MgO(100), the lattice mismatch with YBO(111) is expected to be large and epitaxial strain should hence have no effect on the lattice parameter. Instead, EDX yields a very similar Y:Bi ratio of 1.34:1 highlighting again the influence of the stoichiometry on the unit cell dimensions.

For very thin samples prepared with 600 laser pulses, XRD yields only a (100) and (111) out-of-plane preferential orientation on YSZ(001) and MgO(100), respectively, see Fig. 9.12. The in-plane epitaxial relationship on MgO(100) is $[100]_{YBO}\|[011]_{MgO}$, as shown in Fig. 9.13(a). YBO(111) aligns on MgO(100) within 4 rotational domains with 30° spacing due to its 3m surface point symmetry [104]. On YSZ(001), the in-plane epitaxial relationship is found to be $[011]_{YBO}\|[110]_{YSZ}$, see Fig. 9.13(b). The growth is thus cube-on-cube and YBO(100) (4mm)

aligns on YSZ(001) (4*mm*) within 1 rotational domain [104]. Clearly, MgO(100) is a suitable structural template for (111)-oriented growth of YBO. On YSZ, the observed cube-on-cube epitaxy suggests domain-matching epitaxy with a -6 % lattice mismatch. For typical ϕ-χ pole figures, see Fig. A.7(c,d).

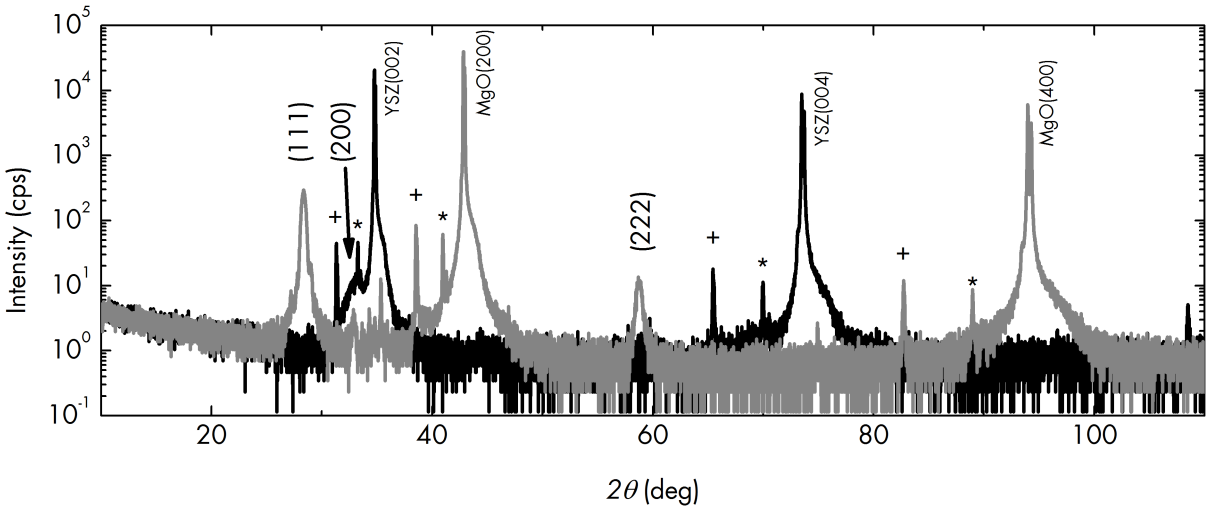

Figure 9.12 XRD 2Θ-ω scans of 600-ps $YBiO_3$ thin films deposited on YSZ(001) (black) and MgO(100) (gray) at p_{O2} = 0.05 mbar and 550 °C. On MgO, $a_{out} = 5.407(19)$ Å is extrapolated from the (111) and (222) reflexes. [Samples: E3991 and E3992.]

From the (100)-oriented 600-ps film grown on YSZ, one can conclude that, similar to LAO and STO substrates, film relaxation above a critical thickness involves the formation of an additional (111)-orientation. The possibility of tuning either a (100) or (111) surface configuration by choice of the substrate might become relevant for a study of the predicted topological surface states [37]. Irrespective of the preferred orientation, the surface morphologies on YSZ and MgO are equivalent to films on LAO and STO and are indicative of island growth.

9.1.4 YBO on *a*-Al_2O_3

For the determination of the bandgap energy by means of a combined optical transmission and spectroscopic ellipsometry study, see Sec. 9.2, a 2,000-ps YBO film was deposited on an *a*-plane Al_2O_3 substrate at p_{O2} = 0.05 mbar and 550 °C. The XRD 2θ-ω scan, shown in Fig. 9.14, clearly reveals (111)-oriented YBO with a domain ratio of $I_{(200):(111)} \approx$ 1:62. Extrapolation of the YBO (111) and (222) *d*-values yields $a_{out} = 5.41(4)$ Å assuming a cubic epilayer. Because of the high lattice mismatch with *a*-plane sapphire (about $\pm$40 %), at a film thickness of $d \approx$ 57 nm, see Sec. 9.2, the assumption of relaxed growth is justified. Ruling out

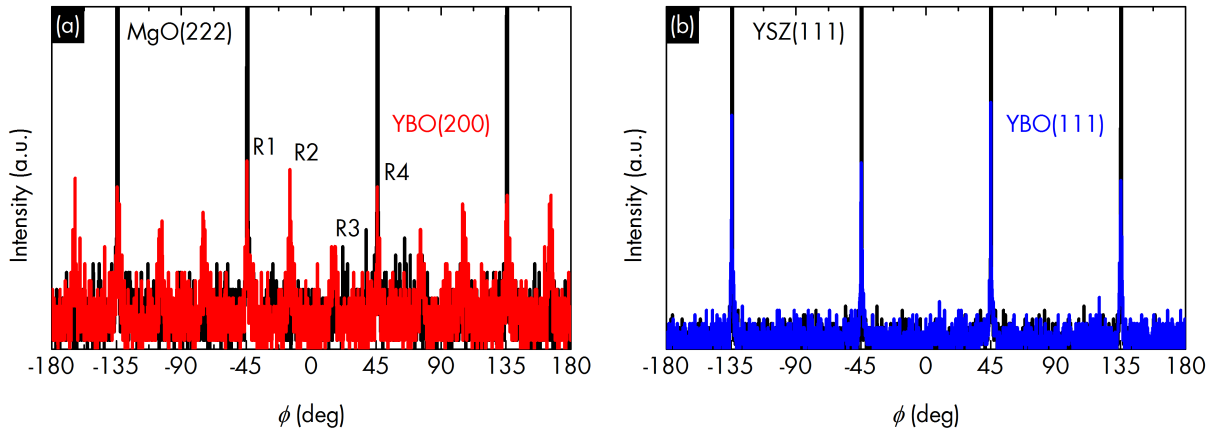

Figure 9.13 (XRD ϕ-scans of: (a) asymmetric MgO (222) and YBO (200), and (b) YSZ (111) and YBO (111) reflexes. YBO(111) grows on MgO(100) within 4 rotational domains R1 to R4 and an in-plane epitaxial relationship of $[100]_{YBO}\|[011]_{MgO}$. On YSZ(001), the in-plane epitaxial relationship with YBO(100) is $[011]_{YBO}\|[110]_{YSZ}$ and 1 rotational domain is formed. [Samples: E3991, E3992]

substrate-mediated strain the reduced out-of-plane lattice constant most probably results from off-stoichiometry.

The in-plane epitaxial relationship on a-Al_2O_3 was investigated on the 57-nm and an additional 1660-nm film by measuring a ϕ-χ pole figure within the YBO (200) plane, see Fig. A.7(e,f). Both at a film thickness of about 57 and 1660 nm, a random distribution of the in-plane crystallite orientation is indicated by a distinct circular intensity feature. This result excludes lattice- and domain-matching epitaxy and thus justifies the assumption of a fully relaxed, cubic epilayer.

Similar to all previously discussed YBO films, the surface morphology is characterized by crystalline grains and droplets. It provides evidence for a three-dimensional growth mode. From the 3×3 μm^2 AFM topography image shown in Fig. 9.15, a root-mean-squared roughness of 2.68 nm is calculated. In summary, the results for 57-nm YBO on a-plane sapphire are in line with all other films discussed so far. In particular, XRD supports the notion of YBO orienting along (111) when unstrained.

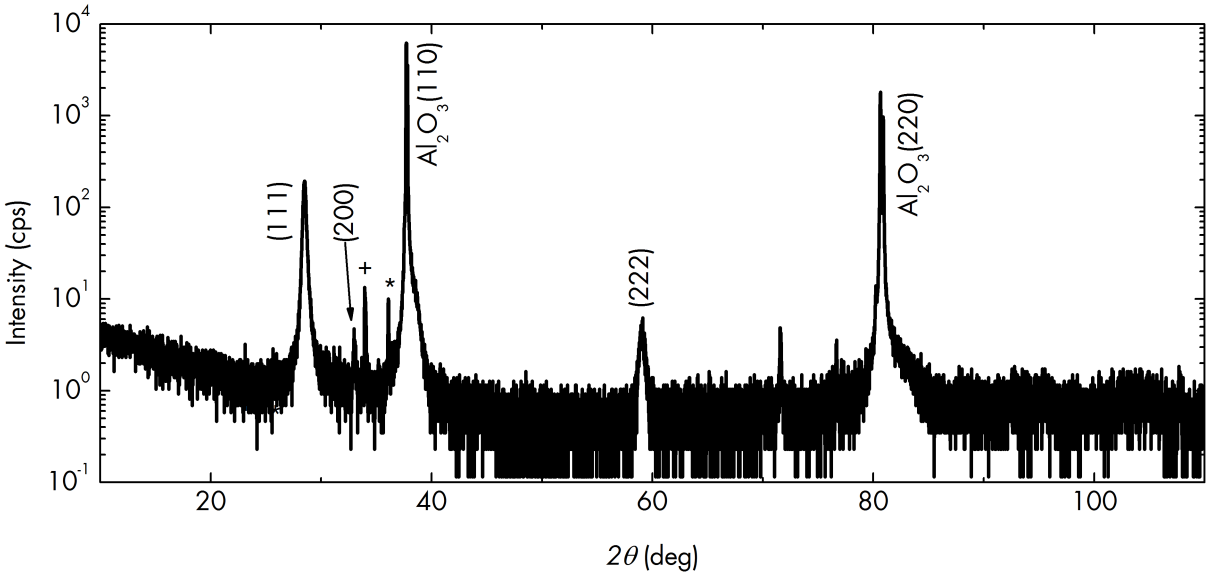

Figure 9.14 XRD 2Θ-ω scan of ≈ 57-nm thick YBO(111) deposited on a-plane Al_2O_3 at p_{O2} = 0.05 mbar and 550 °C. The domain ratio is $I_{(200):(111)} \approx 1{:}62$. $a_{out} = 5.41(4)$ Å is obtained by extrapolating the (111) and (222) peak positions. K_β and W lines are denoted by + and ∗. [Sample: E4048.]

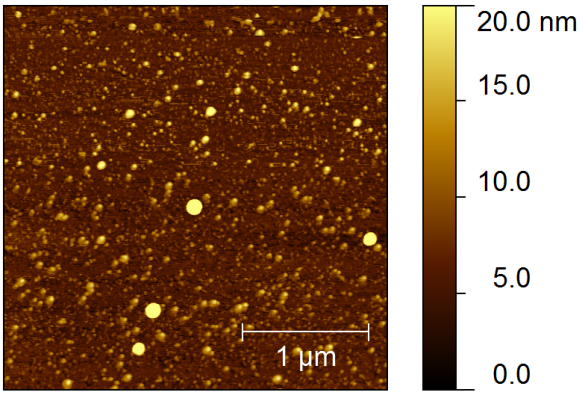

Figure 9.15 AFM topographic image of a 57-nm thick YBO(111) film deposited on a-plane sapphire. The surface morphology is characterized by crystalline grains and droplets. The root-mean-squared surface roughness is 2.68 nm. [Sample: E4048.]

9.2 Dielectric function and bandgap energies

Jin *et al.* [37] proposed YBO in the assumed undistorted $Pm\bar{3}m$ cubic perovskite structure as a novel topological oxide insulator with a topologically non-trivial direct bandgap of 0.330 eV and a trivial indirect gap at 0.183 eV. However, it was subsequently shown that the assumed $Pm\bar{3}m$ crystal structure is in fact unstable and instead YBO was predicted to be a trivial insulator in the stable but distorted *Pnma* structure [38]. Although no precise values were given in

Ref. [38], the trivial direct and indirect bandgaps in YBO are expected to be significantly larger but still smaller than 1 eV in energy. To date, no experimental bandgap energies of YBO in the experimental defective fluorite crystal structure with space group $Fm\bar{3}m$ [90–93] were reported. In order to provide some necessary experimental feedback to these band structure calculations, the dielectric function and experimental bandgap energies of $YBiO_3$ thin films are determined by coupled modeling of spectroscopic ellipsometry and optical transmission data in the 0.03 to 6.00 eV spectral range. Ellipsometry and transmission spectroscopy were performed respectively by Steffen Richter, who also performed the modeling, and Ulrike Teschner of Leipzig University.

The measurements were performed on a relaxed grown, 57 nm-thick, (111)-oriented YBO thin film deposited on a one-sided polished *a*-plane Al_2O_3 substrate. Using the IR-VASE and VASE instruments, isotropic reflection ellipsometry was applied between 0.03 and 4 eV at angles of incidence from 45° to 75°. The optical transmission spectroscopy was performed under normal incidence in the spectral range between 0.62 and 6.20 eV.

Coupled modeling of the reflection ellipsometry and optical transmission data is performed in the 0.03 to 6.00 eV spectral range. The model contains layers for the substrate, the YBO film and the surface roughness. The sapphire substrate dielectric function is taken from a tabulated list. The thin film dielectric function is modeled using a Kramers-Kronig consistent numerical B-spline model with 22 control points and 0.7 eV spacing [150]. An effective medium approximation is used for the thin film surface roughness. The backside roughness scattering from the one-sided polished *a*-sapphire substrate is corrected by a reference transmisson measurement of a double-sided polished substrate of the same thickness and a wavelength-dependent correction factor $T_{\mathrm{double-sided}}/T_{\mathrm{one-sided}}$. Finally, the absorption coefficient α is calculated from the numerical B-spline model, from which also the film thickness and effective surface roughness are obtained.

Figure 9.16 shows the measured ellipsometric parameters Ψ and Δ and the corresponding results of the coupled numerical B-spline modeling. In general, the numerical model shows excellent agreement with the experimental data in the entire measured spectral range. A film thickness of 5(2) nm including a surface roughness of between 2 and 4 nm is obtained. The modeled roughness value is in very good agreement with the 2.68 nm RMS roughness obtained via AFM (cf. Sec. 9.1.4). The infrared spectral range below about 0.11 eV is characterized by the restrahlenbande of the substrate and by phonon contributions of both substrate and film, respectively. Between about 0.15 and 0.3 eV, the additional oscillating intensity is due to substrate backside reflections, which were not considered in the numerical B-spline model.

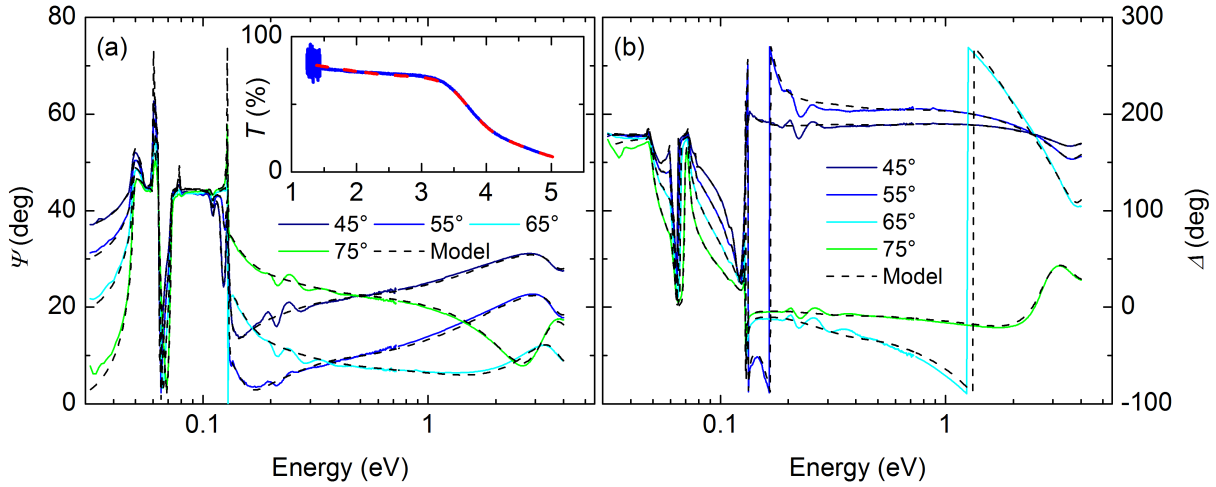

Figure 9.16 Spectra of the ellipsometric parameters Ψ (a) and Δ (b) of 57 nm YBO on *a*-plane Al_2O_3 measured at angles of incidence as indicated. The inset in (a) shows the optical transmission spectrum T and the model in red. Dashed lines represent the numerical B-spline model. [Sample: E4048.]

The calculated absorption spectrum of the YBO film is shown in Fig. 9.17. From the present data, indirect and direct bandgaps at 0.183 and 0.330 eV as predicted by Jin *et al.* [37] can be excluded with certainty. Instead, strong absorption is evident above 3 eV together with a continuous onset at 1.5 eV. The strong absorption peak is interpreted in analogy to Trimarchi *et al.* [38] as the allowed direct bandgap transition between the Bi 6*s* and 6*p* bands at the *R* point. For an estimate of the direct bandgap energy E_{gd}, linear regression of the $(nE\alpha)^2$ spectrum between 4.00 and 4.30 eV is performed [151], see Fig. 9.17(a). The extrapolation of the straight line fit to 0 yields E_{gd} = 3.7(1) eV. Similarly, the absorption between 1.5 and 3 eV is interpreted as the allowed indirect bandgap transition from the valence band maximum at the Γ point to the conduction band minimum at the *R* point [38]. From an equivalent extrapolation of $(n\alpha/E)^{1/2}$ [151] in the 1.66 to 2.07 eV spectral range, see Fig. 9.17(b), an indirect bandgap energy of E_{gi} = 1.1(1) eV is approximated. The obvious discrepancy between the predicted [37, 38] and the larger experimental bandgaps is currently not fully understood. Density functional theory models of a material's band structure typically underestimate the real bandgap by up to 40 % [152]. However, the obtained bandgaps of the nominally unstrained YBO thin film are reasonable as they interpolate between the end members of the $Y_xBi_{1-x}O_{1.5}$ solid solutions: While as grown thin films of cubic δ-Bi_2O_3 ($a \approx 5.65$ Å [91]) have an indirect optical gap of 1.73 eV [153], pulsed laser-deposited cubic Y_2O_3 thin films with a = 10.6 Å exhibit a direct bandgap of 5.6 eV [154].

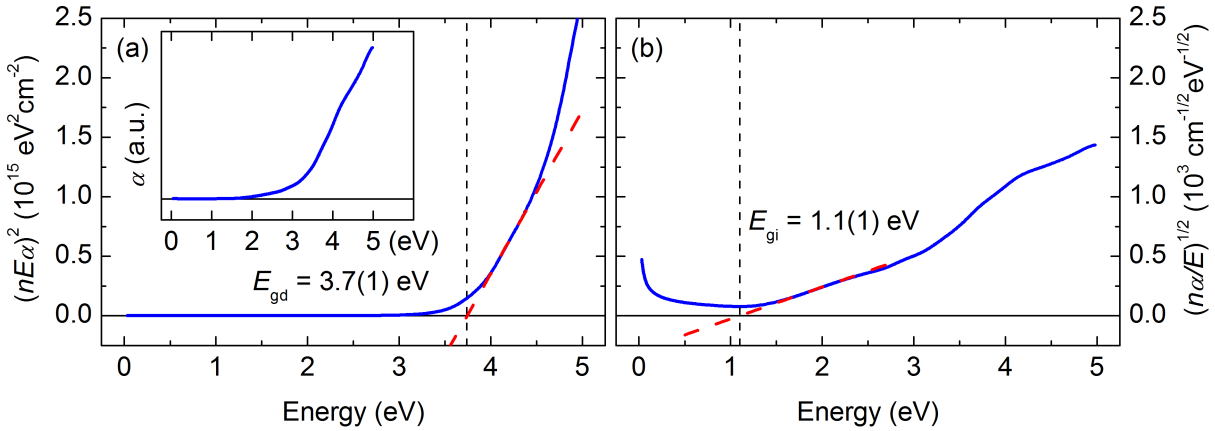

Figure 9.17 Calculated absorption coefficient α of a 57-nm YBO thin film. The absorption spectrum is plotted versus the incident photon energy as $(nE\alpha)^2$ (a) and $(n\alpha/E)^{1/2}$ (b); the inset of (a) shows $\alpha(E)$. Linear regression and extrapolation to 0 yield a direct and indirect bandgap of 3.7(1) and 1.1(1) eV, respectively. The adjusted R^2 value of both fits is 0.99991. [Sample: E4048.]

9.3 Summary

Heteroepitaxy of YBO thin films on various single-crystalline substrates was performed by PLD. The effect of substrate-induced epitaxial strain on the structure and morphology of YBO thin films was investigated. LAO(001), STO(001) and STO:Nb(001) allowed lattice-matching epitaxy of (100)-oriented YBO thin films with a defined $[010]_{YBO}\|[011]_{LAO}$ in-plane epitaxial relationship up to film thicknesses of about 200 nm. At higher thickness, film relaxation leads to the formation of an additional (111)-orientation together with a decrease in the out-of-plane lattice parameter a_{out}. In comparison, similar biaxially textured YBO thin films were previously synthesized on LAO(001) by chemical solution deposition up to a thickness of about 40 nm [53].

Results on YSZ(001) are similar and indicate domain-matching epitaxy due to the -6 % lattice mismatch. Conversely, epitaxial YBO(111) thin films were realized on MgO(100) and a-Al_2O_3, on which the large lattice mismatch permits only fully relaxed growth. The tunability of the chemistry with oxygen partial pressure was common to all samples. Partial pressures below 0.05 mbar led to an off-stoichiometric incorporation of Y and a resulting decrease of a_{out}. Oxygen vacancies were not quantified in this work. Increasing the growth temperature from 550 to 650 °C resulted in a significant improvement of crystalline quality and a stabilization of the (100)-orientation. The surface morphology can be accounted for by a three-dimensional growth mode on all substrates. Island growth is already present well below film thicknesses of 15 nm. Surface roughnesses were reduced by optimization of PLD process parameters to RMS values of as low as 1.3 nm, which represents a slight improvement over a previous report [53]. Sample annealing in a 700-mbar oxygen atmosphere at temperatures from about 840 to 950 °C could

reduce the surface roughness in average by 22 %, but is accompanied by a considerable loss of Bi. Reliable temperature- and thickness-dependent electrical resistivity data were not obtained because of an extremely large bulk resistivity that was already reported in Ref. [51]. Similarly, paramagnetism down to 5 K was confirmed by SQUID-magnetometry (cf. Fig. A.6).

Room-temperature infrared spectroscopic ellipsometry found no evidence of either an indirect bandgap of 0.183 eV or a non-trivial direct gap of 0.33 eV as predicted by Jin *et al.* [37]. In their band structure calculations, they wrongly considered the $Pm\bar{3}m$ perovskite primitive cell with its larger $a = 5.428$ Å [50] lattice constant of the cubic fluorite-type cell. Instead, coupled modeling of optical transmission and spectroscopic ellipsometry data in the 0.03 to 4.00 eV spectral range found a direct and indirect bandgap at E_{gd} = 3.7(1) eV and E_{gi} = 1.1(1) eV. (Sec. 9.2). These values interpolate well between the end members of the $Y_xBi_{1-x}O_{1.5}$ solid solutions and are in favor of band structure calculations by Trimarchi *et al.* [38], who instead predicted a topological trivial state for YBO in the theoretical, but stable, *Pnma* perovskite structure.

This work provided indirect evidence of a topologically *trivial* state in YBO thin films. However, to elucidate the true band structure of YBO and its topology, the current band structure calculations should be reassessed using the experimentally observed random fluorite-type structure with $a = 5.4188$ Å [93] and the bandgap energies of E_{gd} = 3.7(1) eV and E_{gi} = 1.1(1) eV determined in this work. It would furthermore be interesting to include the effect of epitaxial strain into these calculations. In addition, direct experimental evidence may be obtained by, e.g., photoelectron spectroscopy or scanning tunneling microscopy. For such experiments, however, atomically flat surfaces are required, that in the future may be achieved on YBO thin films by interval PLD [149].

10 Summary and outlook

In this thesis, heteroepitaxy of the ternary oxides Na_2IrO_3, Li_2IrO_3, $Y_2Ir_2O_7$ and $YBiO_3$ was performed by pulsed laser deposition (PLD) on various single-crystalline substrates. All of these oxide materials are novel candidates for either a topological insulator or a spin liquid [30–36]. These states of matter are one possible starting point for the future realization of scalable quantum computation, but may also find application in magnetic memory [8] or low-power electronic devices [9]. The realization of high-quality, heteroepitaxial thin films presented here, represents a first step towards these future device applications. Research on the iridates was at times restricted by the small size of available single crystals and experimental results were often based on powder-averaged data. Thus, with their inherently large surface-to-volume ratios, heteroepitaxial thin films are an attractive object of study and could benefit certain experimental methods, such as neutron diffraction or pump-probe spectroscopy. $YBiO_3$ was mainly studied as a buffer material for the $YBa_2Cu_3O_{7-\delta}$ high-temperature superconductor [50–53]. Its recently proposed topological insulator phase has still been under debate [37, 38], to which the present study contributed.

Na_2IrO_3 The first heteroepitaxial (001)-oriented Na_2IrO_3 films with well-defined in-plane epitaxial relationship were realized previously on single-crystalline Al_2O_3, $YAlO_3$ and ZnO 5×5 and 10×10 mm^2 substrates [MJ1]. In this work, Na_2IrO_3 films were deposited on up to 2”-inch diameter sapphire wafers. Deposition of intermediate ZnO or a ZnO:Al/ZnO bilayer led to a considerable reduction of in-plane mosaicity. These results warrant renewed neutron diffraction experiments and also prove the feasibility of epitaxial bottom gating to probe the proposed topological surface state conduction [124, 125].

Li_2IrO_3 The first Li_2IrO_3 thin films with preferential (001) and (10-1) out-of-plane crystalline orientation and defined in-plane epitaxial relationship were grown on different single-crystalline substrates, namely Al_2O_3, $YAlO_3$, ZrO_2:Y and ZnO [MJ3]. Temperature-dependent electrical resistivity was dominated by three-dimensional Mott variable range hopping, as was similarly observed in Na_2IrO_3 films [MJ1] and single crystals [39]. Conventional magnetoresistance between 10 and 100 K was small, positive and isotropic in applied magnetic fields of up to 8 T, and explained by phonon scattering and small charge carrier mobilities. SQUID-magnetometry could not detect the antiferromagnetic phase transition expected at around 15 K. Furthermore, the dielectric function was determined below 3.34 eV by means of spectroscopic ellipsometry. On the basis of j_{eff}-physics and by comparison with previous reports and related iridates, the combined data gave insight into electronic excitations. These excitations were associated to

d-d transitions from which a splitting of the $5d$-t_{2g} manifold was inferred. In-gap states were attributed to phonons and possibly magnons. In particular, transitions across the Mott gap indicated an optical gap of $\approx$ 300 meV, which was smaller than in Na_2IrO_3 films [MJ1] and single crystals [72].

$Y_2Ir_2O_7$ Attempts were made to realize heteroepitaxial $Y_2Ir_2O_7$ thin films on (001)- and (111)-oriented ZrO_2:Y substrates. X-ray diffraction indicates a possible preferential (111) out-of-plane-orientation on ZrO_2:Y(111), but also revealed the presence of Y_2O_3, Ir and IrO_2 phases. Temperature-dependent resistivity was dominated by three-dimensional Mott variable range hopping, which was associated rather with the sample's structural quality and possible amorphicity than with its correlated nature. In conclusion, the obtained results serve as a reference for future experimental efforts.

$YBiO_3$ Heteroepitaxy of $YBiO_3$ thin films on various single-crystalline substrates was performed. In particular, lattice-matching epitaxy of (100)-oriented $YBiO_3$ thin films with biaxial in-plane texture was achieved on $LaAlO_3$(001) and $SrTiO_3$(001) up to film thicknesses of about 200 nm. Previously, fully textured $YBiO_3$ films were synthesized by chemical solution deposition with a thickness of about 40 nm [53]. On MgO(100) and *a*-plane sapphire, (111)-oriented YBO was realized. The flexibility of tuning the surface configuration by choice of substrate is beneficial for a direct investigation of the proposed surface states and their different properties in the future [37]. Furthermore, the Y:Bi ratio was tunable by the applied oxygen partial and affected the out-of-plane lattice constant due to the slightly different ionic radii of Y^{3+} and Bi^{3+}. Surface roughnesses were reduced to root-mean-squared values as low as 1.3 nm, which represents a slight improvement over a previous report [53]. Sample annealing in an oxygen atmosphere at high temperatures could further reduce the surface roughness in average by 22 %, but was accompanied by a considerable loss of Bi. Paramagnetism down to 5 K was confirmed by SQUID magnetometry. A coupled modeling of optical transmission and spectroscopic ellipsometry data revealed both a direct and indirect bandgap at E_{gd} = 3.7(1) eV and E_{gi} = 1.1(1) eV, respectively. Rietveld refinement of X-ray diffraction data of the polycrystalline source target supported a fluorite-type $Fm\bar{3}m$ crystal structure. These results were in favor of band structure calculations predicting a topological *trivial* state in $YBiO_3$ [38].

Outlook For all materials investigated, further improvement of the surface morphology is required if surface-sensitive angle-resolved photoelectron spectroscopy or scanning tunneling microscopy experiments are to be performed in the future. These methods could provide direct evidence of the proposed topological insulator state but require atomicly flat surfaces. For this matter, further improvement of the source target's density and employment of interval PLD [149] are suggested. Due to a minimal lattice mismatch, $YAlO_3$(011) may be a promising

substrate for Li_2IrO_3. This work also provided indirect evidence of a topologically *trivial* state in $YBiO_3$ thin films. However, to elucidate the true band structure of $YBiO_3$ and its topology, the current band structure calculations should be reassessed using the experimentally observed random fluorite-type structure and the direct and indirect bandgap energies of E_{gd} = 3.7(1) eV and E_{gi} = 1.1(1) eV. It would furthermore be interesting to include the effect of epitaxial strain into these calculations.

Bibliography

[1] A. Kitaev. *Ann. Phys. (N. Y).* **303**(1), 2–30 (2003). http://dx.doi.org/10.1016/S0003-4916(02)00018-0.

[2] C. Nayak, A. Stern, M. Freedman, and S. Das Sarma. *Rev. Mod. Phys.* **80**(3), 1083–1159 (2008). http://dx.doi.org/10.1103/RevModPhys.80.1083.

[3] A. Stern. *Nature* **464**(7286), 187–93 (2010). http://dx.doi.org/10.1038/nature08915.

[4] A. Kitaev. *Ann. Phys. (N. Y).* **321**(1), 2–111 (2006). http://dx.doi.org/10.1016/j.aop.2005.10.005.

[5] L. Fu and C. Kane. *Phys. Rev. Lett.* **100**(9), 096407 (2008). http://dx.doi.org/10.1103/PhysRevLett.100.096407.

[6] B. A. Bernevig, T. L. Hughes, and S.-C. Zhang. *Science* **314**(5806), 1757–61 (2006). http://dx.doi.org/10.1126/science.1133734.

[7] M. König, S. Wiedmann, C. Brüne, A. Roth, H. Buhmann, L. W. Molenkamp, X.-L. Qi, and S.-C. Zhang. *Science* **318**(5851), 766–70 (2007). http://dx.doi.org/10.1126/science.1148047.

[8] I. Garate and M. Franz. *Phys. Rev. Lett.* **104**(14), 146802 (2010). http://dx.doi.org/10.1103/PhysRevLett.104.146802.

[9] Z.-H. Pan, a. V. Fedorov, D. Gardner, Y. S. Lee, S. Chu, and T. Valla. *Phys. Rev. Lett.* **108**(18), 187001 (2012). http://dx.doi.org/10.1103/PhysRevLett.108.187001.

[10] L. He, X. Kou, and K. L. Wang. *Phys. status solidi - Rapid Res. Lett.* **7**(1-2), 50–63 (2013). http://dx.doi.org/10.1002/pssr.201307003.

[11] M. Z. Hasan and C. L. Kane. *Rev. Mod. Phys.* **82**(4), 3045–3067 (2010). http://dx.doi.org/10.1103/RevModPhys.82.3045.

[12] L. Fu, C. Kane, and E. Mele. *Phys. Rev. Lett.* **98**(10), 106803 (2007). http://dx.doi.org/10.1103/PhysRevLett.98.106803.

[13] J. Moore and L. Balents. *Phys. Rev. B* **75**(12), 121306 (2007). http://dx.doi.org/10.1103/PhysRevB.75.121306.

[14] R. Roy. *Phys. Rev. B* **79**(19), 195322 (2009). http://dx.doi.org/10.1103/PhysRevB.79.195322.

[15] Y. Ran, Y. Zhang, and A. Vishwanath. *Nat. Phys.* **5**(4), 298–303 (2009). http://dx.doi.org/10.1038/nphys1220.

[16] D. Hsieh, D. Qian, L. Wray, Y. Xia, Y. S. Hor, R. J. Cava, and M. Z. Hasan. *Nature* **452**(7190), 970–4 (2008). http://dx.doi.org/10.1038/nature06843.

[17] D. Hsieh, Y. Xia, L. Wray, D. Qian, a. Pal, J. H. Dil, J. Osterwalder, F. Meier, G. Bihlmayer, C. L. Kane, Y. S. Hor, R. J. Cava, and M. Z. Hasan. *Science* **323**(5916), 919–22 (2009). http://dx.doi.org/10.1126/science.1167733.

[18] Y. Xia, D. Qian, D. Hsieh, L. Wray, a. Pal, H. Lin, a. Bansil, D. Grauer, Y. S. Hor, R. J. Cava, and M. Z. Hasan. *Nat. Phys.* **5**(6), 398–402 (2009). http://dx.doi.org/10.1038/nphys1274.

[19] H. Zhang, C.-X. Liu, X.-L. Qi, X. Dai, Z. Fang, and S.-C. Zhang. *Nat. Phys.* **5**(6), 438–442 (2009). http://dx.doi.org/10.1038/nphys1270.

[20] Y. L. Chen, J. G. Analytis, J.-H. Chu, Z. K. Liu, S.-K. Mo, X. L. Qi, H. J. Zhang, D. H. Lu, X. Dai, Z. Fang, S. C. Zhang, I. R. Fisher, Z. Hussain, and Z.-X. Shen. *Science* **325**(5937), 178–81 (2009). http://dx.doi.org/10.1126/science.1173034.

[21] H. Zhang and S.-C. Zhang. *Phys. status solidi - Rapid Res. Lett.* **7**(1-2), 72–81 (2013). http://dx.doi.org/10.1002/pssr.201206414.
[22] D. Xiao, Y. Yao, W. Feng, J. Wen, W. Zhu, X.-Q. Chen, G. M. Stocks, and Z. Zhang. *Phys. Rev. Lett.* **105**(9), 096404 (2010). http://dx.doi.org/10.1103/PhysRevLett.105.096404.
[23] S. Chadov, X. Qi, J. Kübler, G. H. Fecher, C. Felser, and S. C. Zhang. *Nat. Mater.* **9**(7), 541–5 (2010). http://dx.doi.org/10.1038/nmat2770.
[24] H. Lin, L. A. Wray, Y. Xia, S. Xu, S. Jia, R. J. Cava, A. Bansil, and M. Z. Hasan. *Nat. Mater.* **9**(7), 546–9 (2010). http://dx.doi.org/10.1038/nmat2771.
[25] H. Lin, R. S. Markiewicz, L. A. Wray, L. Fu, M. Z. Hasan, and a. Bansil. *Phys. Rev. Lett.* **105**(3), 036404 (2010). http://dx.doi.org/10.1103/PhysRevLett.105.036404.
[26] B. Yan, C.-X. Liu, H.-J. Zhang, C.-Y. Yam, X.-L. Qi, T. Frauenheim, and S.-C. Zhang. *EPL (Europhysics Lett.* **90**(3), 37002 (2010). http://dx.doi.org/10.1209/0295-5075/90/37002.
[27] Y. L. Chen, Z. K. Liu, J. G. Analytis, J.-H. Chu, H. J. Zhang, B. H. Yan, S.-K. Mo, R. G. Moore, D. H. Lu, I. R. Fisher, S. C. Zhang, Z. Hussain, and Z.-X. Shen. *Phys. Rev. Lett.* **105**(26), 266401 (2010). http://dx.doi.org/10.1103/PhysRevLett.105.266401.
[28] T. Sato, K. Segawa, H. Guo, K. Sugawara, S. Souma, T. Takahashi, and Y. Ando. *Phys. Rev. Lett.* **105**(13), 136802 (2010). http://dx.doi.org/10.1103/PhysRevLett.105.136802.
[29] W. Feng, D. Xiao, J. Ding, and Y. Yao. *Phys. Rev. Lett.* **106**(1), 016402 (2011). http://dx.doi.org/10.1103/PhysRevLett.106.016402.
[30] G. Jackeli and G. Khaliullin. *Phys. Rev. Lett.* **102**(1), 017205 (2009). http://dx.doi.org/10.1103/PhysRevLett.102.017205.
[31] A. Shitade, H. Katsura, J. Kuneš, X.-L. Qi, S.-C. Zhang, and N. Nagaosa. *Phys. Rev. Lett.* **102**(25), 256403 (2009). http://dx.doi.org/10.1103/PhysRevLett.102.256403.
[32] J. Chaloupka, G. Jackeli, and G. Khaliullin. *Phys. Rev. Lett.* **105**(2), 027204 (2010). http://dx.doi.org/10.1103/PhysRevLett.105.027204.
[33] D. Pesin and L. Balents. *Nat. Phys.* **6**(5), 376–381 (2010). http://dx.doi.org/10.1038/nphys1606.
[34] B.-J. Yang and Y. Kim. *Phys. Rev. B* **82**(8), 085111 (2010). http://dx.doi.org/10.1103/PhysRevB.82.085111.
[35] M. Kargarian, J. Wen, and G. Fiete. *Phys. Rev. B* **83**(16), 1–12 (2011). http://dx.doi.org/10.1103/PhysRevB.83.165112.
[36] C. H. Kim, H. S. Kim, H. Jeong, H. Jin, and J. Yu. *Phys. Rev. Lett.* **108**(10), 106401 (2012). http://dx.doi.org/10.1103/PhysRevLett.108.106401.
[37] H. Jin, S. H. Rhim, J. Im, and A. J. Freeman. *Sci. Rep.* **3** (2013). http://dx.doi.org/10.1038/srep01651.
[38] G. Trimarchi, X. Zhang, A. J. Freeman, and A. Zunger. *Phys. Rev. B* **90**(16), 161111 (2014). http://dx.doi.org/10.1103/PhysRevB.90.161111.
[39] Y. Singh and P. Gegenwart. *Phys. Rev. B* **82**(6), 064412 (2010). http://dx.doi.org/10.1103/PhysRevB.82.064412.
[40] X. Liu, T. Berlijn, W.-G. Yin, W. Ku, A. Tsvelik, Y.-J. Kim, H. Gretarsson, Y. Singh, P. Gegenwart, and J. P. Hill. *Phys. Rev. B* **83**(22), 220403 (2011). http://dx.doi.org/10.1103/PhysRevB.83.220403.
[41] F. Ye, S. Chi, H. Cao, B. C. Chakoumakos, J. A. Fernandez-Baca, R. Custelcean, T. F. Qi, O. B. Korneta, and G. Cao. *Phys. Rev. B* **85**(18), 180403 (2012). http://dx.doi.org/10.1103/PhysRevB.85.180403.

[42] S. K. Choi, R. Coldea, A. N. Kolmogorov, T. Lancaster, I. I. Mazin, S. J. Blundell, P. G. Radaelli, Y. Singh, P. Gegenwart, K. R. Choi, S.-W. Cheong, P. J. Baker, C. Stock, and J. Taylor. *Phys. Rev. Lett.* **108**(12), 127204 (2012). http://dx.doi.org/10.1103/PhysRevLett.108.127204.

[43] H. Kobayashi, M. Tabuchi, M. Shikano, H. Kageyama, and R. Kanno. *J. Mater. Chem.* **13**(4), 957–962 (2003). http://dx.doi.org/10.1039/b207282c.

[44] Y. Singh, S. Manni, J. Reuther, T. Berlijn, R. Thomale, W. Ku, S. Trebst, and P. Gegenwart. *Phys. Rev. Lett.* **108**(12), 127203 (2012). http://dx.doi.org/10.1103/PhysRevLett.108.127203.

[45] J. Reuther, R. Thomale, and S. Rachel. *Phys. Rev. B* **90**(10), 100405 (2014). http://dx.doi.org/10.1103/PhysRevB.90.100405.

[46] L. Fu and C. Kane. *Phys. Rev. B* **76**(4), 045302 (2007). http://dx.doi.org/10.1103/PhysRevB.76.045302.

[47] N. Alidoust, C. Liu, S.-Y. Xu, I. Belopolski, T. Qi, M. Zeng, M. Neupane, G. Bian, Y.-T. Liu, S. D. Wilson, H. Lin, A. Bansil, G. Cao, and M. Z. Hasan. *Arxiv Prepr.* pp. 1–16 (2014). 1410.6389, http://arxiv.org/abs/1410.6389v1.

[48] H.-S. Kim, C. H. Kim, H. Jeong, H. Jin, and J. Yu. *Phys. Rev. B* **87**(16), 165117 (2013). http://dx.doi.org/10.1103/PhysRevB.87.165117.

[49] J. Reuther, R. Thomale, and S. Trebst. *Phys. Rev. B* **84**(10), 100406 (2011). http://dx.doi.org/10.1103/PhysRevB.84.100406.

[50] G. Li, M. Pu, X. Du, Y. Zhang, H. Zhou, and Y. Zhao. *Phys. C Supercond.* **452**(1-2), 43–47 (2007). http://dx.doi.org/10.1016/j.physc.2006.12.001.

[51] Y. Zhao, M. Pu, G. Li, X. Du, H. Zhou, Y. Zhang, X. Yang, Y. Wang, R. Sun, and C. Cheng. *Phys. C Supercond. its Appl.* **463-465**, 574–579 (2007). http://dx.doi.org/10.1016/j.physc.2007.05.022.

[52] Y. Meiqiong, W. Xianhua, T. Yuancheng, and H. Junjun. *Chinese J. Vac. Sci. Technol.* **29**(5) (2009).

[53] G. Pollefeyt, S. Rottiers, P. Vermeir, P. Lommens, R. Hühne, K. De Buysser, and I. Van Driessche. *J. Mater. Chem. A* **1**(11), 3613 (2013). http://dx.doi.org/10.1039/c3ta00826f.

[54] F. Wang and T. Senthil. *Phys. Rev. Lett.* **106**(13), 136402 (2011). http://dx.doi.org/10.1103/PhysRevLett.106.136402.

[55] B. J. Kim, H. Jin, S. J. Moon, J. Y. Kim, B. G. Park, C. S. Leem, J. Yu, T. W. Noh, C. Kim, S. J. Oh, J. H. Park, V. Durairaj, G. Cao, and E. Rotenberg. *Phys. Rev. Lett.* **101**(7), 076402 (2008). http://dx.doi.org/10.1103/PhysRevLett.101.076402.

[56] B. Kim, H. Ohsumi, T. Komesu, S. Sakai, and T. Morita. *Science (80-.).* **323**(March), 1329–1332 (2009). http://www.sciencemag.org/content/323/5919/1329.short.

[57] X. Wan, A. M. Turner, A. Vishwanath, and S. Y. Savrasov. *Phys. Rev. B* **83**(20), 205101 (2011). http://dx.doi.org/10.1103/PhysRevB.83.205101.

[58] W. Witczak-Krempa and Y. B. Kim. *Phys. Rev. B* **85**(4), 045124 (2012). http://dx.doi.org/10.1103/PhysRevB.85.045124.

[59] J. P. Clancy, N. Chen, C. Y. Kim, W. F. Chen, K. W. Plumb, B. C. Jeon, T. W. Noh, and Y.-J. Kim. *Phys. Rev. B* **86**(19), 195131 (2012). http://dx.doi.org/10.1103/PhysRevB.86.195131.

[60] H. Gretarsson, J. P. Clancy, X. Liu, J. P. Hill, E. Bozin, Y. Singh, S. Manni, P. Gegenwart, J. Kim, A. H. Said, D. Casa, T. Gog, M. H. Upton, H. S. Kim, J. Yu, V. M. Katukuri, L. Hozoi, J. van den Brink, and Y. J. Kim. *Phys. Rev. Lett.* **110**(7), 076402 (2013). http://dx.doi.org/10.1103/PhysRevLett.110.076402.

[61] S. J. Moon, M. W. Kim, K. W. Kim, Y. S. Lee, J. Y. Kim, J. H. Park, B. J. Kim, S. J. Oh, S. Nakatsuji, Y. Maeno, I. Nagai, S. I. Ikeda, G. Cao, and T. W. Noh. *Phys. Rev. B* **74**(11), 113104 (2006). http://dx.doi.org/10.1103/PhysRevB.74.113104.

[62] I. I. Mazin, H. O. Jeschke, K. Foyevtsova, R. Valentí, and D. I. Khomskii. *Phys. Rev. Lett.* **109**(19), 197201 (2012). http://dx.doi.org/10.1103/PhysRevLett.109.197201.

[63] S. Bhattacharjee, S.-S. Lee, and Y. B. Kim. *New J. Phys.* **14**(7), 073015 (2012). http://dx.doi.org/10.1088/1367-2630/14/7/073015.

[64] X. Liu, V. M. Katukuri, L. Hozoi, W.-G. Yin, M. P. M. Dean, M. H. Upton, J. Kim, D. Casa, A. Said, T. Gog, T. F. Qi, G. Cao, A. M. Tsvelik, J. van den Brink, and J. P. Hill. *Phys. Rev. Lett.* **109**(15), 157401 (2012). http://dx.doi.org/10.1103/PhysRevLett.109.157401.

[65] A. Biffin, R. D. Johnson, S. Choi, F. Freund, S. Manni, A. Bombardi, P. Manuel, P. Gegenwart, and R. Coldea. *Phys. Rev. B* **90**(20), 205116 (2014). http://dx.doi.org/10.1103/PhysRevB.90.205116.

[66] T. Takayama, A. Kato, R. Dinnebier, J. Nuss, H. Kono, L. S. I. Veiga, G. Fabbris, D. Haskel, and H. Takagi. *Phys. Rev. Lett.* **114**(7), 077202 (2015). http://dx.doi.org/10.1103/PhysRevLett.114.077202.

[67] Y. Luo, C. Cao, B. Si, Y. Li, J. Bao, H. Guo, X. Yang, C. Shen, C. Feng, J. Dai, G. Cao, and Z.-a. Xu. *Phys. Rev. B* **87**(16), 161121 (2013). http://dx.doi.org/10.1103/PhysRevB.87.161121.

[68] C. Cao, Y. Luo, Z. Xu, and J. Dai. *Archive* pp. 2–6 (2013). 1303.4675, http://arxiv.org/abs/1303.4675.

[69] H.-S. Kim, V. S. V., A. Catuneanu, and H.-Y. Kee. *Phys. Rev. B* **91**(24), 241110 (2015). http://dx.doi.org/10.1103/PhysRevB.91.241110.

[70] S. Hwan Chun, J. J.-W. Kim, J. J.-W. Kim, H. Zheng, C. C. Stoumpos, C. D. Malliakas, J. F. Mitchell, K. Mehlawat, Y. Singh, Y. Choi, T. Gog, A. Al-Zein, M. M. Sala, M. Krisch, J. Chaloupka, G. Jackeli, G. Khaliullin, and B. J. Kim. *Nat. Phys.* **11**(6), 462–466 (2015). http://dx.doi.org/10.1038/nphys3322.

[71] H.-C. Jiang, Z.-C. Gu, X.-L. Qi, and S. Trebst. *Phys. Rev. B* **83**(24), 245104 (2011). http://dx.doi.org/10.1103/PhysRevB.83.245104.

[72] R. Comin, G. Levy, B. Ludbrook, Z. H. Zhu, C. N. Veenstra, J. A. Rosen, Y. Singh, P. Gegenwart, D. Stricker, J. N. Hancock, D. van der Marel, I. S. Elfimov, and A. Damascelli. *Phys. Rev. Lett.* **109**(26), 266406 (2012). http://dx.doi.org/10.1103/PhysRevLett.109.266406.

[73] J. Chaloupka, G. Jackeli, and G. Khaliullin. *Phys. Rev. Lett.* **110**(9), 097204 (2013). http://dx.doi.org/10.1103/PhysRevLett.110.097204.

[74] I. Kimchi and Y.-Z. You. *Phys. Rev. B* **84**(18), 2–5 (2011). http://dx.doi.org/10.1103/PhysRevB.84.180407.

[75] S. Manni, Y. Tokiwa, and P. Gegenwart. *Phys. Rev. B* **89**(24), 241102 (2014). http://dx.doi.org/10.1103/PhysRevB.89.241102.

[76] S. Das, E. J. Guo, and K. Roychowdhury. *Arxiv Prepr.* (2015). 1506.08279, http://arxiv.org/abs/1506.08279.

[77] G. Cao, T. F. Qi, L. Li, J. Terzic, V. S. Cao, S. J. Yuan, M. Tovar, G. Murthy, and R. K. Kaul. *Phys. Rev. B* **88**(22), 220414 (2013). http://dx.doi.org/10.1103/PhysRevB.88.220414.

[78] S. Manni, S. Choi, I. I. Mazin, R. Coldea, M. Altmeyer, H. O. Jeschke, R. Valentí, and P. Gegenwart. *Phys. Rev. B* **89**(24), 245113 (2014). http://dx.doi.org/10.1103/PhysRevB.89.245113.

[79] K. Rolfs, S. Toth, E. Pomjakushina, D. Sheptyakov, J. Taylor, and K. Conder. *Phys. Rev. B* **91**(18), 180406 (2015). http://dx.doi.org/10.1103/PhysRevB.91.180406.

[80] S. Nakatsuji, Y. Machida, Y. Maeno, T. Tayama, T. Sakakibara, J. Duijn, L. Balicas, J. Millican, R. Macaluso, and J. Chan. *Phys. Rev. Lett.* **96**(8), 087204 (2006). http://dx.doi.org/10.1103/PhysRevLett.96.087204.

[81] N. Taira, M. Wakeshima, and Y. Hinatsu. *J. Phys. Condens. Matter* **13**(23), 5527–5533 (2001). http://dx.doi.org/10.1088/0953-8984/13/23/312.

[82] M. C. Shapiro, S. C. Riggs, M. B. Stone, C. R. de la Cruz, S. Chi, a. a. Podlesnyak, and I. R. Fisher. *Phys. Rev. B* **85**(21), 214434 (2012). http://dx.doi.org/10.1103/PhysRevB.85.214434.

[83] H. Fukazawa and Y. Maeno. *J. Phys. Soc. Japan* **71**(10), 2578–2579 (2002). http://dx.doi.org/10.1143/JPSJ.71.2578.

[84] W. K. Zhu, M. Wang, B. Seradjeh, F. Yang, and S. X. Zhang. *Phys. Rev. B* **90**(5), 054419 (2014). http://dx.doi.org/10.1103/PhysRevB.90.054419.

[85] S. M. Disseler, C. Dhital, A. Amato, S. R. Giblin, C. de la Cruz, S. D. Wilson, and M. J. Graf. *Phys. Rev. B* **86**(1), 014428 (2012). http://dx.doi.org/10.1103/PhysRevB.86.014428.

[86] S. M. Disseler. *Phys. Rev. B* **89**(14), 140413 (2014). http://dx.doi.org/10.1103/PhysRevB.89.140413.

[87] D. Yanagishima and Y. Maeno. *J. Phys. Soc. Japan* **70**(10), 2880–2883 (2001). http://dx.doi.org/10.1143/JPSJ.70.2880.

[88] H. Liu, W. Tong, L. Ling, S. Zhang, R. Zhang, L. Zhang, L. Pi, C. Zhang, and Y. Zhang. *Solid State Commun.* **179**, 1–5 (2014). http://dx.doi.org/10.1016/j.ssc.2013.11.004.

[89] R. Singh, V. Medicherla, K. Maiti, and E. Sampathkumaran. *Phys. Rev. B* **77**(20), 201102 (2008). http://dx.doi.org/10.1103/PhysRevB.77.201102.

[90] P. D. Battle, C. R. A. Catlow, J. Drennan, and A. D. Murray. *J. Phys. C Solid State Phys.* **16**(17), L561–L566 (1983). http://dx.doi.org/10.1088/0022-3719/16/17/003.

[91] P. Battle, C. Catlow, J. Heap, and L. Moroney. *J. Solid State Chem.* **63**(1), 8–15 (1986). http://dx.doi.org/10.1016/0022-4596(86)90146-5.

[92] K. V. Kale, K. M. Jadhav, and G. K. Bichile. *J. Mater. Sci. Lett.* **18**(1), 9–11 (1999). http://dx.doi.org/10.1023/A:1006652705028.

[93] X. J. Zhang, W. T. Jin, S. J. Hao, Y. Zhao, and H. Zhang. *J. Supercond. Nov. Magn.* **23**(6), 1011–1014 (2010). http://dx.doi.org/10.1007/s10948-009-0615-1.

[94] R. de Putter. *Towards stochiometric growth of YBiO3 thin films using pulsed laser deposition: a plasma approach*. Master thesis, University of Twente (2014).

[95] M. Lorenz. *Gepulste Laser-Plasmaabscheidung (PLD) von oxidischen Dünnfilm- und Nanostrukturen*. Hablitiationsschrift, University of Leipzig (2008).

[96] J. Zippel. *Gepulste Laserabscheidung und Charakterisierung funktionaler oxidischer Dünnfilme und Heterostrukturen*. Dissertation, Universität Leipzig (2012).

[97] D. P. Norton. In *Pulsed Laser Depos. Thin Film. Appl. Growth Funct. Mater.*, edited by R. Eason, chap. 1, pp. 3–32, (Wiley-Interscience, 2007).

[98] D. Bäuerle. In *Landolt-Börnstein New Ser. VIII/1C*, edited by R. Poprawe, H. Weber, and G. Herziger, pp. 311–354, (Springer, Berlin, 2004).

[99] D. P. Norton, C. Park, J. D. Budai, S. J. Pennycook, and C. Prouteau. *Appl. Phys. Lett.* **74**(15), 2134 (1999). http://dx.doi.org/10.1063/1.123780.

[100] R. Riedel and I. W. Chen. *Ceramics Science and Technology, Synthesis and Processing*. Ceramics Science and Technology, (Wiley, 2011). ISBN 9783527311576.

[101] R. Orrù, R. Licheri, A. M. Locci, A. Cincotti, and G. Cao. *Mater. Sci. Eng. R Reports* **63**(4-6), 127–287 (2009). http://dx.doi.org/10.1016/j.mser.2008.09.003.
[102] J. Krizan, J. Roudebush, G. Fox, and R. Cava. *Mater. Res. Bull.* **52**, 162–166 (2014). http://dx.doi.org/10.1016/j.materresbull.2014.01.021.
[103] L. Spieß. *Moderne Röntgenbeugung: Röntgendiffraktometrie für Materialwissenschaftler, Physiker und Chemiker*, (Teubner, Wiesbaden, 2005). ISBN 3-519-00522-0.
[104] M. Grundmann. *Phys. status solidi* **248**(4), 805–824 (2011). http://dx.doi.org/10.1002/pssb.201046530.
[105] J. B. Nelson and D. P. Riley. *Proc. Phys. Soc.* **57**(3), 160–177 (1945). http://dx.doi.org/10.1088/0959-5309/57/3/302.
[106] T. Degen, M. Sadki, E. Bron, U. König, and G. Nénert. *Powder Diffr.* **29**(S2), S13–S18 (2014). http://dx.doi.org/10.1017/S0885715614000840.
[107] H. M. Rietveld. *J. Appl. Crystallogr.* **2**(2), 65–71 (1969). http://dx.doi.org/10.1107/S0021889869006558.
[108] M. Ladd and R. Palmer. *Structure Determination by X-ray Crystallography*, (Springer US, Boston, MA, 2013). ISBN 978-1-4614-3956-1. http://dx.doi.org/10.1007/978-1-4614-3954-7.
[109] R. A. Young, E. Prince, and R. A. Sparks. *J. Appl. Crystallogr.* **15**(3), 357–359 (1982). http://dx.doi.org/10.1107/S0021889882012138.
[110] R. J. Hill and R. X. Fischer. *J. Appl. Crystallogr.* **23**(6), 462–468 (1990). http://dx.doi.org/10.1107/S0021889890006094.
[111] G. Cicognani (Ed.). *The Yellow Book 2008. Guide to Neutron Research Facilities*. 1st ed., (Institut Laue-Langevin, Grenoble, 2008). www.ill.eu/instruments-support.
[112] Park Systems Corp. *XE-150 High Accuracy Large Sample SPM: User's Manual* (2009).
[113] D. Nečas and P. Klapetek. *Open Phys.* **10**(1) (2012). http://dx.doi.org/10.2478/s11534-011-0096-2.
[114] H. Fujiwara. *Spectrocopic ellipsometry: principles and applications*, (John Wiley & Sons, Chichester, England; Hoboken, NJ, 2007). ISBN 978-0-470-01608-4.
[115] J. A. Woolam Co. Inc. *Guide to Using WVASE32®* (2010).
[116] S. Adachi. *Phys. Rev. B* **35**(14), 7454–7463 (1987). http://dx.doi.org/10.1103/PhysRevB.35.7454.
[117] L. van der Pauw. *Philips Res. Reports* **13**, 1–9 (1958).
[118] National Instiute of Standards and Technology (NIST). *Resistivity and Hall measurements* (2010). http://www.nist.gov/pml/div683/hall_resistivity.cfm.
[119] J. Clarke and A. I. Braginski. *The SQUID Handbook. Vol. I: Fundamentals and Technology of SQUIDs and SQUID systems*, (WILEY-VCH Verlag, Weinheim, 2004). ISBN 3-527-40229-2.
[120] J. Clarke and A. I. Braginski (Eds.). *The SQUID Handbook. Vol. II: Applications of SQUIDs and SQUID systems*, (WILEY-VCH Verlag, Weinheim, 2005). ISBN 3-527-40408-2.
[121] M. J. O'Malley, H. Verweij, and P. M. Woodward. *J. Solid State Chem.* **181**(8), 1803–1809 (2008). http://dx.doi.org/10.1016/j.jssc.2008.04.005.
[122] Z. Alpichshev, F. Mahmood, G. Cao, and N. Gedik. *Phys. Rev. Lett.* **114**(1), 017203 (2015). http://dx.doi.org/10.1103/PhysRevLett.114.017203.

[123] M. Lorenz, E. Kaidashev, H. von Wenckstern, V. Riede, C. Bundesmann, D. Spemann, G. Benndorf, H. Hochmuth, A. Rahm, H.-C. Semmelhack, and M. Grundmann. *Solid. State. Electron.* **47**(12), 2205–2209 (2003). http://dx.doi.org/10.1016/S0038-1101(03)00198-9.

[124] J. Chen, H. Qin, F. Yang, J. Liu, T. Guan, F. Qu, G. Zhang, J. Shi, X. Xie, C. Yang, K. Wu, Y. Li, and L. Lu. *Phys. Rev. Lett.* **105**(17), 176602 (2010). http://dx.doi.org/10.1103/PhysRevLett.105.176602.

[125] J. Lee, J. Park, J.-H. Lee, J. S. Kim, and H.-J. Lee. *Phys. Rev. B* **86**(24), 245321 (2012). http://dx.doi.org/10.1103/PhysRevB.86.245321.

[126] N. F. Mott. *Philos. Mag.* **19**(160), 835–852 (1969). http://dx.doi.org/10.1080/14786436908216338.

[127] B. Shklovskii and A. Efros. *Electronic properties of doped semiconductors*, (Springer, Berlin ; Heidelberg ; New York ; Tokyo, 1984). http://adsabs.harvard.edu/abs/1979MoIzN....T....S.

[128] N. Arginskaya and V. Kozub. *Zh. Eksp. Teor. Fiz* **106**(3), 848–859 (1994). http://www.jetp.ac.ru/cgi-bin/dn/e_079_03_0466.pdf.

[129] N. Mott. *J. Non. Cryst. Solids* **1**(1), 1–17 (1968). http://dx.doi.org/10.1016/0022-3093(68)90002-1.

[130] V. Shante. *Phys. Lett. A* **43**(3), 249–250 (1973). http://dx.doi.org/10.1016/0375-9601(73)90292-2.

[131] C. Kittel and C. Y. Fong. *Quantum theory of solids <dt.>*. 2nd ed., (Oldenbourg Verlag, München, Wien, 1988). ISBN 3-486-20748-2.

[132] V. D. Kagan. *Sov. Phys. JETP* **48**(2), 277–281 (1978). http://www.jetp.ac.ru/cgi-bin/dn/e_048_02_0277.pdf.

[133] V. K. Arora. *Phys. Rev. B* **26**(12), 7046–7048 (1982). http://dx.doi.org/10.1103/PhysRevB.26.7046.

[134] M. Ge, T. F. Qi, O. B. Korneta, D. E. De Long, P. Schlottmann, W. P. Crummett, and G. Cao. *Phys. Rev. B* **84**(10), 100402 (2011). http://dx.doi.org/10.1103/PhysRevB.84.100402.

[135] C. Wang, H. Seinige, G. Cao, J.-S. Zhou, J. B. Goodenough, and M. Tsoi. *Phys. Rev. X* **4**(4), 041034 (2014). http://dx.doi.org/10.1103/PhysRevX.4.041034.

[136] G. E. Jellison, L. A. Boatner, D. H. Lowndes, R. A. McKee, and M. Godbole. *Appl. Opt.* **33**(25), 6053–6058 (1994). http://dx.doi.org/10.1364/AO.33.006053.

[137] G. E. Jellison and F. A. Modine. *Appl. Phys. Lett.* **69**(3), 371 (1996). http://dx.doi.org/10.1063/1.118064.

[138] H. Yoshikawa and S. Adachi. *Jpn. J. Appl. Phys.* **36**(Part 1, No. 10), 6237–6243 (1997). http://dx.doi.org/10.1143/JJAP.36.6237.

[139] J. Kim, D. Casa, M. H. Upton, T. Gog, Y.-J. Kim, J. F. Mitchell, M. van Veenendaal, M. Daghofer, J. van den Brink, G. Khaliullin, and B. J. Kim. *Phys. Rev. Lett.* **108**(17), 177003 (2012). http://dx.doi.org/10.1103/PhysRevLett.108.177003.

[140] S. J. Moon, H. Jin, K. W. Kim, W. S. Choi, Y. S. Lee, J. Yu, G. Cao, A. Sumi, H. Funakubo, C. Bernhard, and T. W. Noh. *Phys. Rev. Lett.* **101**(22), 226402 (2008). http://dx.doi.org/10.1103/PhysRevLett.101.226402.

[141] H. R. Hoekstra and K. A. Gingerich. *Science (80-.).* **146**(3648), 1163–1164 (1964). http://dx.doi.org/10.1126/science.146.3648.1163.

[142] T. C. Fujita, Y. Kozuka, M. Uchida, A. Tsukazaki, T. Arima, and M. Kawasaki. *Sci. Rep.* **5**, 9711 (2015). http://dx.doi.org/10.1038/srep09711.

[143] J.-H. Chu, S. C. Riggs, M. Shapiro, J. Liu, C. R. Serero, D. Yi, M. Melissa, S. J. Suresha, C. Frontera, A. Vishwanath, X. Marti, I. R. Fisher, and R. Ramesh. *arXiv Prepr.* (111), 3–8 (2013). 1309.4750, http://arxiv.org/abs/1309.4750.

[144] J. J. Ishikawa, E. C. T. O'Farrell, and S. Nakatsuji. *Phys. Rev. B* **85**(24), 245109 (2012). http://dx.doi.org/10.1103/PhysRevB.85.245109.

[145] S. Bueble, K. Knorr, E. Brecht, and W. W. Schmahl. *Surf. Sci.* **400**(1-3), 345–355 (1998). http://dx.doi.org/10.1016/S0039-6028(97)00891-1.

[146] B. C. Chakoumakos, D. G. Schlom, M. Urbanik, and J. Luine. *J. Appl. Phys.* **83**(4), 1979 (1998). http://dx.doi.org/10.1063/1.366925.

[147] Z. Zhang, X. Feng, M. Guo, Y. Ou, J. Zhang, K. Li, L. Wang, X. Chen, Q. Xue, X. Ma, K. He, and Y. Wang. *Phys. status solidi - Rapid Res. Lett.* **3**, n/a–n/a (2010). http://dx.doi.org/10.1002/pssr.201206391.

[148] M. Grundmann, T. Böntgen, and M. Lorenz. *Phys. Rev. Lett.* **105**(14), 146102 (2010). http://dx.doi.org/10.1103/PhysRevLett.105.146102.

[149] G. Koster, G. J. H. M. Rijnders, D. H. A. Blank, and H. Rogalla. *Appl. Phys. Lett.* **74**(24), 3729 (1999). http://dx.doi.org/10.1063/1.123235.

[150] B. Johs and J. S. Hale. *Phys. status solidi* **205**(4), 715–719 (2008). http://dx.doi.org/10.1002/pssa.200777754.

[151] P. Y. Yu and M. Cardona. *Fundamentals of Semiconductors*. 4th ed. Graduate Texts in Physics, (Springer Berlin Heidelberg, Berlin, Heidelberg, 2010). ISBN 978-3-642-00709-5. http://dx.doi.org/10.1007/978-3-642-00710-1.

[152] J. P. Perdew. *Int. J. Quantum Chem.* **28**(S19), 497–523 (2009). http://dx.doi.org/10.1002/qua.560280846.

[153] H. T. Fan, S. S. Pan, X. M. Teng, C. Ye, and G. H. Li. *J. Phys. D. Appl. Phys.* **39**(9), 1939–1943 (2006). http://dx.doi.org/10.1088/0022-3727/39/9/032.

[154] S. Zhang and R. Xiao. *J. Appl. Phys.* **83**(7), 3842 (1998). http://dx.doi.org/10.1063/1.366615.

Own and contributed work

[MJ1] M. Jenderka, J. Barzola-Quiquia, Z. Zhang, H. Frenzel, M. Grundmann, and M. Lorenz. *Phys. Rev. B* **88**(4), 045111 (2013). http://dx.doi.org/10.1103/PhysRevB.88.045111.

[MJ2] M. Jenderka. *Growth and Properties of Na2IrO3 Thin Films*. Master thesis, Universität Leipzig (2012). http://nbn-resolving.de/urn:nbn:de:bsz:15-qucosa-201974.

[MJ3] M. Jenderka, R. Schmidt-Grund, M. Grundmann, and M. Lorenz. *J. Appl. Phys.* **117**(2), 025304 (2015). http://dx.doi.org/10.1063/1.4905790.

[MJ4] M. Lorenz, H. Hochmuth, M. Kneiß, M. Bonholzer, M. Jenderka, and M. Grundmann. *Semicond. Sci. Technol.* **30**(2), 024003 (2015). http://dx.doi.org/10.1088/0268-1242/30/2/024003.

[MJ5] C. Kranert, J. Lenzner, M. Jenderka, M. Lorenz, H. von Wenckstern, R. Schmidt-Grund, and M. Grundmann. *J. Appl. Phys.* **116**(1), 013505 (2014). http://dx.doi.org/10.1063/1.4886895.

[MJ6] C. Kranert, M. Jenderka, J. Lenzner, M. Lorenz, H. von Wenckstern, R. Schmidt-Grund, and M. Grundmann. *J. Appl. Phys.* **117**(12), 125703 (2015). http://dx.doi.org/10.1063/1.4915627.

[MJ7] M. Kneiß, M. Jenderka, K. Brachwitz, M. Lorenz, and M. Grundmann. *Appl. Phys. Lett.* **105**(6), 062103 (2014). http://dx.doi.org/10.1063/1.4892811.

[MJ8] H. Wei, M. Jenderka, M. Bonholzer, M. Grundmann, and M. Lorenz. *Appl. Phys. Lett.* **106**(4), 042103 (2015). http://dx.doi.org/10.1063/1.4907011.

[MJ9] H. Wei, M. Jenderka, M. Grundmann, and M. Lorenz. *Phys. status solidi* **212**(9), 1925–1930 (2015). http://dx.doi.org/10.1002/pssa.201431695.

A Appendix

A.1 List of samples

Table A.1 List of all samples fabricated by pulsed laser deposition during the doctoral research. Square substrate dimensions are given in mm^2; $\varnothing$ denotes the diameter of circular wafers. T is the heater temperature prior to deposition and P is the corresponding heater power. Growth temperature T_g is estimated via $T - 50$ °C. Deposition processes involving more than one target are indicated by a "+". Abbreviations: p_{O2} oxygen partial pressure, ps: laser pulses, YSZ: ZrO_2:Y, YAO: $YAlO_3$, GZO: ZnO:Ga(4 at%).

Sample ID	**Substrate**	**Epilayer**	p_{O2} **(mbar)**	T **(°C),** P **(W)**	**Steps [ps/freq. (Hz)]**
E3313	*c*-Al_2O_3 5×5	Na_2IrO_3	0.016	-, 400	300/1, 30000/15
E3437	*a*-Al_2O_3 10×10	Na_2IrO_3	3×10^{-4}	600, 400	300/1, 30000/15
E3438	*a*-Al_2O_3 10×10	Na_2IrO_3	3×10^{-4}	600, 400	300/1, 30000/15
E3439	*a*-Al_2O_3 10×10	Na_2IrO_3	3×10^{-4}	600, 400	300/1, 30000/15
E3440	*a*-Al_2O_3 10×10	Na_2IrO_3	3×10^{-4}	600, 400	300/1, 30000/15
E3441	*a*-Al_2O_3 10×10	Na_2IrO_3	3×10^{-4}	600, 400	300/1, 30000/10
E3442	*a*-Al_2O_3 10×10	Na_2IrO_3	0.016	-, 400	300/1, 30000/15
E3443	*a*-Al_2O_3 10×10	Na_2IrO_3	3×10^{-4}	-, 400	300/1, 20000/2
E3458	*a*-Al_2O_3 10×10	Li_2IrO_3	0.016	600, 400	300/1, 30000/15
E3466	*c*-Al_2O_3 10×10	Li_2IrO_3	0.016	605, 400	300/1, 30000/15
E3468	YSZ(001) 10×10	Li_2IrO_3	0.016	608, 400	300/1, 30000/15
E3469	YAO(010) 10×10	Li_2IrO_3	0.016	605, 400	300/1, 30000/15
E3470	*a*-Al_2O_3 10×10	Li_2IrO_3	3×10^{-4}	603, 400	300/1, 30000/15
E3474	*a*-Al_2O_3 10×10	Li_2IrO_3	0.1	-, 400	300/1, 30000/15
E3485	YSZ(001) 10×10	Li_2IrO_3	3×10^{-4}	-, 600	300/1, 30000/15
E3486	*a*-Al_2O_3 10×10	Li_2IrO_3	3×10^{-4}	-, 550	300/1, 30000/15
E3488	YSZ(001) 10×10	Li_2IrO_3	3×10^{-4}	-, 500	300/1, 30000/15
E3489	*a*-Al_2O_3 10×10	Li_2IrO_3	3×10^{-4}	-, 500	300/1, 15000/15
E3491	*a*-Al_2O_3 10×10	Li_2IrO_3	3×10^{-4}	-, 500	300/1, 30000/15
E3492	*a*-Al_2O_3 10×10	Li_2IrO_3	3×10^{-4}	-, 500	300/1, 7500/15
E3494	*a*-Al_2O_3 10×10	Li_2IrO_3	3×10^{-4}	-, 500	300/1, 5000/15
E3495	*a*-Al_2O_3 10×10	Li_2IrO_3	3×10^{-4}	-, 300	1000/1, 12000/10, 1000/1, 12000/10
E3500	*a*-Al_2O_3 10×10	Li_2IrO_3	3×10^{-4}	-, 500	300/1, 3000/15
E3501	*a*-Al_2O_3 10×10	Li_2IrO_3	3×10^{-4}	-, 500	300/1, 30000/15
E3506	*a*-Al_2O_3 10×10	Li_2IrO_3	3×10^{-4}	-, 200	300/1, 30000/15
E3507	*a*-Al_2O_3 10×10	Li_2IrO_3	3×10^{-4}	-, 200	1000/1, 12000/10, 1000/1, 12000/10
E3508	*a*-Al_2O_3 5×5	Li_2IrO_3	3×10^{-4}	-, 500	300/1, 30000/15
E3509	*a*-Al_2O_3 5×5	Li_2IrO_3	3×10^{-4}	-, 500	300/1, 30000/15

(Continued on next page)

Table A.1 (Continued) List of all samples fabricated by pulsed laser deposition during the doctoral research. Square substrate dimensions are given in mm^2; ∅ denotes the diameter of circular wafers. T is the heater temperature prior to deposition and P is the corresponding heater power. Growth temperature T_g is estimated via $T - 50$ °C. Deposition processes involving more than one target are indicated by a "+". Abbreviations: p_{O2} oxygen partial pressure, ps: laser pulses, YSZ: ZrO_2:Y, YAO: $YAlO_3$, GZO: ZnO:Ga(4 at%).

Sample ID	Substrate	Epilayer	p_{O2} (mbar)	T (°C), P (W)	Steps [ps/freq. (Hz)]
E3510	*a*-Al_2O_3 10 × 10	Li_2IrO_3	3×10^{-4}	-, 500	300/1, 15000/15
E3511	*a*-Al_2O_3 5 × 5	Li_2IrO_3	3×10^{-4}	-, 500	300/1, 30000/15
E3512	*a*-Al_2O_3 5 × 5	Li_2IrO_3	3×10^{-4}	-, 500	300/1, 30000/15
E3513	*a*-Al_2O_3 5 × 5	Li_2IrO_3	3×10^{-4}	-, 500	300/1, 30000/15
E3524	*a*-Al_2O_3 10 × 10	Li_2IrO_3	3×10^{-4}	-, 500	300/1, 45000/15
E3525	*a*-Al_2O_3 5 × 5	Li_2IrO_3	3×10^{-4}	664, 500	300/1, 45000/15
E3549	*a*-Al_2O_3 10 × 10	Na_2IrO_3	3×10^{-4}	-, 400	300/1, 30000/15
E3555	YAO(010) 10 × 10	Li_2IrO_3	3×10^{-4}	-, 500	300/1, 30000/15
E3556	YAO(010) 10 × 10	Li_2IrO_3	3×10^{-4}	-, 500	300/1, 30000/15
E3557	YSZ(001) 10 × 10	$Y_2Ir_2O_3$	3×10^{-4}	-, 400	300/1, 30000/15
E3558	YSZ(001) 10 × 10	$Y_2Ir_2O_3$	3×10^{-4}	-, 500	300/1, 30000/15
E3559	YSZ(001) 10 × 10	$Y_2Ir_2O_3$	0.016	-, 400	300/1, 60000/15
E3560	*a*-Al_2O_3 10 × 10	Li_2IrO_3	3×10^{-4}	-, 500	300/1, 30000/15
E3564	YSZ(001) 10 × 10	$Y_2Ir_2O_3$	0.016	-, 400	300/1, 30000/15
E3565	*a*-Al_2O_3 10 × 10	Na_2IrO_3	3×10^{-4}	-, 400	300/1, 30000/15
E3566	YSZ(001) 10 × 10	$Y_2Ir_2O_3$	3×10^{-4}	728, 600	300/1, 40000/15
E3571	*a*-Al_2O_3 10 × 10	$Y_2Ir_2O_3$	0.1	-, 400	300/1, 30000/15
E3581	YSZ(001) 10 × 10	Li_2IrO_3	3×10^{-4}	-, 500	300/1, 30000/15
E3582	YSZ(001) 10 × 10	$Y_2Ir_2O_3$	3×10^{-4}	-, 400	5000/1
E3583	YSZ(001) 10 × 10	Li_2IrO_3	3×10^{-4}	-, 500	300/1, 30000/15
E3585	YSZ(001) 10 × 10	Li_2IrO_3	3×10^{-4}	-, 500	300/1, 30000/15
E3596	YSZ(001) 5 × 5	Li_2IrO_3	3×10^{-4}	-, 500	300/1, 30000/15
E3622	YSZ(001) 10 × 10	Li_2IrO_3	3×10^{-4}	-, 500	300/1, 30000/15
E3623	YAO(011) 10 × 10	Li_2IrO_3	3×10^{-4}	664, 500	300/1, 30000/15
E3643	*a*-Al_2O_3 10 × 10	$Y_2Ir_2O_3$	0.1	, 400	300/1, 30000/10
E3644	*a*-Al_2O_3 10 × 10	$Y_2Ir_2O_3$	3×10^{-4}	604, 400	300/7, 30000/10
E3648	*a*-Al_2O_3 10 × 10	$Y_2Ir_2O_3$	3×10^{-4}	, 600	300/7, 30000/15
E3649	YSZ(002) 10 × 10	$Y_2Ir_2O_3$	0.1	603, 400	300/7, 30000/15
E3652	YSZ(111) 10 × 10	$Y_2Ir_2O_3$,	0.066	, 400	300/7, 30000/15
E3657	*a*-Al_2O_3 10 × 10	$Y_2Ir_2O_3$,	0.1	, 400	300/1, 30000/15
E3664	YSZ(001) 5 × 5	Li_2IrO_3	3×10^{-4}	, 500	300/1, 45000/15
E3675	*a*-Al_2O_3 10 × 10	Li_2IrO_3	3×10^{-4}	622, 500	300/1, 30000/15
E3687	YSZ(001) 10 × 10	$Y_2Ir_2O_3$	3×10^{-4}	-, 400	300/1, 30000/15
E3701	YSZ(111) 10 × 10	$Y_2Ir_2O_3$	0.025	-, 600	300/1, 50000/10
E3738	*a*-Al_2O_3 10 × 10	Li_2IrO_3	3×10^{-4}	575, 400	300/1, 30000/15
E3739	*a*-Al_2O_3 10 × 10	Li_2IrO_3	3×10^{-4}	601, 550	300/1, 30000/15

(Continued on next page)

Table A.1 (Continued) List of all samples fabricated by pulsed laser deposition during the doctoral research. Square substrate dimensions are given in mm^2; ∅ denotes the diameter of circular wafers. T is the heater temperature prior to deposition and P is the corresponding heater power. Growth temperature T_g is estimated via $T - 50$ °C. Deposition processes involving more than one target are indicated by a "+". Abbreviations: p_{O2} oxygen partial pressure, ps: laser pulses, YSZ: ZrO_2:Y, YAO: $YAlO_3$, GZO: ZnO:Ga(4 at%).

Sample ID	**Substrate**	**Epilayer**	p_{O2} **(mbar)**	T (°C), P **(W)**	**Steps [ps/freq. (Hz)]**
E3752	*a*-Al_2O_3 5 × 5	Li_2IrO_3	3×10^{-4}	-, 400	300/1, 45000/15
E3753	YSZ(001) 10 × 10	Li_2IrO_3	3×10^{-4}	-, 500	300/1, 30000/15
E3767	*a*-Al_2O_3 10 × 10	Na_2IrO_3	3×10^{-4}	-, 400	300/1, 30000/15
E3768	YAO(001) 10 × 10	Na_2IrO_3	3×10^{-4}	-, 400	300/1, 30000/15
E3769	YAO(001) 10 × 10	Na_2IrO_3	3×10^{-4}	-, 400	300/1, 30000/15
E3774	*r*-Al_2O_3 10 × 10	Na_2IrO_3	3×10^{-4}	-, 400	300/1, 30000/15
E3775	*c*-Al_2O_3 10 × 10	Na_2IrO_3	3×10^{-4}	-, 400	300/1, 30000/15
E3776	*a*-Al_2O_3 ∅ 2”	Na_2IrO_3	0.016	-, 400	300/1, 50000/15
E3777	*c*-ZnO 10 × 10	Na_2IrO_3	3×10^{-4}	-, 400	300/1, 30000/15
E3778	*c*-Al_2O_3 ∅ 2”	Na_2IrO_3	0.016	-,400	300/1, 50000/15
E3781	*c*-Al_2O_3 10 × 10	Na_2IrO_3	3×10^{-4}	-, 400	300/1, 30000/15
E3782	*c*-Al_2O_3 10 × 10	Na_2IrO_3	3×10^{-4}	-, 400	300/1, 30000/15
E3783	*c*-Al_2O_3 10 × 10	Na_2IrO_3	3×10^{-4}	-, 400	300/1, 30000/15
E3784	*c*-Al_2O_3 10 × 10	Na_2IrO_3	3×10^{-4}	-, 400	300/1, 30000/15
E3786	*a*-Al_2O_3 ∅ 2”	Li_2IrO_3	0.016	-, 500	300/1, 50000/15
E3791	YSZ(001) 10 × 10 (5° miscut to (100))	Na_2IrO_3	3×10^{-4}	-, 400	300/1, 50000/15
E3792	YSZ(001) 10 × 10	Na_2IrO_3	3×10^{-4}	-, 400	300/1, 50000/15
E3809	YSZ(001) 10 × 10	$YBiO_3$	0.04	-, 400	300/1, 30000/15
E3810	MgO(100) 10 × 10	$YBiO_3$	0.04	-, 400	300/1, 30000/15
E3812	$LAlO_3$(001) 10 × 10	$YBiO_3$	0.04	-, 400	300/1, 30000/15
E3813	$LAlO_3$(001) 10 × 10	$YBiO_3$	0.04	-, 400	300/1, 30000/15
E3815	$LAlO_3$(001) 5 × 5	$YBiO_3$	0.1	-, 400	300/1, 30000/15
E3816	$LAlO_3$(001) 5 × 5	$YBiO_3$	0.002	-, 400	300/1, 30000/15
E3817	$LAlO_3$(001) 5 × 5	$YBiO_3$	3×10^{-4}	-, 400	300/1, 30000/15
E3818	$LAlO_3$(001) 5 × 5	$YBiO_3$	0.04	-, 400	300/1, 30000/15
E3819	$LAlO_3$(001) 5 × 5	$YBiO_3$	0.01	607, 400	300/1, 30000/15
E3820	$LAlO_3$(001) 5 × 5	$YBiO_3$	0.006	-, 400	300/1, 30000/15
E3821	$LAlO_3$(001) 5 × 5	$YBiO_3$	0.002	-, 400	300/1, 30000/15
E3822	$LAlO_3$(001) 5 × 5	$YBiO_3$	0.002	640, 450	300/1, 30000/15
E3823	$LAlO_3$(001) 5 × 5	$YBiO_3$	0.002	660, 500	300/1, 30000/15
E3824	$LAlO_3$(001) 5 × 5	$YBiO_3$	0.002	650, 550	300/1, 30000/15
E3825	$LAlO_3$(001) 5 × 5	$YBiO_3$	0.002	-, 600	300/1, 30000/15
E3829	$LAlO_3$(001) 5 × 5	$YBiO_3$	0.05	-, 400	300/1, 15000/8
E3830	$LAlO_3$(001) 5 × 5	$YBiO_3$	0.05	-, 400	300/1, 15000/8
E3831	$LAlO_3$(001) 5 × 5	$YBiO_3$	0.05	-, 400	300/1, 15000/8

(Continued on next page)

Table A.1 (Continued) List of all samples fabricated by pulsed laser deposition during the doctoral research. Square substrate dimensions are given in mm^2; ∅ denotes the diameter of circular wafers. T is the heater temperature prior to deposition and P is the corresponding heater power. Growth temperature T_g is estimated via $T - 50$ °C. Deposition processes involving more than one target are indicated by a "+". Abbreviations: p_{O2} oxygen partial pressure, ps: laser pulses, YSZ: ZrO_2:Y, YAO: $YAlO_3$, GZO: ZnO:Ga(4 at%).

Sample ID	**Substrate**	**Epilayer**	p_{O2} **(mbar)**	T **(°C),** P **(W)**	**Steps [ps/freq. (Hz)]**
E3832	$LAlO_3$(001) 5×5	$YBiO_3$	0.05	-, 400	300/1, 15000/8
E3833	$LAlO_3$(001) 5×5	$YBiO_3$	0.05	-, 400	300/1, 15000/8
E3834	*a*-Al_2O_3 ∅ 2"	$YBiO_3$	0.05	-, 400	300/1, 15000/8
E3835	*a*-Al_2O_3 10×10	Na_2IrO_3	0.016	602, 400	300/1, 30000/15
E3836	$LAlO_3$(001) 5×5	$YBiO_3$	0.05	-, 400	300/1, 3750/8
E3837	$LAlO_3$(001) 5×5	$YBiO_3$	0.05	600, 400	300/1, 7500/8
E3838	$LAlO_3$(001) 5×5	$YBiO_3$	0.05	600, 400	300/1, 1875/8
E3839	$LAlO_3$(001) 5×5	$YBiO_3$	0.05	600, 400	300/1, 15000/8
E3840	*c*-Al_2O_3 ∅ 1,5"	Na_2IrO_3	0.016	600, 400	300/1, 60000/15
E3841	*c*-Al_2O_3 ∅ 1,5"	Na_2IrO_3	0.016	600, 400	300/1, 60000/15
E3842	*c*-Al_2O_3 ∅ 1,5"	Na_2IrO_3	0.016	600, 400	300/1, 60000/15
E3859	*a*-Al_2O_3 ∅ 2"	Na_2IrO_3	0.016	-, 400	300/1, 60000/15
E3860	*a*-Al_2O_3 ∅ 2"	Na_2IrO_3	0.1	580, 400	300/1, 30000/15
E3861	*a*-Al_2O_3 ∅ 2"	Na_2IrO_3	0.016	591, 400	300/1, 30000/15
E3862	*a*-Al_2O_3 ∅ 2"	Na_2IrO_3	0.002	594, 400	300/1, 30000/15
E3863	*a*-Al_2O_3 ∅ 2"	Na_2IrO_3	3×10^{-4}	580, 400	300/1, 30000/15
E3864	*a*-Al_2O_3 ∅ 2"	Na_2IrO_3	0.1	584, 400	300/1, 3000/15
E3865	*a*-Al_2O_3 ∅ 2"	Na_2IrO_3	0.1	607, 450	300/1, 3000/15
E3866	*a*-Al_2O_3 ∅ 2"	Na_2IrO_3	0.1	831, 500	300/1, 3000/15
E3867	*a*-Al_2O_3 ∅ 2"	Na_2IrO_3	0.1	623, 550	300/1, 3000/15
E3868	*a*-Al_2O_3 ∅ 2"	Na_2IrO_3	0.1	633, 600	300/1, 3000/15
E3869	*a*-Al_2O_3 ∅ 2"	Na_2IrO_3	0.16	395, 400	300/1, 30000/15
E3870	*a*-Al_2O_3 ∅ 2"	Na_2IrO_3	0.16	395, 450	300/1, 30000/15
E3871	*a*-Al_2O_3 ∅ 2"	Na_2IrO_3	0.16	-, 450	300/1, 30000/15
E3872	*a*-Al_2O_3 ∅ 2"	Na_2IrO_3	0.16	603, 500	300/1, 30000/15
E3873	*a*-Al_2O_3 ∅ 2"	Na_2IrO_3	0.16	617, 500	300/1, 30000/15
E3874	*a*-Al_2O_3 ∅ 2"	Na_2IrO_3	0.16	620, 550	300/1, 30000/15
E3875	*a*-Al_2O_3 ∅ 2"	Na_2IrO_3	0.16	520, 600	300/1, 30000/15
E3876	*a*-Al_2O_3 ∅ 2"	Na_2IrO_3	0.002	-, 400	300/1, 30000/1
E3877	*a*-Al_2O_3 ∅ 1,5"	Na_2IrO_3	0.016	639, 450	300/1, 50000/15
E3878	*a*-Al_2O_3 ∅ 1,5"	Na_2IrO_3	0.016	632, 450	300/1, 50000/15
E3879	*a*-Al_2O_3 ∅ 1,5"	Na_2IrO_3	0.016	632, 450	300/1, 50000/15
E3880	*a*-Al_2O_3 ∅ 1,5"	Na_2IrO_3	0.016	626, 450	300/1, 50000/15
E3881	*a*-Al_2O_3 ∅ 1,5"	Na_2IrO_3	0.016	632, 450	300/1, 50000/15
E3882	*a*-Al_2O_3 ∅ 1,5"	Na_2IrO_3	0.016	630, 450	300/1, 50000/15
E3883	*a*-Al_2O_3 ∅ 1,5"	Na_2IrO_3	0.016	632, 450	300/1, 50000/15

(Continued on next page)

Table A.1 (Continued) List of all samples fabricated by pulsed laser deposition during the doctoral research. Square substrate dimensions are given in mm^2; ∅ denotes the diameter of circular wafers. T is the heater temperature prior to deposition and P is the corresponding heater power. Growth temperature T_g is estimated via $T - 50$ °C. Deposition processes involving more than one target are indicated by a "+". Abbreviations: p_{O2} oxygen partial pressure, ps: laser pulses, YSZ: ZrO_2:Y, YAO: $YAlO_3$, GZO: ZnO:Ga(4 at%).

Sample ID	**Substrate**	**Epilayer**	p_{O2} **(mbar)**	T (°C), P **(W)**	**Steps [ps/freq. (Hz)]**
E3884	*a*-Al_2O_3 ∅ 1,5"	Na_2IrO_3	0.016	-, 450	300/1, 50000/15
E3885	*a*-Al_2O_3 ∅ 1,5"	Na_2IrO_3	0.016	-, 450	300/1, 50000/15
E3886	*a*-Al_2O_3 ∅ 1,5"	Na_2IrO_3	0.016	-, 450	300/1, 50000/15
E3887	*a*-Al_2O_3 ∅ 1,5"	Na_2IrO_3	0.016	639, 450	300/1, 50000/15
E3901	*a*-Al_2O_3 ∅ 1,5"	Na_2IrO_3	0.016	-, 450	300/1, 30000/15
E3909	ZnO:Al(1 at%) (W3205)	Na_2IrO_3	0.016	-, 450	300/1, 10000/15
E3912	Ti:N on MgO(100) 10 × 10	Na_2IrO_3	0.016	-, 450	300/1, 30000/15
E3913	ZnO:Al(1 at%) + ZnO (W3238)	Na213	0.016	-, 450	300/1, 30000/15
E3915	ZnO:Al(1 at%) + ZnO (W3247)	Na213	0.016	-, 450	300/1, 30000/15
E3920	*c*-Al_2O_3 10 × 10	GZO	0.2	411, 250	300/1, 10000/5
E3921	*c*-Al_2O_3 10 × 10	GZO + Na_2IrO_3	0.2	443, 230	300/1, 10000/15 + 300/1, 15000/15
E3922	*c*-Al_2O_3 10 × 10	GZO	0.002	-, 300	300/1, 10000/15
E3925	*c*-Al_2O_3 10 × 10	ZnO + Na_2IrO_3	0.002 + 0.016	-, 450	300/1, 2500/15 + 300/1, 1500/15
E3926	*c*-Al_2O_3 10 × 10	ZnO + Li_2IrO_3	0.002 + 0.016	-, 450	300/1, 2500/15 + 300/1, 1500/15
E3927	*a*-Al_2O_3 10 × 10	GZO + Na_2IrO_3	0.01	-, 450	300/1, 10000/15 + 300/1, 10000/15
E3928	E3927	GZO	0.01	-, 450	300/1, 10000/15
E3929	$LAlO_3$(001) 10 × 10	$YBiO_3$	0.05	-, 400	300/1, 1875/8
E3930	$LAlO_3$(001) 10 × 10	$YBiO_3$	0.05	-, 400	300/1, 1200/8
E3931	$LAlO_3$(001) 10 × 10	$YBiO_3$	0.05	-, 400	300/1, 600/8
E3932	$LAlO_3$(001) 10 × 10	$YBiO_3$	0.05	-, 400	300/1,
E3933	$LAlO_3$(001) 5 × 5	$YBiO_3$	0.05	-, 400	300/1, 1875/8
E3934	$LAlO_3$(001) 5 × 5	$YBiO_3$	0.05	-, 400	300/1, 1200/8
E3935	$LAlO_3$(001) 5 × 5	$YBiO_3$	0.05	-, 400	300/1, 600/8
E3936	$LAlO_3$(001) 5 × 5	$YBiO_3$	0.05	-, 400	300/1,
E3937	$LAlO_3$(001) 5 × 5	$YBiO_3$	0.05	-, 600	300/1, 600/8
E3940	$LAlO_3$(001) 5 × 5	$YBiO_3$	0.05	-, 600	300/1, 1875/15
E3941	$LAlO_3$(001) 5 × 5	$YBiO_3$	0.05	-, 600	300/1, 1200/15
E3942	$LAlO_3$(001) 5 × 5	$YBiO_3$	0.05	-, 600	300/1, 600/15

(Continued on next page)

Table A.1 (Continued) List of all samples fabricated by pulsed laser deposition during the doctoral research. Square substrate dimensions are given in mm^2; ∅ denotes the diameter of circular wafers. T is the heater temperature prior to deposition and P is the corresponding heater power. Growth temperature T_g is estimated via $T - 50$ °C. Deposition processes involving more than one target are indicated by a "+". Abbreviations: p_{O2} oxygen partial pressure, ps: laser pulses, YSZ: ZrO_2:Y, YAO: $YAlO_3$, GZO: ZnO:Ga(4 at%).

Sample ID	**Substrate**	**Epilayer**	p_{O2} **(mbar)**	T **(°C),** P **(W)**	**Steps [ps/freq. (Hz)]**
E3954	$LaAlO_3$(001) 5 × 5	$YBiO_3$	0.05	-, 600	300/1, 600/15
E3955	$LaAlO_3$(001) 5 × 5	$YBiO_3$	0.05	-, 200	300/1, 600/15
E3956	$LaAlO_3$(001) 5 × 5	$YBiO_3$	0.05	-, 400	300/1, 600/15
E3959	$LaAlO_3$(001) 5 × 5	$YBiO_3$	0.05	-, 400	300/1, 600/4
E3960	$LaAlO_3$(001) 5 × 5	$YBiO_3$	0.05	-, 400	300/1, 600/2
E3961	$LaAlO_3$(001) 5 × 5	$YBiO_3$	0.05	-, 400	300/1, 600/1
E3962	*a*-Al_2O_3 10 × 10	ZnO + Na_2IrO_3	0.002 + 0.016	-, 450	300/1, 2500/15 + 300/1, 15000/15
E3969	$LaAlO_3$(001) 5 × 5	$YBiO_3$	0.05	-, 600	300/1, 30000/10
E3981	$LaAlO_3$(001) 5 × 5	$YBiO_3$	0.05	-, 600	300/1, 600/8
E3987	$SrTiO_3$(001) 5 × 5	$YBiO_3$	0.05	-, 600	300/1, 600/8
E3988	$SrTiO_3$(001) 5 × 5	$YBiO_3$	0.1	-, 600	300/1, 600/8
E3989	$SrTiO_3$(001) 5 × 5	$YBiO_3$	0.2	-, 600	300/1, 600/8
E3990	$LaAlO_3$(001) 5 × 5	$YBiO_3$	0.05	-, 600	300/1,
E3991	MgO(001) 10 × 10	$YBiO_3$	0.05	-, 600	300/1,
E3992	YSZ(001) 10 × 10	$YBiO_3$	0.05	-, 600	300/1,
E3993	$LaAlO_3$(001) 5 × 5	$YBiO_3$	0.05	-, 600	300/1, 1800/8
E3994	$LaAlO_3$(001) 5 × 5	$YBiO_3$	0.05	-, 600	300/1, 3000/8
E3995	$LaAlO_3$(001) 5 × 5	$YBiO_3$	0.05	-, 600	300/1, 5000/8
E3996	$LaAlO_3$(001) 5 × 5	$YBiO_3$	0.05	-, 600	300/1, 7500/8
E3998	$LaAlO_3$(001) 5 × 5	$YBiO_3$	0.05	-, 600	300/1, 7500/8
E4010	$SrTiO_3$:Nb(001) 5 × 5	$YBiO_3$	0.1	-, 600	300/1, 5000/5
E4011	$SrTiO_3$:Nb(001) 5 × 5	$YBiO_3$	0.1	-, 600	300/1, 600/5
E4015	$SrTiO_3$(001) 5 × 5	$YBiO_3$	0.05	-, 600	300/1, 7500/8
E4016	$SrTiO_3$(001) 5 × 5	$YBiO_3$	0.05	-, 600	(20/1, 30 s pause) x 45,
E4017	$SrTiO_3$(001) 5 × 5	$YBiO_3$	0.05	-, 600	(20/1, 60 s pause) x 45,
E4018	$SrTiO_3$(001) 5 × 5	$YBiO_3$	0.2	-, 600	(20/1, 60 s pause) x 45,
E4026	$SrTiO_3$:Nb(001) 5 × 5	$YBiO_3$	0.05	-, 600	300/1, 10000/5
E4028	*c*-Al_2O_3 10 × 10	Na_2IrO_3	0.016	-, 450	300/1, 15000/15
E4029	*c*-Al_2O_3 10 × 10	ZnO + Na_2IrO_3	0.002 + 0.016	-, 450	300/1, 2500/15 + 300/1, 15000/15
E4034	*c*-Al_2O_3 10 × 10	ZnO + Na_2IrO_3	0.002 + 0.016	-, 450	300/1, 2500/15 + 300/1, 15000/15
E4035	*c*-Al_2O_3 10 × 10	ZnO + Na_2IrO_3	0.002 + 0.016	-, 450	300/1, 2500/15 + 300/1, 15000/15
E4036	*a*-Al_2O_3 10 × 10	$YBiO_3$	0.05	-, 600	300/1, 60000/5

(Continued on next page)

Table A.1 (Continued) List of all samples fabricated by pulsed laser deposition during the doctoral research. Square substrate dimensions are given in mm^2; ∅ denotes the diameter of circular wafers. T is the heater temperature prior to deposition and P is the corresponding heater power. Growth temperature T_g is estimated via $T - 50$ °C. Deposition processes involving more than one target are indicated by a "+". Abbreviations: p_{O2} oxygen partial pressure, ps: laser pulses, YSZ: ZrO_2:Y, YAO: $YAlO_3$, GZO: ZnO:Ga(4 at%).

Sample ID	**Substrate**	**Epilayer**	p_{O2} **(mbar)**	T (°C), P **(W)**	**Steps [ps/freq. (Hz)]**
E4039	a-Al_2O_3 10 × 10	ZnO +	0.002 +	-, 450	300/1, 2500/15 +
		Na_2IrO_3	0.016		300/1, 15000/15
E4040	a-Al_2O_3 10 × 10	ZnO +	0.002 +	-, 450	300/1, 2500/15 +
		Na_2IrO_3	0.016		300/1, 15000/15
E4047	MgO (001) 10 × 10	$YBiO_3$	0.05	-, 600	300/1, 1200/5
E4048	a-Al_2O_3 10 × 10	$YBiO_3$	0.05	706, 600	300/1, 2000/5
E4049	a-Al_2O_3 10 × 10	ZnO +	0.002 +	-, 450	300/1, 2500/15 +
		Na_2IrO_3	0.016		300/1, 15000/15
E4050	a-Al_2O_3 10 × 10	ZnO +	0.002 +	-, 450	300/1, 2500/15 +
		Na_2IrO_3	0.016		300/1, 15000/15
E4051	a-Al_2O_3 10 × 10	ZnO +	0.002 +	-, 450	300/1, 2500/15 +
		Na_2IrO_3	0.016		300/1, 15000/15

A.2 Exciton ionization field in Na_2IrO_3 - sample preparation for pump-probe spectroscopy

Together with Dr. Zhanybek Alpichshev, member of Prof. Nuh Gedik's group at the Massachusetts Institute of Technology (MIT), an ongoing collaboration was initiated in 2014 to perform ultrafast terahertz and optical pump-probe spectroscopy. In the terahertz range, large-area thin film samples are preferable. Previously, Alpichshev *et al.* [122] performed an ultrafast optical study of photoexcitations in Na_2IrO_3 single crystals. Across the Neél temperature, they observed a sharp increase in the binding energy of excitons formed upon entering the ordered phase. This finding was interpreted as evidence of spin-liquid physics. Within the scope of this collaboration, terahertz and optical pump-probe studies are to be performed on Na_2IrO_3 thin films to put the experimental evidence on a firmer foundation.

Similar to the previous experiment [122], the proposed optical pump-probe experiment is performed with a pulsed Ti:sapphire laser with 800 nm center wavelength and 60 fs pulses. An external pulse picker is used to reduce the repetition frequency to 1.6 MHz in order to avoid

heating effects on the sample. The laser spot has a Gaussian beam with a size of about 100 μm FWHM. In standard pump-probe experiments, a single pump pulse optically excites the sample. The resulting dynamical response of the system is measured by a change in reflectivity of a separate probe beam as a function of time delay between pump and probe pulse. To achieve phase-sensitivity and thus distinguish the physical origins of the dynamical response of the system a variation of the pump-probe technique, called the heterodyne transient grating method, is employed. The pump-probe technique and its phase-sensitive variant are described in detail elsewhere [122].

Sample passivation Since Na_2IrO_3 has a chemical instability in air, thin film samples require passivation prior to shipping to MIT. The instability primarily affects the sample surface and can be recognized by a dull film surface or a white precipitate, see also Ref. [MJ2]. Degradation occurs in the simultaneous presence of CO_2 and H_2O [102] and the primary decomposition product is hydrated sodium carbonate (cf. Sec. 5.3). There are indications that a pristine film surface can be recovered by a treatment with phosphoric acid diluted with water in a ratio of 1:80. Light microscopy of a decomposed sample before and after acid treatment is shown in Fig. A.1 and demonstrates the removal of the decomposition products. A subsequent XRD experiment showed no negative effect on the bulk structure and suggests that this holds true also for other bulk properties. In conclusion, this treatment might be viable when performing measurements of bulk properties after an extended period of time and is generally desirable when performing any type of top contacting as in the present case. Initially, photoresist from the standard lithography process was used as a passivation layer. However, it produces visible cracks during cooling and must hence be removed with acetone prior to the experiment. For this reason, passivation instead involves acrylic (PMMA) which is transparent in the infrared and might furthermore be more resistant to thermal cycles. A removal of the passivation layer during optical (800 nm) pump-probe experiments is then unnecessary.

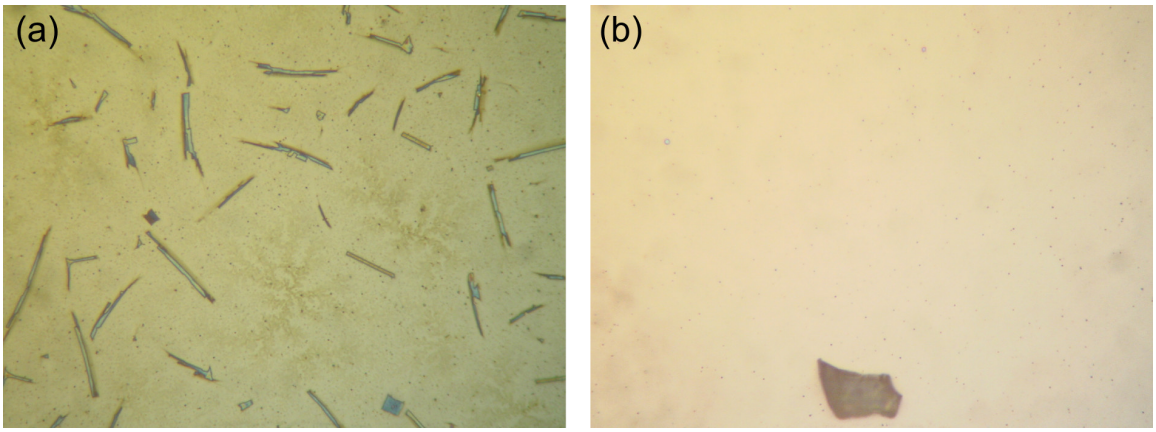

Figure A.1 Light microscopic images of a typical Na_2IrO_3 sample, $\approx$ 100x magnification: (a) as-grown but several days old, (b) same sample after treatment with diluted phosphoric acid.

Terahertz pump-probe spectroscopy Preliminary terahertz pump-probe measurements on Na_2IrO_3 films grown on YAO(001) were unsuccessful; no change in signal was observed above and below the Neél temperature. A possible explanation is that the pump pulse heated up the sample. In hope of providing a better heat sink, sapphire substrates were used in subsequent measurements. Prior to film deposition, the substrates' optical properties relevant to the experiment were thoroughly characterized by the collaborators at MIT. However, experimental difficulties in performing terahertz pump-probe spectroscopy on the present film samples yet remain.

Optical pump-probe spectroscopy Alternatively, an optical pump-probe study is proposed to verify the excitonic nature of the photoexcitations in Na_2IrO_3 and investigate their ionization field. The binding energy is about 4 meV. By a comparison with GaAs, which has a similar binding energy, its radius is estimated to be approximately 10 nm. For these excitons, the ionization field is thus of the order of about 500 V per millimeter. Such large dc voltages can in principle be applied in thin film samples without the risk of destroying them. Due to an estimated ionization radius of 10 nm, the film thickness is required to be at least 100 nm. Because Na_2Ir_3 has a quasi-two-dimensional, layered structure, the exciton effective mass along the *c*-direction is presumably very large. It is thus more difficult to separate an exciton in that transversal direction. Instead, the optical pump-probe experiment seeks to investigate the in-plane interaction and ionization field, respectively. For (001)-oriented Na_2IrO_3 thin films, this requires a contact geometry capable of providing in-plane electrical fields. For this purpose, interdigital contacts are applied by means of a photolithography mask and dc-magnetron sputtering, see Fig. A.2. During the experiment, only about a hundred volts can practically be applied. To achieve sufficiently high in-plane electric fields, the photolithography mask is designed to produce a "finger"

thickness and spacing of about 5 μm each. The interdigital part, as well as the contact pads, each enclose an area of 1 mm^2 which is sufficient for wiring and the accommodation of the 800 nm laser beam having a spot size greater than 100 μm. Again, the sample is passivated by PMMA.

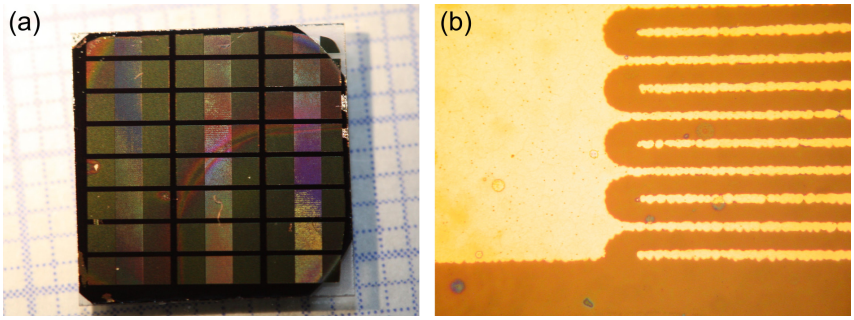

Figure A.2 Interdigital contacts for optical pump-probe spectroscopy. (a) Photograph of a Na_2IrO_3 film sample with dc-sputtered interdigital gold contacts and PMMA passivation. (b) Light microscopy image of the same sample in $\approx$ 100x magnification. Obviously, the interdigital size and spacings deviate from the desired 5 μm.

A.3 $YBiO_3$ thin films

A.3.1 Rietveld refinement of polycrystalline $YBiO_3$ PLD source targets

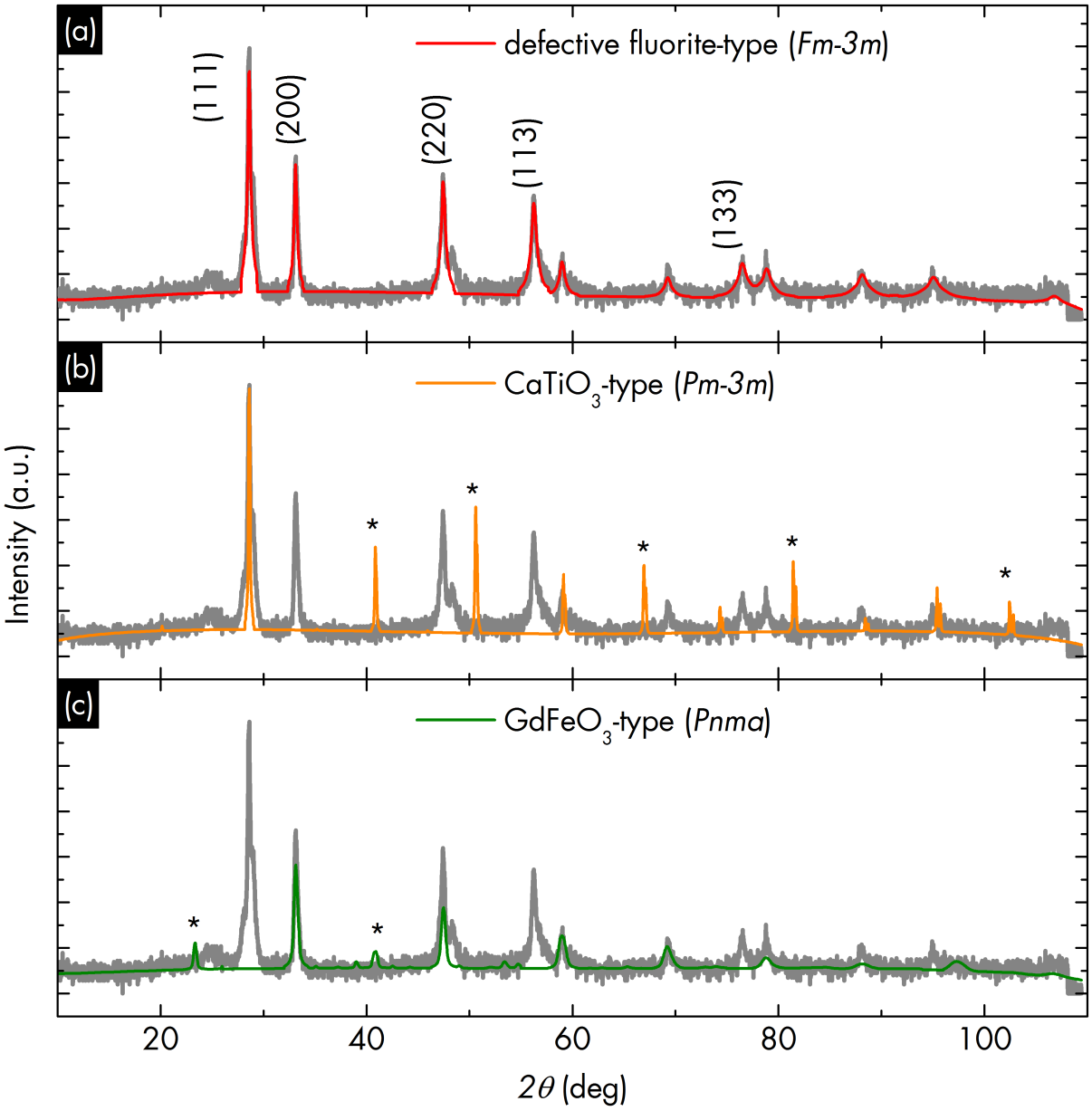

Figure A.3 Rietveld refinement of a polycrystalline $YBiO_3$ source target using the defective fluorite-type [93] (a), $CaTiO_3$-type (ICSD 31865, a = 4.405 Å [38]) (b) and $GdFeO_3$-type (ICSD 16688) (c) structural models. The refined lattice parameters are a = 5.4279(4) Å (a), a = 4.420(1) Å (b), and a = 5.461(5) Å, b = 7.711(8) Å, c = 5.415(5) Å. Only the fluorite-type structure can explain all of the experimentally observed (111) (200), (220), (113) and (133) reflexes (a). Bragg reflexes not observed in the pattern are denoted by $*$ (b,c). Additional Y_2O_3 and Bi_2O_3 phases, indicating an incomplete reaction of the starting materials, were not refined. Goodness of fits χ^2: 3.98 (a), 20.99 (b), 6.91 (c).

A.3.2 Substrate pre-treatment

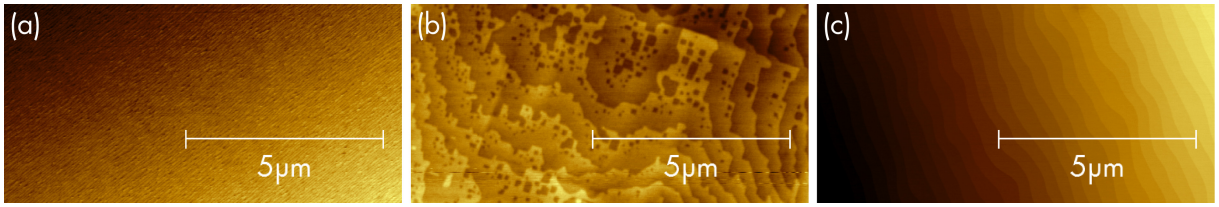

Figure A.4 AFM topographical images of single-crystalline substrate after chemical etching and annealing. LAO(001) (a) was annealed in a tube furnace for 2 h at $T = 1050$ °C and $p_{O2} = 1000$ mbar. After chemical etching in a NH_4F-HF buffer solution for 30 s, STO(001) (b) and STO:Nb(001) (c) substrates were annealed for 2 h at $T \approx 950$ °C and $p_{O2} = 700$ mbar. RMS surface roughnesses in (a-c) range from 0.1 to 0.2 nm. Especially for STO:Nb, the treatment leads to the formation of uniformly stepped surfaces with smooth terraces.

A.3.3 YBO on STO(001):Nb - Out-of-plane orientation

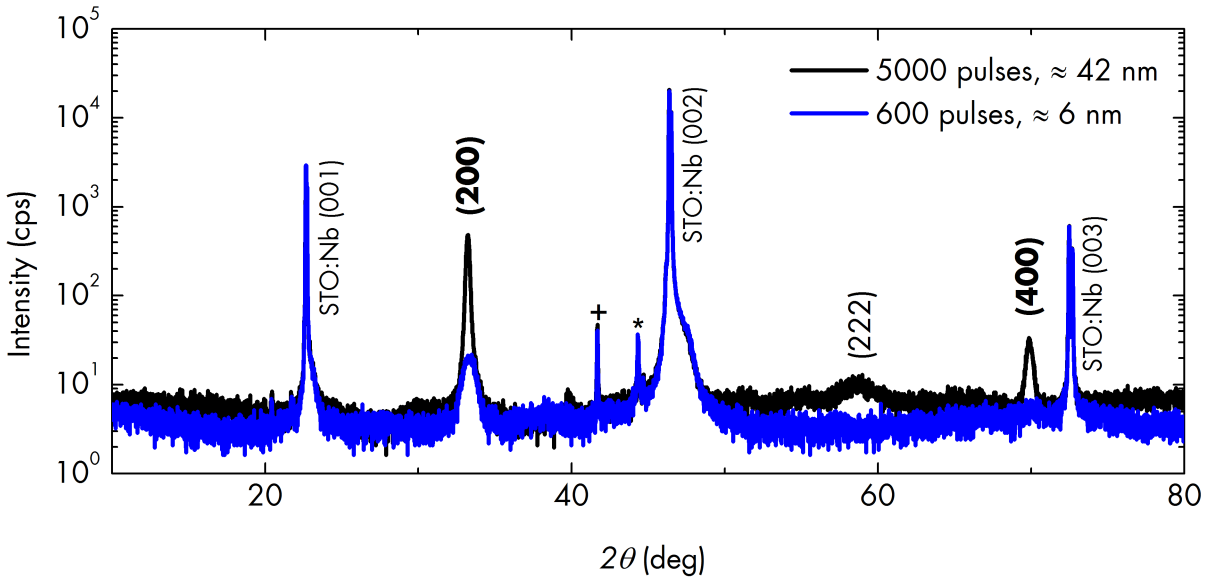

Figure A.5 XRD 2θ-ω scans of (100)-oriented YBO thin films deposited on STO(001). [Samples: E4010, E4011.]

A.3.4 SQUID magnetometry of YBO on LAO(001)

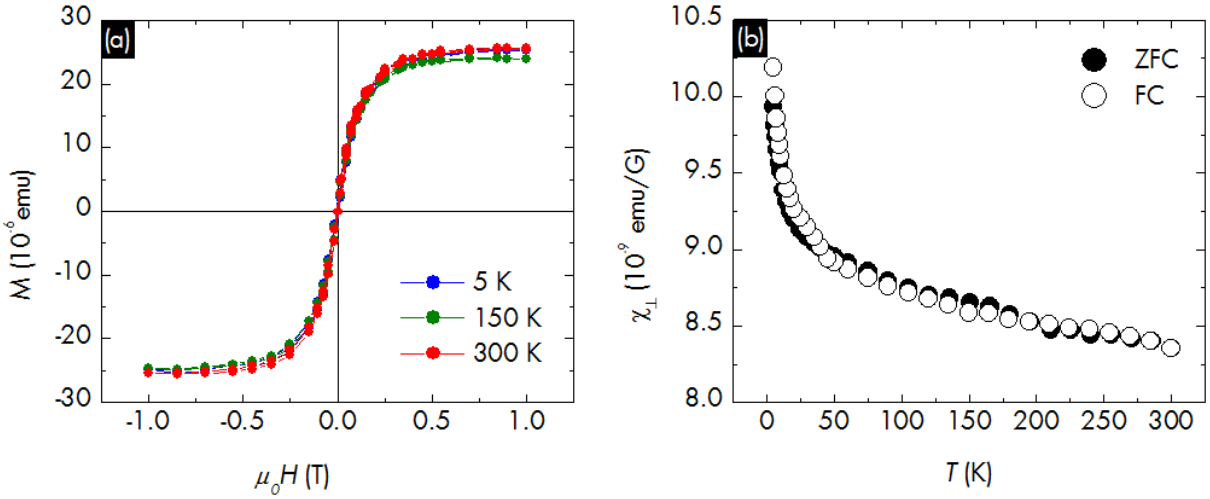

Figure A.6 SQUID magnetometry performed on a 600-ps YBO thin film deposited on LAO(001) at 0.05 mbar and 550 °C. (a) Isothermal magnetization M versus applied magnetic field $\mu_0 H$ at temperatures as indicated. (b) Temperature-dependent transverse magnetic susceptibility $\chi_\perp = M/H$ in an applied magnetic field of $\mu_0 H = 0.25$ T. The sample was free of ferromagnetic impurities and only a temperature-independent diamagnetic contribution of $M_{\text{dia}} = -1.85 \times 10^{-8} \mu_0 H$ emu was subtracted from both datasets. The data confirms that YBO is paramagnetic between 5 and 300 K. Paramagnetic behavior was expected since Y^{3+} and Bi^{3+} are non-magnetic ions and was previously reported in Ref. [51]. [Sample: E3959.]

A.3.5 XRD pole figures

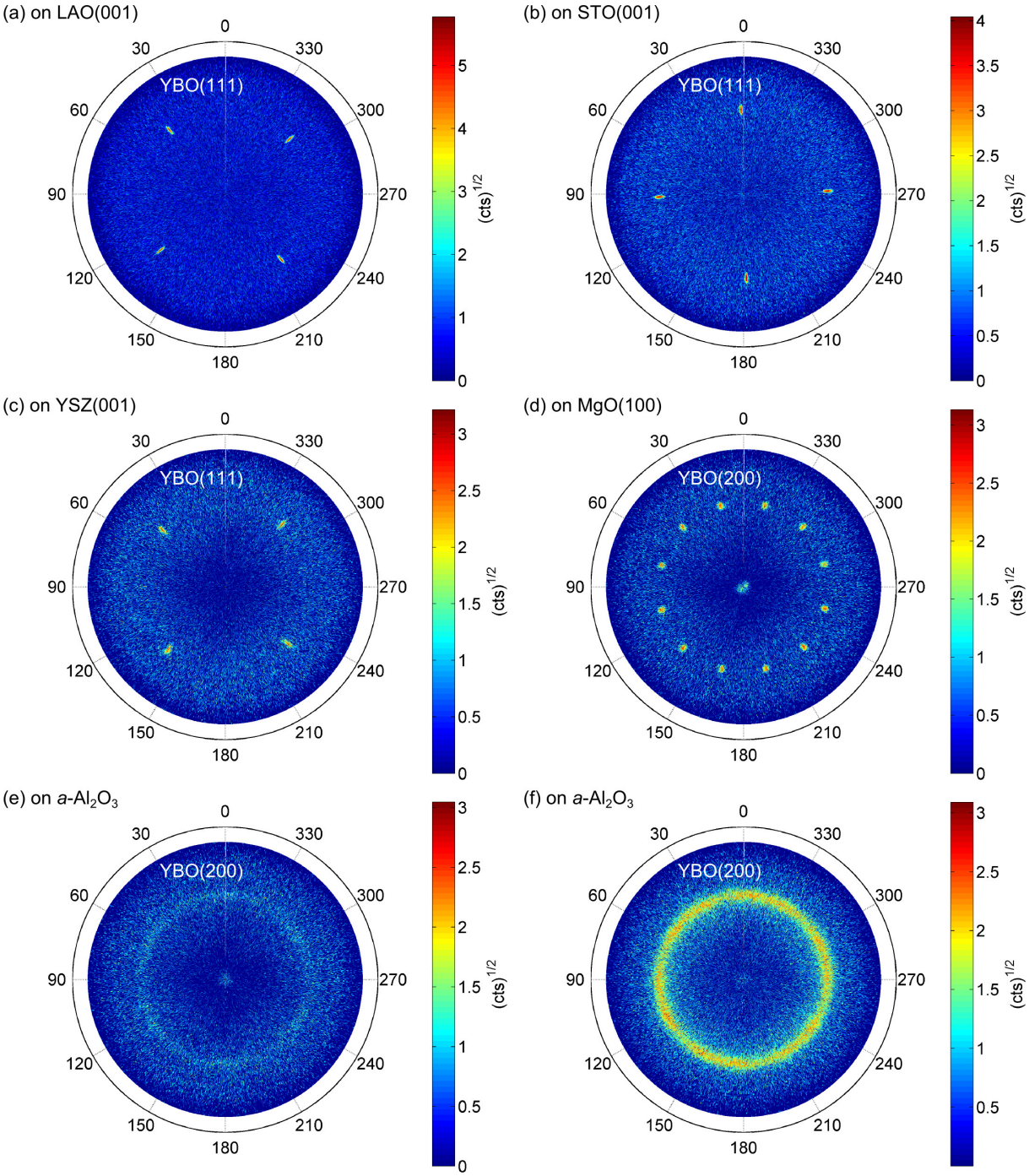

Figure A.7 XRD ϕ-χ pole figures (PF) of YBO thin films deposited on various substrates. The substrate material and the measured asymmetric YBO reflex are indicated in the figures. The measured YBO films have an out-of-plane orientation (hkl) and a thickness d of: (a) (100), $d \approx 29$ nm, (b) (100), $d \approx 10$ nm, (c) (100), $d \approx 10$ nm, (d) (111), $d \approx 38$ nm, (e) (111), $d \approx 57$ nm, and (f) (111), $d \approx 1660$ nm. [Samples: E3981 (a), E3989 (b), E3992 (c), E4047 (d), E4048 (e), E4036 (f).]

Acknowledgments

I wish to express my sincere gratitude to Prof. Dr. Michael Lorenz for proposing the initial research topic that has led to the present thesis, and for his continuing and committed support in my research. I am grateful also to Prof. Dr. Marius Grundmann for accepting me into the Semiconductor Physics Group. I very much thank Gabriele Ramm for the preparation of the many source targets and SNMS measurements, Monika Hahn for performing most of the sample contacting and photolithography, Jörg Lenzner for SEM and EDX measurements, Ulrike Teschner for optical transmission measurements, and Holger Hochmuth for his technical support in PLD. Further, I am thankful to Dr. Rüdiger Schmidt-Grund and Steffen Richter for the measurement and more involved analysis of spectroscopic ellipsometry data, and the helpful review of my manuscript. I am indebted to Dr. José Barzola-Quiquia and Francis Bern of the Division of Superconductivity and Magnetism for magnetometry and magnetoresistance measurements and the discussion of the data produced. Prof. Dr. Dmytro Inosov's (TU Dresden) initiative in securing beam time for a joint neutron diffraction experiment at Institut Laue-Langevin, Grenoble is greatly acknowledged. I thank Prof. Dr. Yvonne Joseph and Uwe Sczech (TU Bergakademie Freiberg) for high pressure sintering, and Dr. Ji Zou and Prof. Dr. James Shen (Stockholm University) for spark plasma sintering of PLD targets. Funding by Deutsche Forschungsgemeinschaft (DFG) within research project LO790/5-1 "Oxide topological insulator thin films" and the collaborative research centre (SFB) 762 "Functionality of Oxide Interfaces" is greatly acknowledged.